Modelling and prediction of non-linear scale-up from an Ultra Scale-Down membrane device to process scale tangential flow filtration

A thesis submitted to University College London for the degree of
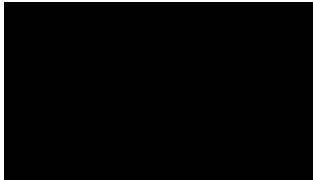
Doctor of Philosophy

by

Mohd Shawkat Hussain

July 2019

Department of Biochemical Engineering
University College London
Torrington Place
WC1E 7JE

Declaration

I, Mohd Shawkat Hussain, confirm that the work presented in this thesis is my own. Where information has been derived from other sources, I confirm that this has been indicated in the thesis.

Mohd Shawkat Hussain

23 July 2019

Abstract

Ultra scale-down (USD) tools have demonstrated the huge potential for accelerated process development by significantly reducing the material requirements and providing better solutions, as part of the Quality by Design initiative. Key benefits of using USD techniques include the relatively small quantities of feedstock and minimal capital equipment needed to generate large volumes of statistically significant process data in a short period, leading to significant time and cost savings during process development. However, the use of small scale devices such as the stirred cell filtration units have been primarily limited to preliminary testing and initial screening due to their geometric and flow dissimilarities to tangential flow filtration at scale. As a result, process development and optimisation trials are generally carried out using the smallest commercially available TFF cassettes, the use of which are primarily limited by time and material constraints that are invariably present at the early stages of process development. Therefore, the central focus of this work was to develop a USD methodology and model to accurately predict the performance of large scale tangential flow filtration (TFF) using a USD membrane filtration device.

The commercial package COMSOL was used to carry out computational fluid dynamics (CFD) modelling and simulation of the fluid flow dynamics in Pellicon TFF cassettes with different feed screens and a USD membrane device, in order to develop average wall shear rate correlations and channel pressure drops expressed as functions of the respective hydrodynamic conditions across scales. In addition, the impact of non-TFF related factors such as the system and cassette-specific hydraulic resistances on TFF performance was characterised using semi-empirical models. Finally, a scale-up methodology and mathematical model to predict the large scale performance using USD data was developed by combining the various resistances, channel pressure drop correlations and an empirical USD-derived model that characterises the specific feed-membrane interactions. The CFD simulations were independently verified using 2D particle imaging velocimetry to compare experimental data to the CFD simulated data.

100-fold scale-up experiments were carried out based on equivalent averaged wall shear rates $(\overline{\gamma}_w)$ as the geometry-independent parameter. Permeate flux excursions were carried out to validate the USD methodology and prediction model, by comparing USD model predictions against the large scale experimental data. Different membranes, feed screens (A, C and V) and feedstock, ranging from simple

proteins like Bovine Serum Albumin (BSA) to more complex, multicomponent feed such as *Escherichia coli* homogenate, were used. Predicted flux and transmission results were in good agreement with the large scale experimental data, showing less than 5% difference across scales, demonstrating the robustness of the non-linear scale-up model.

Following the successful validation of the scale-up methodology and prediction model, other potential applications of the USD membrane device such as the optimisation of TFF microfiltration was demonstrated using *Saccharomyces cerevisae* and *Chlorella sorokiniana*. Fed-batch concentration experiments using *Saccharomyces cerevisae* were done to compare the volumetric throughput limits. The USD-predicted capacity limit of 49.2 L/m^2 was very similar to the experimental large scale capacity value of 52.0 L/m^2, and considered fully scalable within experimental errors. Finally, fouling studies were performed using *Chlorella sorokiniana* and the USD device to investigate the impact of media type and growth conditions on the filtration performance. The results indicated a strong correlation between soluble fouling species, such as exopolysaccharides and carbohydrates, rather than the algal biomass. A novel, dynamic flux control methodology was developed based on empirically determined critical fluxes expressed as a function of cell concentration. The dynamic control strategy was successfully verified by performing a 50-fold concentration experiment using a hollow fibre module and the USD device. An improvement of greater than 50% in average throughput was achieved using the 3-step flux cascade compared to the traditional flux-time/capacity optimised fluxes, with no observable increase in TMP throughout.

The work presented here demonstrates the potential of ultra scale-down tools coupled with a mathematical modelling approach to establish a predictable scale-up performance, which can be used to rapidly develop and optimise tangential flow filtration processes, regardless of differences in geometry, flow configuration and system setup.

Impact statement

The scaling of tangential flow filtration processes in industry is something that is still not entirely well understood or well characterised (unlike dead-end filtration), particularly for scaling between dissimilar geometries, which significantly limits the use of small scale devices for high throughput optimisation due to the inability for small scale data to be successfully translated to large scale performance. The work, and more importantly, the methodology and approach presented here demonstrates a novel CFD-aided approach to developing a robust scale-up across any two systems, regardless of the differences in equipment, flow configuration, or feed screens. CFD was used to understand the various phenomenon observed in tangential flow filtration processes, to be able to accurately characterise them using semi-empirical models and translate USD-generated data into the performance expected at large scale.

The developed USD methodology and prediction model can be readily applied and implemented by anyone, both in industry and academia, who uses screened TFF cassettes for their filtration needs, such as concentration, buffer exchange (UF/DF) between steps and for final fill/formulation (particularly for high viscosity solutions). Since the Pellicon cassette range (from Millipore) was the choice of large scale cassette in this study, all the CFD characterisation work, models and methodology have been specifically designed to suit Pellicon cassettes and thus, both the company (Millipore) and its customers stand to readily benefit from using this model to optimise their scaling requirements. However, this approach can be readily implemented by anyone using a USD membrane device and Pellicon cassettes. The models presented here could be complemented with a graphical user interface (GUI), where the user could, for example, select the type of feed screen (A, C or V), input the feed and permeate viscosities and the empirical USD model parameters. All of the user inputs would then be used to automatically compute and output simulated data for process scale, either graphically or numerically (capacity, critical fluxes/TMP).

The methodology described in this thesis can also be applied to, for example, other TFF cassettes (with different screens and path lengths) and small scale devices, provided the respective geometries are known and can be accurately modelled using CFD, and using the appropriate physics and model assumptions to capture the appropriate boundary conditions and fluid flow. The CFD modelling approach and method development steps described within this thesis can thus be readily replicated

by anyone competent in using CFD techniques, to carry out the model simulations and generate their geometry-specific average wall shear rate and pressure drop correlations needed for an accurate and predictable scale-up performance.

The work presented here also creates opportunities for further research to be carried out, such as advancing the use of CFD as a powerful tool to understand and resolve any fluid flow problem, and how the increased understanding of the simulated processes at the micro-scale can aid the development of process optimisation and scale-up. This research has been presented at various conferences, while the research papers (currently being drafted) will further facilitate the applications of using CFD and USD technologies within both academia and the bioprocessing community as a whole. The use of USD membrane device as a high throughput tool also benefits UCL and academia, and this work has demonstrated a robust and scalable USD model that is able to replicate the large scale TFF performance using millilitre quantities of feed and general lab-scale equipment.

Acknowledgements

Firstly, thanks to the Almighty for His continual wisdom and guidance throughout the four years. This research project would have been that much more difficult without the supervision and continuous guidance from Dr. Yuhong Zhou – a better supervisor I could not have wished for/had. I would like to thank Yuhong for her constant support and mentoring during this project, particularly towards the end, for providing me with valuable feedback and suggestions without which this thesis would not have been a complete work. I would also like to thank UCL and ORS for funding my PhD during its entirety.

A special acknowledgement and gratitude to Dr. Paul Beckett, who provided me with a wealth of industrial based knowledge in tangential flow filtration and was there to support me all the way, despite his extremely busy schedule and work commitments. Without his inputs and comments, this thesis may not have been to the same quality as it is now.

A massive thank you to all my friends, colleagues and the staff at UCL. I would like to personally thank Dr. Gareth Mannall (for helping me with any filtration related queries and keeping the lab running in good order to be able to carry out quality research), Professor Panagiota Angeli and her students (for the PIV work to be carried out at such short notice), Dr Joseph Newton, Dr. Alex Chatel, Dr. Andrea Rayat, Professor Mike Hoare, Dr. Mike Sulu, Jim Davy, and countless people who have assisted me in some way or the other during the course of this PhD. Not to forget the continuous support I received from Merck Life Sciences KGaA, both technical (special thanks to Zoe Blanck, Frederic Sangler) and commercial (Adina Paun). Similarly, many thanks to Sartorius Stedim Biotech, and namely Dr. John Emerson and Andy Passmore, who have greatly helped out with all technical issues with the Sartoflow and being generous enough to loan me the unit to complete my experiments on time. Finally, a special mention to the COMSOL support staff, who were always there to explain and point me towards the right direction for my CFD work and replying promptly to any of my queries.

Last but not least, I am extremely grateful to my family and close friends for their continued love and unwavering support, who kept me going through my difficult periods.

Table of contents

List of figures

List of tables

Nomenclature

AOM   Algogenic organic matter

BBM   Bold's Basal Medium

BSA   Bovine serum albumin

CAD   Computer-aided design

CFD   Computational fluid dynamics

EG:JM   *Euglena Gracilis*: *Jaworski's* Medium

EOM   Extracellular organic matter

EPS   Exopolymeric substances/exopolysaccharides

Fab'   Fragment, antigen binding

FDA   Food and Drug Administration

FEL   Fluid entrance/exit length

LMH   Litres per hour per square meter of membrane surface area

LMM   Litres per minute per square meter of membrane surface area

mAb   Monoclonal antibody

MF   Microfiltration

NWP   Normalised water permeability

PES   Polyethersulfone

PGP   PIPES-Glucose-Phosphate

PIPES   Piperazine-N,N′-bis(2-ethanesulfonic acid)

PP   Polypropylene

PSD   Particle size distribution

PVDF   Polyvinylidene Difluoride

PVP   Polyvinylpyrrolidone

QbD   Quality by Design

RDF   Rotating disc filter

RO   Reverse osmosis

SS   Stainless steel

SST   Shear Stress Transport

TEP   Transparent exopolymeric particles

TFF   Tangential flow filtration

TMP'   Flow initialised TMP at zero net permeate flux

TMP   Transmembrane pressure

UF   Ultrafiltration

USD   Ultra scale-down

1 Introduction

During a typical product development cycle, there are many occasions when processes need to be scaled-up and scaled-down. A few prime examples include transfer from research/clinical trials to a pilot-scale production, increasing commercial supply to match rising product demand or more specifically in the biopharmaceutical industry, coping with increasing upstream product titres because of optimised cell lines, processes and operating conditions. The global demand for biopharmaceutical products such as enzymes, vaccines, antibiotics, and therapeutics are on the rise (Tripathi and Shrivastava, 2018), and puts immense pressure on the separation and purification unit operations downstream.

Tangential flow filtration (TFF) is a technique that is widely used in pharmaceutical, biopharmaceutical and purification industries (Baruah et al., 2005). Ultrafiltration (UF) and microfiltration (MF) are two of the most widely used processes, and applications include concentration of monoclonal antibodies, high viscosity final fill/formulation, protein fractionation and concentration, buffer exchange, to name a few. Tangential flow filtration benefits from running in mild operating conditions (low temperatures and pressures) and high throughputs, which is beneficial for processing shear-sensitive biological macromolecules, thus making it an essential purification technology for biopharmaceutical applications.

To be able to determine suitable filtration processes and subsequently develop optimised operating conditions, numerous lab-scale experiments are conventionally required, and for expensive products such as monoclonal antibodies and novel proteins, the associated costs to produce relatively large volumes of feed for such experiments can be very high. To reduce costs, scale-down experiments and/or appropriate mathematical models are generally used (Brown et al., 2011). However, scale-up of tangential flow filtration presents quite a few significant challenges. The flow fields, pressure gradient and concentration profiles along the membrane govern the performance of tangential flow filtration. The current understanding of such complex phenomenon is limited, making it difficult to model their behaviour at different scales by conventional methods. Linear scaling is the established form of TFF scaling in industry and is done empirically over multiple step-ups (minimum scale-up ratio=1:10), which requires large quantities of feedstock that may not be readily available at early stages of the product development cycle. Furthermore, most of the scale-down work is limited by the availability of the cassettes themselves, the smallest

commercial lab-scale cassettes requiring >100 mL of feedstock per experiment (Shukla et al., 2007), while the concept of scaling-up by maintaining constant channel/path length is linear, albeit only theoretically. In practice, both the system setup and flow distribution changes upon scale-up, contributing to added resistances and pressure losses which are not encountered nor accounted for in the scale-down experiments, and could lead to significant differences between experimental and predicted performances.

Stirred-cell units operated in dead-end mode are commonly used at lab-scale for trial work with membranes to obtain an indication of the desired performance and specification, including fouling, filter retention and throughput studies, due to their simplicity and ease of operation (Janson, 2011). However, such lab-scale concepts do not scale-up well due to their non-linearity with respect to geometry and hydrodynamics across scales and consequently require large scale verification studies using TFF cassettes. Flat-sheet discs used for experimental prediction of large-scale tangential flow filtration have proven to be problematic and shown discrepancies in performance; a 40-55% difference compared to large-scale, depending on cassette, crossflow system and feedstock used (Brown et al., 2011). Therefore, it is of great interest to carry out USD tests and, more importantly, be able to transfer the ultra scale-down data from dead-end stirred-cell devices to tangential flow filtration in narrow, screened channels. To date, not much work or research have been done to establish non-linear scale-up, primarily due to lack of relevant understanding of fluid dynamics and mass transfer effects occurring at both scales. Ma et al. (2009), Fernandez-Cerezo et al. (2019) and Guo et al. (2016) recently demonstrated non-linear scale-up from 25 mm flat-sheet membrane discs to lab-scale tangential flow filtration, for recovery of Fab' and concentration of mAb feedstock, respectively. However, both scale-ups were carried out using a single feedstock, with reported fluxes of ±20 % across scales; therefore, these studies merely serve as a framework and proof-of-concept for establishing non-linear scaling and do not provide a robust model for reproducible and accurate prediction of large-scale TFF performance. Furthermore, validation for most scale-up models and predictions are typically done using a single combination of feedstock and membrane type (material, pore size). Thus, even though the model predictions were validated against the particular combination of feedstock and membrane, there were no indications to the robustness or accuracy of those models if parameters such as the choice of feedstock and/or membrane are varied. A robust model is one that behaves consistently for

31

different input variables and is able to generate statistically representable data similar to the experimental data each time.

Even though scale-down devices have the potential for high throughput optimisation at early stages of process development, manufacturing processes at large scale often look quite different to those at lab-scale, in terms of system geometry, ancillary equipment and volume of feed material processed. Two key aspects still need to be considered to address the potential issues of robustness, scalability and reproducibility upon scale-up. Firstly, any differences in design and flow patterns between the devices need to be accounted for; secondly, the system itself, which changes upon scale-up. For example, a large dead volume at large-scale due to ancillary equipment and pipework could lead to an over-prediction of the tangential flow filtration step and limiting the use and application of the scale-down model (Lutz, 2015). Despite the limitations of existing scale-down methods, their use is strongly recommended for process characterisation and investigate processing challenges and are instrumental in supporting biopharmaceutical process development (Challener, 2016). Therefore, a comprehensive understanding of the fluid flow and associated phenomenon across scales to improve predictive scalability of scale-down filtration techniques is needed. Scale-down tools enable accelerated process characterisation and optimisation and help solve processing challenges at much earlier stages of process development than traditionally possible. Thus, there is a significant and urgent need for a robust scale-down model to deliver results that are statistically representative of large-scale, thereby reducing both time and number of scale-ups needed to get to production scale, leading to increasing productivity and reduced manufacturing risks.

1.1 Overview of filtration technology

Filtration is a pressure-driven process that involves the separation of solids from a solid/liquid mixture by forcing the mixture through a semi-permeable membrane; pressure applied to the upstream feed side forces the fluid through the membrane pores and out as permeate. The necessary pressure difference can be generated using pressurised gas on the feed side, vacuum applied on the filtrate side or typically using a piston/pump on the upstream side of the membrane. Relatively small molecular weight species such as water molecules, soluble proteins and salts pass through the membrane as permeate, while the larger molecules are retained on the feed side of the membrane and forms the retentate.

Microfiltration can be defined as a filtration process that separates out un-dissolved species (solids) from dissolved species using a micro-porous (typically 0.1-10 μm) or an 'open UF' membrane (typically >300 kDa), characterised by low transmembrane pressures (0.3-0.6 bar) and high permeation fluxes of 30-100 LMH on average (Noble and Stern, 1995). Figure 1.1 highlights some of the common separation techniques used to separate different particles.
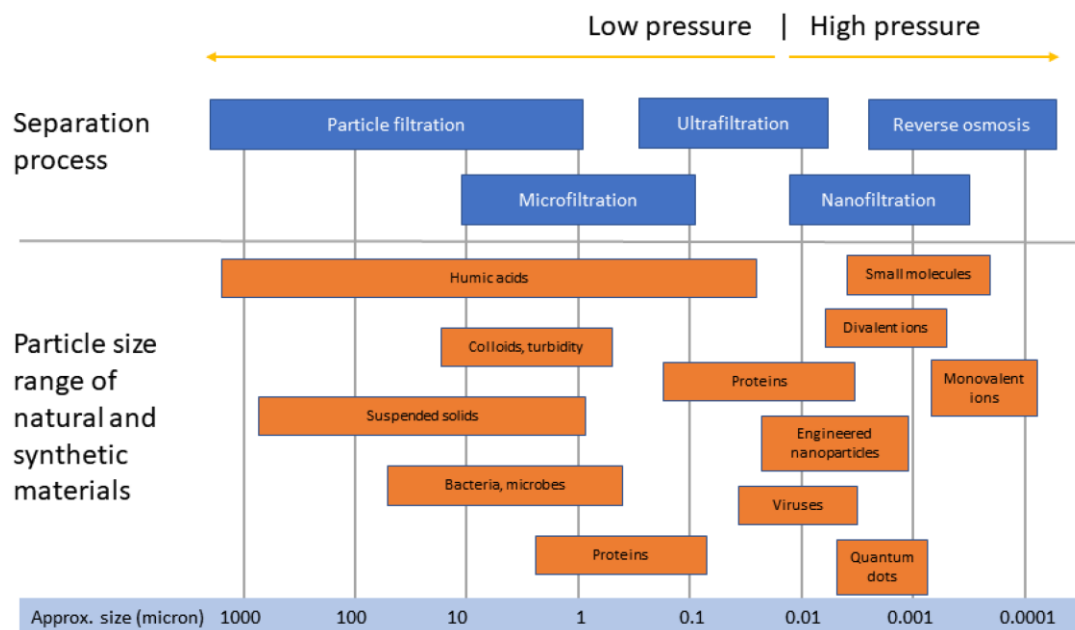
Figure 1.1 Overview of common particles with recommended filtration separation technology based on size and/or type of particle (Ostarcevic et al., 2018).

Membrane filters are available in different materials, configurations and pore sizes. Membranes are usually made of polymers, both synthetic and natural, such as cellulose, ceramic, nylon, polyvinylidene fluoride (PVDF), etc. In terms of membrane configurations, there are various types of modules commercially available. In most biopharmaceutical industrial applications, three such membrane configurations, namely, hollow fibre (Figure 1.2a), spiral-wound (Figure 1.2b) and flat sheet cassettes (Figure 1.2c), have been shown to be useful. Flat sheet cassettes are most commonly used in the biopharmaceutical industry as they generally have high packing densities (Millipore, 2003), although hollow fibres are also a very cost-effective format for concentration/diafiltration of dilute biomolecule solutions. Hollow fibres predominantly operate within the laminar flow regime and are ideal in cases where single use devices that are easy to use/operate are desired (WaterSep, 2009). Moreover, the small lumen diameters of the fibres make it one of the more efficient design with

respect to pumping and energy costs. Some of the key drawbacks of hollow fibre membranes include higher fouling tendencies compared to TFF cassettes, scalability limitations and low operating feed pressure ratings (<1-1.5 bar).
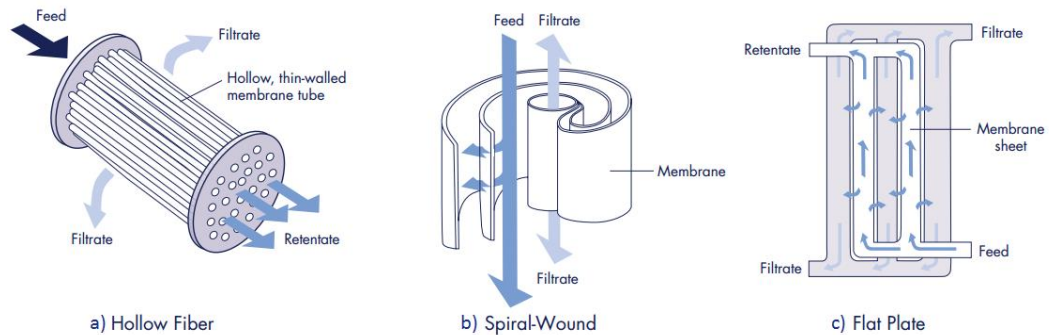
Figure 1.2 Different TFF configurations and the flow paths through the respective modules (Millipore, 2003).

Microfiltration can be carried out in three primary configurations, namely, dead-end, stirred and crossflow. Crossflow/tangential is when the feed flows tangentially to the membrane surface, compared to dead-end/normal mode of operation, where the feed flow applied is perpendicular to the membrane. Stirred configuration is essentially dead-end but includes a stirrer/agitator that creates added turbulence to reduce solids deposition on the membrane and thus the flux approaches a steady-state value with time, just like tangential flow filtration. Figure 1.3 illustrates the difference between crossflow and dead-end modes of operation.

A. Dead-end mode

FEED
(Q_F, P_F, C_F)

Flow

TMP

PERMEATE
(Q_p, P_P, C_p)

B. Crossflow mode

FEED
(Q_F, P_F, C_F)

RETENTATE
(Q_R, P_R, C_R)

Flow

TMP

PERMEATE
(Q_p, P_P, C_p)

Surface of
porous membrane

●	Solid particle
〜→	Path of fluid flow
Q_x	Flow rate
P_x	Pressure
C_x	Concentration
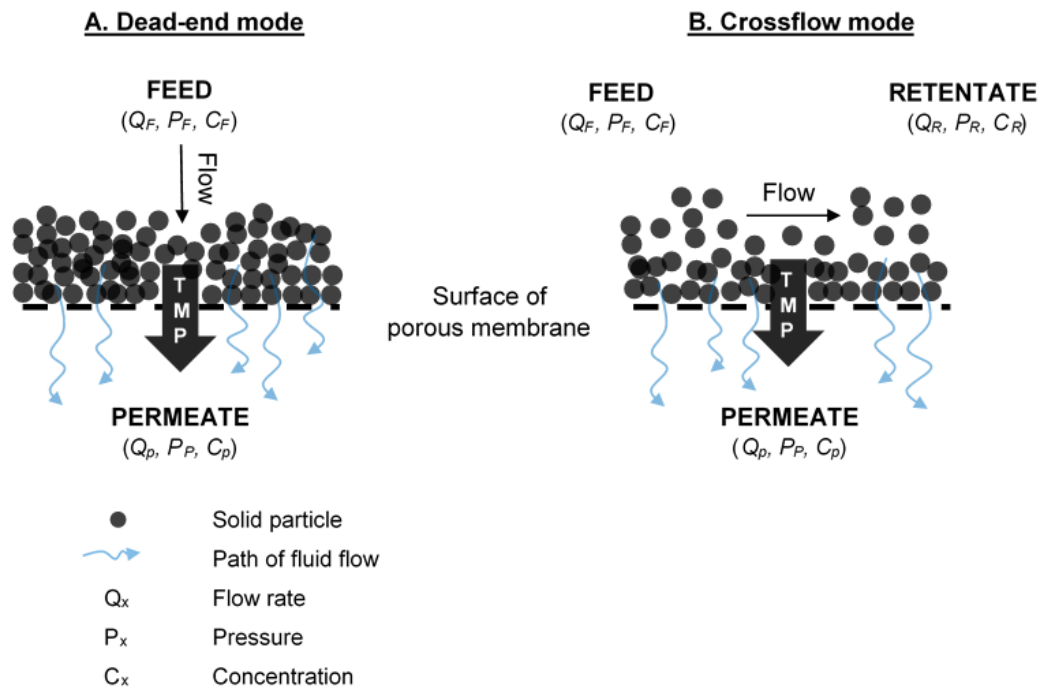
Figure 1.3 Illustration of dead-end (A) and crossflow (B) configurations.

Microfiltration and ultrafiltration processes incorporating tangential flow filtration are utilised in a wide range of biopharmaceutical applications. A few of the typical applications include purification and recovery of antibodies or recombinant proteins, vaccines, concentration and diafiltration, fermentation broth clarification/concentration, water and buffer purification (Saraswat et al., 2013). In the biopharmaceutical industry, tangential flow filtration is usually the preferred mode of operation over dead-end filtration because it allows for a longer uptime between cleaning cycles. The principal advantage is that the 'filter cake', which can clog the filter, is continuously flushed away during tangential flow filtration (the axial flow across the membrane surface minimises solids deposition and hence fouling), which increases the lifespan of the filter unit. For a fixed membrane area, TFF can be used as a continuous process unlike dead-end filtration, which is run in batches and hence TFF is recommended for valuable feeds containing a high proportion of small particulates (GE Healthcare, 2014). Crossflow velocities for screened cassettes are usually in the range of 0.1-1 m/s.

Furthermore, tangential flow filtration results in a non-zero steady-state permeate flux (J_{ss}) as the overall permeability approaches a final limiting value over time. In contrast, the permeate flux rapidly declines to zero as the cake approaches its limiting

thickness when operating in dead-end mode. Figure 1.4 shows the typical flux profiles generated during dead-end and crossflow modes operated at constant TMP.
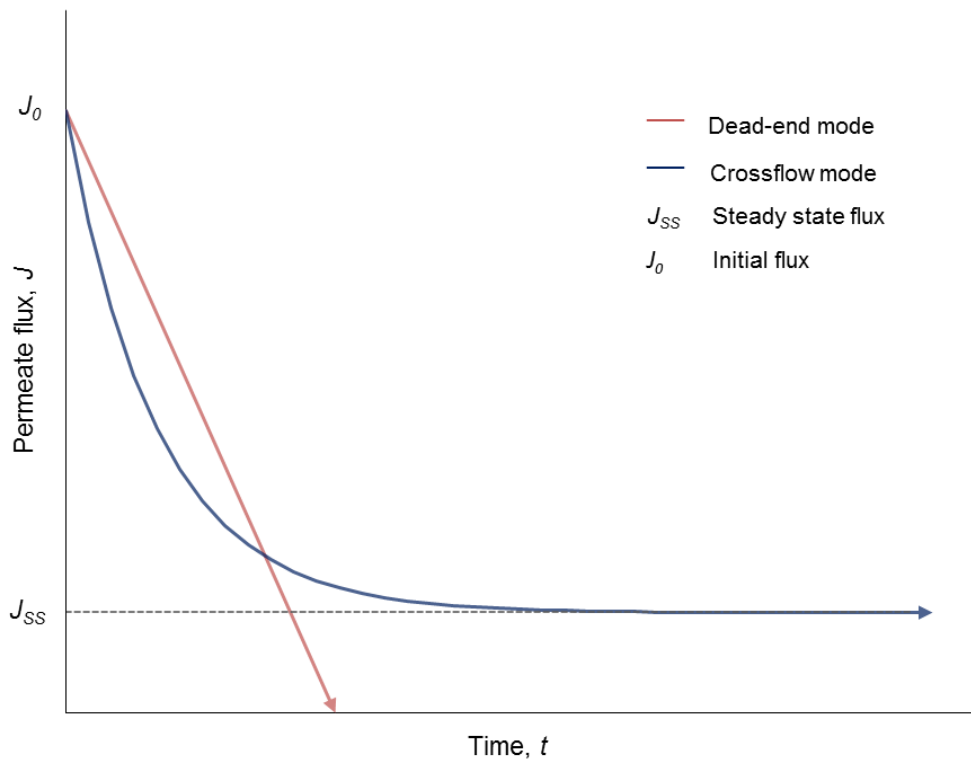
Figure 1.4 Illustration of typical flux decline profiles for dead-end and crossflow/stirred dead-end filtration operated at constant transmembrane pressure.

Tangential flow filtration is primarily used for two applications, namely concentration and diafiltration (desalting, buffer exchange or product recovery). Concentration is the process where fluid is removed from a feed solution while the solute molecules are retained by the membrane and gets concentrated as a function of the volume of liquid removed; the solute concentration increases with the decreasing feed volume over time. Diafiltration (DF) is when a diafiltration buffer is introduced in the feed tank whilst the permeate flows out of the system (Millipore, 2003); diafiltration can be performed with either a UF or MF membrane.

TFF can be operated and controlled in two ways, depending on whether the permeate flux or process TMP is kept constant and maintained at the set point throughout. When operating under a permeate flux control regime, the permeate flux is fixed at a desired set point using a permeate pump or valve, and a steady increase in TMP is usually observed as the foulants continuously accumulate on the membrane surface

over time. For a TMP controlled process, TMP is maintained at the desired set point by adjusting the feed or retentate pressures while the permeate flux is allowed to decline gradually, as the resistances to mass transfer (gel-polarisation and/or cake) build up with processing time. Figure 1.5 compares constant TMP and constant flux operation modes.
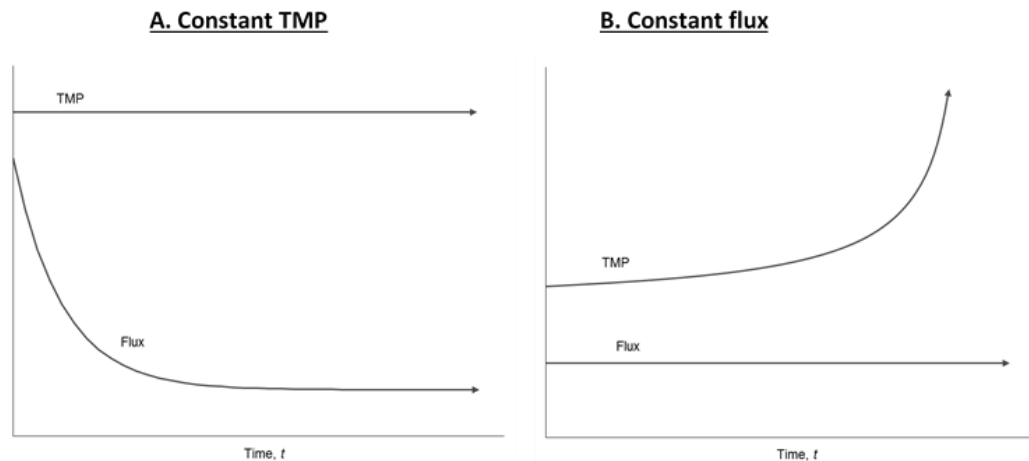
Figure 1.5 Comparison of constant TMP and constant permeate flux modes of operation. In A, the initial TMP is constant, resulting in higher initial fluxes compared to constant flux mode. In B, the initial permeate flux is constant and maintained at a lower value while the TMP increases with processing time.

Constant flux filtration is a mode of operation that has been used in research into fouling reduction (Foley et al., 1995). It has been shown that during constant flux, a low initial transmembrane pressure followed by a gentle increase, results in a lower rate of fouling and reduced degree of irreversible fouling, due to lower fluxes (Field et al., 1995). By contrast, during constant TMP, the high initial fluxes* (J_0) that start from the pure water flux can prove to be quite detrimental as they might cause irreversible fouling, long before the permeate flux reaches steady-state. During constant TMP (as seen in Figure 1.5A), a sudden drop in permeate flux is observed because of the high initial flux. These high permeate fluxes result in the solute particles being convected towards the membrane surface much quicker than are transported away, thus more particles are deposited per unit volume of filtrate in constant TMP mode than in constant flux mode (Yoon, 2011). The cake layer formation is not only enhanced at high permeate fluxes, but the cake layer could also solidify to an extent where the cake formed is static on the membrane surface; this cake layer is not easily removed by flushing the membrane. Thus, for long-term processing, it is vital to avoid

excessively high permeate fluxes at any point during the filtration process by operating at constant flux either using a permeate pump or valve to regulate the flow.

Constant flux is usually opted for in industry for 'open' membranes (>300 kDa) because it allows a consistent rate of permeate production with negligible irreversible fouling of the membrane and hence is easier to clean. During constant flux filtration, the TMP is a function of the resistance of a fouling layer. An increase in TMP over time generally indicates an increase in the degree of fouling/resistance. As a result, TMP is monitored as a function of time (dTMP/dt) for constant permeate flux operations to characterise the filtration performance. A more in-depth research and analysis can be found in a recent review by Miller et al. (2014), where a comparative study of membrane fouling at constant flux and constant transmembrane pressure conditions was performed. Although there is some evidence to suggest that deposition during constant flux operations might be relatively more irreversible as the fouling mechanism tends to be predominantly internal membrane fouling, it is still generally deemed to be the preferred option for sustained operation. Minimum membrane fouling and constant hydrodynamic conditions may be achieved when permeate flux is constant (Le-Clech et al., 2006).

* For constant TMP operations, the term initial flux is generally used to describe the initial flux at $t=t_0$ because the permeate flux decreases due to increasing hydraulic resistance of the accumulating particles near the membrane (Yoon, 2011).

1.2   Hydrodynamics of tangential flow filtration

1.2.1   Turbulence-promoting screens

Most TFF cassettes and spiral modules have meshes/screens within the feed and permeate channels, forming part of the construction of the cassette and manifold. These screens provide structural support for the channels and often define channel height, while also serving as a static mixer. However, the primary purpose of the screens is to increase the mass transfer rate by enhancing wall shear stress and formation of eddies, although at the expense of a larger pressure drop across the channel from feed to retentate. The screens promote higher permeate fluxes at lower flow rates, making them more efficient than open, unscreened channels operated at the same flow rate. The fibres of the screen generally touch and protrude into the surface of the membranes and increase mass transfer rates via an overall reduction

in voidage of the feed channel, as well as localised fluid acceleration effects in regions where the screens touch the membrane. The permeate screen is purely there for structural purposes and has no impact on fluid flow, and so the permeate screens tend to be much tighter than feed screens as the permeate stream tends to be low viscosity, particulate free liquids flowing at a relatively low velocity. Figure 1.6 illustrates a typical TFF channel (two permeate channels enveloping a feed channel).
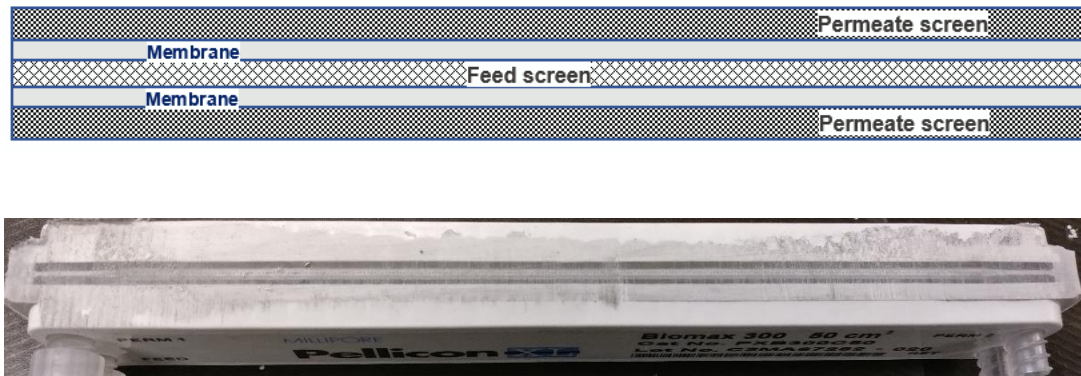
Figure 1.6 2D schematic of a typical single-feed channel screened TFF cassette (top) and a comparative cut open Pellicon XL cassette (bottom), showing membranes and feed and permeate channels**.**

In terms of commercial screened cassettes, Millipore offer four different screen types, namely the tight (A) screen, coarse (C) screen, medium (D) screen and a suspended (V) screen; the characteristics of the different screens are summarised in Table 1.1. A and C screen cassettes are used to generate high fluxes using less viscous solutions, whereas the D and V screens support more viscous suspensions but have relatively worse flux performance. C screen and V screen cassettes utilise the same screen, but in the C screen device, the screen is slightly held off the membrane surface by non-woven spacers that run along the sides of the membrane. The thickness of the feed screen directly relates to the overall height of the feed channel, while the 'tightness' of the screen refers to the overall thickness and number of fibres per unit length that make up the screen. Tight screens are usually thinner and as a result, can only accommodate liquids with relatively low viscosity compared to the thicker, more open/coarse screens that can process viscous feed and operate at higher flow rates without generating significant pressure drops. However, there exists a trade-off between high mass transfer rates and channel pressure drops. For instance, the suspended V screen cassette has a significantly lower pressure drop due to the more open feed channel (due to spacers holding the membrane off the

screen) but the mass transfer is greatly reduced because of smaller wall shear rates in the open channel, at a given flow rate.

Material	Screen	Mesh count Warp	Mesh count Weft	Wire diameter Warp	Wire diameter Weft	Nominal thickness
		n/cm	n/cm	µm	µm	µm
	A	20	20	215	215	420
	C	16.2	16.2	270	270	515
	D	12.2	12.2	340	340	610
Polypropylene (PP)	V	16.2	16.2	270	270	915 (515 µm C screen + 2 x 200 µm spacers)
	B' (permeate screen)	27.6	27.6	165	165	320

Table 1.1 Characteristics of the commercially available feed and permeate screens within Millipore TFF cassettes (Lutz et al., 2016; Ngan et al., 2014).

The D screen is similar to the coarse C screen, but has an altered weave pattern designed to overcome flux performance limitations seen in suspended V screens. Thus, it can operate at a lower feed channel pressure drop than the tighter C screen without a significant drop in flux performance (Sengler et al., 2015).

1.2.2 Channel hydraulics, flow path and profiles

TFF cassettes consist of feed/retentate and permeate channels; feed channels can be considered to be individual, discrete channels composed of two flat sheets of membrane separated by a screen, and intertwined by permeate channels in between. The design and arrangement of feed and permeate channels vary depending on the manufacturer; for instance, the outermost channels (first and last) of the cassette can either be a permeate channel (Millipore) or a feed channel (Sartorius).
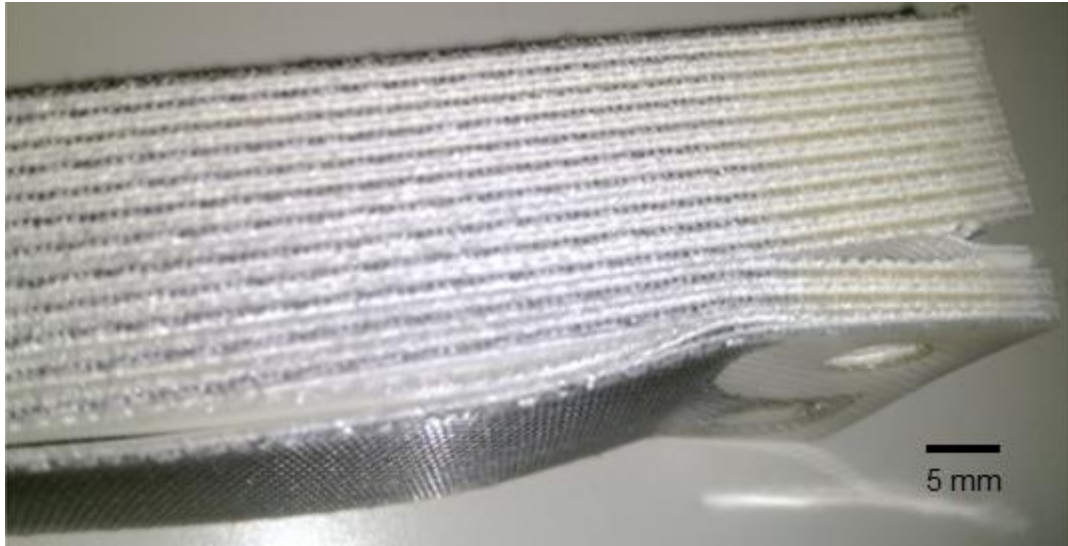
Figure 1.7 Side view of a cut open Pellicon 2 mini cassette (V screen), showing the intercalated feed and permeate channels.

Although feed channel height is normally assumed as the height of the feed screen, it can also be estimated empirically using the Ergun pressure drop equation, which correlates pressure drop, viscosity and characteristic channel height, based on skin and form drag (Bird et al., 1961). Another basis for determining the hydraulic diameter, d_h, for slit geometry is approximating it to 4 times h (w>>h), or more specifically for screened cassette channels if spacer geometry is known (Lutz, 2015) using Equation 1.1:

$$d_h = \frac{4\varepsilon}{\frac{2}{h}+(1-\varepsilon)\cdot s}$$

Equation 1.1

where ε is spacer porosity (-), $2h$ is the height of the feed screen (m) and s is spacer specific surface area per unit volume (m^2/m^3).

The hydraulics and flow within the channel are dependent on the effective channel height and screen characteristics. In standard TFF cassettes, flow passes into the feed port through the cassette manifold, passes along through the feed screen (retentate) or through the membrane (permeate), and out the end and then a 90° turn to pass along the retentate/permeate channel and out. As shown in Figure 1.7 and

Figure 1.8, there are no discrete retentate channels per se, but instead a single 'packet' comprises of two flat sheets of membranes held apart by a rigid permeate channel on either side and feed screen in between the membrane sheets. The permeate flows through the membrane and into the permeate channel, and it runs parallel to the feed channel. All flow paths in a cassette are identical in length, height, screen, and run in parallel, and as a result, each channel operates with same crossflow, pressure drop, and concentration profile along the length of the channel.
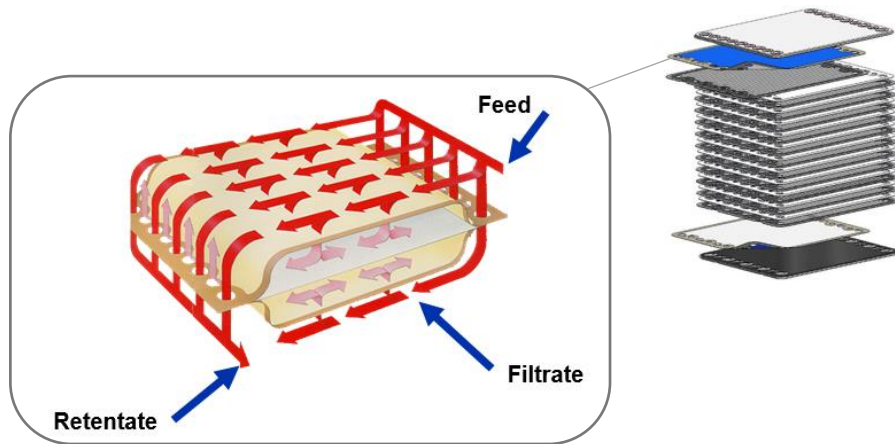
Figure 1.8 Flow path in a typical flat sheet cassette. Image courtesy of Merck Life Sciences KGaA.

As feed fluid travels along the length of the feed channel, there is a pressure drop incurred due to friction between the fluid and the membrane skin and feed screen; part of this flow passes through the membrane and causes a reduction in flow in the feed channel and a corresponding increase in concentration along the channel path. The pressures, flux, mass transfer and tangential flow rate all decrease along the length of the channel, and thus these parameters for tangential flow filtration tend to be expressed as module averaged quantities, as shown in Equation 1.2, Equation 1.3 and Equation 1.4.

$$\overline{TMP}_{CFF} = \frac{(P_F + P_R)}{2} - P_P$$

Equation 1.2

$$\bar{Q}_F = \frac{(Q_F + Q_R)}{2} = Q_F - \frac{Q_P}{2}$$

<div align="right">**Equation 1.3**</div>

$$J = \frac{1}{L} \int_0^L j(x)dx$$

<div align="right">**Equation 1.4**</div>

where $\bar{Q}_F$ is average crossflow rate/feed flow rate, $\overline{TMP}$ is the average module transmembrane pressure, and J is the average permeate flux across the module, equal to the integral of the local permeate flux j across the channel length L (m); subscripts F, R and P refer to the feed, retentate and permeate streams respectively.

As the feed enters the channel, the flow rate across the channel effectively decreases from the start of the flow path to the end, with a possibility of starling flow at the end of the path length. Starling flow refers to the unusual reverse flow of liquid from the permeate channel back into the feed channel for the remainder of the channel length, usually the last few centimetres (Lutz, 2015). Flow and pressure gradients exist across membrane length from feed (inlet) to retentate (outlet) and the profile depends on applied forces and membrane permeability. Figure 1.9 shows a typical C screen cassette spatial profile, performed using finite element analysis for a single component protein feed.
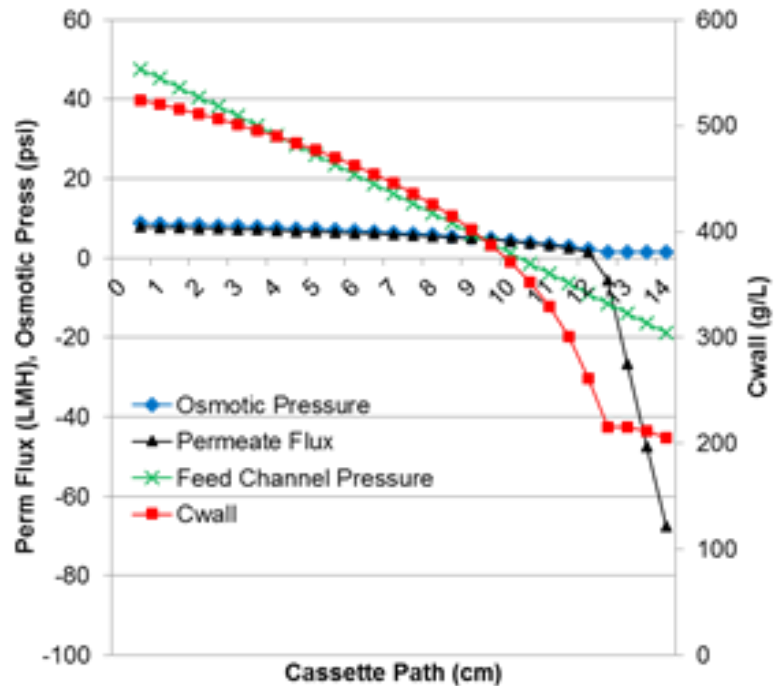
Figure 1.9 Cassette spatial profile for a C screen versus feed channel path length, for a single protein in a clean feed stream. Data and graph courtesy of Merck Life Sciences GmbH (2018) and Lutz (2015).

The pressure decreases significantly over the length of the feed channel and as a result, so does osmotic pressure drop and C_m in response to the change in feed pressure. The C_m and osmotic pressure are driven by product concentration and pressure. In standard TFF cassettes for a single pass, it does not concentrate up that far; however, the pressure does change greatly. Therefore, on aggregate, the C_m and osmotic pressure tend to drop by the end of the feed channel. Starling flow can also be seen in Figure 1.9, where feed pressure becomes negative near the end of the feed channel and the permeate flow is effectively reversed for that section. Thus, flow, pressure, concentration and mass transfer all change across the length of a TFF channel depending on the position along the transverse axis.

1.2.3 Concentration polarisation (CP) and mass transfer

There are two primary mechanisms at play in tangential flow filtration, namely concentration polarisation (CP) and fouling. The polarisation layer is not well characterised but is typically described as a thin and highly concentrated boundary layer that forms under pressure with large molecules that are rejected by the

membrane. CP is an evitable consequence in filtration processes and is a function of hydrodynamic conditions (Cheryan, 1998) and the key difference to fouling is that concentration polarisation is entirely reversible, achieved by releasing pressure and/or increasing crossflow, whereas fouling usually tends to be irreversible.

The other mechanism is fouling. Fouling is often a result of excessive concentration polarisation on the membrane at high pressures but could be due to other reasons as well. Generally, as the TMP is increased, the polarisation layer thickens due to greater convective flux towards the membrane, and once the membrane becomes polarised, the membrane starts to foul. Membrane fouling is indicated by a rapid rise in TMP (for permeate flux controlled operations) which occurs due to the uncontrolled polarisation layer formed at the membrane and the mass transfer rates not being large enough to depolarise the consolidating layer (thus mass transfer limited). The impurities or the product can also bind/adsorb to the membrane and is not reversible unless a chemical solution is applied, and can form from a polarisation layer if high pressures are applied for too long. However, a small amount of fouling is unavoidable even with the cleanest and dilute protein solutions. Both mechanisms will reduce the permeate flux but only the polarisation layer is directly and consistently affected by shear across the surface. For irreversible fouling, the process would have a very low mass transfer (k) value as it is difficult to get the entirety of foulants off the membrane, and only a chemical cleaning regime is effective to remove the foulants from within the pores. In tangential flow filtration, the distinction between true cake formation and uncontrollable polarisation is very difficult, unlike dead-end filtration where the pressure profile provides an indication as to what mode of plugging has occurred. However, in the case of TFF it is difficult to distinguish between the two, as both a polarised membrane and dynamic cake formed would cause a rapid increase in observed pressures.

Concentration polarisation is essential for TFF processes and dictates the mass transfer rates. In a typical UF or MF process, mass transfer occurs by both pressure and diffusion. There are three key components of the mass transfer phenomenon occurring in tangential flow filtration; convective flux towards the membrane (J), back diffusion away from the membrane, and convective mass transfer away from the membrane (k). Figure 1.10 illustrates the various phenomenon occurring within a TFF channel.
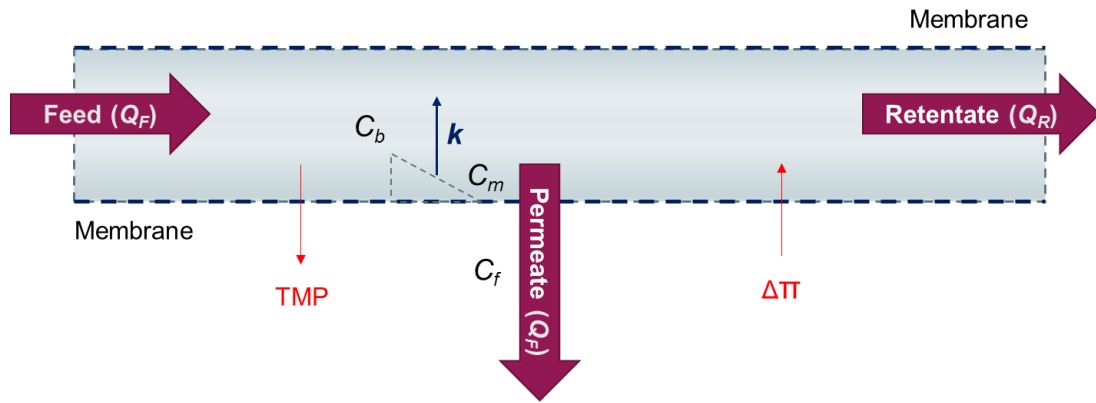
Figure 1.10 Simplified diagram showing mass transfer phenomenon and concentration gradients in a crossflow feed channel. *C* is the concentration of solute/particles, and the subscripts *b*, *m* and *f* refer to the concentrations in the bulk, membrane/wall and filtrate/permeate respectively.

During a typical tangential flow filtration process, feed material (of bulk concentration C_b) enters the TFF channel and for a correctly selected membrane type and pore size, C_f is very small (≈0), while C_m is the concentration of particles at the wall/membrane, *i.e.*, concentration of the membrane polarisation layer. The net driving force is the difference between TMP (the average module pressure that drives fluid flow across the membrane) and the osmotic pressure $\Delta\pi$ (generated because of the product concentration gradient across the membrane). The osmotic pressure component is usually significant during UF applications that involve solutes like proteins and other macromolecules, unlike in TFF-MF processes with insoluble particles, where it is often assumed to be negligible. The TMP drives net positive flow through the membrane into the permeate, while the osmotic pressure causes reversal of flow (starling flow) down the concentration gradient (C_m-C_p) and transports the solutes from the wall back into the bulk solution. The most important parameter illustrated in Figure 1.10 is the mass transfer coefficient, *k* (LMH), and is directly related to the steady-state permeate flux (higher mass transfer usually translates to higher process fluxes, for a given set of operating conditions) and covers a multitude of factors. Simply put, the mass transfer fundamentally describes the rate of back-transport away from the membrane and reflects the flux of particles moving away from the polarisation layer back into the bulk solution (C_m turning into C_b). The mass transfer coefficient controls the flux decline due to polarisation, which is the essential difference between crossflow and dead-end filtration, where the steady-state

permeate fluxes tend to be higher for the former due to this crossflow effect/mass transfer coefficient.

The polarisation layer in a TFF process typically dictates the process fluxes and controls the filtration process, and so a higher feed flow rate translates to a greater sweeping action and a higher k, which means a thinner polarisation layer and consequently higher permeate fluxes. The crossflow action essentially strips away the polarisation layer and back into the bulk solution, thus preventing the polarisation layer from thickening uncontrollably and significantly slowing down the filtration process or fouling the membrane, or both. k describes how quickly the polarisation layer comes off the membrane surface and is a function of the wall shear rate (feed flow rate), temperature and the bulk concentration of the feed.

The mass transfer, expressed as a coefficient instead of an absolute quantity, describes the back-transport of solutes and particles away from the membrane surface; it is an empirical coefficient that can be determined by plotting the log-log plot of permeate flux versus concentration (section 1.3.1). The mass transfer coefficient mainly applies to the polarised region of the flux versus TMP curve where the process is purely mass transfer dominated rather than the pressure applied or membrane permeability. In most real-life applications, the dimensionless mass transfer coefficient, *i.e.*, the Sherwood number (Sh), expresses the ratio of convective mass transfer to diffusive mass transfer and is generally used to describe mass transfer depending on the flow regime. For Newtonian fluids, the dimensionless Sherwood number can be expressed as shown in Equation 1.5.

$$Sh = \frac{k \cdot d_h}{D} = \beta \cdot Re^a \cdot Sc^b \cdot \left(\frac{d_h}{L}\right)^c$$

Equation 1.5

where k is the convective mass transfer coefficient (LMH or m/s), D is diffusivity of solute (m^2/s), d_h is the hydraulic diameter (m), Reynolds number (Re), Schmidt number (Sc), are dimensionless numbers, and β, a b, and c are flow and geometry dependent coefficients. Table 1.2 summarises the mass transfer coefficients for different module configurations and flow regimes.

Conditions	β	a	b	c	Reference
Laminar tube (***Re*<2000**)	1.62	0.33	0.33	0.33	(Leveque, 1928)
Laminar slit (***Re*<2000**)	1.86	0.33	0.33	0.33	(Leveque, 1928)
Developing	0.66	0.50	0.33	0.50	(Gröber et al., 1961)
Turbulent (***Re*>4000**)	0.023	0.80	0.33	-	(Chilton and Colburn, 1934)
Screened channel (***Re*<2000**)	0.66	0.50	0.33	0.33	(Da Costa et al., 1994)
Stirred cell laminar (***Re*<25000**)	0.29	0.55	0.33	-	(Smith et al., 1968)
Stirred cell turbulent (***Re*>32000**)	0.044	0.8	0.33		

Table 1.2 Sherwood number parameters and coefficients for the various tangential flow filtration modules.

Since membrane polarisation and mass transfer coefficients are both vital characteristics of a TFF process as they characterise and dictate the performance, the characterisation and control of the mass transfer is the cornerstone for the successful and accurate scaling of tangential flow filtration. The correlations in Table 1.2 can be used to predict mass transfer and flux for UF; however, these models tend to be predominantly empirical correlations and work best with single component solutions, which is more applicable for final fill/formulation steps that use tangential flow filtration for buffer exchange and concentration.

1.2.4   Critical and limiting permeate fluxes

For a tangential flow filtration process, increasing fluxes generally tend to result in greater fouling rates as the increased convective forces bring greater number of particles to the membrane surface and therefore thickening the polarisation layer, which makes selecting a high permeate flux that could achieve a sustained filtration process very challenging. The concept of critical flux, first introduced by Field et al. (1995), is vital in filtration operations and helps achieve a balance between achieving maximum fluxes and minimum rates of fouling. It could also be used to compare the fouling propensity of membranes or feeds (Bilad et al., 2012).

At a fixed feed flow rate, permeate flux increases with an increase in TMP; however, beyond a certain TMP, the crossflow velocity is no longer sufficient to sweep the retentate side of the membrane clean, resulting in a build-up in 'cake'. Increasing the TMP beyond this point causes an increase in cake thickness and/or blocking of the membrane pores, which reduces the effective flux and thus no increase in permeate flux is observed. The critical flux is the point where this transition occurs, defined as the maximum achievable permeate flux with slight or negligible fouling, or the flux at which a transition from concentration polarisation to cake formation occurs. Critical flux can generally be defined in two ways (Field et al., 1995); it can be defined to be the permeate flux at which the transmembrane pressure starts to deviate from the pure water line (strong form of critical flux), or as the permeate flux at which irreversible fouling starts to occur. For a constant permeate flux controlled operation, irreversible fouling is typically indicated by a rapid and uncontrollable rise in TMP (weak form of critical flux).

In terms of the overall forces acting on the particles, when operating below the critical flux, the hydrodynamic forces bringing the foulants *to* (convection associated with permeate flux) and *from* (crossflow shear forces, back diffusion and inertial lift/Brownian diffusion) the membrane balance each other out to reach a quasi steady-state. At steady-state, permeation continues without any further deposition of particles or any further increase in observed TMP. Beyond the critical flux, deposition of larger particles occurs because of the high permeation velocities that are much larger than the particle back-transport velocity, and thus, the pressures become unstable and increase rapidly to compensate for the growing/compacting cake layer.

The critical flux is a function of the hydrodynamic conditions, system properties (particle characteristics, pH, ionic strength, and temperature) and spatial position on the membrane surface. Operating the filtration process in the region below the critical flux, otherwise known as the sub-critical region, is usually desirable from an experimental perspective, as no or little fouling would occur thus eliminating cleaning complexities and associated costs. The point just below the critical flux is the point where maximum fluxes could be achieved, without exerting excessive pressure or approaching significantly high protein wall concentrations that lead to uncontrolled membrane polarisation/fouling (Millipore, 2015).

Another flux-related concept, illustrated in Figure 1.11, is that of the limiting permeate flux. The limiting flux can be described as the maximum attainable flux at steady-state

beyond which, sustainable operation is not possible in a TFF operation. It corresponds to the state where the operating permeate flux is greater than the critical flux at all points of the membrane surface, for the given hydrodynamic conditions.

The relationships between permeate flux, critical flux and limiting flux versus transmembrane pressure can be understood by generating a TMP versus flux curve, shown in Figure 1.11. Astudillo-Castro (2015) developed and used a first-order exponential model to describe the permeate flux as a function of TMP:

$$J = \alpha \cdot \left(1 - e^{-\beta \cdot TMP}\right)$$

Equation 1.6

where coefficients α (LMH) and β (1/bar) are empirically derived material specific coefficients describing the limiting flux in the pressure independent range and the rate of flux change from pressure-dependent to pressure-independent regime, respectively.
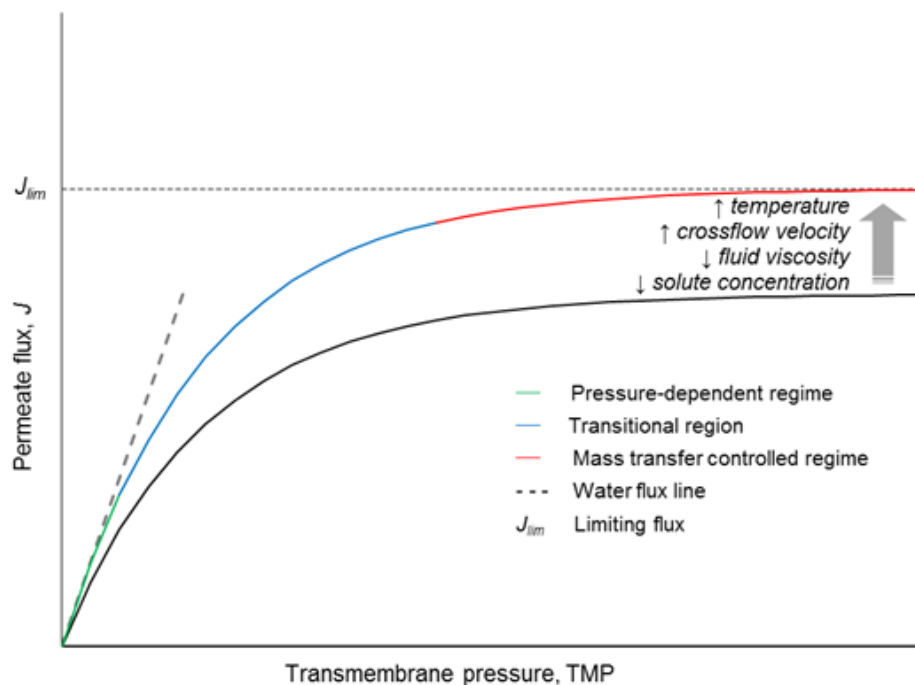
Figure 1.11 Typical flux versus TMP profile for a tangential flow filtration process operated in total recycle mode.

At low pressures, flux increases linearly with TMP as the amount of solute deposition is proportional to the permeate flux. The TMP-flux relationship is completely reversible in this pressure-controlled region, *i.e.*, original fluxes can be re-established when the pressure is reduced. At higher pressures, the TMP-flux behaviour starts to deviate from linearity (the pure water flux line) as more particles begin to deposit on the surface of the membrane to create additional resistances to fluid flow and leading to correspondingly smaller gains in flux. If the pressures are increased beyond the transitional area into the post-critical flux region, the flux becomes independent of the pressure applied due to the compaction of the particle/solute deposits. This increases the specific cake/gel layer resistance to a point where it negates the added driving force (TMP) and the maximum attainable flux under the given set of operating conditions, *i.e.*, the limiting flux, is reached.

The limiting permeate flux (in the mass transfer dominated region) is no longer a function of the pore size, membrane permeability or pressure, but is solely controlled by the mass transfer and only a change in hydrodynamic conditions of the system (such as feed flow rate) would result in a further increase in flux. The TMP at which the limiting flux can be obtained depends on the specific properties of the particles and the concentration of the feed. In cases where a fully polarised layer forms, depending on factors such as the particle sphericity and compressibility, further increases in TMP could cause the cake/gel layer to collapse and create additional resistances to flow to an extent where an undesirable flux decline could be observed. Beyond the critical flux, reducing the TMP does not re-establish the original permeate flux but would result in a lower one instead, as the membrane would have already been fouled when the critical flux was exceeded.

1.3 Existing tangential flow filtration models

During the past few decades, various theoretical models such as the polarisation, osmotic or gel layer model have been developed to describe concentration polarisation effects and predict fluxes for tangential flow filtration, but they are all largely empirical. Apart from that, their use is often limited to simple feedstock containing few dissolved species (with minimal interactions with each other) and often fail to predict performances for TFF microfiltration involving multicomponent, particulate rich feedstock. They also tend to be very time consuming and require relative large volumes of feed material to carry out the experimental work needed to generate the model parameters (Van der Berg et al., 1989). Some of the key models

developed and frequently used for tangential flow filtration, along with their limitations, are discussed in this section.

1.3.1 Gel layer model

When there is a net permeate flux through the membrane, the solute concentration at the membrane surface, C_m, is a lot higher than in bulk, C_b, due to concentration polarisation effects. At steady-state, assuming total solute rejection, convective mass transfer of solute towards the membrane (J) is equal to mass transfer of solute (via convective and diffusive forces) away from the membrane surface (k), which is equal to the permeate flux as described by Equation 1.7.

$$J = k \cdot ln\left(\frac{C_m - C_p}{C_b - C_p}\right)$$

Equation 1.7

where J is the permeate flux (LMH), k is the mass transfer coefficient (LMH), and C_m, C_b and C_p represent solute concentrations at the membrane surface (or the polarisation layer), in the bulk solution and permeate stream respectively (g/L).

For macromolecules and other solutes (high molecular weight and small D), high levels of concentration polarisation (C_m/C_b>10) may lead to super saturation of protein components, resulting in the formation of a localised gel layer near the membrane surface. Once the gel layer develops, a limiting flux is reached where permeate flux is no longer dependent on the TMP or membrane permeability, but is solely mass-transfer limited and the relationship can be expressed as:

$$J_{lim} = k \cdot ln\left(\frac{C_g}{C_b}\right)$$

Equation 1.8

where J_{lim} is the limiting permeate flux (LMH), C_g is the concentration of species forming the gel layer (g/L), C_b is the concentration of retained species in the bulk fluid

(g/L), and k is the mass transfer coefficient (LMH). k can be expressed as the ratio of the diffusion coefficient, D (m^2/s), and the thickness of the polarisation layer, δ (m):

$$k = \frac{D}{\delta}$$

For a standard TFF concentration, a linearised log-log plot of permeate flux versus concentration can be used to determine k; the slope of the linear line is $1/k$, and extrapolation to $J=0$ yields ln C_g. The gel layer model has been used as a theoretical basis for developing MF models, where shear-induced diffusion and inertial lift components are incorporated into this theoretical framework to establish a better fit to the empirical data (Song and Elimelech, 1995). For most applications, the permeate flux is well described by the gel model and is useful for describing and correlating experimental limiting fluxes in the pressure-independent region. However, the predicted gel concentration was found to be unreliable in some cases (Wijmans et al., 1984), while Porter (1972) reported significant differences of up to 30% between the predicted and experimental fluxes for the UF of macromolecular solutions. Other potential limitations include the inability of the model for conditions where the flux is pressure-dependent, *i.e.*, before the limiting flux condition is reached (Song and Elimelech, 1995) and the need for the C_m to be estimated from empirical relationships and experiments.

1.3.2   Osmotic pressure model

The gel model describes limiting flux in the mass transfer-controlled region, but it assumes a well-defined gel layer with 100% solute rejection, unaffected by membrane resistance and independent of operating conditions. However, as discussed earlier, experimental C_g values may not always fit the criteria for the gel model; a lower C_g value than expected could occur for less viscous solutions, or a higher value than expected, typical of feed containing particles/colloids (Cheryan, 1998).

The osmotic pressure model is based on the gel layer model, but it also considers osmotic pressure effects, which become significant due to concentration polarisation at the membrane surface, due to high C_m. The C_m is a function of many variables,

such as the crossflow across the cassette, the TMP applied and the nature of rejected species. Permeate flux in this case is expressed as:

$$J = \frac{TMP - \Delta\pi}{R_M}$$

Equation 1.10

where TMP is the transmembrane pressure (bar), $\Delta\pi$ is the osmotic pressure differential (bar) and R_m is the intrinsic membrane resistance (1/m). A 100% solute rejection is assumed, and osmotic pressure is proportional to C_m, which is a function of permeate flux. In some cases, depending on feed solution properties, the osmotic pressure could show a virial expansion and increase exponentially with C_m (Wijmans et al., 1984).

This model shows that for macromolecular solutions, there is an opposing osmotic pressure gradient established due to concentration polarisation, because of convective flux towards the membrane, and that the applied pressure for crossflow must overcome this $\Delta\pi$ to initiate net permeate flow. It also explains observations where an increased TMP does not lead to a proportionate increase in permeate flux, and sometimes, even leads to reduced flux. For colloidal or particulate feed, the osmotic pressure model does not apply, and osmotic pressure is considered negligible for filtration using open membranes (>300 kDa).

1.3.3   The resistance-in-series model

The two models discussed earlier describes the flux profile in the pressure-independent region and do not predict the entire flux behaviour seen during standard crossflow UF and MF, especially pressure-controlled region at low operating pressures, typical for open membranes. Thus, a resistance model, used in series, is a better approach, and something that is commonly used in heat transfer applications (Cheryan, 1998). Flux decline in tangential flow filtration is a result of many factors such as concentration polarisation, fouling and cake/gel formation, all of which contribute to additional resistances to flow. The resistance model considers all these resistances and describes flux performance for MF and UF of particulate feed and

macromolecule containing solutions such as proteins, polysaccharides, peptides (Bouchard et al., 1994; Yeh and Tsai, 1998).

Thus, for an ideal membrane and feed solution, permeate flux/mass transfer can be expressed using:

$$J = \frac{\Delta P - \Delta \pi}{\mu_P \cdot \left(R_m + R_c + R_a + R_p \right)}$$

Equation 1.11

where ΔP is the hydraulic pressure differential (bar), $\Delta \pi$ is the osmotic pressure difference (bar), μ_P is the permeate viscosity (Pa.s), R_m is the intrinsic membrane resistance (1/m), R_c is cake resistance (1/m), R_a is the initial adsorption resistance (1/m), and R_p is the resistance of the concentration polarisation layer (1/m).

The resistances mentioned in Equation 1.11 can be determined using various semi-empirical methods and experiments, as described by Juang et al. (2008) and Ousman and Bennasar (1995). Membrane resistance can be determined from a water flux test, while R_a, the resistance because of particle adsorption to membrane pores/surface on contact, can be determined performing a water flux test (same conditions as pure water flux) after contacting the membrane with feed solution without any net permeate flux for a few hours. The difference between the measured resistance and R_m gives R_a.

Cake resistance can be measured by performing small scale dead-end experiments (Lee and Clark, 1998). For solid insoluble particles, it leads to formation of a 'cake' layer, and the permeate flux is then a function of the thickness of the cake layer and its properties:

$$R_C = \alpha \cdot \frac{c \cdot V}{A}$$

Equation 1.12

where R_c is the cake resistance (1/m), α is the specific cake resistance relative to dry mass (m/g), c is the solids concentration (g/L), V is the filtrate volume (L) and A is the membrane surface area (m^2).

Equation 1.12 is applicable for spherical and rigid molecules only, and as such, the specific cake resistance, α, does not vary with cake thickness and pressure drop. However, for most complex biological feed, the particles tend to be compressible and thus, α is proportional to the pressure drop applied:

$$\alpha = \alpha_0 \left(1 + k_c \cdot \Delta P\right)$$

Equation 1.13

where k_c (1/bar) is a material specific cake resistance parameter that needs to be experimentally determined and ΔP is the pressure drop across the membrane (bar).

1.4   Scale-up/down of tangential flow filtration

1.4.1   Scale-down requirements and role in bioprocessing

Once a process is scaled up to production scale, it is essential to be able to accurately scale down processes to carry out validation, troubleshooting and impromptu investigations to actively support large scale operations in cases of deviation (van Reis et al., 1997). In order to successfully develop a process, the availability of reliable equipment at laboratory and pilot-scale is crucial. However, in most cases, access to capital equipment is limited and numerous large scale experiments are neither feasible nor possible to perform. Thus, product and process validation at large scale tends to be less thorough compared to small scale experiments that allow a greater number of critical parameters to be assessed.

Increase in upstream product titres and volumes are normally accompanied by increased impurities, which intensify the burden on the purification processes downstream and more often than not, are unable to keep up with the changes (Chapman and Krishnan, 2011). In such cases, manufacturing is greatly challenged with the plethora of validation needed; scaling and manufacturing qualification/validation runs are often carried out on a tight schedule, with little or no

time for large scale runs (Shukla et al., 2007). At the same time, troubleshooting requires going back to small scale to resolve potential issues, which greatly add to manufacturing costs and development times. Furthermore, scaling-up typically leads to unexpected deviations from the predicted performance due to the invariably changing operating conditions that occur upon scale-up. Such changes can be difficult to predict and can cause major delays whilst the process undergoes troubleshooting to try to re-establish desired performance. Use of scale-down models can predict these changes and help avoid any surprises encountered upon scaling.

Although process modelling and simulations remain an ideal alternative, there is no theoretical model that can fully substitute a physically scaled-down model due to their inherent inaccuracy and relative complexity (Challener, 2016). Practical experiments are usually needed to gain information for predicting performance for complex biological feed that have various complex interactions and scale-down models are useful for carrying out characterisation work, viral clearance and continuous process improvement (Challener, 2016). Requirements for developing a robust and optimised TFF process depend on the phase of drug development, relative timelines and volume of feedstock available. Figure 1.12 highlights the focus of process development based on product development timelines.

| Preclinical | 50 mL-1 L → | Phase I/II | 100 mL-10 L → | Late phase | 100-1000 L → |

- Membrane, device/screen selection
- Fouling studies
- TMP, dP, throughput screening

- Optimisation of operating parameters (J, Q, yield,..)
- Membrane sizing
- Capacity

- Robustness studies
- Validation
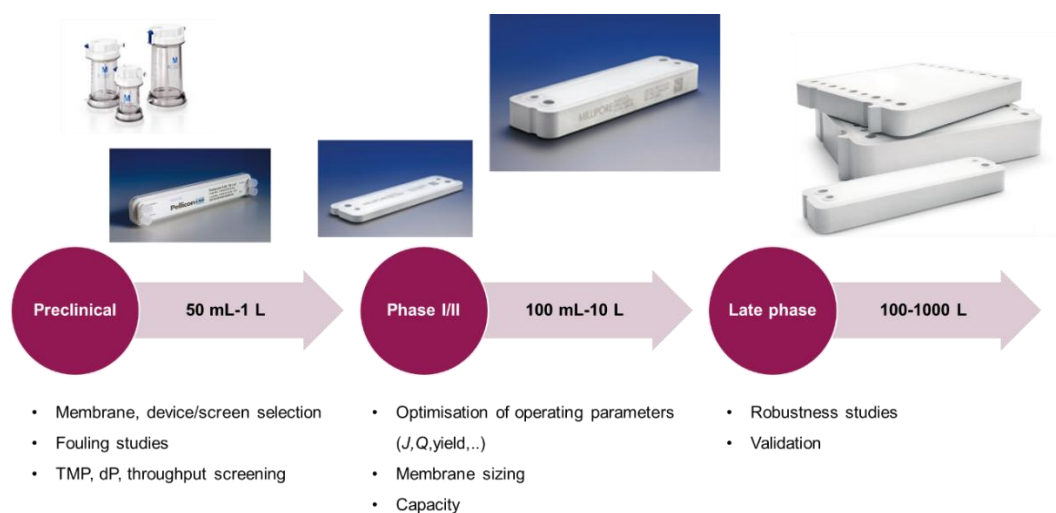
Figure 1.12 Depiction of process development timelines, feed volumes used and specific objectives within a typical drug development process. Images courtesy of Merck Life Sciences KGgA.

Small scale models can be used to analyse the impact of different batches of feedstock with variable levels of impurities. This is usually unfeasible at full scale as it can be very expensive to carry out such studies at scale and is normally done over many steps as part of good engineering practice (minimum 10-fold scale-up per step), all the way to the final test run at the production scale. The limitation in nearly all cases is the quantity of feedstock available. For instance, the use of the smallest commercial cassettes by Millipore, namely the Pellicon XL and P3 micro devices, are primarily limited to initial screening, membrane selection and feasibility studies (as recommended by the manufacturer). The larger Pellicon mini and maxi devices (>0.1 m^2) are the ones generally used for process optimisation and scale-up/scale-down purposes, with a minimum feed volume requirement of 100-150 mL (in some cases, this could be much larger depending on total hold up volume and system configuration). This is where the expense usually comes in, on the bioreactors required to generate the volumes needed (dictated by the smallest commercially available linear TFF cassette) to carry out the lab-scale experiments.

Scale-down is as important as scale-up, and an unsuccessful scale-up can have severe economic and regulatory consequences (Ball, 2000). Current process development and optimisation occurs towards the end of the product development cycle, which limits the volume of material and time available for a robust and optimised process design. Considering that potential drug candidates spend between 6-10 years in the preclinical and clinical trials phase (Mohs and Greig, 2017), combined with an estimated average cost of $2.6 billion (DiMasi et al., 2016) to develop a new therapeutic, gaining early process understanding is of paramount importance to help de-risk the process, and potentially reduce both costs and time to market. As such, it is generally advisable to maximise understanding of both process and product at small scale, since it is preferable and generally acceptable to fail at small scale rather than at a production scale from a bioprocessing cost and time perspective.

As a result, there is significant advantage in developing and optimising tangential flow filtration processes at small scale that require very low volumes of feedstock and use common laboratory equipment to operate, since speed of scale-up and reduction in number of intermediate scale-up tests translate to higher productivity by getting the product to market quicker and safer. An ideal scale-down model would mimic conditions at large-scale and accurately predict performance, thus enabling process

understanding at much earlier stages of process development than is traditionally possible.

1.4.2 Types and adaptations of scale-up

Scaling-up/down are essential requirements in the biopharmaceutical industry, particularly at early stages of drug/process development, and is based on maintaining constant conditions across scales and making use of a scaling parameter, which is ideally dimensionless. To cope with increased processing volumes at production scale, the concept of linear scaling is generally used to ensure similar filtration performances across scales. There are two types of scaling, namely, linear and non-linear scaling, and are discussed in sections 1.4.2.1 and 1.4.2.2.

1.4.2.1 Linear scaling

Conventional scale-up/down of tangential flow filtration is performed linearly, where the module type (membrane and screen type within the device) and channel length are kept constant; the feed flow rate is scaled up linearly with increasing membrane area to keep the polarisation, membrane loading and mass transfer unchanged upon scaling. The module width is increased/decreased, with more channels added or removed in parallel to increase/decrease surface area in order to achieve reliable and true linear scaling by establishing the same mass transfer, concentration, pressure and flow profiles across scales.

Linear scaling operates on the principle of geometric similarity to maintain equivalent conditions across both scales, and requires use of the same feed material, membrane, screen type/device format, permeate flux and same membrane loading (feed volume:membrane area). A 400-fold (van Reis et al., 1997) and 1000-fold (Foster et al., 1976) linear scale-up has been successfully achieved using linear scaling method.

Variations of linear scaling include varying the channel length (serial module scaling) or exceeding the membrane loading, and works mainly for UF/DF operations that are limited to <2-fold process time extension (Cyganowski, 2005). In such cases of scaling, the different fouling risks and permeate flux-TMP profiles also need to be considered. However, for MF operations, the membrane loading must not be

exceeded during scale-up due to the capacity limitations associated with particulate feed using open membranes.

1.4.2.2 Non-linear scaling

Non-linear scaling ensures similar concentration profiles at both small and large scales, but between dissimilar geometries. It is also known as model-based scaling, as it uses model data to predict and estimate performance at different scales. For similar geometries, all parameters apart from membrane loading and mass transfer are kept constant, and the mass transfer is obtained from mass transfer correlations. Whereas for scaling between different geometries, such as flat sheets to spiral-wound membranes or rotating disc filters to screened cassettes, the aim is to achieve equivalent polarisation at both scales by operating at same average k and use filtration and sizing models to estimate process performance at large scale. Table 1.3 highlights the main characteristics and differences between linear and non-linear scaling.

Linear	Non-linear
Same 'everything': MWCO, membrane material, module, k, permeate flux, crossflow	Same MWCO, same membrane material, same membrane loading
Same polarisation	Dissimilar geometry/module
Same processing time or V/A loading	Similar average permeate flux, equivalent k
Only module width changes upon scaling	

Table 1.3 Summary of key characteristics of linear versus non-linear scaling in tangential flow filtration.

Non-linear scale-up between dissimilar geometry is normally discouraged since it requires equivalent operating conditions across both scales, which can be done using a regime analysis and a suitable model to translate results that are statistically equivalent at large scale. Ma et al. (2010), Fernandez-Cerezo et al. (2019) and Guo et al. (2016) have successfully demonstrated non-linear scale-up from custom small scale devices to TFF cassettes for the UF/DF of Fab', concentration of mAb and diafiltration of *Escherichia coli* phage/mAb molecules, respectively.

1.4.3 Considerations and challenges during scale-up

Various challenges are associated with scale-ups and a good scale-down model should represent relevant commercial scales and help generate data needed for validation tests and control strategies. However, when processes are scaled-up, process engineers usually have limited empirical data lacking critical information, and failure to recognise them can result in different performances upon scale-up. The reliability and accuracy of data obtained from scale-down models in comparison to the experimental data from large scale equipment remains a central question during scaling.

For tangential flow filtration, there are numerous challenges and key considerations to developing a robust and scalable USD model. For example, the fluid flow dynamics tend to be quite different in the small scale devices compared to the large scale counterparts. This is primarily due to the design of large scale TFF with features that directly influence process performance and are difficult to model; the differences in fluid flow profiles because of geometrical differences across scales make it extremely challenging to predict large scale outcomes in an accurate and reliable manner. This is particularly important for tangential flow filtration with spatially distributed variables such as pressure and concentration gradients that exist within the feed channels and as a result, geometrical factors that influence flow and pressure profiles would have a significant impact on process performance. Conditions across the length of the feed channel in TFF cassettes are non-uniform; the frictional drag decreases the flow velocity, the feed volume decreases as part of it is converted into permeate, and the solute concentration increases moving from feed to retentate.

Upon scale-up, systems and equipment scale too, and components, such as valves, elbows, pumps, that can contribute to added pressure losses and changes in flow distribution are invariably introduced. These effects cannot be ignored and can potentially lead to a situation where the actual TMP (the pressure driving net permeate flux through the membrane) is lower than the measured TMP, resulting in lower experimental permeate fluxes compared to predicted data. Furthermore, a change in flow distribution and flow path upon scaling would affect the associated convective mass transfer effects and polarisation, which are key for tangential flow filtration. Stirred cell devices are typically operated in dead-end mode due to their simplicity and ease of operation, offering significant advantages for use in scale-down studies. However, this poses the biggest challenge of successfully scaling up from a

dead-end flow to tangential flow filtration: to translate performance from a uniform, forward flow to a differential, crossflow mode of operation; Figure 1.13 illustrates the differences in flow profiles through the membrane across both scales, generated using 2D CFD simulations.
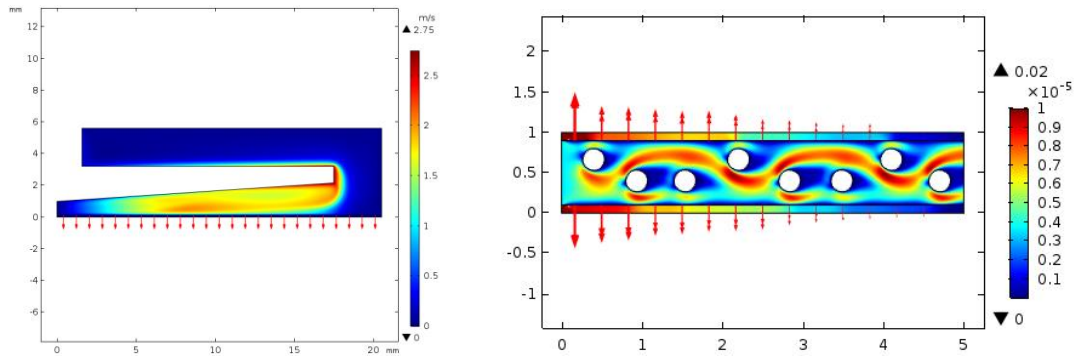
Figure 1.13 2D arrow surface plots for stirred cell device (left) and a screened TFF channel (right), generated by CFD modelling. Arrows in red represent permeate flow through the membrane, and arrow lengths are proportional to the magnitude of the velocity (m/s).

From Figure 1.13, the permeate flux, TMP and by extension, concentrations, can be seen to be uniform for the stirred dead-end units, unlike in TFF channels, where pressure through the membrane decreases from inlet to outlet, resulting in an inhomogeneous permeate flux. Failure to recognise these differences and issues mentioned earlier could lead to inaccurate scale-up, and shortfalls in performance could severely affect process economics and yield. The impact of such differences and their consequences on the performance of scale-down models and their predictability needs to be assessed.

1.5 Dynamic filtration systems

Conventional crossflow systems make use of high crossflow velocities to generate shear at the membrane surface required to minimise membrane clogging/fouling and maintain modest permeate fluxes. Feed flow rate and shear rates are intrinsically coupled for traditional tangential flow filtrations systems and thus for high concentration suspensions, the shear rates needed to minimise cake formation and fouling would require very large feed flow rates, which would result in the generation of unacceptable pressure drops across the channel. In contrast, dynamic filtration systems operate by creating relative motion between the membrane and its

housing/disc, and the wall shear rate is therefore independent of the feed flow rate, *i.e.*, flow and pressure are decoupled, allowing use of low feed flow rates to maintain low pressure drops across the channels without sacrificing mass transfer. Since low TMP can be controlled and maintained, the combination of high shear rates and low TMP enhances solute transmission through the membrane. For ultrafiltration applications, the high shear generated effectively depolarises the concentration polarisation layer and thus relatively higher TMP can be employed to enhance permeate flux and transmission. There are several different types of dynamic filtration systems commercially available, however they occupy a small share of the tangential flow filtration market (Jaffrin, 2008).

Dynamic filtration systems are typically of two configurations, namely vortex flow filters (VFF) and rotating disc filters (RDF) (Castilho et al., 2008). VFF consist of concentric cylinders which house the membranes and the relative motion of the cylinders create turbulence. For RDF, the membrane is generally kept stationary and the disc is rotated to generate shear stress and crossflow over the membrane. The hydrodynamics of the system tend to be a function of different operating conditions, such as flow rate, RPM, and geometric parameters such as the disc diameter, shape and position of disc (Serra and Wiesner, 2000). As shear rate is primarily a function of the disc rotational speed, the shear level in the module can be controlled accurately. Therefore, these systems tend to be most useful in microfiltration operations to clarify concentrated suspensions and the separation of biological products (Frenander and Jönsson, 1996; Lee et al., 1995). Rotating disc modules have been commercially available for a long time and primarily used in biotechnology applications to determine preliminary filtration characteristics. Some of the main drawbacks of RDFs include the complexity of mounting large discs, high speed rotation of multiple discs on the same axis and the cost of building process scale modules (Charcosset, 2012).

Vibrating Membrane Filtration (VMF) technology generates shear forces that are limited to a narrow layer on the membrane surface and hence very little energy is dissipated in the bulk fluid (PallSep Biotech Systems, 2009). The primary advantage is that a lower energy input is required to achieve comparable permeate fluxes and solute transmission levels using other TFF technologies. Postlethwaite et al. (2004) studied the protein recovery and fluxes for a commercial VMF system using *Saccharomyces cerevisae*. Average permeate fluxes of 45 LMH and 67%

transmission was achieved and maintained over long operating periods at a high cell concentration of 500 g/L.

The performance of a vibratory shear-enhanced processing (VSEP) laboratory module was investigated by Akoum et al. (2002), who demonstrated that shear enhancement using vibrations increased permeate flux. Vigo et al. (1990) developed a module where a cylindrical membrane was longitudinally vibrated inside a concentric cylindrical housing. A four-fold increase in the filtrate flux for an oil-water emulsion was observed when the membrane was oscillated with an amplitude of 10 mm. Energy requirements in the system were minimal due to the use of a relatively large channel height and low feed flow rate, although the energy loss due to friction associated with the mechanical forces used to generate the vibrations was quite high. More recently, Slater et al. (2015) studied the performance of a VSEP process for dewatering of freshwater microalgae, *Chlorella vulgaris*; high shear rates desirable for TFF microfiltration were generated by high-frequency torsional oscillations of the membrane unit. Permeate fluxes observed in the dynamic filtration mode were higher by a factor of 5, compared to fluxes generated in traditional TFF mode. These high fluxes were achieved and maintained with a relatively low energy consumption of 1.6 kWh/m^3 of water removed.

One of the most important characteristics of the various dynamic filtration systems is that the shear rate is a useful scale-up parameter and can help predict permeate fluxes, for a given set of conditions and geometrical parameters. Thus, permeate fluxes obtained at small scale can be reproduced at larger scales if they are operated at the same shear rates. Jaffrin (2012) has performed a comprehensive review and looked at various hydrodynamic techniques and designs, including RDF and other dynamic filtration systems, confirming that appropriate use of fluid instability and turbulence can improve the performance of membrane filtration.

1.6 Ultra Scale-Down technology

For filtration operations, it is crucial to develop an accurate mimic of the large scale TFF operation with significant reductions in operating volumes to cut down the cost of experiments. As part of the quality by design (QbD) approach to process development, ultra scale-down (USD) technology has been developed over the last decade or so, making use of small scale devices, which may not be geometrical similar to large scale counterparts. The small scale devices are used to generate data

rapidly, and combined with regime analysis and bioprocess modelling, can be used to accurately carry out predictable scale-up of various biopharmaceutical unit operations (Titchener-Hooker et al., 2008). FDA's initiative and emphasis on Quality by Design (QbD) of building quality into the product is currently valued at generating more than US$20 billion a year in annual profits, via a 25% reduction in time-to-market and more robust manufacturing process (Fuhr et al., 2009). This can only be achieved by a thorough and improved understanding of how the various process inputs and parameters influence the operation performance and key outputs. A well-defined model allows a relationship between the process parameters and overall performance to be established and to simulate the effects of varying different parameters on outputs.

USD techniques are different from approaches typically used for scale-down purposes, as they mimic and replicate scale-invariant critical parameters that control mass transfer and thus process performance, rather than geometry-based scaling (Titchener-Hooker et al., 2008). The USD technology revolves around regime analysis, biochemical engineering principles and defined bioprocess models to predict performance of industrial scale operations. This approach has been successfully developed and applied to several downstream processing operations such as centrifugation, flocculation and chromatography, where scale down models were used to predict large scale performance (Berrill et al., 2008; Chan et al., 2006; Delahaye et al., 2015; Lau et al., 2013; Li et al., 2013; Masri et al., 2017; McCoy et al., 2009; Noyes et al., 2015; Rayat et al., 2016; Shekhawat et al., 2018; Tait et al., 2009).

To scale bioprocesses, it is important to establish the relevant physical parameters. For a TFF system, the key operational variables to be considered during scale-up and optimisation include shear across membrane (governed by the crossflow rate), TMP and solids concentration in the feed stream, channel length, amongst others. The membrane pore size would also affect the throughput performance; a larger pore size would allow greater yields but produce a relatively 'dirty' permeate of poor clarity. Flat plate modules generally allow linear scaling; however, due to the complexity of the channels and spacer geometries of certain filter modules, a linear scaling might be difficult to achieve because the membrane configurations need to be kept constant too, apart from fixing the same operating parameters, identical loading ratio of solids loading to membrane area and using the same membrane material. The concept of critical flux is widely used in membrane research and development studies. One of

the key aims of USD studies is to carry out flux excursions and fouling studies, so that optimum operating fluxes can be determined for the large scale process.

Over the last decade or so, stirred cell devices have gained popularity and are commonly used in laboratories to characterise membranes and their separation behaviour, as well as to generate protein separation data for process scale-up (Becht et al., 2008). The high shear rates generated by the moving component, either via magnetic stirring or a rotating disc, on the membrane surface significantly improves flux, lowers energy requirements and minimises fouling and build-up of cake. Numerous scale-down work and methodologies have been developed over the last few decades. Previously, a rotating disc filter (RDF) in recycle mode was used in an attempt to scale-down large scale TFF (Lee et al., 1995). The study demonstrated that average fluxes greater than 200 LMH could be achieved for the microfiltration of recombinant *Saccharomyces cerevisae* cells. However, the results indicated the presence of a critical rotational speed, below which the performance of the rotating disk dynamic filtration system was like that of a flat sheet system, at a given solid concentration. The volume of feed material required could not be reduced effectively, resulting in long experimental times. In addition, operating conditions such as the transmembrane pressure were hard to maintain due to the small size of membrane and the inaccurate monitoring/control of the permeate flow, rendering the accurate operation at USD very difficult to achieve.

One of the most important characteristics of dynamic filtration systems, such as rotating disc filters or stirred-cell devices, is the ability to accurately define and control shear rates, a useful scale-up parameter that can help predict permeate fluxes, for a given set of conditions and geometrical parameters. Ma et al. (2010) successfully developed an ultra scale-down membrane device capable of replicating TFF performance at small scale to overcome these drawbacks. Adopted from the pulsed sample injection technique by Ghosh and Cui (2000), the rotating disc filter was modified by building in inserts to allow the flexibility of the chamber volume, so that a large volume reduction can be achieved and only 1.5 mL of processing material was needed for each diafiltration experiment. The new USD method used the modified rotating disc filter operated in dead-end mode; feed material was prefilled in the USD device and suitable buffer was pumped in through inlet port and out through to permeate. This new set-up was much simpler and accurate control of operating conditions has been achieved. In large scale operation, constant flux is easier to control than constant TMP (Forman et al., 1990), while for modelling purposes, step

increasing TMP at small scale is preferred because the fluxes behave in a time-independent manner, which can provide more reliable data. More recently, Fernandez-Cerezo et al. (2019) and Guo et al. (2016) have demonstrated successful scale-up performance from small scale devices to lab-scale Pellicon devices for molecule such as mAbs and phages.

The shear rate was identified as the key factor that determines the filtration performance and hence was used as the scaling parameter. The mass transfer coefficient, k, is directly related to the shear at the membrane surface, plus a multitude of chemical and physical interactions, which are constant with the same feed. Thus, for a given feed, a constant shear rate between scales would result in similar performances, in terms of process flux and transmission. To develop a successful USD mimic using wall shear rates as the scaling parameter, reliable wall shear rate correlations for both scales is crucial. Existing analytical models like the correlation developed by Bouzerar et al. (2000a), expressing local shear rate produced by a rotating disc as a function of rotational speed and viscosity, cannot be used to generate reliable shear rate estimation for this specific USD device as the rotating disc does not cover the entire membrane surface, apart from the obvious differences in chamber and disc geometry.

Process optimisation at small scale is vital as the yields and efficiencies of these early recovery steps determine the maximum quantity of protein that can be recovered and purified through the entire downstream purification train. Thus, the successful development of models and simulations using USD technologies are extremely important to help minimise experimental costs and identify optimum operation conditions at early stages, to maximise yield and throughput.

1.7   Computational fluid dynamics

Computational fluid dynamics (CFD) is the simulation of engineering systems using mathematical modelling and numerical methods/algorithms to analyse and solve fluid flow problems (Kuzmin, 2006). CFD is fundamentally based on and governed by the Navier-Stokes (NS) equations, which effectively describe the motion of fluid (Anderson, 1995). The key advantage of CFD simulation is that it provides an inexpensive method for qualitative prediction of fluid flow and flow patterns that might have been otherwise difficult or impossible to study using experimental techniques.

CFD technology is well established and heavily relied upon in the aerospace and automotive industries, and it has entered the chemical industries in the last 20 years.

Employing the use of CFD methods can accelerate product and process development, facilitate optimisation of existing processes, energy saving and efficient designs of products and processes, amongst others. Processes that require or handle large volumes of liquid, for instance, unit operations in the biopharmaceutical industry, can benefit through significant cost reductions as a result of small increments in efficiency (Pordal et al., 2002). Biopharmaceutical processes that could benefit from CFD analysis include turbulent flow in bioreactors, multiphase flow, heat and mass transfer and porous media flow. In a review by Ghidossi et al. (2006), it was seen that CFD yielded a better understanding of membrane processes without the need of extensive experimentation. Prototypes of various kinds of systems can be modelled and visualised, thus fulfilling the goal to develop better membrane designs more rapidly and in a cost-effective manner.

In recent times, the biopharmaceutical industry has reported increased interest in using CFD techniques to gain insights into fluid dynamics to focus on process modelling and system design. Extensive CFD studies have been done to simulate fluid flow in various processes such as in bioreactors (Davidson et al., 2003; Williams et al., 2002), centrifuge designs (Pordal et al., 2002), membrane filtration systems (Darvishmanesh et al., 2010; Pak et al., 2008; Rahimi et al., 2005; Rainer et al., 2002; Taha and Cui, 2002; Zare et al., 2013), membrane bioreactors (Amini et al., 2013; Ratkovich et al., 2012), rotating disc filters (Castilho and Anspach, 2003; Francis et al., 2006) and chromatography columns (Pathak et al., 2008; Schmidt et al., 2011).

With regards to RDFs, a lot of work has been done in the past, looking at flow patterns within the system and the impact of geometry and flow conditions on their relative performances (Bouzerar et al., 2000; Castilho and Anspach, 2003; Ding et al., 2015; Francis et al., 2006; Hwang and Lin, 2014; Jaffrin, 2008; Ladeg et al., 2018; Rainer et al., 2002; Ratkovich et al., 2012; Taamneh, 2010; Thundil Karuppa Raj et al., 2014; Torras et al., 2009, 2006; Valencia, 2010). Similarly, plenty of research has been carried out for screened channels using a CFD-based approach and investigating flow in such channels and the impact of screen geometry on flow, pressure, concentration and mass transfer profiles (Da Costa et al., 1994; Darvishmanesh et al., 2010; Fimbres-Weihs and Wiley, 2007; Koutsou et al., 2007; Li et al., 2004, 2002; Lipnizki et al., 2003; Schwinge et al., 2002; Subramani et al., 2006; Wiley and

Fletcher, 2002). There have also been instances where concentration polarisation and permeate flux models have been derived using CFD modelling (Marcos et al., 2009; Rahimi et al., 2005; Wardeh and Morvan, 2008; Yuanfa et al., 2012).

The results generated by CFD simulations are never a 100% reliable for numerous reasons; for instance, the input data may involve too much imprecision, the physics used to model the problem might be inadequate in capturing the flow of interest, or perhaps the accuracy of the solution is limited by the available computing power (Kuzmin, 2006). Consequently, extensive experimental validation of the CFD model is required to ensure the CFD simulations, the underlying boundary conditions and the assumptions involved are correct. Laser Doppler Velocimetry (LDV) and Particle Image Velocimetry (PIV) are well established non-intrusive techniques that can be used to measure fluid velocity for transparent systems, which can then be compared against predicted CFD flow fields (Hyun et al., 2003).

1.8   Performance metrics for tangential flow filtration

1.8.1   Permeate flux

Permeate flux is the volumetric flow rate of permeate per effective unit membrane area. Permeate flux can be described using Equation 1.14:

$$\text{Permeate flux (LMH)} = \frac{\text{Permeate flow rate (mL/min)}}{\text{Membrane area} \, (m^2)} \times 0.06$$

Equation 1.14

*LMH: $(L/h)/m^2$ (non-SI unit commonly used in industry)

For microfiltration, the permeate flux through the porous membrane can be described by Equation 1.15, a modified form of Darcy's Law; the permeate flux is a function of pressure applied, fluid viscosity, and the sum of hydraulic resistances (at a fixed crossflow rate).

69

$$J = \frac{TMP}{\mu \cdot R_T}$$

<div align="right">**Equation 1.15**</div>

where J is the permeate flux $((m^3/s)/m^2$ or m/s), TMP is the transmembrane pressure/pressure gradient (Pa), R_T is the total hydraulic resistance (1/m) and μ is the dynamic viscosity of the permeate (Pa.s).

1.8.2 Transmission

The fractional transmission of proteins through membranes is an important measure, particularly in cases where the protein is the desired product. The observed transmission (T), otherwise known as the sieving coefficient (S), is generally defined as the ratio of the concentration of the solute in the permeate (C_P) to the concentration of solute in the retentate or bulk solution (C_R):

$$T = \frac{C_P}{C_R}$$

<div align="right">**Equation 1.16**</div>

where C_P and C_R are the concentrations of solute (g/L) in the permeate and retentate, respectively.

Solute transmission can be used to measure the efficiency of a filtration system by determining the yield for diafiltration processes. Product transmission in MF is determined by the ratio of effective membrane pore size to the particle size unlike in UF, where transmission is primarily dependent on the permeate flux since the pore size is much larger in MF compared to UF.

1.9 Research aim and objectives

The primary aim of the work in this thesis was to develop a scale-down methodology and robust model that can accurately predict large scale tangential flow filtration performance using the USD membrane device, and subsequently demonstrate its

potential applications in bioprocess development and optimisation. The research focuses on characterising the fluid flow at both scales and establish equivalent operating conditions that is scale invariant, using a computational fluid dynamics approach.

The primary objectives of this research are:

- to characterise and develop wall shear rate correlations for the USD membrane filtration device and Pellicon TFF cassettes using CFD modelling, followed by 2D particle image velocimetry (PIV) verification studies to verify CFD simulated data against experimental data,
- to overcome limitations of existing scale-down methodologies by developing a specific USD based methodology and prediction model, to successfully scale-up and predict tangential flow filtration at scale, accounting for potential differences in geometries, systems, cassettes and flow across scales,
- to validate scale-up methodology by performing comparative USD and large scale tangential flow filtration experiments using different biological feedstock of varying complexities, such as BSA, *Escherichia coli* homogenate and *Pichia pastoris,*
- to demonstrate real life bioprocessing applications of the validated USD methodology and model using the USD membrane device using *Saccharomyces cerevisae* and *Chlorella sorokiniana.*

1.10 Thesis Synopsis

The investigations and results within the thesis are presented across four chapters and their specific objectives are summarised as follows:

Chapter 3: Computational fluid dynamics modelling of USD membrane device and TFF cassettes

CFD was used in this chapter to investigate fluid flow in both the USD membrane device and screened channels in tangential flow filtration, and correlations for equivalent operating conditions developed using characteristic wall shear rates at both scales. The impact of geometry on wall shear rates profiles was also investigated.

Chapter 4: Formulation of an Ultra Scale-Down methodology and prediction model for tangential flow filtration scale-up

This is the keystone of the research carried out. Data generated from the CFD work in Chapter 3 were incorporated into an experimental methodology, and phenomenon in TFF cassettes investigated and accounted for in a mathematical model to enable a more accurate and predictable scale-up to large scale tangential flow filtration using USD data. Rules for scale-up were also established.

Chapter 5: Validation of scale-up methodology and model for USD tangential flow filtration

This chapter contains four validation studies for non-linear scaling, scaling-up from the USD membrane device to pilot-scale TFF cassettes, using USD methodology and scale-up rules developed in Chapter 3. The prediction model was validated by comparing predicted data against large scale data generated by performing equivalent large scale experiments.

Chapter 6: Case studies for USD-based bioprocessing applications

This final chapter investigated the applicability of proposed USD membrane technology, for real life bioprocessing situations, including novel methods to optimise tangential flow filtration processes and improve volumetric throughputs.

2   Materials and methods

2.1   Materials

2.1.1   Chemicals and reagents

All chemicals, including D-glucose, PBS, potassium phosphate dibasic (K_2HPO_4), sodium hydroxide, sodium phosphate monobasic (for HPLC), employed were purchased from Sigma-Aldrich (Dorset, UK) and ACROS Organics and were of analytical grade, unless stated otherwise.

2.1.2   PVP-40

Polyvinylpyrrolidone (PVP), average molecular weight 40 kDa, was dissolved in RO water and mixed thoroughly to make up a final concentration of 10 g/L.

2.1.3   *Saccharomyces cerevisiae* suspensions

Dried, active *Saccharomyces cerevisia* (Affymetrix, UK) was used to make up fresh *Saccharomyces cerevisae* suspensions in phosphate buffer (20 mM K_2HPO_4, pH 7) supplemented with 5 g/L D-glucose and mixed at 200 RPM for 4 hours. The mixture was spun down and the resulting cell paste was washed with PBS buffer, after which, the paste was re-dissolved in appropriate volumes of phosphate buffer to make up the desired cell concentrations. Prepared suspensions were well mixed and kept homogenous throughout the experiment.

2.1.4   *Pichia pastoris* feed

Pichia pastoris cells were cultured in 100 mL buffered complex glycerol media (BMGY) using 1 L shake flasks, till an OD_{600} of ~15 was reached; the detailed procedure is outlined in Pichia Fermentation Process Guidelines (Invitrogen Corporation, 2002). 500ml Basal synthetic media (BSM) was transferred to an Infors 1 L bioreactor, and after pH and dissolved oxygen (DO) were adjusted, Pichia trace metal 1 (PTM1) was added to the media. Appropriate volume of the inoculum was added to bioreactors to obtain a starting OD_{600} value of about 1. After all the initial glycerol in the medium was used up, indicated by a DO spike, 50% (v/v) glycerol was

fed to the bioreactors at the rate of 12 mL/L/h for 6 hours. Starvation for 1 hour was then followed by glycerol feeding, to ensure all residual glycerol was exhausted. After starvation, methanol was used to induce expression, fed at a flow rate of 3.6 mL/L/h for the first 2 hours to induce the expression of alcohol oxidase 1 (AOX1), following which, feed flow rate was increased and kept at 10.8 mL/L/h until point of harvest (total induction time was about 115 hours). Fresh feed was kindly donated by Dr. Baolong Wong (Department of Biochemical Engineering, University College London).

2.1.5 *Escherichia coli* homogenate feed

An *Escherichia coli* w3110 strain (ATCC 27325) containing the plasmid pTTOD A33 IGS2, was kindly donated by UCB Pharma Ltd. (Slough, UK), coding for a 46 kDa antibody fragment (Fab') utilising a *tac* promoter. Fermentation methods and procedures are detailed in the paper by Newton et al. (2016). Final average wet cell weight of the broth was determined to be around 150 g/L and the typical Fab' concentration was approximately between 1-1.5 g/L.

Following cell harvest, 5 L of the broth was disrupted using a pilot-scale homogeniser (one pass at 500 bar pressure), APV Manton-Gaulin Lab 60, and the resulting homogenate was then frozen. To achieve the desired cell concentration, pre-determined sample volumes were thawed and RO water used to dilute it. The feed was well mixed throughout the experiments and kept at room temperature. The *Escherichia coli* feed was kindly donated by Dr. Joseph Newton (Department of Biochemical Engineering, University College London).

2.1.6 *Chlorella sorokiniana* strain and culture conditions

Axenic *Chlorella sorokiniana* culture, CCAP 211/8K (Argyll, Scotland), was used as the master cell bank and sub-cultured for all algal studies in this thesis. Cells were inoculated at 10% (v/v) and sub-cultured in 250 mL Corning Erlenmeyer flasks (vented caps), shaken in Brunswick Innova 44/44R (Eppendorf AG, Hamburg) at 100 RPM and 25±1 °C. Phototrophic and mixotrophic cultures were illuminated with cool-white fluorescent light (80-100 $\mu E.m^{-2}.s^{-1}$), while heterotrophic and mixotrophic cultures supplemented with 5-15 g/L D-glucose or in the case of TAP media, 17.4 mM acetate. The autotrophic cultures used atmospheric air containing ~0.03% (v/v) CO_2 as their only inorganic carbon source. All cells were grown to the end of their respective exponential phases before harvest and stored for experiments.

Three different media, namely Tris-Acetate-Phosphate (TAP), modified Bold's basal medium (3N-BBM+V) and *Euglena gracilis* medium:*Jaworski's* medium (EG:JM) in a 1:1 ratio, were used to cultivate the *Chlorella sorokiniana* cells. Table 2.1 shows the composition of the three different media. All media were autoclaved at 1 bar (15 psi) for at least 15 minutes, and the glucose solution filter sterilised using a Millipore Stericup before being added to the sterilised media. The basic TAP formulation was slightly altered for some experiments, with respect to the carbon source used (acetate substituted with D-glucose), as well as the primary buffer component (PIPES instead of Tris). The initial pH of all media were adjusted between 6.6 and 7.5, depending upon the media.

In order to obtain and maintain axenic cultures, an antibiotic cocktail mix comprising of broad-spectrum antibiotics was added to the media (Campbell, 2005). 20 mL of stock solution was made in pure water and contained Cefotaxime (500 mg/L), Carbenicillin (500 mg/L), Kanamycin (200 mg/L), and, Augmentin (200 mg/L). The antibiotic stock solution was then filter sterilised using a 0.22 μm sterile Durapore PVDF membrane (Stericup Filter unit, Merck KGaA, Darmstadt, Germany) and frozen at -20 °C. 1 mL of this mixture was added to cell cultures, upon inoculation. However, it is important to note that this method is not guaranteed to be completely successful at eliminating all bacterial species, as *Chlorella sorokiniana* has been known to have a symbiotic relationship with bacteria and is suspected to be incapable of prolonged, high cell density growth without bacteria (Fuentes et al., 2016).

TAP media (Andersen, 2005)		3N-BBM+V (Bischoff, 1963)		EG:JM (CCAP)	
Component	**[ ]**	**Component**	**[ ]**	**Component**	**[ ]**
Tris-base	20 mM	$NaNO_3$	2.94 mM	$CaCl_2$	0.010 mM
NH_4Cl	7 mM	$MgSO_4.7H_2O$	0.304 mM	$C_2H_3NaO_2.3 H_2O$	7.50 mM
$MgSO_4 .7H_2O$	0.83 mM	NaCl	0.428 mM	"Lab-Lemco" powder	1 g/L
$CaCl_2.2H_2O$	0.45 mM	K_2HPO_4	0.431 mM	Tryptone	1 g/L
K_2HPO_4	1.65 mM	KH_2PO_4	1.29 mM	*Saccharomyces cerevisae* extract	2 g/L
KH_2PO_4	1.05 mM	$CaCl_2.2H_2O$	0.170 mM	$Ca(NO_3)_2.4H_2O$	0.085 mM
$Na_2EDTA.2H_2O$	0.134 mM	$ZnSO_4.7H_2O$	0.307 µM	KH_2PO_4	0.09 mM
$ZnSO_4.7H2O$	0.136 mM	$MnCl_2.4H_2O$	7.28 µM	$MgSO_4.7H_2O$	0.20 mM
H_3BO_3	0.184 mM	MoO_3	4.93 µM	$NaHCO_3$	0.190 mM
$MnCl_2.4H_2O$	0.04 mM	$CuSO_4.5H_2O$	6.29 µM	EDTAFeNa	6.06 µM
$FeSO_4.7H_2O$	32.9 µM	$Co(NO_3)_2.H_2O$	1.68 µM	$EDTA.Na_2$	6.65 µM
$CoCl_2.6H_2O$	12.3 µM	H_3BO_3	0.185 mM	H_3BO_3	40.1 µM
$CuSO_4.5H_2O$	10 µM	$EDTA.Na_2$	0.171 mM	$MnCl_2.4H_2O$	7.02 µM
$(NH_4)_6MoO_3$	4.44 µM	KOH	0.553 mM	$(NH_4)_6Mo_7O_{24}.4H_2O$	0.809 µM
CH_3COOH	17.4 mM	$FeSO_4.7H_2O$	17.9 µM	Vit. B12 (Cyanocobalamin)	0.295 µM
		H_2SO_4 conc.	1 mL/L media	Vit. B1 (Thiamine HCl)	1.186 µM
		Vit. B1 (Thiamine HCl)	2.97 µM	Vit. H (Biotin)	1.637 µM
		Vit. H (Biotin)	1.02 nM	$NaNO_3$	0.941 mM
		Vit. B12 (Cyanocobalamin)	0.111 nM	$Na_2HPO_4.12H_2O$	0.101 mM

Table 2.1 Composition of TAP (Tris Acetate Phosphate), EG:JM and 3N-BBM-V+ media used in this work.

2.1.7 Pilot-scale equipment

The pilot-scale equipment used in this study was a Sartoflow Advanced filtration rig, kindly donated by Sartorius Stedim Biotech GmbH (Göttingen, Germany), and used for cassettes $\geq 0.1\text{m}^2$ process area. All process data was logged by BioPat MFCS/DA v4.2 (on a Windows 7 x64 4GB system), and values recorded every second. Figure 2.1 and Figure 2.2 show the experimental setup and the process and instrumentation (P&I) diagram of the rig, respectively.
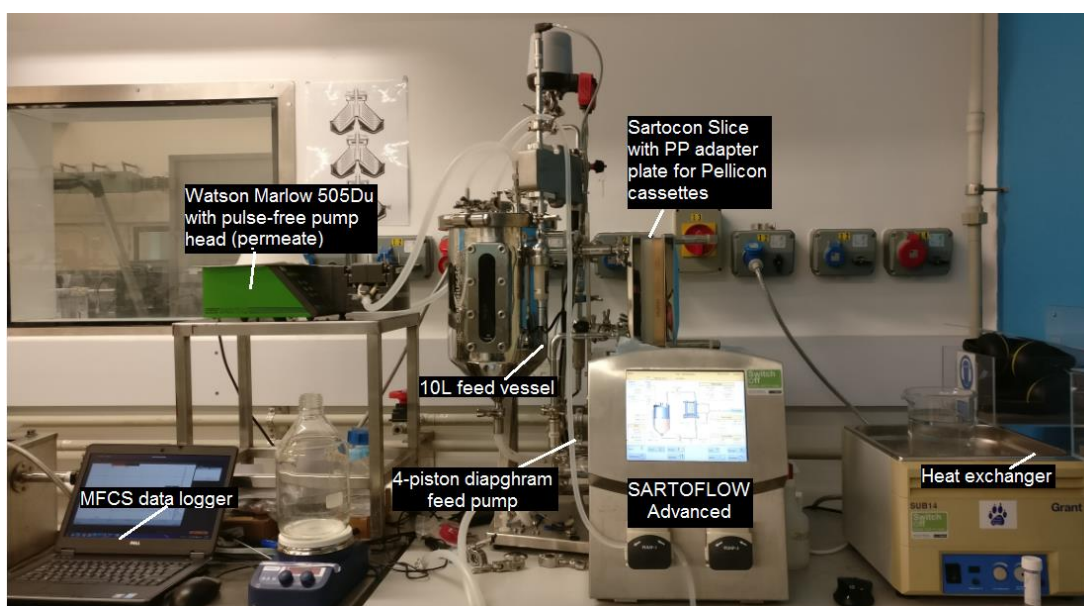
Figure 2.1 Experimental setup for large scale TFF using the Sartoflow Advanced filtration rig, with data logger and external permeate pump for flux control.
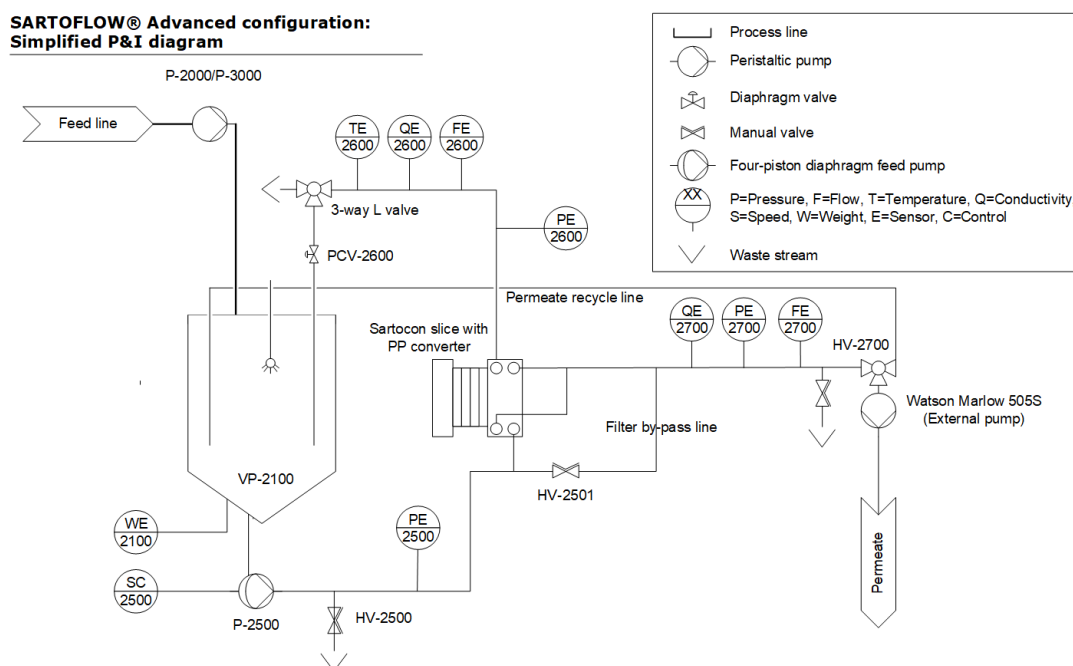
Figure 2.2 Sartoflow Advanced filtration rig schematics, with the respective components and sensors labelled.

Two custom-made, L-port 3/4" Sanitary Stainless Steel 3-Way Ball Valves (Valves online, UK) were installed on the permeate and retentate lines to help switch between total recycle and flushing modes of operation, where permeate and retentate line are diverted to the feed vessel and drain, respectively. The rig comprised of an in-line diaphragm feed pump, pressure, temperature and conductivity sensors, Sartoflow 10 L double jacket tank and a Sartocon Slice filter holder. Sartocon Slice polypropylene mirror inverted adapter plates (Sartorius Stedim UK Limited, Surrey) were used to make the Pellicon 2 mini filter modules (Merck Life Sciences KGaA, Germany) compatible with the Sartocon slice holder, by changing the configuration of the Sartocon slice holder from an oval to round port configuration.

The feed vessel had two SS dip tubes for both retentate and permeate return; the retentate line was directed to the bottom of the vessel, whilst the permeate flow was directed to the side of the vessel to minimise formation of vortices and foaming within the feed vessel at high recirculation flow rates. The filtration setup had a measured hold-up volume of around 175±10 mL (including dead volume of retentate side of the cassette). The feed pump was limited to a pressure of 4 bar, and a 100 µm nylon mesh pre-filter used to filter all feed solutions before entering the system.

Finally, an external peristaltic pump, Watson Marlow 505*Du* (with 505L twin offset pulse-free pump head), was used to regulate the permeate flux, since the TFF rig did not have an existing permeate pump or automatic pressure control valve to control the permeate flux.

2.1.8 Lab-scale equipment

The AKTA Crossflow demo system, kindly loaned by GE Healthcare Life Sciences (Amersham, UK), was used to carry out lab-scale studies involving Pellicon XL and P3 micro cassettes and ultra scale-down experiments using the USD membrane filtration device (section 2.1.9). 2.9 mm (i.d.) tubes were used for all the inlet and outlet lines and the system had a dead volume of around 20-25 mL, excluding the cassette hold-up. UNICORN v5.11 was used to control, record and monitor all process variables and data, including the setup of custom methods for the dynamic flux control (section 6.2.2.3.2). A custom-made 350 mL SS-316 reservoir, equipped with a magnetic stirrer and a cooling jacket, was used with the AKTA Crossflow. The system was sanitised, cleaned and stored in 0.1 M NaOH solution, unless stated otherwise.

A Pellicon mini cassette holder (Merck Life Sciences KGaA, Germany) was used to house the P3 micro cassettes; PEEK plastic connectors TC 5/16" (GE Healthcare Life Science, UK) were used to connect the mini cassette holder to the AKTA Crossflow system, whilst the Pellicon XL cassettes used female 5/16" to male luer converters (GE Healthcare Life Science, UK).

2.1.9 USD membrane filtration device

AKTA Crossflow (GE Healthcare Life Sciences, UK) was used to carry out the USD experiments using the USD membrane filtration device, designed to allow filtration of the material across the membrane at a set flux/pressure. It mimics tangential flow filtration despite being operated in a dead-end mode. Ma et al. (2010) developed and used a 1.7 mL device with inserts; however, throughout this thesis, a geometrically similar device of larger capacity, 5.3 mL, and thus larger membrane are was used, to allow a larger feed volume:membrane area loading upon scale-up compared to the smaller 1.7 mL USD device. Figure 2.3 shows a 3D CAD model construct and a simplified cross-sectional view of the USD membrane filtration device.
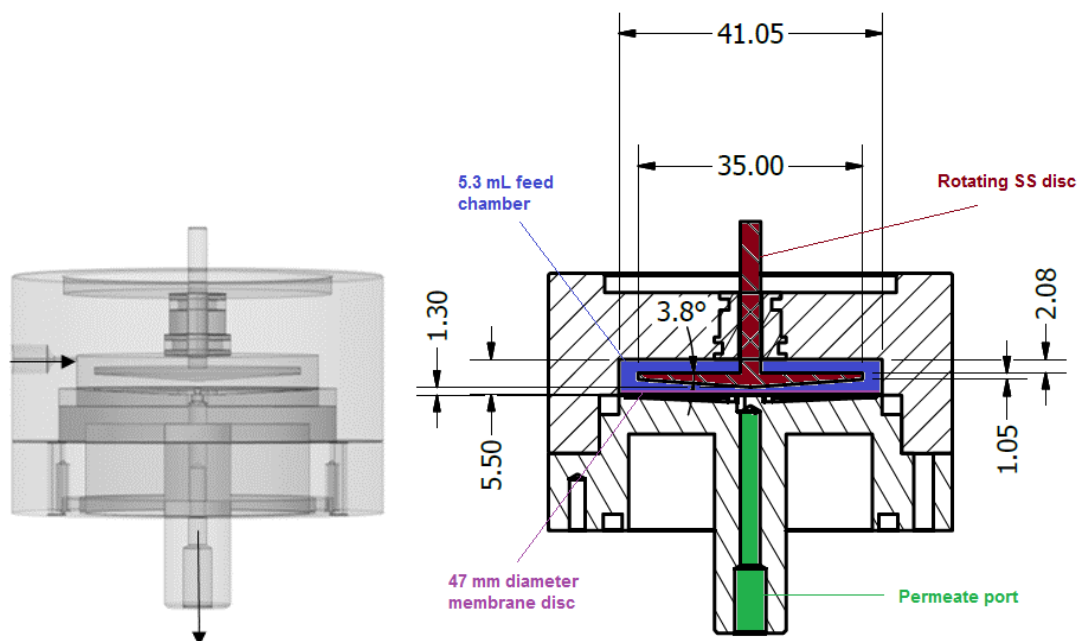
Figure 2.3 Transparent side-on view of the USD membrane filtration device (left) and a simplified 2D cross-sectional illustration of the USD membrane filtration device (right). Images are not to scale and all units shown in mm.

The USD device comprises of a transparent Perspex shear chamber with a centrally mounted SS grade-316 rotating disc, which provides the crossflow effect at the membrane surface. The disc is 35 mm in diameter with a 3.8° conical cross-section. The rationale behind a disc angle of <4° was to provide a uniform shear at the membrane surface; the angle was 4° design wise but fabricating the disc at that scale had tolerances, and thus the actual angle was ~3.8°. The motor is controlled by a speed control unit and is disc capable of rotating at speeds between 2000-12000 RPM. The speed control unit was programmed to operate at fixed speeds of 3000, 3500 and 4000 RPM to mimic linear crossflow rates typically achieved in UF/MF operations (0.1-1 m/s). The discrete speed setting, as opposed to a continuous speed band, allows use of a feedback control loop to provide constant rotation irrespective of the viscosity of the process material, especially during concentration operations, where the feed becomes more viscous over time. The chamber houses 47 mm diameter flat-sheet membrane discs, providing an effective membrane surface area of 13.2 cm^2, as part of the membrane is blocked off by the O-ring. A PTFE body two-way valve (Sigma-Aldrich, Dorset, UK), shown in section 2.2.2, was installed to prevent gravity-assisted flow through the open membranes (>300 kDa) before feed flow was initiated at the start of the run.

The USD device was equipped with a K-type thermocouple, connected to an EL-USB-TC thermocouple USB data logger (Lascar Electronics Ltd., Wiltshire, UK), and combination with the cooling jacket (operated using an external pump to recirculate cooling water through the jacket), were used to control operating temperatures to 25±1 °C.

2.1.10 Filter membranes/cassettes

All membranes were obtained from Merck Life Sciences KGaA (Darmstadt, Germany). 47mm discs and Pellicon XL (50 cm^2), P3 micro (88 cm^2) and P2 mini (0.1 m^2) were used throughout. Table 2.2 lists the main characteristics, pore sizes and key operational data for each membrane format and type used throughout this thesis.

Membrane type	Membrane material[2]	Applicable feedstock (average size)	Pore size/ NMWL	Key specifications and cleaning regime used[3]
Durapore	*m*PVDF	*Escherichia coli* (2-3 µm)*, Pichia pastoris* (4-6 µm), mammalian cells (10+ µm)*, Saccharomyces cerevisae* (5-10 µm)*,* flocculated suspensions	0.65 µm 0.45 µm 0.22 µm	• 0.125±0.05 mm thick* • High throughput, robust material • 0.5%(m/v) Tergazyme, followed by 0.1 N H$_3$PO$_4$ @ 25-40 °C
Biomax	*m*PES	Lysates (<1 µm), homogenates (<0.1 µm), mAbs, BSA, lysozyme	1000 kDa 500 kDa 300 kDa 10 kDa	• 0.308±0.02 mm thick* • Very low protein binding • 0.1-1 M NaOH (+100 ppm NaOCl, if needed) @ 25-40 °C

---

[2] *m*=modified; since PVDF and PES are intrinsically hydrophobic polymers, the membranes are treated to have a hydrophilic surface
[3] Merck Millipore Pellicon 2 Cassettes FAQ webpage (http://www.merckmillipore.com/GB/en/product/Pellicon-2-Ultrafiltration-Cassettes,MM_NF-C613?CatalogCategoryID=#specifications). Accessed 10/01/17

Ultracel	Composite regenerated cellulose (CRC)	BSA, PVP-10, molecules > 30-40 kDa	30 kDa	• 0.100±0.02 mm thick* • Higher integrity and flux due to composite membrane (UF layer cast upon a MF base) • 0.1-0.5 M NaOH @ 25-40 °C

average thicknesses reported since membranes compress under pressure at high flow rates

Table 2.2 Types and characteristics of the membranes used in the study.

For the USD device, Typar base 30 (0.2 mm thick) was placed underneath the membrane disc (when using CRC Ultracel) to prevent occlusion of the membrane due to the permeate channel ridges, which compacts the membrane under high pressure (>1.5-2 bar), typical for tight cut-off UF membranes.

Table 2.3 lists the various Pellicon cassettes and membrane types used for the experiments, and the various screens and respective operating flow rates and hold-up volumes. All cassettes/membranes were stored in 1% (v/v) acetic acid+0.12 N H_3PO_4 solution at 4 °C in between experiments.

Membrane configuration	Type	Typical flow rates/ max. pressure[4]	Total number of retentate,permeate channels	Approximate retentate hold-up volume (mL)[5]
φ47 mm flat-disc (17.3 mm^2)	UF (< 300 kDa)	4.8 bar (70 psi)	-	-
	MF (≥300 kDa)	0.7 bar (10 psi)		
Pellicon XL (50 cm^2)	A-screen	4-8 LMM	1,2	0.7
	C-screen	4-8 LMM		0.9
P3 micro (88 cm^2)	A-screen	Same as above	1,2	1.3
	C-screen			1.5
P2 mini (0.1 m^2)	A-screen	Same as above	12,13	17
	C-screen			18
	V-screen	8-15 LMM		20.3

Table 2.3 Types of cassettes used for the experiments, with key design and operational data.

2.2   Methods

2.2.1   Pilot-scale filtration

0.1 m^2 cassettes were installed into the Sartocon slice holder and manually tightened to a torque of 22-24 Nm, required to achieve the minimum axial compression needed to fully seal the internal gaskets and sealants of the TFF cassette(s). The rig was completely flushed and recirculated with at least 5L RO water to remove any air and residual solution, followed by taring the pressure sensors and weight cell to read zero. TMP was either varied by restricting the retentate valve (R-PCV), or for open membranes, the peristaltic pump on the permeate line was used to regulate flux.

---

[4] Merck Life Science KGaA (2018), Dr. PJ Beckett, Technology Consultant - Merck Life Sciences KGaA (personal communication, 16/04/2018)
[5] Merck Life Science KGaA (2013), Merck Millipore Pellicon 2 product web page. http://www.merckmillipore.com/GB/en/product/Pellicon-2-Ultrafiltration-Cassettes,MM_NF-C613?CatalogCategoryID=#specifications. Accessed: 25/01/2017

When using permeate pump control to achieve low TMP, a minimum of 0.05 bar permeate backpressure was maintained to ensure the permeate pump flow rate was always lower than the spontaneous permeate flux through the membrane, thereby avoid introduction of air via suction.

All process feed was pre-filtered using a 100 µm nylon mesh in-line filter, which is particularly important for tight screen cassettes (such as the A and C screen), where larger particulates and aggregates could potentially block the narrow feed channel/inlet port, leading to an inlet pressure surge.

The filtration protocol (as recommended in the Pellicon 2 Filters user guide) that was used for a typical TFF run is as follows:

All cassettes were flushed with RO water, through both retentate and permeate side out to drain, until a total volume of at least 30 L/m^2 and conductivity on both lines returned to baseline. A TMP of 1-2 bar was used occasionally to completely flush out any trapped air within the cassette screen and membrane pores, mainly for tight cut-off membranes (<100 kDa). Pre- and post- operational cleaning was done using appropriate cleaning regimes (outlined in Table 2.2); the cleaning solution was recirculated in total recycle mode, for >30-60 minutes at 1-2 bar feed pressure and at least 30% permeate conversion. The cleaning regimes were followed by rigorous water flushes to remove all traces, until a value of <0.1 mS/cm was registered on both retentate and permeate conductivity meters, to ensure all residues of cleaning reagent was removed. All three pressure sensors and the load cell were tared to zero, while the flow meters were manually calibrated using a measuring cylinder and stopwatch, while the pressure sensors were calibrated using a digital pressure gauge (Sartorius Stedim Biotech GmbH, Germany) during initial system setup.

Experiments were carried out depending whether it was a flux excursion, concentration or a diafiltration run. Most operations were performed at constant feed flow rate and constant permeate flux, unless stated otherwise.

2.2.1.1 Concentration

Both batch and fed-batch concentrations were carried out under constant permeate flux mode; for the latter, process feed was continuously pumped into the feed vessel to maintain a constant retentate volume of 500 mL (~0.5 kg). The feed flow rate was

slowly increased to the desired flow rate, with permeate valve closed. Once a relatively constant dP was achieved, permeate flow was initiated by slow increasing the pump speed to the desired permeate flux. TMP was constantly monitored and recorded, and operation stopped either when the desired concentration factor (CF) was achieved, or when the pre-defined TMP limit of 0.7-0.8 bar was reached, whichever occurred first. A minimum retentate volume of 500 mL (to ensure retentate return line dips below the liquid level) was always maintained in the system to avoid the introduction of any air into the system and to prevent localised concentration of cells on the membrane, which could form a stagnant cake layer due to the relatively low volume of liquid available for recirculation/crossflow.

2.2.1.2 Diafiltration

Buffer conditioning, particularly for diafiltration applications, helps ensure that the membrane is air free (especially on the permeate side), adjust system temperature and as a final step, to remove any remaining traces of cleaning solution that could interact with biomolecules in the feed. First, the membrane and system was washed twice using RO water, after which, the appropriate buffer was pumped into the system and recirculated at the appropriate operational flow rate, at a TMP of 1 bar, and carried out till both the retentate and permeate lines registered the same conductivity value.

Continuous diafiltration was carried out in constant retentate volume mode, where diafiltration buffer was fed into the feed vessel at the same rate as permeate flux, using the WIRC-2100 controller, which automatically pumped buffer to the vessel to maintain constant load cell weight as liquid left the system as permeate. At least 7 diavolumes were collected and all experiments carried out at 25±1 °C.

At the end of the run, after the feed material was recovered and the system thoroughly purged using RO water, NWP was re-measured and the cleaning of the cassette and Sartoflow systems was carried out. Cleaning was repeated with harsher conditions, *i.e.*, elevated temperatures and concentrations if needed, to help restore permeability closer to the pre-experimental baseline NWP.

2.2.2   Lab-scale filtration

When using Pellicon XL and P3 micro cassettes, both permeate ports were made use of and connected to the permeate return line of the AKTA Crossflow using a Y-connector (3xUNF 5/16" female) from GE Healthcare Life Sciences (Amersham, UK) to help even out permeate pressures and equilibrate pressures across the membrane (discussed in section 4.2.2.2). Pressure alarms for feed, retentate and TMP were set at 3.5 bar, 3 bar and 2 bar respectively.

Operational methods were similar, as described for pilot-scale filtration in section 2.2.1. All feed was prefiltered (100 µm) before being fed into the reservoir, which was kept well mixed and stirred at ≥300 RPM throughout the experiments.

2.2.3   Ultra Scale-Down (USD) membrane filtration

The USD membrane filtration device was run in constant flux mode using AKTA Crossflow (GE Healthcare Life Sciences, UK) as the feed pump. Single-use φ47 mm membranes obtained from Merck Life Sciences KGaA (Darmstadt, Germany) were used. The experimental setup for the USD filtration study is shown in Figure 2.4. The AKTA pressure sensors were calibrated and tested using a Kvick Lab Pressure Gauge Kit (0-4 bar) from GE Healthcare Life Sciences (Amersham, UK). All USD studies were carried out using the setup and methodology described here.
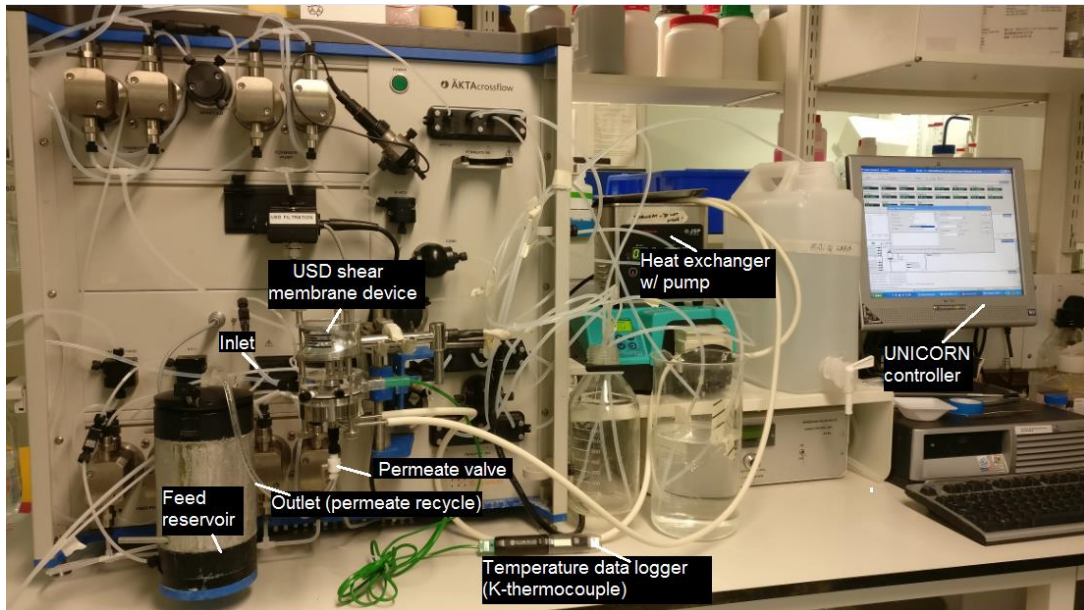
Figure 2.4 Experimental setup of the USD membrane filtration device and AKTA Crossflow system.
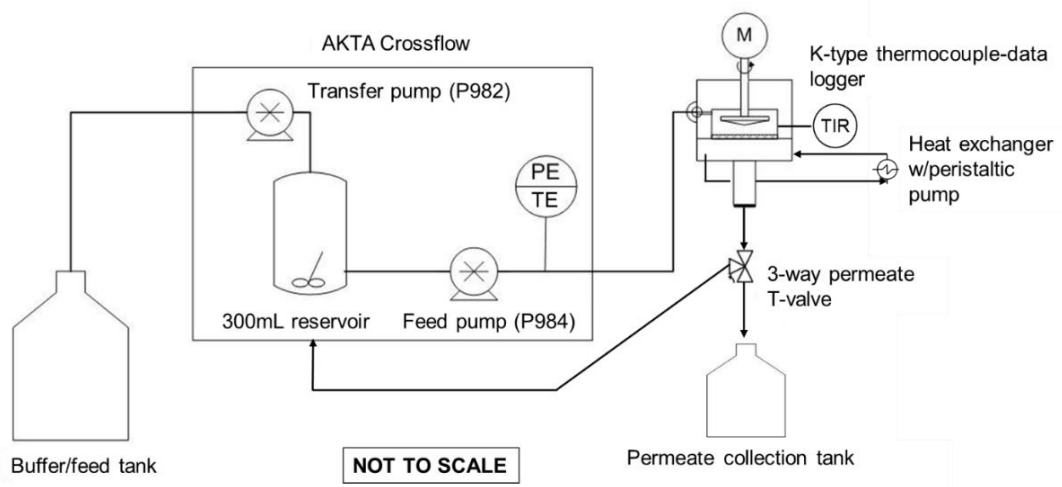
Figure 2.5 Cross-sectional illustration of the USD membrane filtration device and simplified process diagram of the setup used**.**

2.2.3.1 Operation

Using a similar approach to Ma et al. (2009), the USD membrane device was operated in a dead-end configuration, but with crossflow capabilities due to the controlled shear generated by the rotating disc. For standard operations such as flux excursions and NWP measurements, the feed material was prefilled in the USD device and only buffer/pre-filtered feed was pumped in through the inlet port while permeate flows out of the device, and back into the reservoir. The feed material was carefully injected into the 5.3 mL shear chamber, and the filtration solution fed into the USD membrane filtration device using the feed pump of the AKTA Crossflow system. It is important to prevent the introduction of any air bubbles into the chamber, as these bubbles can contribute to added shear and pressure changes upon implosion. In dead-end mode, the permeate pressure is zero (P_P=0, as the permeate flow is unrestricted and hence equal to atmospheric pressure), the retentate and feed pressures are equal (P_F=P_R) and hence, TMP is equal to the feed pressure:

$$TMP = P_F$$

Equation 2.1

The membrane was immersed and pre-conditioned using a suitable buffer solution or milli-Q water before being placed (shiny side up) on the bottom filtration plate. A new membrane was used for each experiment. The USD membrane device was then connected to the RVB-1 feed line of the AKTA Crossflow system via a GE Healthcare Union Connector (5/16" female to M6 male), and the feed pressure monitored and recorded as TMP over the course of the experiment. Permeate flux was controlled by adjusting the flow rate of the feed pump, using the AKTA control software, UNICORN v5.11. The AKTA Crossflow can pump fluids up to 600 mL/min, and records process variables such as feed pressure, temperature and TMP every few seconds (~1.5–3.0 seconds).

2.2.3.2 Concentration

Process feed was injected into the USD device and held in the shear chamber, whilst fresh process material was then pumped into the USD membrane device from the reservoir and permeate stream direction to waste (no recycle). Concentration was carried out at a fixed disc rotational speed and the TMP constantly monitored throughout the run. The experiment was ended when either the desired concentration factor (VCF) or the pre-defined TMP limit of 0.7-0.8 bar was reached, whichever occurred first. A minimum volume of 30 mL was always maintained in the reservoir to meet minimum operating volume requirements.

Volumetric concentration factor for USD can be expressed as the ratio of permeate volume to the volume of the shear cell:

$$\text{VCF}_{\text{USD}} = 1 + \frac{\text{Cumulative permeate volume, mL } (V_P)}{5.3 \text{mL}}$$

Equation 2.2

2.2.3.3 Diafiltration

Diafiltration was carried out by pre-filling the shear chamber of the USD membrane device with process material, and feeding diafiltration buffer through the USD device at fixed RPM of the disc. Prior to the diafiltration run, the USD device and membrane were both flushed with RO water and diafiltration buffer (≥20 L of permeate/m^2 at TMPs of 0.7 bar and 2 bar for MF and UF membranes, respectively) to equilibrate and condition the membrane. One diavolume (USD) was equal to 5.3 mL, and a minimum of 7 diavolumes were collected. All experiments were carried out at 25±1 °C.

2.2.4 Normalised water permeability (NWP)

Pure water flux or NWP tests were performed to provide an indication of the membrane permeability and to evaluate the effectiveness of the cleaning regime, comparing pre-cleaning and post-cleaning membrane resistances. Water flux data is normally expressed as normalised water permeability (NWP) value and serves as a benchmark to evaluate any drop in permeability due to potential fouling as well as to

assess the effectiveness of the cleaning step to restore process flux. The same operating conditions, *i.e.*, feed flow rate and permeate flow rate, were used each time NWP was measured to ensure accuracy when determining cleaning efficiency or relative fouling. NWP, at 25 °C, was then calculated using Equation 2.3.

$$\text{NWP}_{25\,°C} = \frac{F \cdot Q_P}{A \cdot \text{TMP}}$$

Equation 2.3

where F is the temperature correction factor (Table 2.4), Q_P is the permeate flow rate (L/h), A is the installed membrane area (m^2) and TMP is the applied transmembrane pressure (bar).

A minimum TMP of 0.5 bar is recommended during a NWP test using cassettes, and the same feed flow rate should ideally be used for all subsequent measurements for a given cassette and system to ensure NWP results are directly comparable.

T (°F)	T (°C)	F	T (°F)	T (°C)	F	T (°F)	T (°C)	F
125.6	52	0.595	96.8	36	0.793	68	20	1.125
123.8	51	0.605	95	35	0.808	66.2	19	1.152
122	50	0.615	93.2	34	0.825	64.4	18	1.181
120.2	49	0.625	91.4	33	0.842	62.6	17	1.212
118.4	48	0.636	89.6	32	0.859	60.8	16	1.243
116.6	47	0.647	87.8	31	0.877	59	15	1.276
114.8	46	0.658	86	30	0.896	57.2	14	1.31
113	45	0.67	84.2	29	0.915	55.4	13	1.346
111.2	44	0.682	82.4	28	0.935	53.6	12	1.383
109.4	43	0.694	80.6	27	0.956	51.8	11	1.422
107.6	42	0.707	78.8	26	0.978	50	10	1.463
105.8	41	0.72	77	25	1	48.2	9	1.506
104	40	0.734	75.2	24	1.023	46.4	8	1.551
102.2	39	0.748	73.4	23	1.047	44.6	7	1.598
100.4	38	0.762	71.6	22	1.072	42.8	6	1.648
98.6	37	0.777	69.8	21	1.098	41	5	1.699

Table 2.4 Temperature correction factor F as a function of temperature (Pellicon 2 User Guide).

2.2.5 Critical flux determination/flux excursions

2.2.5.1 Lab and pilot-scale

For pilot-scale and lab-scale studies, flux excursions were done at a fixed feed flow rate under total recycle to maintain steady-state, *i.e.*, the composition and volume of the feed were maintained, in terms of concentration, ionic strength, pH, conductivity. With the permeate pump/valve closed off, the feed flow was slowly increased to the desired crossflow rate and the feed recirculated at the constant crossflow rate for either a minimum of 5 minutes or until a relatively constant dP was observed, whichever occurred first. The permeate pump was then adjusted to obtain an initial permeate flux of 5 LMH and the respective inlet, outlet and permeate pressures monitored and recorded every 5 minutes, over a 20 minute interval (Pattnaik et al., 2014). Once the TMP was stable, the permeate flow was subsequently increased (in 5-15 LMH steps) and at each permeate flux, a minimum time of 10 minutes was needed to allow the polarisation profile to stabilise.

The flux step-ups were carried out incrementally until the critical flux was reached. The critical point was deemed to have been reached when $TMP_f/TMP_i > 1.5$; where subscripts i and f refer to the beginning and end of the 20 minute period, respectively. A small amount of retentate backpressure was also used when required, to allow the exploration of a broader range of TMPs. Process variables were automatically recorded by the MFCS/DA software connected to the Sartoflow Advanced and the UNICORN software.

2.2.5.2 USD

For the USD membrane device, the process material was injected into the shear chamber and the prefiltered feed solution permeate was used as the feed to the USD membrane filtration device (run in dead-end mode). The permeate was recycled back to the AKTA reservoir via a C-flex tubing connected to the permeate valve, and the device was operated at constant rotational disc speed. Since the permeate of the USD in dead-end mode could not be recycled directly to the shear cell due to pressure instabilities (Ma et al., 2009), it was necessary to replenish the lost permeate with an almost identical solution that can keep the volume and composition of the feed constant. Prefiltered feed, which is essentially the permeate stream in the recycle mode, was the ideal solution because it maintains the solute concentration, pH, and

ionic strength of the feed. Ma et al. (2009) reported a similar USD approach, but using a replacement solution with similar conductivity as prefiltered lysate to feed through the USD membrane device in a flow-through mode and permeate going to waste. The viscosity of feed held in the shear chamber was observed to decrease with time, as permeate was replaced by a replacement solution of lower viscosity (~ 1 mPa.s), thereby changing feed composition with time and resulting in lower TMP than expected at constant steady-state operating conditions, affecting the USD model data and subsequent scale-up and prediction. This effect is particularly noticeable with feed containing macromolecules (proteins, DNA) and cell debris that could permeate the membrane, which are not replaced when using substitute solutions instead of prefiltered feed, thus altering polarisation of the membrane and consequently, observed process fluxes/TMP.

Prefiltered permeate solutions were generated using a 200 mL Amicon stirred UF unit (Millipore, UK), housing φ63 mm diameter membranes, and using a regulated nitrogen source to provide forward pressure. Using at least 40 mL of process material and the same membrane as in the USD membrane device, a minimum of 25 mL of prefiltered solution was generated, which was the minimum volume required to overcome hold-up in the AKTA Crossflow. Using prefiltered feed permeate as the feed maintains the composition of feed held in the USD device, and recycling permeate back to the reservoir helps minimise total volume of feed material needed to carry out USD experiments (<50 mL). The required RPM was achieved using the speed controller and step ramps for inlet flow rates performed every 20 minutes using UNICORN, whilst monitoring the corresponding feed pressure (TMP). Maximum operating feed flow rate was determined based on the real-time pressure readings and the step ramps concluded either when pressures became very unstable ($TMP_{final}/TMP_{initial}$ >1.5) or approached pre-defined TMP limits. All permeate fluxes reported were temperature corrected to 25 °C.

2.2.6   Determination of volumetric throughput limits

Volumetric concentration experiments (≥5-10) at a certain feed flow rate, feed concentration and permeate flux were carried out to determine the volumetric capacity limits. The volumetric concentration factor (VCF) can range between 2 to 10-fold depending on the initial feed concentration. For instance, 5 to 10-fold for mammalian cell cultures, but only about 1 to 2-fold for a typical *Saccharomyces cerevisae* cell culture with high cell densities and 3 to 5-fold *for Escherichia coli* cultures (Raghunath

et al., 2012) for algae cell cultures, this is usually between 50 to 200-fold (Al Hattab et al., 2015). The experiment was started with an appropriate volume of feedstock required to obtain the estimated L/m^2 capacity at the desired target concentration factor, and the TMP continuously monitored as a function of volumetric throughput/feed concentration since permeate flux was constant. The capacity limit at a specific feed flow rate, feed concentration and permeate flux was then determined based on a predetermined TMP limit set by the user, typically between 0.3-0.7 bar for TFF cassettes. A minimum volume of 0.7 L and 75 mL was required to overcome total system hold-up volume and maintain the membrane loading for large scale experiments using the Sartoflow Advanced and AKTA Crossflow respectively. This approach assumes no change in the transmission of the desired product and is a good approximation even if small changes in the passage of molecules occur during the volume reduction experiment.

For the USD membrane device, the feed material was held within the shear chamber and fresh feed continuously pumped into the USD device at a constant feed flow rate (equal to the permeate flux for a dead-end filtration), and capacity limit was defined as the point where a rapid increase in TMP was observed during the course of the experiment.

2.2.7 Dry cell weight determination

The solids fraction analysis was performed in independent laboratory experiments by spinning down 2 mL samples in pre-dried and pre-weighed 2.2 mL Eppendorf tubes. The samples, in triplicates, were centrifuged at 16,000 g/13,200 RPM (Eppendorf 5415R bench-top centrifuge, Eppendorf, Germany) for 40 minutes at 4 °C. The samples were left in an oven at 90 °C overnight to dry out completely, before the total mass of solids remaining in the Eppendorf tube were weighed. Equation 2.4 was used to estimate the dry cell weight:

$$DCW\left(\%\frac{w}{v}\right) = \frac{m_s - m_t}{V}$$

Equation 2.4

where DCW is the equivalent dry cell weight (%w/v), m_s is the mass of solid pellet and empty, pre-dried tube (g), m_t is the mass of empty, pre-dried Eppendorf tube (g) and V is the volume of sample in the Eppendorf tube (mL).

For low cell density feed, such as microalgae, 5 mL volumes of different cell concentrations were filtered through pre-dried, pre-weighed 47 mm discs (Whatman qualitative filter paper, Grade 1) using a vacuum filtration unit (Merck Life Sciences KGaA, Germany). 10 mL of RO water was added to rinse out salts through the filter paper. The filter paper was then dried in an oven (at least 24 hours) at 80 °C and weighed using the analytical balance ME54T/00 (Metler Toledo, UK), until a constant mass was recorded. Finally, an Ultrospec 500 Pro spectrophotometer (Amersham Biosciences Ltd., Amersham, UK) was then used to measure absorbance of the feed material at 750 nm (for microalgae) and used to generate a calibration curve of g/L_{DCW} versus $OD_{750\ nm}$ (Figure 10.1), and subsequently used to determine the dry cell weight of algal samples by measuring absorbance at 750 nm wavelength.

In all cases, calibration curves of OD versus dry cell weight were generated to allow rapid determination of dry cell weight by measuring OD of a given sample at the appropriate wavelengths and back calculating the dry cell weight via the calibration curve.

2.2.8   Viscosity measurement

Viscosity measurements were performed using a Kinexus Lab+ (Malvern Instruments, Malvern, UK), using 50 mm parallel (PU-50) plates and a 300 µm gap size. The viscometer was initially auto-zeroed, followed by torque and inertia calibration runs, prior to sample measurements. A standard loading sequence in the Kinexus+ software was used for the loading and measurement of all samples to ensure the samples were subject to a consistent and controlled loading protocol. 0.6-1 mL aliquots of the sample were pipetted on to the loading plate and the shear stress/viscosity measurements were recorded for a range of shear rates (100-1000 s^{-1}), once a stable baseline at steady-state was maintained for 10 seconds. Before measurement, all samples were pre-sheared at 1000 s^{-1} using the PU-50 for 30 seconds, followed by a 30 second rest period, to make sure it was well dispersed and to avoid potential errors due to settling of particles. A static heat exchanger was used

to control temperature to user requirements and a control performed using oil standards (0.1 Pa.s).

Shear viscosity versus applied shear rate data was then plotted on a logarithmic scale, and the Sisko model fit was used to fit the measured data for most of the measurements, since most biological feed tend to exhibit shear-thinning properties. The Sisko model allows determination of shear viscosity at infinite shear rate (γ_∞) and is described as shown in Equation 2.5:

$$\mu = \mu_\infty + K \cdot \left(\frac{d\gamma}{dt} \right)^{n-1}$$

Equation 2.5

where μ_∞ is the infinite shear viscosity (Pa.s), K is the flow consistency index ($(Pa.s)^n$), and n is the flow behaviour index (dimensionless). The Sisko model describes the infinite shear plateau and the power law region, as illustrated in Figure 2.6:
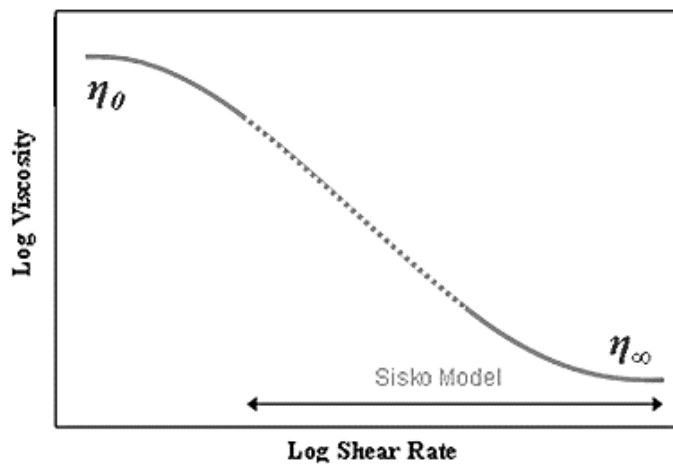
Figure 2.6 Ideal flow curve and the Sisko model used to describe the relevant region of the curve (Panalytical, 2015).

2.2.9 Fab' quantification (HPLC)

1 mL Hi-Trap protein G columns (GE Healthcare, Uppsala, Sweden) were used and analysed by HPLC, on an Agilent 1200 system (Agilent, Technologies UK, West Lothian, UK). Fab' concentrations in the feed and permeate streams were measure in triplicate. 20 mM sodium phosphate monobasic (Sigma-Aldrich, Dorset, UK) was used as loading and elution buffers, of pH 7.4 and 2.5, respectively. The buffers were pre-filtered using a 0.22 µm PES 1000 mL Stericup (Merck Life Sciences KGaA, Germany) and degassed by sparging using nitrogen gas. The HPLC system was flushed with loading buffer, followed by elution buffer to get rid of any proteins bound to the column and finally with the loading buffer again, to equilibrate the column prior to loading the samples. 20 mM phosphate buffers, pH 2.5 and 7.4, were used as elution and loading buffers, respectively.

Purified Fab' (24 mg/mL concentration) was kindly provided by UCB Pharma Ltd (Slough, UK) and was used to generate a standard curve (Figure 10.2). The concentration of eluted Fab' was calculated by measuring absorbance at 220 nm and peak integration to work out areas.

2.2.10 Particle size distribution

Particle size distributions were measured using a laser diffraction-scattering method. Malvern Mastersizer 3000 (Malvern Instruments, Malvern, UK), along with a Hydro MV medium volume sample dispersion unit was used for the particle size analysis of samples. The Mastersizer 3000 measures particles sizes between 0.01 and 3500 µm. For all the analyses, a constant volume of 60 mL milli-Q water was used as the dispersant and the pump/stir speed set at ≥1000 RPM.

Enough sample volume was added to achieve >5% laser obscuration, to ensure a good sample representation. Samples were measured in triplicates and for each measurement, three counts were performed. Absolute particle size distributions were relatively difficult to generate as the optical properties of the homogenate, which consists of a mixture of particles such as cell debris, DNA and free proteins, all of which have relatively different refractive and absorption indices. Thus, a refractive index value of 1.50 was used for *Pichia pastoris* (whole *Saccharomyces cerevisae* cells have a refractive index value between 1.49 and 1.53), 1.59 for *Escherichia coli* homogenate (Balaev et al., 2002) and 1.06 (Aas, 1996) for algal samples. An

absorption index of 0.001 was used for all samples, and all the measurements were used relative to each other.

The Mastersizer was calibrated against certified size standard, monodisperse polymer microspheres in water, of known diameter (30.1 µm). Volume frequency distributions were used, as they are deemed more accurate than number distributions, which require use of transformation techniques and consequently compound the overall uncertainty in the measurement values.

2.2.11 Optical density measurements

Optical density (OD) measurements were performed on a Thermo Scientific BioMate 3 UV-Visible spectrophotometer at a wavelength of 600 nm and 750 nm. OD values were measured in triplicates.

Sarstedt acrylic (PMMA) cuvettes were used and the spectrophotometer was blanked with milli-Q water/appropriate buffer prior to analysis. The linear range for detection was between 0.1-1 AU; samples with OD values falling outside this linear range were diluted with milli-Q water/dispersant and re-measured.

All other spectrophotometric measurements for different wavelengths (for instance, BCA, total carbohydrate, EPS) were performed in Nunc 96-well plates, using TECAN *i*-control software (TECAN Infinite 200).

2.2.12 Computational Fluid Dynamics (CFD)

The commercial CFD package, COMSOL Multiphysics v5.3a (Stockholm, Sweden) was used for all CFD simulations. All simulations were carried out using an Intel Xeon E5-2687W v2 3.40 GHz (2 cores, 256 GB RAM) Dell workstation. Relative and absolute tolerances were set to 1×10^{-3} and 1×10^{-6}, respectively, for all simulations, unless stated otherwise.

2.2.13 Numerical methods and statistical analysis

Sum of least squares method was used for all curve fittings throughout the thesis, particularly for non-linear curve fitting to model shear rate and pressure correlations for USD and screened cassettes. The curve fitting feature available within the

commercial package SigmaPlot v13.0 was used to generate correlations for the various sets of data. All numbers reported in the thesis are given either to 3 significant figures or to 3 decimal places, where appropriate. MATLAB 2016 was also used for the processing of raw data and analysis.

2.2.14 Microscopy imaging

2.2.14.1 Optical microscopy

A Nikon Eclipse TE 2000-U microscope (Nikon Instruments Europe B.V, Netherlands) was used to carry out microscopic imaging (10-20x) of algal samples.

2.2.14.2 SEM imaging

2 mL of each microalgal broth was initially filtered through 0.45 µm Durapore PVDF (13 mm discs), with a fabricated vacuum block, using Millipore Lab Vacuum-Pressure Pump, operated at 0.5 bar pressure, as the vacuum source. The setup is shown in Figure 2.7. PVDF membrane discs were used as support for the cells and to provide a good visual contrast for imaging. The membranes (with the cells adhered on to them) were then transferred to small beakers and fixed with 2.5% (w/v) glutaraldehyde in 0.1M sodium phosphate buffer solution of pH 7.4 at 40 °C for 1 hour. The samples were then put consecutively in increasing concentrations of ethanol (EtOH), *i.e.*, 25% (v/v), 50% (v/v), 75% (v/v) and 99.95% (v/v) for 10 minutes in each solution except for last two concentrations, where they were kept for 20 minutes.

The EtOH-dried samples were further dried using LeicaEM CPD300 Critical Point Dryer (Leica Mikrosystem GmbH), assisted by Dr. Jemima Burden (MRC Laboratory for Molecular Cell Biology, UCL). Dried membranes were then mounted onto aluminium stubs and sputter coated with gold (for increased resolution), before being examined using low vacuum JSM- 6480LV (Jeol, Massachusetts, USA), voltage of 2-5 kV and working distance between 5-10 mm. The SEM preparation such as coating and equipment initialisation and calibration was done and imaging assisted by Mr. James Davy (Department of Biosciences, UCL).
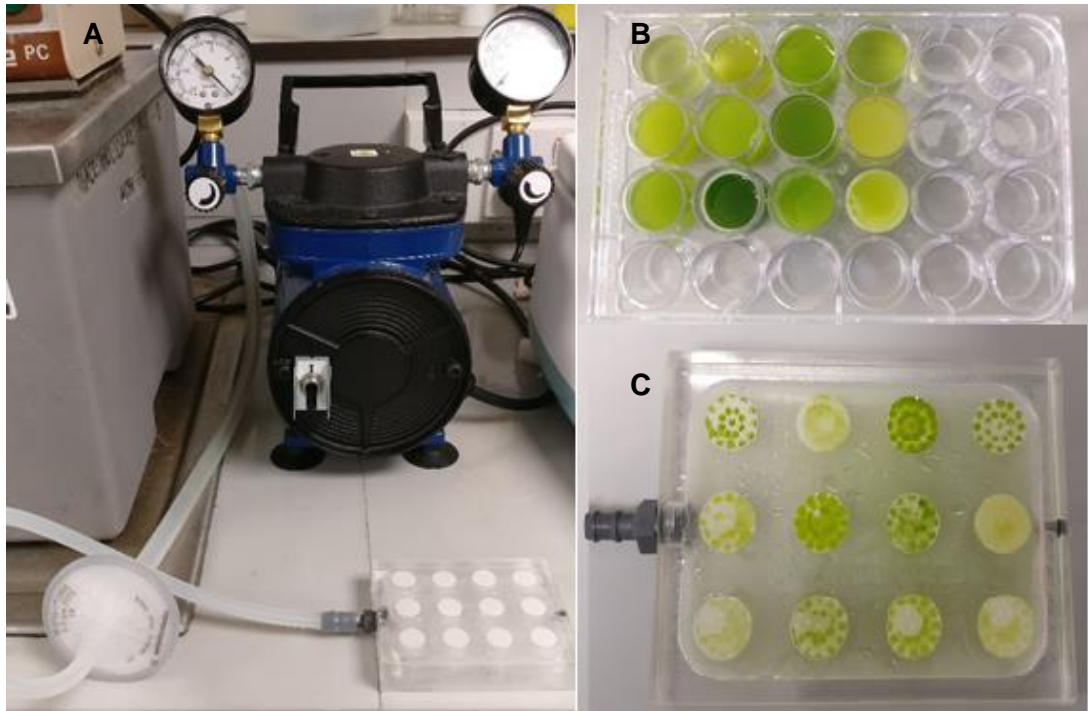
Figure 2.7 Preparation of samples for SEM imaging. A-Sample prep setup, B-Microalgal samples in different media for SEM, C-Vacuum block with 12x13mm membrane slots.

2.2.15 Total carbohydrate assay

The total carbohydrate concentration was determined by the phenol–sulphuric acid method (Dubois et al., 1956). BioVision's Total Carbohydrate assay kit was used to hydrolyse all saccharides, including glycans, glycoproteins and all complex compounds containing carbohydrates present in solution and converted to a chromogen, which can be quantified by measuring absorbance at 490 nm.

Between 1-30 µL of sample was pipetted into a glass 96-well plate (Zinsser Analytic GmbH, Germany), and total volume made up to 30 µL with RO water, to which 150 µL of concentrated sulphuric acid was then added and the plate incubated for 15 minutes at 90 °C. After 15 minutes, 30 µL of the developer solution (to form the chromogen) was added to the wells and left to cool for 5-10 minutes at room temperature. Finally, samples were transferred into a Nunc 96-well plate and OD measured at 490 nm. The concentration of unknown sample was determined using a glucose standard curve (0-0.1 g/L) and all measurements performed in duplicates,

with several dilutions made to unknown samples to ensure readings are within the standard curve range (Figure 10.3).

2.2.16 Total protein assay

Protein concentration was measured using the bicinchoninic acid (BCA) assay (Pierce BCA Protein Assay Kit, Thermo Fisher Scientific Inc., Waltham, MA USA), by preparing samples in a 96-well microplate and diluting them to an optical density range of 0.1-1. 25 µL of sample was added to each well, to which 200 µL working reagent (50:1 ratio of Reagent A to Reagent B) was added and left to incubate at 37 °C for 30 minutes. Post-incubation, the absorbance of the samples in the microwell plate were measured at 562 nm using the TECAN i-control software (Infinite 200). 2 mg/mL BSA standard solution was diluted and used to generate a standard curve (0-1.2 g/L), shown in Figure 10.3.

2.2.17 TEP/EPS analysis

Alcian blue (8G) dye was used to provide a semi-quantitative measure of the concentration of transparent exopolymeric particles (TEP) and exopolymeric substances (EPS). The dye forms an insoluble complex with acidic functional groups of polysaccharides and EPS precursors, and since it can be measured spectrophotometrically, the resulting absorbance of excess dye in supernatant, after centrifugation, is inversely proportional to the concentration of EPS present (Passow and Alldredge, 1994).

A 0.06% (w/v) stock solution of Alcian blue (AB) dissolved in RO water was prepared and mixed thoroughly for 30-60 minutes at room temperature. The mixture was then spun down in an Eppendorf 5424R bench-top centrifuge at 10,000 RPM for 30 minutes at 4 °C. The OD_{610} of the resulting supernatant was measured, before being filtered using a Millex 0.2 µm syringe filter (Merck Millipore, UK) and OD_{610} of the filtrate re-measured. This process was repeated until a constant OD_{610} value was reached, which implied the absence of any precipitate and that all alcian blue had dissolved in solution. The fully dissolved alcian blue solution was stored refrigerated at 4 °C in the dark when not in use.

Feed samples for EPS quantification were centrifuged at 10,000 RPM for 10 minutes in 2 mL Eppendorf tubes, and the supernatant (roughly 2 mL) stained with 0.5 mL of

the Alcian blue stock solution, made up to a final volume of 10 mL and pH 4 using a 0.2 mol/L acetate buffer solution. The mixture was then stirred vigorously for at least 1 minute and spun down, and the absorbance of the supernatant (excess, unbound AB) measured at 602 nm, which corresponds to maximum absorbance peak of AB in water, rather than 787 nm in sulphuric acid (Arruda Fatibello et al., 2004). The OD_{602} value measured is inversely proportional to the number of TEP-AB complexes formed and thus, the amount of TEP/EPS present in solution. Gum xanthan was not used as standard to generate a calibration curve (OD_{602} versus g/L) since the EPS measurements were done to compare the relative amount of EPS in feed and permeate, to work out membrane fouling/amount of EPS retained by filter.

2.2.18 2D Particle Imaging Velocimetry (PIV)

A polypropylene fabricated cassette (UCL Biochemical Engineering Workshop), 12.5 cm effective length, fitted with a C-screen (cut out from an existing Pellicon 2 mini V screen cassette) between two transparent acrylic plates was used to carry out PIV verification studies for the CFD work.

A.
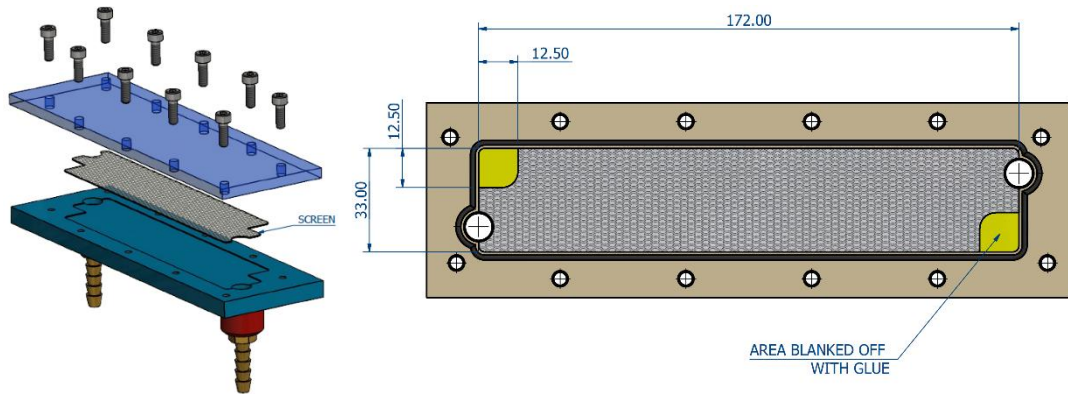
B.
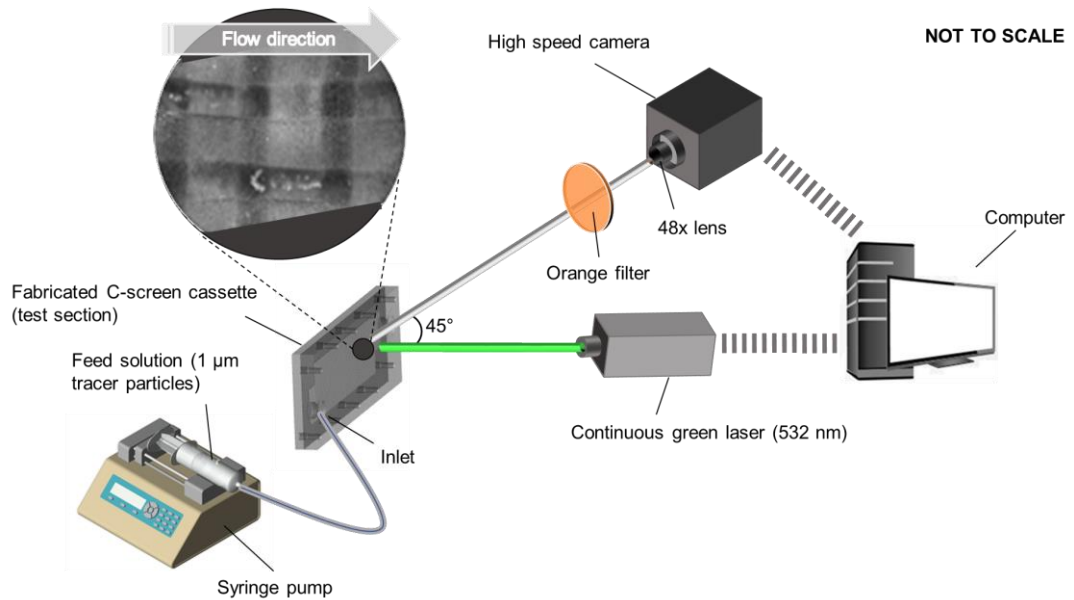
Figure 2.8 Experimental setup and schematics of the fabricated C screen cassette used for the 2D-PIV studies. A: Blow-up diagram of the fabricated cassette enclosed with a C-screen within; all units in mm. B: Schematic of 2D-PIV setup and a snapshot of the test section with seeded particles taken using the camera. Images shown are not to scale.

The PIV system (Figure 2.8) used in this study comprised of a continuous diode laser (Laserglow Technology), and a CMOS high-speed camera (Phantom V1212). The laser had an output power of 3000 mW with a wavelength of 532 nm and illuminated the fabricated C-screen cassette from a 45° angle (volume illumination). The high-

speed camera was equipped with a mono-zoom Nikkor lens, which gave a field of view of 2.24x1.4 mm^2, and an orange filter with a cut-off wavelength of 570 nm was set on the camera lens to minimise reflections. For the investigation of the velocity fields, the fluid was seeded with 1 µm Rhodamine coated spherical particles in 50 g/200 mL aqueous suspension (Dantec Dynamics, UK). The images obtained from the high-speed camera was treated using the open source freeware JPIV, and an adaptive correlation tracking of the full image was applied with a final interrogation window of 32x32 pixels; a 50% window overlap was used to obtain a final resolution of 16x16 pixels. The PIV work was setup and experiments carried out by Dr. Weheliye and Dr. Tsaoulidis (Department of Chemical Engineering, UCL, London).

2.2.19 Measurement of applied torque versus axial compression

Torque-axial compression measurements were performed using a compression tester, kindly donated by Sartorius Stedim Biotech GmbH for use. The kit comprised of a meter with LCD display, and a SS insert with the compressive force sensor, which was placed between the Pellicon cassette and the end plate of the Sartocon Slice holder, to measure the total compressive force on the holder. The nuts of the holder was tightened in increments of 5 Nm, from 10 Nm, up to a maximum of 30 Nm, and the corresponding axial forces were recorded. The experimental set-up used is shown in Figure 2.9.
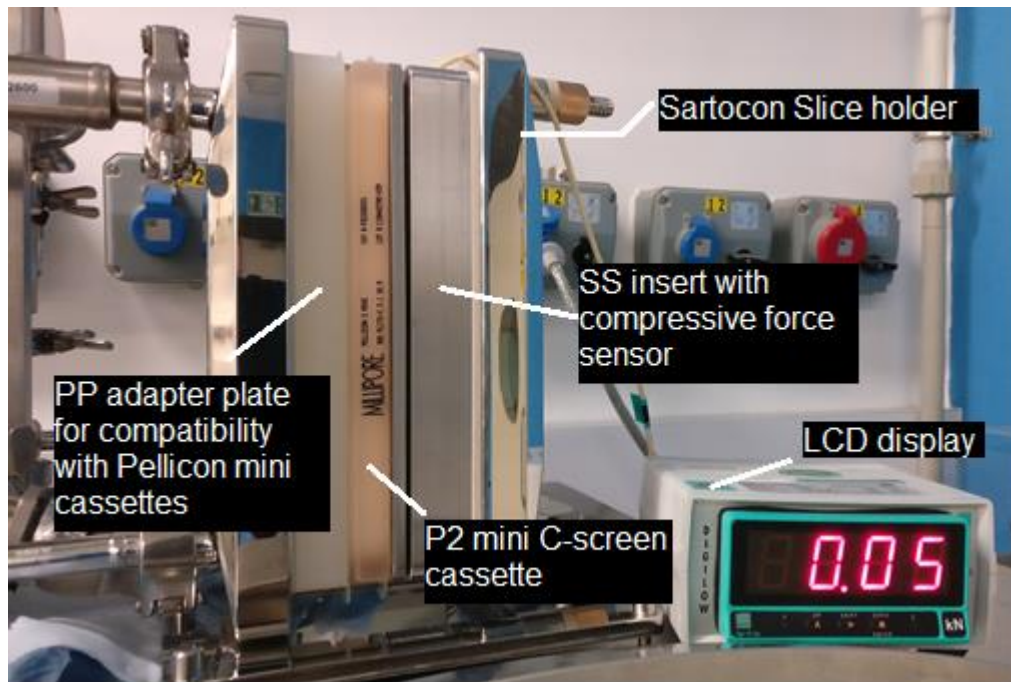
Figure 2.9 Set-up of the Sartorius compression tester in use with the Sartocon Slice holder.

2.2.20 Characterising system pressure drops

System pressure drops were characterised by carrying out feed flow rate versus dP tests (altering feed flow rates and measuring corresponding pressures) using water and 10-30% glycerol/water mixtures. For the AKTA Crossflow, tests were carried out with feed, retentate and permeate lines interconnected via a Y-connector (3xUNF 5/16" female) from GE Healthcare Life Sciences (Amersham, UK), whilst for the Sartoflow Advanced, a fabricated polypropylene dummy cassette (UCL Biochemical Engineering Workshop) without permeate channels, was used instead of cassettes. Temperature was controlled to 25±1 °C and correlations for pressure drop (dP) as a function of feed flow rate and fluid viscosity were developed from experimental data.

3 Computational fluid dynamics modelling of the USD membrane device and Pellicon TFF cassettes

3.1 Fluid flow characterisation of ultra scale-down device and large scale tangential flow filtration cassettes

3.1.1 Introduction

Many filtration processes are usually developed using stirred cell devices at lab-scale and subsequently scaled up using scale-independent parameters such as TMP, mass transfer coefficients, shear rates, etc. (Li et al., 2008). This is particularly important in non-linear scaling, where significant differences in geometries and flow exist across scales. For the USD membrane device and other stirred cell devices, although flow is dead-ended and have uniform flux across the membrane, the wall shear rate is not constant and is a function of radial position across the membrane, and depends on geometric parameters such as position and design of the disc. TFF cassettes with feed screens pose a different challenge altogether; all parameters such as pressure gradient, flux and mass transfer exhibit spatial variations along the length of the channel, and consequently the screen characteristics greatly influence the fluid dynamics and pressure drops across the feed channel and ultimately, mass transfer (Ngan et al., 2014). All performance metrics such as TMP, mass transfer and permeate fluxes are averaged quantities and are usually different to the localised effects and phenomenon occurring within the flow path, particularly near regions where the screen fibres touch the membrane surface for screened cassettes. These averaged quantities often fail to describe the localised flow and mass transfer effects accurately and consequently create barriers to achieving a truly linear/non-linear scalable performance. Furthermore, TFF is generally operated at high pressures that could result in transitional flow regimes within the flow path by creating instabilities in flow by the formation of eddies, which are further difficult to accurately model and characterise (Blake et al., 2011).

The lack of understanding of flow and mass transfer phenomena across both scales has negative consequences on the use of scale-down devices, where a range of rotational speeds are typically used by researchers without any sound justification, and in some cases, rotational speeds are not even disclosed (Koutsou and Karabelas,

2012). This limits the true potential of stirred cell units, which are extensively used in research for convenience and use the same membrane and operating fluxes.

The 'sweeping' effect of flow along the filter is the primary advantage in tangential flow filtration. Linear flow velocity is seldom measured and instead shear rates are used to normalise flow through the cassettes. The wall shear rate (γ_w), *i.e.,* shear rate at the membrane surface, is created by the crossflow across the membrane and for a Newtonian liquid is defined as:

$$\gamma_w \equiv \left(\frac{\partial u}{\partial y} \right)_{y=0} = \frac{\tau_{y=0}}{\mu}$$

Equation 3.1

where τ is the shear stress at the wall (Pa), μ is the viscosity of the fluid (Pa.s), u is the transverse velocity along the boundary (m/s), and y is the height above the boundary (m).

The wall shear rate, *i.e.*, the shear rate at the surface of the membrane, in tangential flow filtration is an important parameter as it directly influences mass transfer and process flux (Belfort et al., 1994). Mass transfer of particles away from the membranes due to shear rates are governed by different mechanisms, all of which depend on the size of the particles. For instance, the back-transport of particles away from the membrane for small, soluble molecules is proportional to $\gamma_w^{1/3}$; however, for microfiltration, mass transfer dependency on wall shear rates are more pronounced, ranging from powers of 0.33, 1, and 2, for small (<0.1 µm), intermediate (1-10 µm), and large (>100 µm) particles, respectively (Lutz, 2015).

From section 1.2.3, the mass transfer coefficient, k, is a function of various operational and geometric parameters and directly controls the filtration process. Rearranging the generalised mass transfer correlation (Equation 1.5), k can be expressed as a function of module geometry, crossflow velocity and diffusivity of the molecule (Lipnizki et al., 2003) in Equation 3.2.

$$k = a \cdot v^{b-c} \cdot D^{1-b} \cdot d_h^{c+d-1} \cdot \left(\frac{u^c}{L^d} \right)$$

<div align="right">**Equation 3.2**</div>

where, k is the mass transfer coefficient (LMH), v is the kinematic viscosity (m^2/s), D is the diffusion coefficient (m^2/s), u is the crossflow velocity (m/s), L is the channel length (m) and d_h is the channel hydraulic diameter (m).

From Equation 3.2, for a fixed path length, channel diameter and feed material, k is directly proportional to u, and since u can be expressed as wall shear rates across geometries, the wall shear rate was identified as the key factor that determines the filtration performance and hence was used as the scaling parameter. The mass transfer coefficient is directly related to shear at the membrane surface, plus a multitude of chemical and physical interactions, which are constant with the same feed. For a given feed, a constant shear rate between scales would result in similar flux/TMP performance regardless of the geometries, and since shear rates can be accurately controlled in stirred cell units, it further strengthens the argument of using wall shear rates as a scale-up parameter. To develop a successful USD mimic based on wall shear rates as the scaling parameter, a reliable shear rate correlation expressed as a function of respective operating conditions between scales is vital.

The specific aims of this chapter are to:

- use CFD to investigate complex fluid flow dynamics and the influence of geometric parameters (disc characteristics, screen type, etc.) on spatial profiles in the USD device and tangential flow filtration in screened channels (Pellicon cassettes),

- define characteristic wall shear rates and subsequently establish correlations for area-averaged wall shear rates for USD and Pellicon screened cassettes, as a function of hydrodynamic conditions and fluid properties,

- develop channel pressure drop models for Pellicon screened cassettes (A, C and V),

- and validate the CFD simulation results using experimental data.

3.1.1.1 Limitations of existing wall shear rate and pressure drop models

Much work has been done over the last few decades involving stirred cell units and using analytical models that describe shear rates at the membrane surface as a function of rotating speed and fluid characteristics (Lee et al., 1995; Bouzerar et al., 2000b; Murkes and Carlsson, 1988; Hwang and Wu, 2015). However, those analytical correlations are geometry specific and vary depending on the geometry of the RDF system, diameter of disc, etc. and hence using them would not yield accurate shear rate values for the USD membrane filtration device. The similarity solution developed by Bouzerar et al. (2000a) was reported to underestimate shear stress by a factor of two, when compared to CFD values (Torras et al., 2006).

For tangential flow filtration, the wall shear rates for flow in the laminar flow regime can be estimated to be equal to $6u/h$, where u is the crossflow linear velocity in the channel and h is the channel height (Cheryan, 1998; Dosmar et al., 2005); however, this primarily applies to rectangular channels without the presence of screens within. Determination of shear rates at the membrane tend to be extremely complicated due to the presence of support screens within cassettes, and for unknown and complex geometry such as the Pellicon cassettes, experimental pressure drop data is generally required to estimate wall shear rates. Perry and Green (2008) and Vogel and Kroner (1999) developed an equation for shear rates based on hydraulic diameter and empirical channel pressure drops, however, from a macroscopic analysis, average wall shear rate cannot be directly determined from channel pressure drop measurements, as would be the case for open channels (Lutz, 2015). There are alternative techniques such as electrochemical techniques using electrodes to measure wall shear stresses (Koutsou and Karabelas, 2012), but tend to be invasive, require specialist equipment and rely on CFD validation to confirm measured shear values.

Likewise, there are existing standard pressure drop expressions for flow in narrow channels, based on friction factors and fluid viscosity, however, such equations tend to be quite simplified. For instance, Shukla et al. (2007) reported an equation to estimate pressure drops in TFF cassettes, but assumed the screen to be a solid separator, as opposed to an interweaved mesh and only applies to pure laminar flow, which may not be the case in channels containing turbulence-promoting screens. A

mathematical model describing pressure drop across channels with different spacer geometries, accounting for kinetic losses, viscous drag and form drag, was proposed by Da Costa et al. (1994). However, the model requires extensive input of parameters such as screen characteristics, angle of filaments, etc. and can be quite challenging to apply in most cases. Apart from that, most pressure drop equations rely on parameters such as friction factor, that need to be determined empirically, it is rather inconvenient and primarily depends on the accuracy and rigor of such experiments.

3.1.1.2 Uses of CFD in tangential flow filtration modelling

CFD is an essential tool that can be used to obtain a comprehensive understanding of the hydrodynamics of a system with minimum cost and effort, and the outputs can be used to help design an efficient process, or help optimise an existing one by saving energy or increasing overall efficiency. It is particularly useful in the biopharmaceutical industry where large volumes of fluid are normally handled, be it for operation or routine cleaning, even a relatively small increase in efficiency could lead to significant cost savings. 2D models are extensively used, and 3D models are becoming increasingly common, making use of simplified geometries and periodicities.

CFD has also been useful in studying the unsteady flows commonly encountered in TFF operations, and 3D models have shown time variations of flow greatly improves mass transfer in cassettes (Fimbres-Weihs and Wiley, 2007). 2D models are commonly used in practice, however, the mass transfer rates were reported to be under-predicted in 2D simulations, thus prompting the need for a 3D model (Shakaib et al., 2009). Although there have been numerous attempts at modelling wall shear rates in screened cassettes, they were primarily used to optimise spacer and channel geometries based on relative Sherwood numbers, rather than for scaling purposes. Furthermore, most 3D models make use of periodic boundary conditions for the model, which do not include entrance regions where transitional flow is likely to exist and impact shear rates and pressure drops (Shakaib et al., 2009).

Ma et al. (2010) developed wall shear rate correlations for a geometrically smaller USD membrane device using the k-ω CFD model; however, the work presented had a few limitations. For instance, the k-ω model was used to derive averaged wall shear rates, which is not an entirely accurate model to characterise wall shear rates. The k-ε model uses wall functions (an empirical relationship) to determine the velocity, turbulent viscosity and therefore the shear rate. The use of other turbulence models

besides the k-ω model that would be a better choice, such as the Low Reynolds number k-ε model or the Shear Stress Turbulence (SST) model, both of which resolves the various 'sub-layers' near the wall. The SST/low Re k-ε formulation will provide the most accurate shear rates, because the velocity near the wall is fully resolved by the mesh and calculated at every point to the wall, unlike the k-ε or k-ω model. Finally, although the CFD work was successfully validated using 2D laser doppler velocimetry (LDV), it was only performed at a single rotational speed and thus did not successfully verify the robustness or accuracy of the CFD results at other rotational speeds.

More recently, Lutz (2015) performed CFD simulations for a 6x6 unit cell and expressed wall shear rate equations for A and C screen Pellicon cassettes, as a function of inlet flow rate. However, the model did not account for intrusion of screen into the membrane, which was a major limitation since most membranes used are highly compressible and the solid screen does emboss into the membranes; this results in a much smaller channel height and influences simulated wall shear rates and pressure drops. Furthermore, the simulations were done using water as the domain material and the effect of fluid viscosity not investigated.

This chapter focuses on using CFD to characterise wall shear rates for both the USD device and Pellicon TFF cassettes and understand flow dynamics at both scales. Since wall shear rates would be used as the scaling parameter, a uniform wall shear rate profile is essential to ensure that global (averaged) wall shear rates provide a good representation of the local shear rates at different points on the membrane. The work here represents a unique approach to scaling with the aid of CFD to accurately characterise wall shear rates across scales, and forms the cornerstone of this project. There have been plenty of work done using CFD, but to date, they have been primarily used as a tool to optimise geometrical designs and/or simulate certain aspects of tangential flow filtration to facilitate understanding.

3.1.2 Methods

A typical CFD modelling procedure can be summarised as follows:

1. Determining the Reynolds number (laminar versus turbulent).

2. Selecting appropriate model based on Reynolds number and size of computational domain and respective turbulence scales.

3. Generating an appropriate mesh to capture the fluid flow effects sufficiently, and optimising number of mesh elements (solution accuracy versus computational resources).

4. Defining appropriate boundary conditions.

5. Running the simulation, followed by experimental verification of the CFD solution.

3.1.2.1 Fluid flow models

COMSOL Multiphysics offers a laminar flow interface that is capable of fully solving for the Navier-Stokes (NS) equations; by using a time dependent study, the temporal and spatial scales over which the 'turbulent' fluctuations occur can be resolved, and this interface will solve the velocity and pressure fields. Normally, this is computationally restrictive and demanding, and hence the Reynolds Averaged Navier-Stokes (RANS) formulation offers an approximate time-averaged solution to the Navier-Stokes equation by a decomposition of the flow solution to an averaged flow field, which allows the smaller perturbations to be resolved with relatively fewer computational resources.

As a general rule of thumb, if a stationary, laminar flow study fails to resolve adequately and the Reynolds number is within the transitional regime or above the critical Reynolds number, the flow is best resolved using a suitable turbulent fluid flow interface. The critical Reynolds number varies depending on the type of flow and the point at which resolving these perturbations becomes computationally too expensive, a switch to RANS formulation is recommended (COMSOL Multiphysics technical support, personal communication).

Although COMSOL Multiphysics offers the use of different turbulence models, the three two-transport-equation models, namely, the *k-epsilon* (*k-ε*), *k-omega* (*k-ω*), and *Shear Stress Transport* (SST) turbulent models were identified to be most suitable for modelling the fluid flow in the two devices and capturing the necessary physics with good accuracy. The *k-ε* model is usually used for industrial applications due to its ease of convergence, low memory requirements and its ability to capture external flows around complex geometries adequately. The *k-ω* model is very similar to the *k-ε* model, but the key difference lies in the different turbulent variables used, which makes the *k-ω* model more computationally taxing but is better suited for internal flows and in particular, cases where the *k-ε* model has difficulty converging (Frei, 2013). However, they both make use of wall functions, and thus the flow in the buffer region, which is the flow next to the boundaries (shown in Figure 3.1), is not simulated.
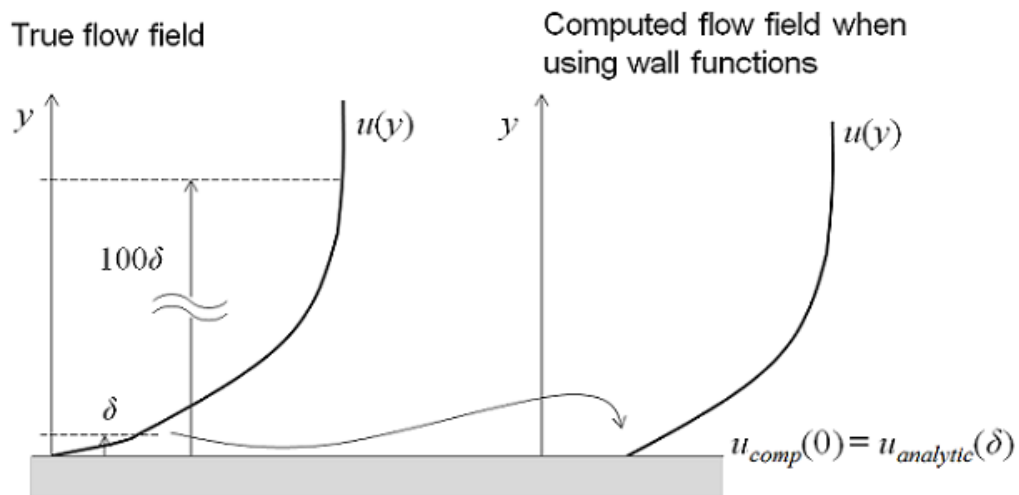
Figure 3.1 Illustration of the differences between the ideal flow field and the computed flow field when using wall functions, as is the case in *k-ε* and *k-ω* turbulent models (Frei, 2013).

The *k-ω* model is generally well suited to internal and rotational flows, which is the case for most stirred cell devices. The main limitation is that the flow field in the viscous sublayer is not explicitly modelled, but is computed using an empirical function.

3.1.2.2 Model definition of computational domains and boundary conditions

3.1.2.2.1 USD membrane device

Since the geometry of the USD membrane device is rotationally symmetric, only half the chamber was modelled as a 2D model, symmetric about the radial axis at r=0 mm (highlighted in red), thus simplifying the model, both in terms of complexity and resources needed to solve the model. Furthermore, the USD membrane filtration device was modelled as a bound system, with no inflow or outflow boundaries. The disc was not included in the computational domain and the domain material (shaded grey) was set as water, at 25 °C.

The simplified geometry of the USD membrane device and computational domain of the model is shown in Figure 3.2, while   lists the key dimensions and physical properties of the system.
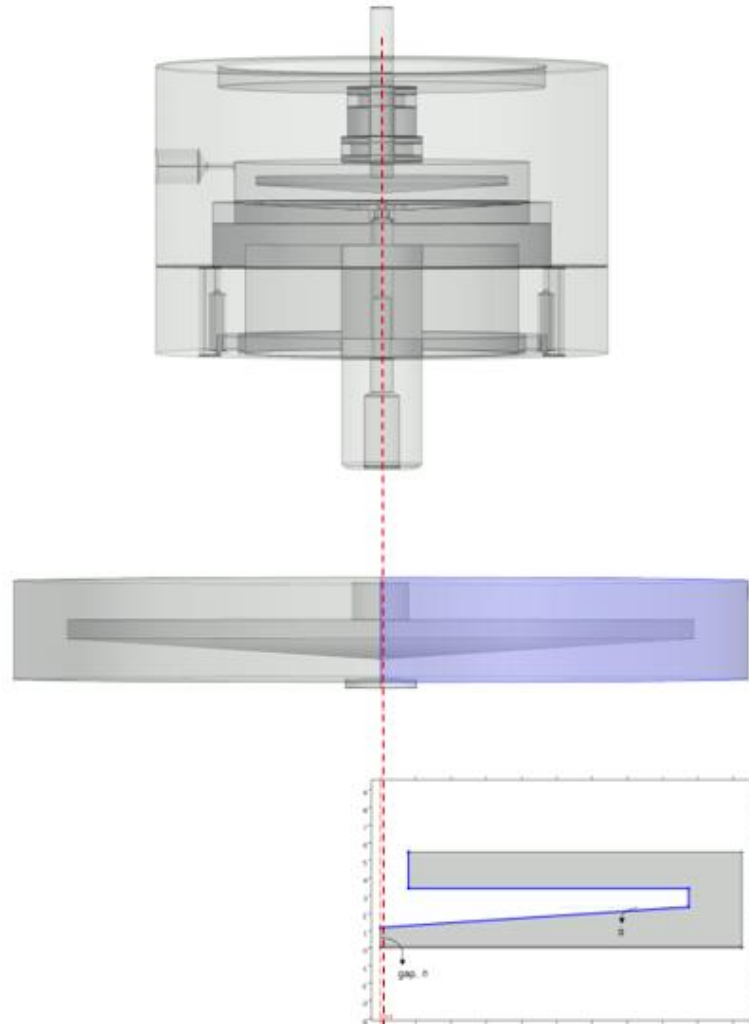
Figure 3.2 Geometry of the USD membrane filtration device. Top: 3D CAD model, Bottom: 2D axi-symmetrical computational domain. Images are not to scale.

Chamber height	5.60 mm
Chamber diameter, D_c	41.05 mm
Disc diameter, D_d	35.00 mm
Disc thickness	1.05 mm
Membrane thickness	0.125 mm
Height of conical section	1.162 mm
Angle of conical disc, α	3.8°
Gap, h	1.175 mm
Domain material density, ρ	997.05 kg/m^3
Domain material viscosity, μ	0.000894 Pa.s
Rotational speed, N	4000 RPM (66.6 Hz)

Table 3.1 USD membrane device specifications.

Most of the flow in the system is predominantly out-of-plane, *i.e.* through the azimuthal angle, and thus the velocities in the angular direction are non-zero. As a result, all three velocity components need to be included in the model, even though the computational domain is in 2D. Standard 2D models include the axial and radial flow velocities. However, COMSOL Multiphysics provides the option of using the swirl flow application, which typically involves steady rotational flow around an axis in a 2D axisymmetric interface. The swirling flow includes all three velocity components; the radial velocity, *u,* azimuthal/rotational velocity, *v*, and the axial velocity, *w*. The swirl flow model assumes that there is no variation of the model variables in the azimuthal direction.
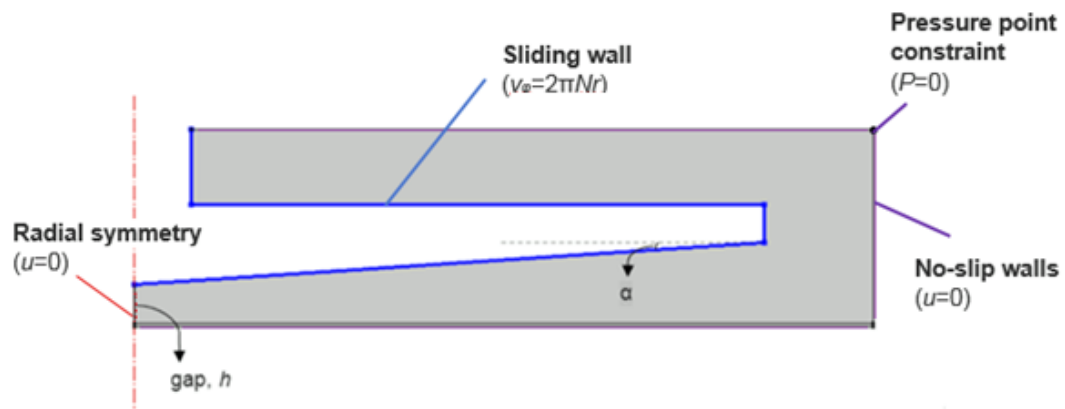
Figure 3.3 Illustration of problem setup and boundary conditions.

The sliding wall condition was applied to the rotating disc boundaries (highlighted blue in Figure 3.3) and no-slip boundary conditions applied to the remaining solid boundaries; the membrane was considered part of the solid phase. Since the membrane thickness can vary, both in terms of batch-to-batch variation for the same membrane type and for different membranes, all the simulations were based on a MF membrane (assuming a mean thickness of 0.125 mm) and hence the effective chamber height was 5.375 mm.

The azimuthal velocity, v_φ (m/s), of the disc was set as:

$$v_\varphi = 2\Pi \cdot N \cdot r$$

Equation 3.3

where *N* is the disc rotational speed (Hz) and *r* is the radius of the disc (m).

As there is no outflow boundary in this CFD model, a reference pressure was needed to be specified and locked in to some point, to allow the solver to reach a unique solution. The NS and RANS equations are primarily dependent on the gradient of the pressure field, and as such, if the boundary conditions were to be defined by velocity only, an infinite number of solutions would exist for a unique velocity field, for a range of different absolute pressure values. Consequently, the pressure was set to an absolute value of 0 at the top right corner of the computational domain.

Even though flow regime is predominantly laminar in the USD device for the typical range of rotational disc speeds used, the perturbations in flow fields near the disc region and stationary walls make the use of a laminar steady-state model unsuitable, and so a stationary laminar flow study often fails. A time dependent laminar study is better suited to solve and capture all the temporal and spatial scales over which the fluctuations occur but would be computationally demanding. Thus, the SST formulation was used to model the USD membrane device as it provides the most accurate calculation of the shear rate at the walls, compared to the other RANS turbulence models. The shear rate is influenced by the spatial gradients of the velocity components, and the SST formulation fully resolves the velocity near the wall and calculates it at every point all the way to the wall, unlike the k-ε model. As the velocity in the SST formulation is the most accurate at no-slip walls, the wall resolved model (SST) was used. However, it sometimes has difficulty converging and thus the k-ε model was solved first to provide good initial conditions for the SST model. A wall distance initialisation step was used, followed by a stationary study step to solve the SST model for each study.

The SST interface makes use of a variable, dimensionless distance to cell centre, which is used to determine the amount of turbulent viscosity to add depending on the velocity and pressure fields, and the distance to the nearest wall. The value of the dimensionless variable has to be between 0.5 and 1 for the optimal balance between numerical stability and sufficiently resolution of the velocity and pressure fields (COMSOL technical support, personal communication). If it is below this minimum threshold of 0.5, the numerical convergence could be problematic and conversely, if it greatly exceeds the upper limit of 1, the resulting mesh would be insufficiently resolved and lead to an inaccurate solution.

Finally, a fully rotational 3D model of the USD device was simulated and solved using a time-dependent laminar flow study to compare and show similarity between 2D and 3D results, in terms of time requirements and flow and shear profiles. The rotating machinery laminar flow interface was used and the computational domain split into rotating and non-rotating domains, which are permitted to slide across the shared boundary. The flow continuity boundary condition was enforced to ensure that the full flow field is continuous between these two frames. The conditions of the simulations were a rotational speed of 4000 RPM, viscosity of 0.000894 Pa.s (viscosity of water at 25 °C) and a study time range [0,0.01,1] seconds.

3.1.2.2.2 Pellicon screened channels

Like the USD membrane device, the entire channel length was not used in the model but instead, the concept of 3D unit cell was made use of to construct the CFD model, relying on the periodic and symmetric nature of the screens (Figure 3.4). Using unit cells significantly reduces the size of the computational domain, reducing memory requirements and time, but more importantly, allows mesh refinement of a much greater resolution of the spatial discretisation needed to capture any turbulent perturbations. The concept of unit cells have been widely used in CFD simulations of screened channels (Gurreri et al., 2014; Koutsou et al., 2007; Li et al., 2002; Ranade and Kumar, 2006; Santos et al., 2007; Shakaib et al., 2007), by making use of temporal and spatial periodicities. This assumption is justified since the flow is fully developed after a few unit cells across the full-length geometry (Li et al., 2004; Shakaib et al., 2009).

Full length system　　　　**Twill weave sequence**　　　　**Unit cell**
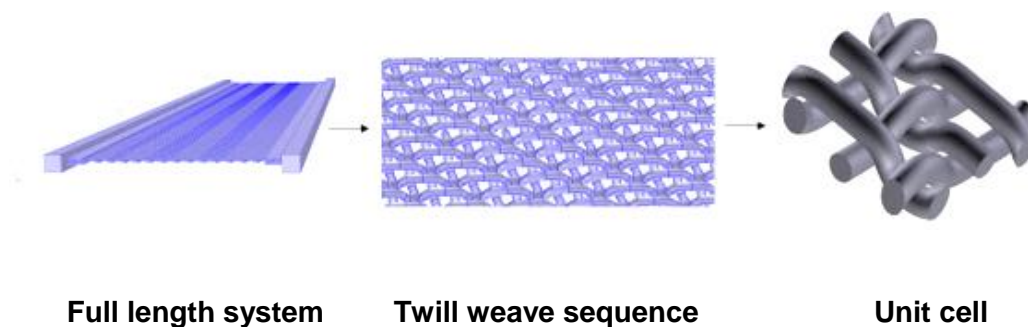
Figure 3.4 Illustration of repeated sequences and selection of the unit cell for a C/V screen.

Considering the aims of this chapter, since the shear rates are only dependent on the velocity profiles that are a function of the pressure gradient, once the flow is fully developed, the velocity profile is repeated periodically along the length of the channel and the wall shear rates will no longer vary. Similarly, pressure drops will vary periodically and scale with the length in the direction of flow, provided the unit cell is taken in the cross-section normal to the flow and the velocity used in the model is identical to that in the full system. Pellicon cassettes are designed such that flow is equally distributed into the channels, each of identical length and approximate height, and thus the flow velocities across the channels would be identical if the inlet flow rate is normalised appropriately.

The weave and sequence of the screen fibres is repeated along the normal and tangential directions of the flow, so a square unit cell consisting of 3 fibres length and width wise (the minimum periodic unit, *i.e,* one twill weave sequence) was modelled as the computational domain, shown in Figure 3.5:
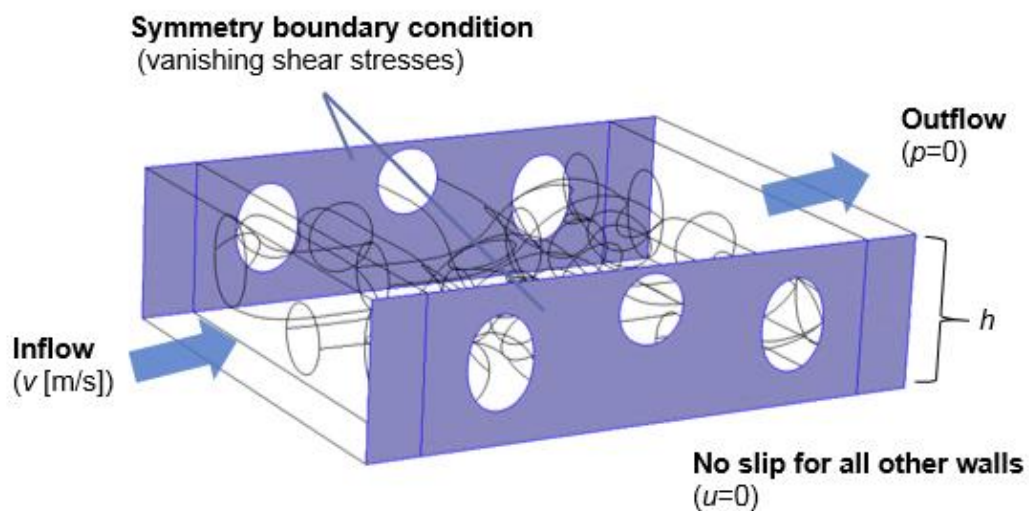
Figure 3.5 Illustration of the computational domain and boundary conditions used for the unit cell CFD model.

Symmetry boundary condition was used for either sides of the unit cells since they represent a parallel cut along the plane of symmetry; this condition imposes a no-penetration condition ($u.n$=0) but the velocity tangential to the boundary can be non-zero, with vanishing viscous stresses. For the remaining boundaries of the computational domain representing physical walls, a no-slip condition was imposed. Finally, the inlet velocity, v, based on Pellicon 2 mini cassettes of 0.1 m^2 membrane area and 12 feed channels, was calculated using Equation 3.4.

$$v = \frac{Q \cdot A}{n \cdot w \cdot h}$$

<div align="right">**Equation 3.4**</div>

where, v is the linear velocity (m/s), Q is the feed flux to the cassette ($(m^3/s)/m^2$), A is the nominal membrane surface area (m^2), n is the number of feed channels (12 for P2/P3 mini cassettes), w is the width of the feed channel (0.03175 m for P2/P3 mini cassettes) and h is the average feed channel height (m).

To minimise any associated entrance/exit effects, the computational domain was extended and partitioned in the direction of flow so that the initial effects of the plug flow region was not included in wall shear rate and pressure drop calculations. The extended domains allow the flow fields to sufficiently develop and represent fully developed flow within the full-scale system.

The 3D flow simulation of the unit cell was carried out using a stationary laminar flow (Newtonian) model, for an inlet flow rate of 5 LMM and fluid viscosity of 0.000894 Pa.s. A laminar flow interface was used since the typical operating flow in tangential flow filtration operations fall within the laminar flow regime (Fimbres-Weihs and Wiley, 2007). Apart from that, the use of a significantly smaller computational domain (unit cell) greatly reduces the temporal scales at which the unsteady flows occur, thus allowing use of a stationary study as opposed to a time-dependent one. Finally, allowances for intrusion of the screen fibres into the membrane were made, without accounting for potential deformation of the membrane upon flow. Table 3.2 shows the average channel heights and screen dimensions for the different Pellicon screens used in the CFD modelling. Average feed channel heights were used since the actual feed channel height during operation varies depending on the device compression and manufacturing tolerances when it comes to the screen characteristics. Although the thickness of the feed screen typically dictates the feed channel height, the nominal screen thicknesses reported in Table 3.2 were different to the average feed channel heights due to the intrusion of the screen fibres into the compressible membrane; the degree of membrane embossing depends on the thickness and hardness of the membrane.
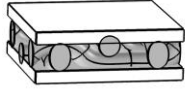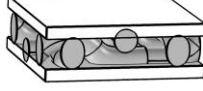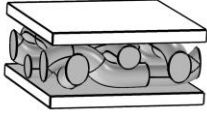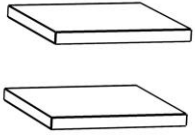
	Screen type			
	A	**C**	**V**	**Unscreened (open)**
Nominal screen thickness (mm)	0.420	0.515	0.915	-
Average channel height, *h* (mm)	0.28	0.32	0.55	0.80
Dimensions of square unit cell, *s* (mm)	0.154	0.170		-

Table 3.2 Screen and feed channel dimensions of the various Pellicon cassettes (Lutz, 2015; Lutz et al., 2016; Ngan et al., 2014). All feed screens in Pellicon cassettes are polypropylene right-hand square twill 2/1 weaves. Specific characteristics of the different feed screens such as mesh opening and mesh count have been detailed and listed by Lutz et al. (2016).

3.1.2.3 Model assumptions

To simplify the problem, both models were developed without any allowances for permeate flux through the membrane. This was particularly important to maintain spatial periodicity across the unit cell, although in practice for tangential flow filtration, part of the feed flow is converted into permeate as the fluid flows along the channel. This permeate closure condition is an acceptable approximation in real life applications if the amount of fluid removed as permeate represents a small proportion of the overall bulk flow in the feed channel (permeate conversion is usually kept to ≤30%). The general assumptions for both models are listed in Table 3.3.

USD membrane device	Screened TFF channel
Newtonian; incompressible fluid; isothermal	
No deformation or compression of membrane upon flow	
Permeate closure (zero permeation through the membrane wall and treated as a no-slip boundary	
Steady-state conditions (time independent)	
Smooth membrane surface (zero surface roughness assumed)	
Constant thickness of the membrane	
No inflow/outflow in domain	Constant channel thickness along direction of flow
	Uniform twill weave of the screen with constant mesh opening and filament angles throughout the mesh sequence, leading to constant depth embossing of screen into the membrane
	No entrance/exit effects
	Fully developed flow

Table 3.3 Summary of assumptions used in the CFD modelling work.

3.1.2.4 Meshing the domain

For finite element method (FEM) used in CFD, the accuracy of the computed solution is dependent on the size and quality of the mesh used. Typically, as the mesh size approaches zero, the closer the result is to the exact numerical solution; however, the size of the mesh that can be practically used is primarily dictated by the availability of finite computational resources and time constraints. As a result, an optimal mesh needs to be used such that the computed solution is a good approximation of the real solution and more importantly, ensure that the solution generated is mesh independent to allow a suitable comparison. A mesh refinement study helps refine a mesh as much as is practical, balancing the solution accuracy, memory and computation time costs.

The resolution of a mesh refers to the discretisation of the geometry by representing the continuous flow field by a discretised flow field, which is the purpose of the mesh. A finer mesh will discretise the underlying equations better, and therefore more likely to capture physical phenomenon defined by the physics. The regions of higher mesh density should correspond to regions where interesting flow phenomenon occur, which in general will correspond to regions with higher gradients. However, an over-refined mesh could lead to numerical instabilities as the solver is likely to include extra fluctuations as opposed to the usual case of treating them as numerical noise.

Mesh refinement studies were performed by multiplying the maximum mesh element size by a user-defined factor to vary the number of mesh elements and help identify optimum mesh size where the characteristic tracking parameter becomes invariant to the mesh size. In general, a very fine mesh is needed to resolve the SST model, as seen in Figure 3.6, particularly in the region next to the walls, where steep velocity gradients are expected.
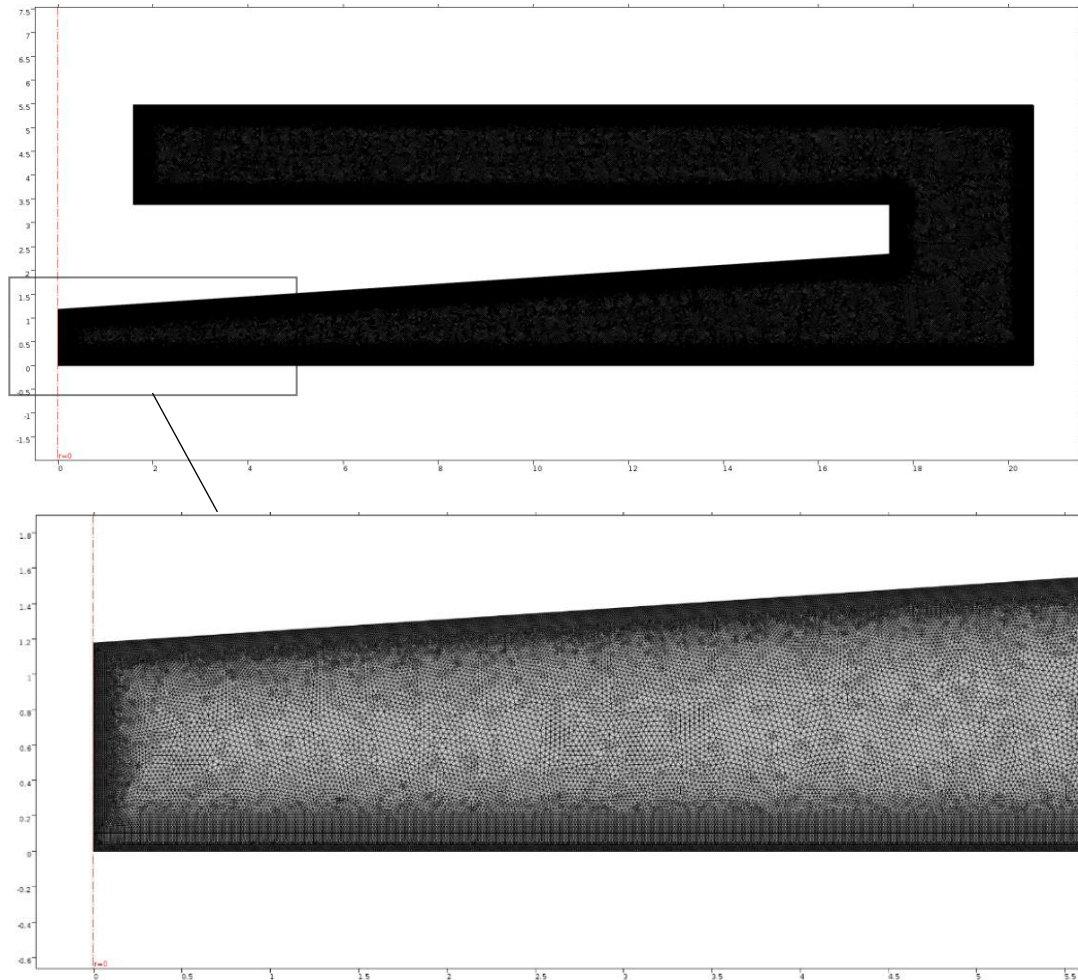
Figure 3.6 Illustration of the extremely fine nature of mesh needed to solve the SST model. Axes shown are in units of mm.

For the 3D unit cell, a fine mesh (>500,000 elements) like the one used for the 2D USD model could not be used due to excessive computational requirements needed to resolve a relatively fine 3D mesh, and thus a custom mesh was used (Figure 3.7); the mesh was finer near the boundary walls to adequately capture the steep flow gradients. Finally, all the 3D unit cell simulations were performed using a dense and high resolution mesh close to the membrane surface, where the average wall shear rate calculations are to be carried out.
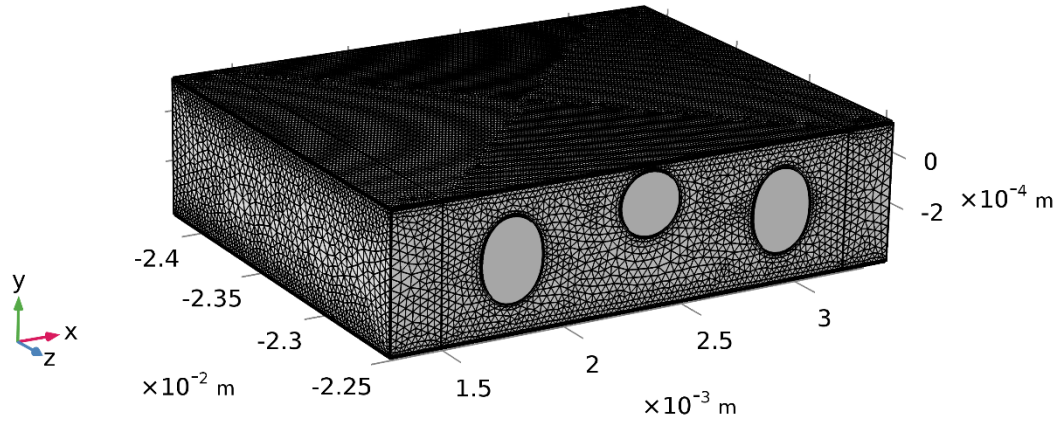
Figure 3.7 3D mesh of the unit cell domain used to carry out the CFD simulations for the screened channels.

Free triangular elements were used to mesh both the USD device and unit cell domains since it was relatively easy to mesh the curved geometry, especially close to the boundaries, without creating skewed mesh elements. Furthermore, the use of triangular elements allows an adaptive mesh refinement study to be performed, where the overall mesh can be iteratively refined, based on either minimising the local error or any user-defined parameter.

3.1.3 Results and discussion

3.1.3.1 Mesh refinement study

For the mesh refinement/grid independence study, the average shear rate at the membrane surface was used as the characteristic output parameter tracked as the mesh size was varied, and pressure drop for the unit cell. Average component couplings on the respective boundaries were used to determinate average shear rates and pressure drops. The mesh size to be used for the subsequent simulations was determined to be the point at which the average wall shear rate value became independent of the number of mesh elements. Figure 3.8 shows a plot of number of mesh elements against the average shear rate, memory requirements and computational time needed for the USD device, and shows a similar plot for the unit cell model.
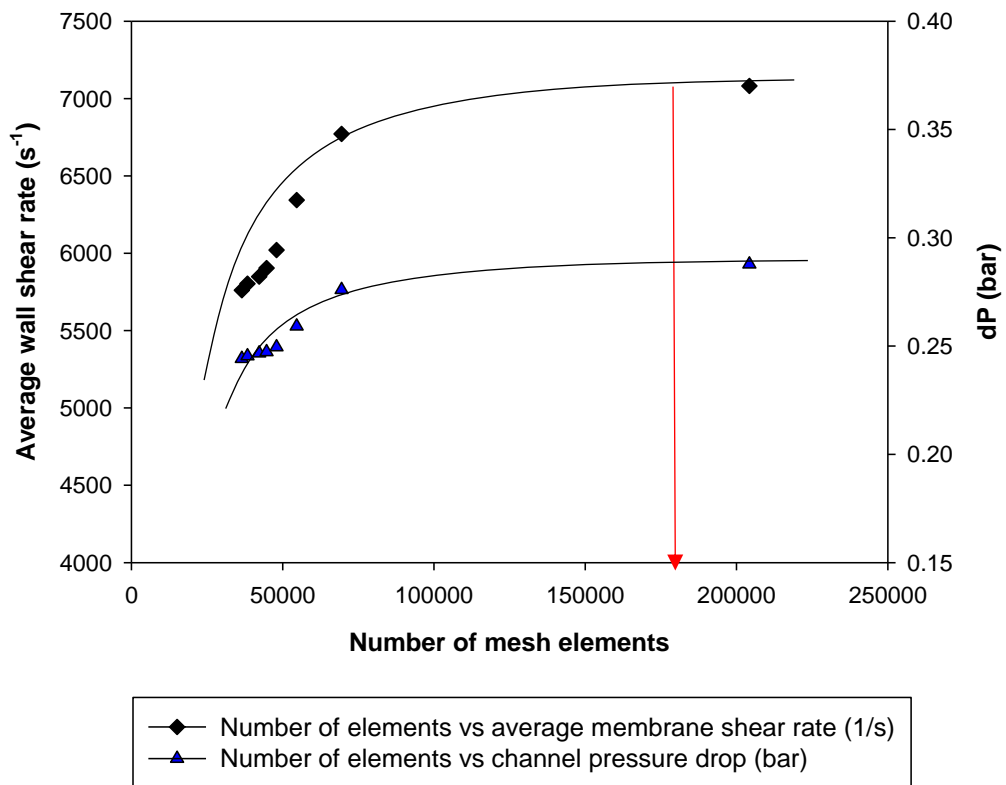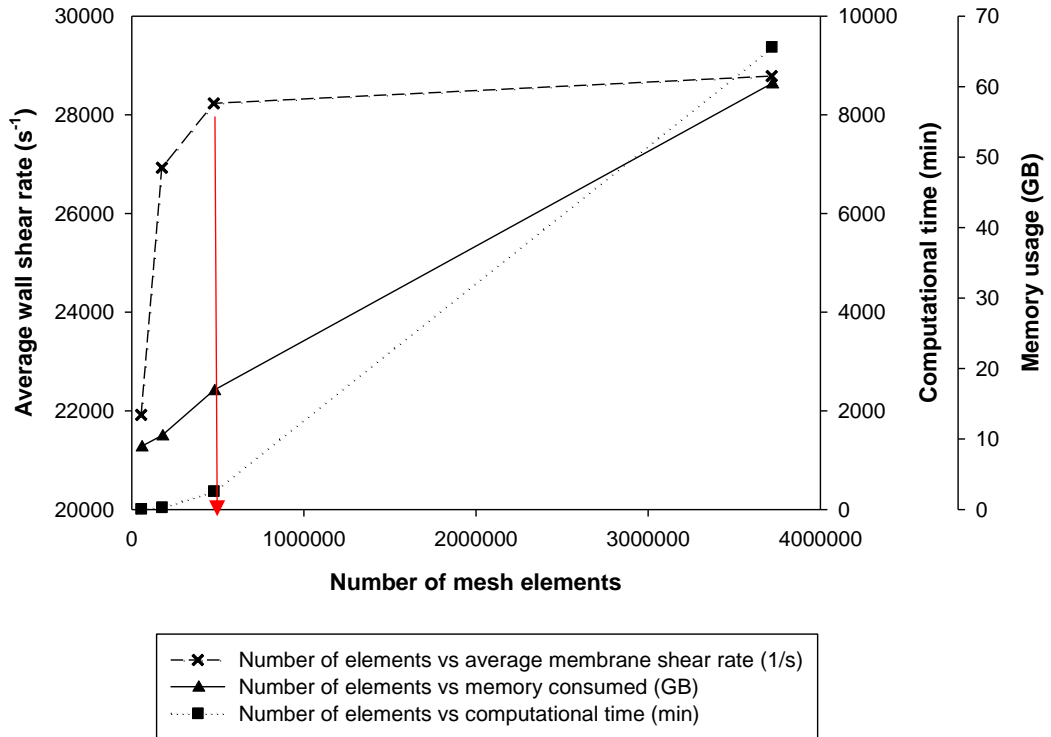
Figure 3.8 Results of the mesh refinement study for the 2D USD model (top) and 3D V screen unit cell (bottom), at simulation conditions of 4000 RPM and 1 LMM, respectively.

For the 2D-axi USD model, the average wall shear rate was seen to increase exponentially, plateauing off around 28,000 s^{-1}. The average wall shear rate did not increase significantly beyond approximately 500,000 mesh elements and appeared to be almost invariant with respect to the mesh size, however, the computational time required increased exponentially, from a matter of minutes to ~6.5 days, for 3.7 million mesh elements. Similarly, for the unit cell, there was no further increase in the averaged wall shear rates and pressure drops when the total number of mesh elements was greater than 200,000. Memory requirements in both cases, for all the different mesh elements, were within the total available memory of the workstation and thus did not contribute to the mesh refinement study.

For this study, the small gains in average shear rate at the expense of significant computational resources was deemed to be unnecessary and therefore, the total number of mesh elements used for the USD model was 503,086, with a minimum element quality (MEQ) of 0.7 (COMSOL recommends a MEQ value > 0.1 for a domain to be considered as well-meshed). For the unit cell, 180,052 mesh elements with a MEQ of 0.1 was used to mesh the computational domain for simulations. The MEQ measures the uniformity of the mesh elements, where skewed elements result in a low quality value. However, skewed elements can often better capture the physical solution with greater resolution in a specified direction, such as those defined by boundary layers for the curved elements in the unit cell model.

For the USD model, in terms of mesh resolution particularly in the viscous and buffer sub-layer close to the boundaries, there are key variables whose respective values can suggest if the mesh is fine enough to sufficiently resolve the flow fields at the walls. For the k-ε model, the 'wall lift-off in viscous units' variable needed to be looked at; a value of 11.06 indicates a fine mesh, but if the mesh resolution in the direction normal to the wall is not fine enough, this value would be greater than 11.06 and the mesh would need to be refined in those regions (Frei, 2013). Figure 3.9 shows the value of the variable for the k-ε model, for the selected mesh.

Similarly, for the SST model, where the flow is resolved everywhere, the 'dimensionless distance to cell centre (lc+)' variable should ideally be close to a value of 0.5 (COMSOL Multiphysics Technical and User Guide, 2015). However, it was difficult to achieve this due to the variations in the flow field and hence a value range of 0.1 to 0.9 was considered acceptable. Figure 3.10 shows the value of the variable

for the SST model, for the selected mesh; for extremely low values, *i.e.*, *lc+* << 0.2, convergence issues were experienced.
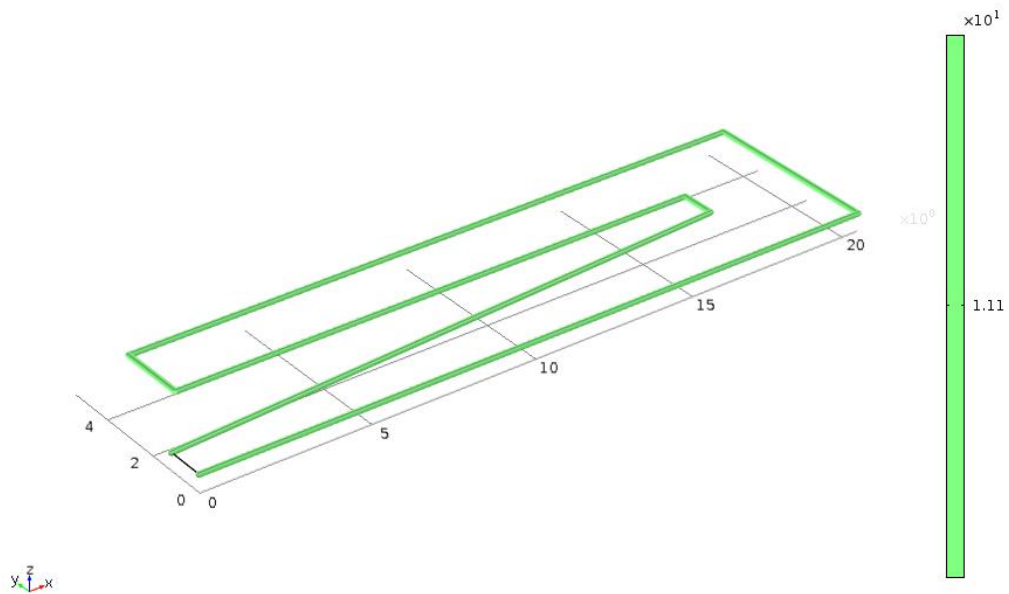
Figure 3.9 Plot of wall lift-off in viscous units at the walls, for the *k-ε* model, showing an uniform dimensionless wall distance of 11.1.
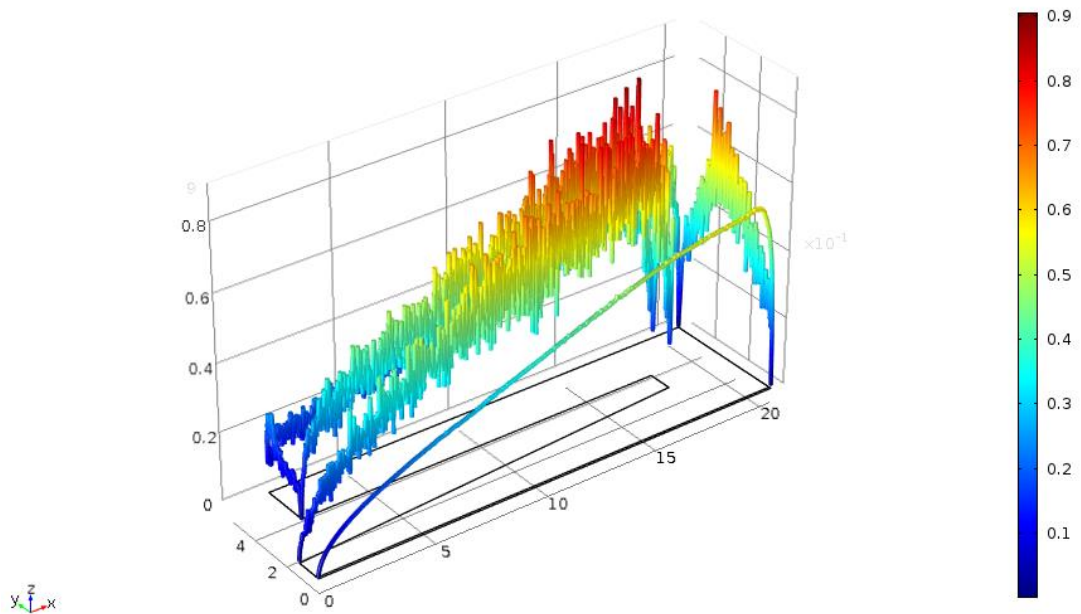
Figure 3.10 Plot of *dimensionless distance to cell centre* (*lc+*) variable at the walls, for the SST model.

3.1.3.2 USD membrane device

3.1.3.2.1 Comparison of 2D-axi versus 3D and k-e versus SST

To be able to use 2D-axi (with swirl flow) as a good approximation to the fully rotational 3D model, it was necessary to compare results from the two models and validate the use of the reduced 2D model. Figure 3.11 shows how the parameters of interest, *i.e.*, average wall shear rate and velocity magnitudes vary during the time-dependent study, up to a simulation time of 1 second.
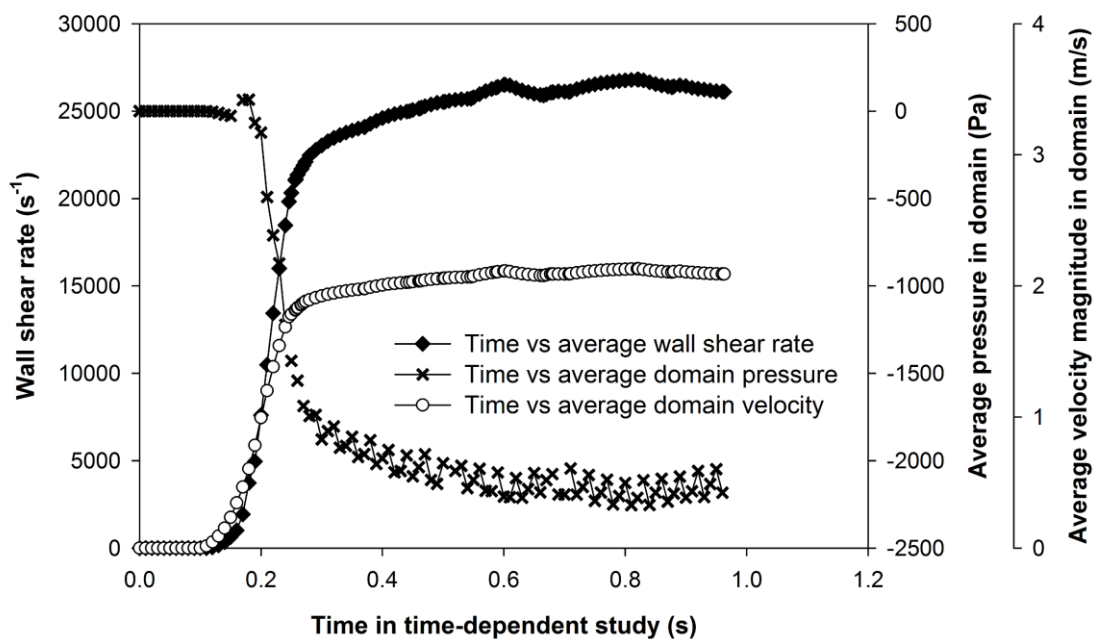
Figure 3.11 Plot of time versus various parameters in the fully rotational 3D model for the USD membrane device solved using a time-dependent laminar study.

As seen in Figure 3.11, steady-state was reached within the first 0.5 seconds of the simulation runtime and was the first point where all the three tracked parameters (wall shear rate, average domain pressure and average velocity magnitude in domain) reached a constant and time-invariant value.

The velocity profiles for the 3D laminar study was seen to be very similar to the 2D-axi solution. Figure 3.12 shows the velocity magnitude plots of the 3D and 2D-axi solutions; in both cases, a maximum velocity magnitude of 7.33 m/s was realised, and the spatial profiles were very similar for both, except for the region between the edge of the disc and solid boundary of the USD device. This difference could be

attributed to the relatively coarser mesh employed in the 3D time-dependent model, and so the temporal and spatial scales in the main rotating body of the fluid was not resolved to the same extent. This was one of the primary reasons for using a much simplified 2D-axi model, which allowed resolution of such fluctuations between the disc and no-slip boundaries to be solved easily using a RANS formulation.
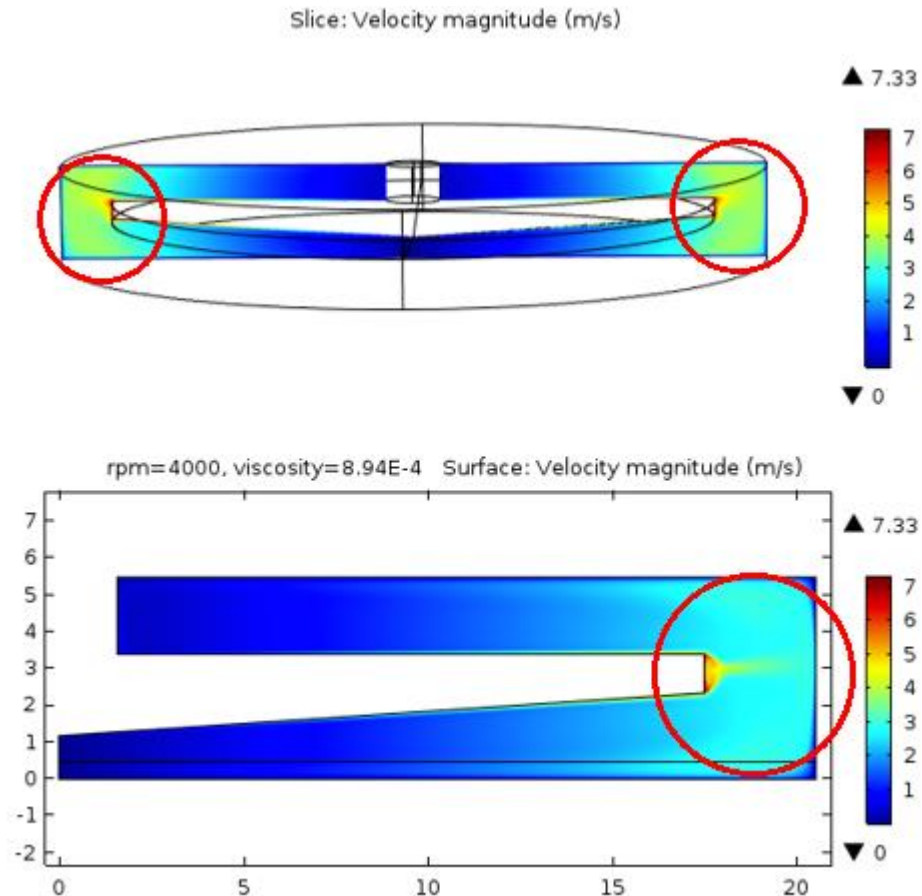
Figure 3.12 Velocity slice plot of the 3D laminar model at t=0.5 s (top) and 2D surface plot of the velocity fields in the 2D-axi SST formulation.

Even though a slight difference in velocity fields near the edge of the rotating disc between the 3D and 2D-axi solutions was seen (marked red in Figure 3.12), the two results were comparable to each other. Since the main objective of this section was to define and calculate the average wall shear rates, some of the main output parameters of interest were calculated and compared as shown in Table 3.4, to provide a quantitative point of comparison. For the time-dependent 3D model, all values were taken from the solution at a simulation time of 1 second (0.5 seconds

after steady-state was first reached) to provide completely steady-state values for a fair comparison to the 2D-axi solutions.

	2D-axi stationary SST model	3D time-dependent laminar flow (t=1s)
Surface-averaged wall shear rate (s^{-1})	26924	26110
Average pressure in computation domain (Pa)	-2181	-2183
Average velocity magnitude in the domain (m/s)	2.086	2.089
Total computational time (min)	24.3	2610
Memory usage (GB)	4.21	33.38

Table 3.4 Summary of key output parameters of the studies and computational resources used to compute solutions (Figure 3.12) for the 2D-axi and 3D models.

The average velocity magnitude in the domain (the USD device), average wall shear rates and average domain pressure for the 2D-axi and 3D models were in very good agreement with each other, which validated the use of 2D-axi domain as a good approximation to the fully rotational 3D model. It also validated the relative accuracy of the SST model (RANS) solution compared to the direct numerical simulation of the laminar flow interface (NS). The key issue with the 3D model was the relatively large memory and time requirements, compared to the simplified 2D-axi model, which was shown to be able to generate good approximations to the true solution at almost 1/100th the time taken by the 3D model.

Similarly, a comparative study between the two k-ε and SST models was performed for the k-ε solutions used to initialise the SST model, and output wall shear rates and radial velocity profiles between the edge of the disc and the boundary wall along y=2.5mm, for the two solutions were plotted in Figure 3.13.
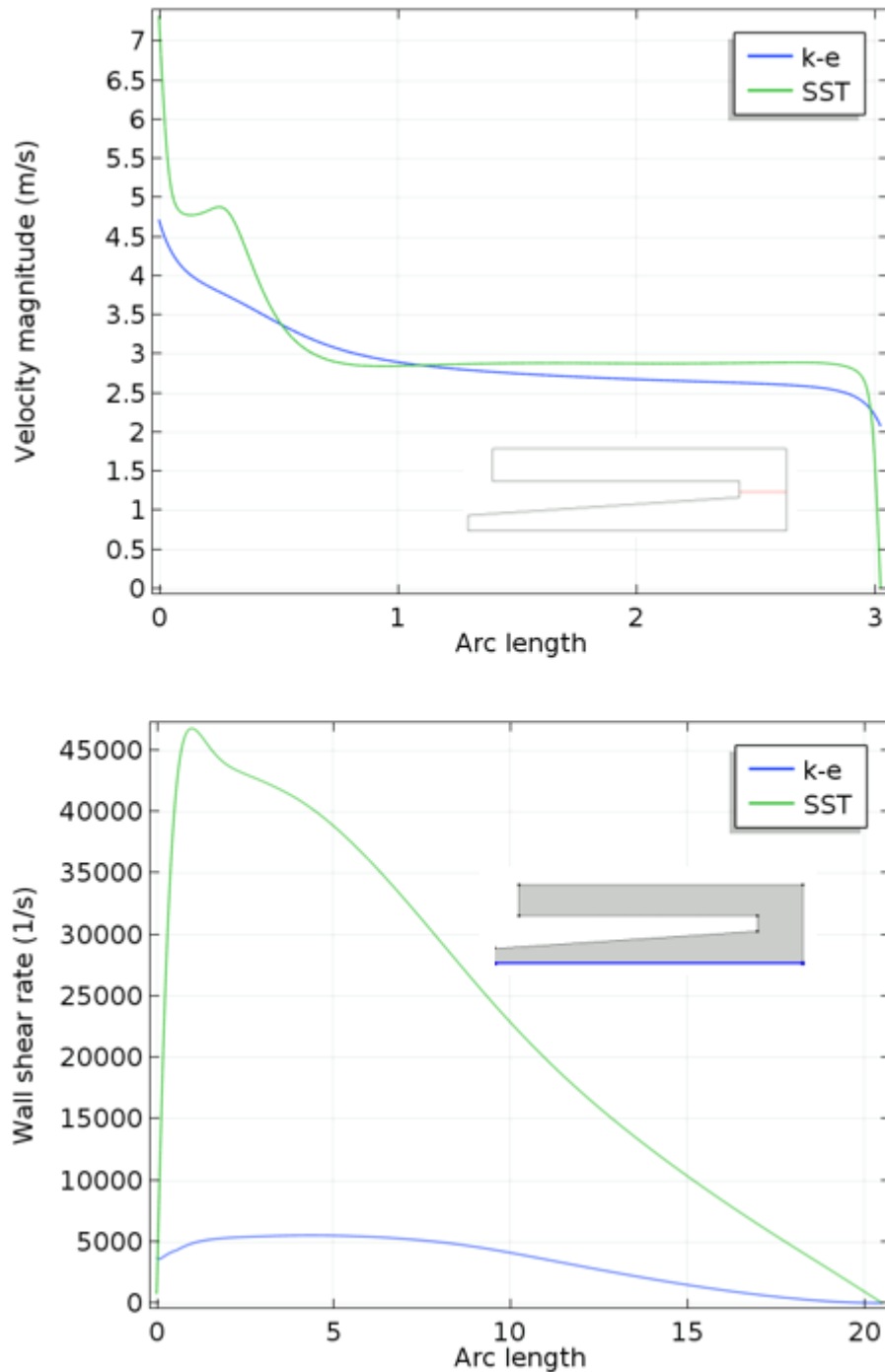
Figure 3.13 1D line plots of velocity magnitude and wall shear rate as a function of radial positions at y=2.5 mm (top) and y=0 mm (bottom), for the SST and k-ε interface (4000 RPM, 0.000894 Pa.s).

As expected and as defined by the underlying physics, the k-ε model wrongly computed the velocity at the edge of the disc to be 4.7 m/s, instead of the calculated tip speed of 7.3 m/s for a rotational speed of 4000 RPM. Apart from that, both models have similar velocity magnitudes in the bulk flow region between the moving wall of

the disc and stationary boundary wall. This discrepancy is because in the k-ε model, the use of "wall functions" boundary condition sets a no-slip condition on the physical walls, and uses wall functions within the viscous sublayer that stops at the wall lift-off distance, which is where the computational domain begins. Thus, only the velocity profile from the wall to the computational domain is solved by an empirically derived equation in the k-ε model.

For the same reason, the k-ε model also greatly miscalculates the wall shear rate profiles along the radial axis. The use of wall functions yields a non-zero velocity on the boundary walls, and such an approximation can lead to inaccurate computation of shear rates, despite the velocity fields being very similar. Since an identical mesh was used for the k-ε and SST model with the dimensionless distance to cell centre ranging from 0.1 to 0.9, the computed wall shear rates for the SST model is more accurate and thus used for the CFD modelling of the USD device.

3.1.3.2.2 Impact of geometry on the hydrodynamics in the USD membrane filtration device

Various studies and investigations on rotating disc systems and their fluid flow characterisation have been done to date. Some of the early work was done by Daily and Nece (1960), who studied the hydrodynamics of RDF systems in a closed cylindrical enclosure. One of their main findings showed that the flow patterns within a RDF system, with disc radius, r, and axial gap, s, can be primarily determined and described by two parameters: disc Reynolds number (Re_d) and gap Reynolds number (Re_s), where the disc radius and gap width are the characteristic lengths, respectively. Daily and Nece (1960) then described the flow patterns between the disc and the boundary and differentiated four different flow regimes based on the two dimensionless Reynolds numbers, Re_d and Re_s. Table 3.5 summarises the four regimes and their respective Reynolds number values.

Flow regime	$\sqrt[2]{Re_s}$	Re_d
I: Laminar flow, narrow gap, merged boundary layers, shear rate varying inversely with spacing, s	≤ 4	$\leq 2.10 \times 10^5$
II: Laminar flow, two separate laminar boundary layers	≥ 4	$\leq 2.10 \times 10^5$
III: Turbulent flow, narrow gap, merged turbulent boundary layers	-	$\geq 2.10 \times 10^5$
IV: Turbulent flow, wide gap, two separate turbulent boundary layers	-	$\geq 2.10 \times 10^5$

Table 3.5 Flow regimes in RDF systems as described by Daily and Nece (1960).

In rotating disc filter systems, the transition from laminar to turbulent flow regime usually occurs close to the stationary walls, since the flow is decelerated close to the walls and is more unstable. The critical disc Reynolds number (Re_d) was reported to be around 2×10^5 for stationary membranes (Randriamampianina et al., 1997).

The boundary layers in flow regimes II and IV are separated by an inviscid core of fluid, rotating with an angular velocity, $k'\omega$, where k' is an empirically determined velocity entrainment factor ($0 < k' < 1$). The turbulent regime was not of interest and thus not discussed, as the flow within the USD membrane device is predominantly laminar for the set of practical operational speeds.

Reynolds numbers, Re_d and Re_s, can be described by Equation 3.5 and Equation 3.6, respectively:

$$Re_d = \frac{\omega \cdot r \cdot R}{\nu}$$

Equation 3.5

$$Re_s = \frac{\omega \cdot s^2}{\nu}$$

Equation 3.6

where ω is the angular velocity (rad/s), r is the radius of the disc (m), R is the radius of the chamber (m), s is the gap between the membrane and disc (m), and v is the kinematic viscosity (m^2/s).

Equation 3.5 was slightly modified, as the original equation uses disc radius as the characteristic length, but since the disc does not span the entire membrane surface in the USD membrane filtration geometry, it was not used as the characteristic length; the chamber radius was used instead. Similarly, for Equation 3.6, the gap term, s, was slightly modified to account for the conical shaped disc, rather than a flat disc assumed for the original equation.

The equivalent gap for a conical shaped disc, s, is given by:

$$s = \frac{r}{2} \cdot \tan\alpha + h$$

Equation 3.7

where r is the radius of the disc (m), h is the distance between the centre of the disc and the membrane surface (m), and α is the angle of conical disc cross section (°).

For the parametric sweep studies done to investigate the impact of varying geometrical parameters of the USD device on the wall shear rate distribution, the operating conditions across the sweep was kept constant at N=4000 RPM, using water as the fluid material. The calculated disc Reynolds numbers for the original geometry at 4000 RPM was 1.63×10^5, which indicated the flow regime to be predominantly laminar. The exact flow patterns and the number of boundary layers were dependent on the gap Reynolds number and the geometry, as the value of s was dependent on the gap and the angle of conical disc cross section (Equation 3.7). The ideal fluid flow within the USD device should consist of two recirculating flows to ensure a uniform wall shear rate profile, such that the average shear rate at the membrane surface due to the rotating fluid should be relatively constant across the radial axis. This is essential for scale-up purposes to have similar flow profiles and wall shear distributions to those experienced within the large scale TFF cassettes, wherein the flow is primarily laminar and uniformly distributed across the length of the channel. The objective of this CFD study was to observe the impact of varying geometric parameters on the wall shear rate profiles and subsequently identify the

optimal geometrical design for the USD membrane device that has minimal variations of shear rate radially across the membrane. This optimal design ensures the area-integrated average value for the USD wall shear rate provides an accurate and close representation of the shear rates generated at any point across the radius.

Results of varying the angle of the conical section of the disc, gap clearance of the disc from the membrane, disc diameter and disc rotational speed, keeping the other geometrical parameters constant, are presented and addressed in following sections 3.1.3.2.2.1, 3.1.3.2.2.2, 3.1.3.2.2.3 and 3.1.3.2.2.4, respectively.

3.1.3.2.2.1 Impact of varying angle of conical disc, α, on wall shear rates

The angle of the conical disc, α, was varied and the flow patterns investigated for the range, α (degrees): {0, 1.9, 3.8, 7.6}, at constant gap, h, of 1.175 mm. Figure 3.14 illustrates the distribution of wall shear rates calculated as a function of chamber radius for the different angles and highlights the different profiles observed at different α values.
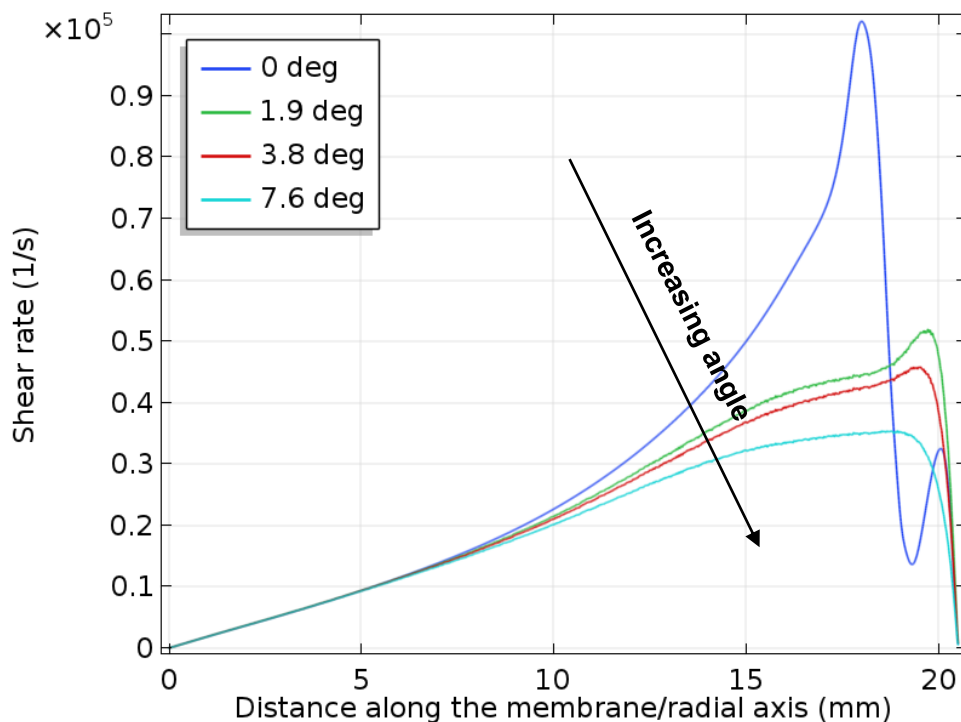
Figure 3.14 Effect of varying α on the shear rate distribution radially across the membrane at 1.175 mm gap clearance from the bottom, 35 mm disc diameter and 4000 RPM disc speed.

Maximum shear rates were observed near the tip of the rotating disc, corresponding to the region close to 17.5 mm on the radial axis, which was expected since the maximum rotational velocity is at the tip of the rotating disc and in the bulk fluid in the vicinity. It was also seen that the shear rate distribution flattened out with increasing values of α, and the most pronounced change in shear rate profile was seen when α was increased from 0 degrees to 1.9 degrees. The shear rates flattened out further as the angle was increased beyond 1.9 degrees, but the profiles displayed a similar trend and the change was not as significant. Thus, the hydrodynamic conditions and flow regimes for α values, 0 and 1.9 degrees, was looked at in more detail, to obtain a better understanding and determine the underlying cause behind the significant differences seen in Figure 3.14. The shear rate distribution at the membrane surface, 2D arrow surface plot of the velocity field and the axial distribution of rotational velocity are shown in Figure 3.15 and Figure 3.16. The top image (2D cut plane view) provides information regarding the distribution of shear rates across the membrane and thus fouling, and how it varies radially across the membrane. Higher degree of fouling is expected to be limited to regions of lower shear, with little/no fouling expected in areas of greater shear.

A.

B.

C.
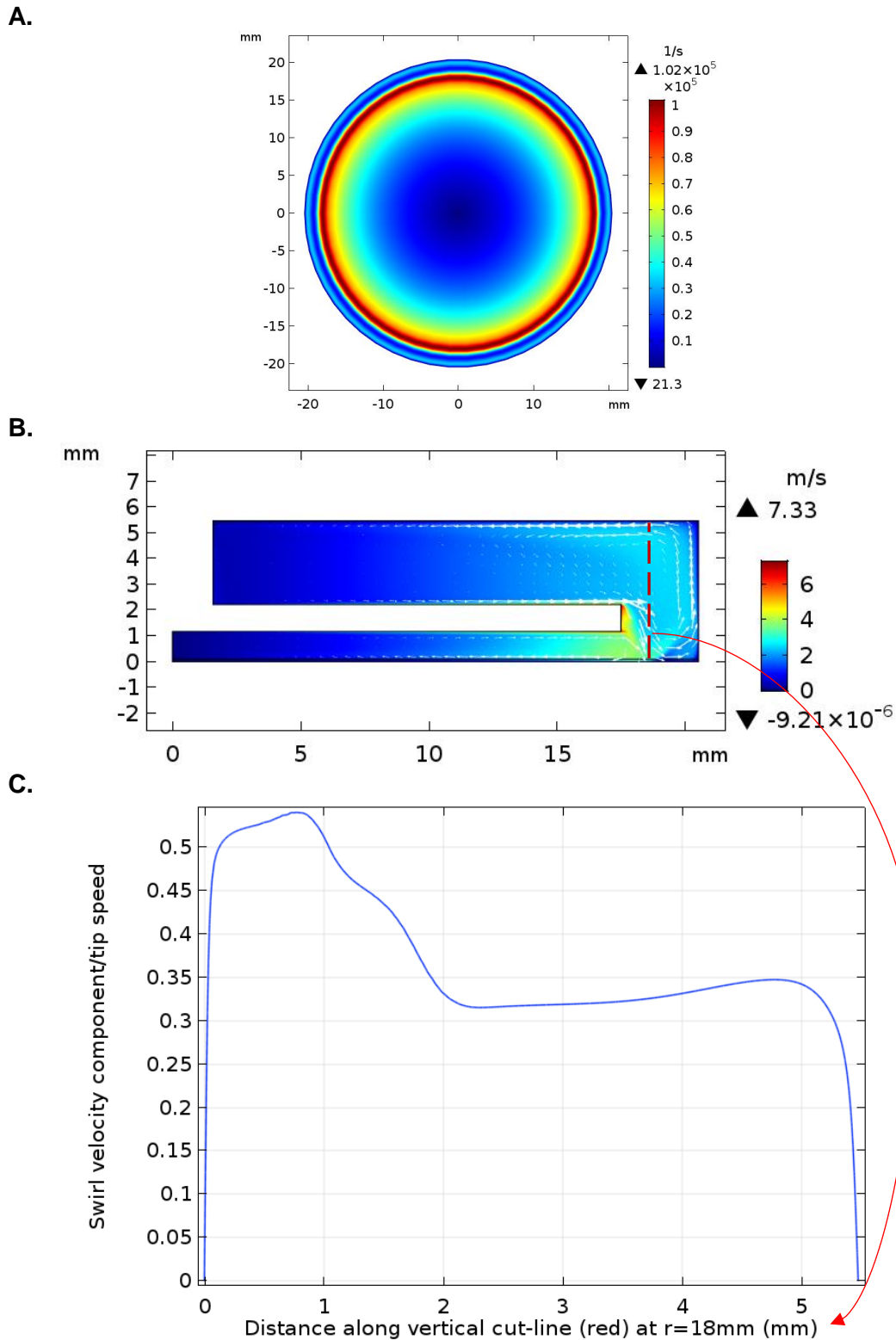
Figure 3.15 Variation of shear rate and velocity magnitudes for disc cone angle $\alpha=0°$. Top: 2D cut plane section of shear rates at $z=0$ mm, middle: 2D velocity magnitude surface plot (r-z plane) and, bottom: axial distribution of swirl velocity ratio at $R=18$ mm.

A.

B.

C.
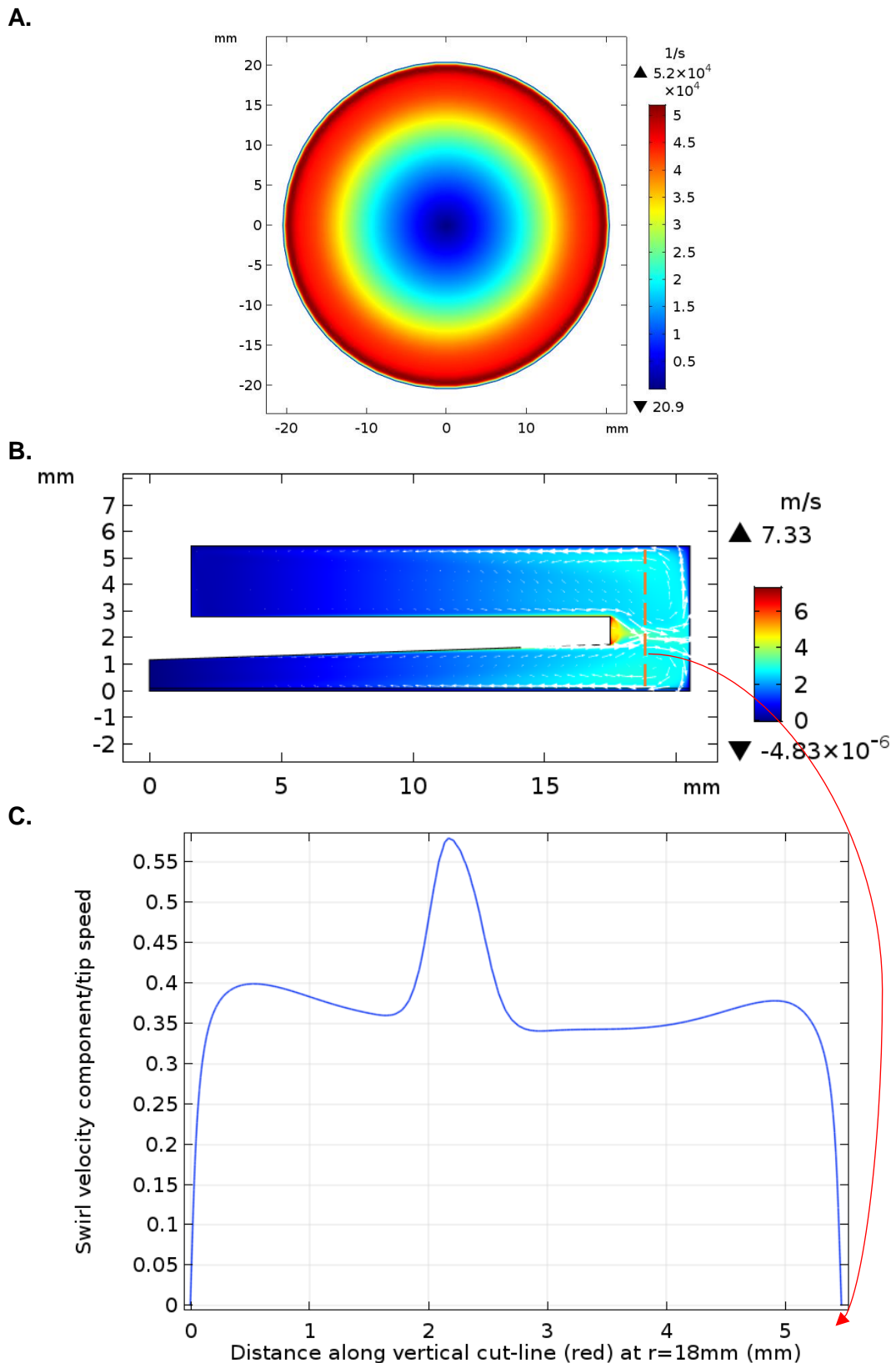
Figure 3.16 Variation of shear rate and velocity magnitudes for disc cone angle α=1.9°. Top: 2D cut plane section of shear rates at z=0 mm, middle: 2D velocity magnitude surface plot (r-z plane) and, bottom: axial distribution of dimensionless swirl velocity at R=18 mm.

The top images in Figure 3.15 and Figure 3.16 provide an alternative perspective of the information plotted in Figure 3.14. They show the relative shear rate profiles at the membrane surface, varying across the radius of the chamber. For 0 degrees, the shear rates were not uniform in any region of the membrane, as indicated by the lack of regions with uniform colour profiles; the shear rate is a strong linear function of radial distance from the centre. Furthermore, shear rates were a minimum between R=0 mm and R=13 mm (the blue region in Figure 3.15), which indicates greater fouling tendencies in roughly 40% of the total available membrane area, while the shear rates increased steeply thereafter for the remaining 60%. For 1.9 degrees, the region corresponding to low shear rates (blue region in Figure 3.16), located in the central part of the membrane was relatively smaller, accounting for ~24% of the total membrane area. There was a relatively significant region of uniform shear distribution, between R=13 mm and R=19 mm, translating to ~46% of the total membrane area and illustrated as the red region on the 2D cut plane surface plot (top) in Figure 3.16. A similar impact can be expected for angles 3.8° and 7.6°, resulting in greater membrane areas with uniform shear.

The middle images in Figure 3.15 and Figure 3.16 illustrate the flow radial and axial components of the velocity field; the arrow lengths are proportional to the velocity magnitude. The radial and rotational flow is essential to the disruption of the boundary layer and reduction of particle deposition on the membrane, while the axial flow promotes convective mixing. There were two distinct recirculating flows seen for 1.9 degrees in Figure 3.16, which can be attributed as the reason for the more even shear distribution, compared to 0 degrees in Figure 3.15, where there was limited recirculation in the *r-z* plane (lower radial velocity below the disc, indicated by the length of the vector arrows) in the region directly below the rotating disc.

Finally, the axial variations of the ratio of rotational velocity component, *v*, to the tip speed, U_{tip}, at a radial distance of 18 mm, corresponding to the region near the tip of the disc, are plotted in Figure 3.15 and Figure 3.16 (bottom). The values of $\sqrt[2]{Re_s}$ were >> 4 for all values of *α*, which indicates a flow regime II: *Laminar flow, two separate laminar boundary layers.* Looking at the axial variations of swirl flow velocity, it can be inferred that the flow does indeed fall under regime II, and the boundary layers on the rotating disc and the membrane surface are not merged but instead separated by a bulk fluid rotating at a constant velocity. The value of *k'* can be estimated by looking at the constant velocity regions in the axial flow distribution plots, shown in the bottom

graphs of Figure 3.15 and Figure 3.16. A quick estimate yielded k' values of 0.525 and 0.375, for 0 and 1.9 degrees, respectively; the bulk fluid rotates at a greater velocity for 0 degrees compared to 1.9 degrees as expected, because the rotating disc gets closer to the membrane surface as the angle is decreased.

It was also noted that the rotational velocity decreases slightly close to the rotating disc, before peaking and approaching its maximum value. This drop is the result of radial movement of the fluid close to the tip of the rotating disc, compensating for the increased radial outflow velocity, because of suction generated by the disc. Finally, the fluid velocity approached zero close to the stationary walls due to the no-slip boundary conditions imposed for the non-rotating parts of the USD device.

3.1.3.2.2.2 Impact of clearance of the disc from the membrane surface, h_c, on wall shear rates

The distance from the centre of the disc to the membrane surface was varied and the flow patterns investigated for the range, h_c (mm): {0.1, 0.3, 0.75, 1, 1.175, 1.3}, at constant α of 3.8°. Figure 3.17 illustrates the distribution of wall shear rates calculated as a function of chamber radius, for the different gaps, and highlights the different profiles observed at different h_c values. This is particularly important in the case of compressive polymeric membranes, where variations in membrane thickness, due to flow-induced compression or manufacturing tolerances, could change the gap between the disc and the membrane surface and effectively alter the wall shear rate profiles across the membrane surface.
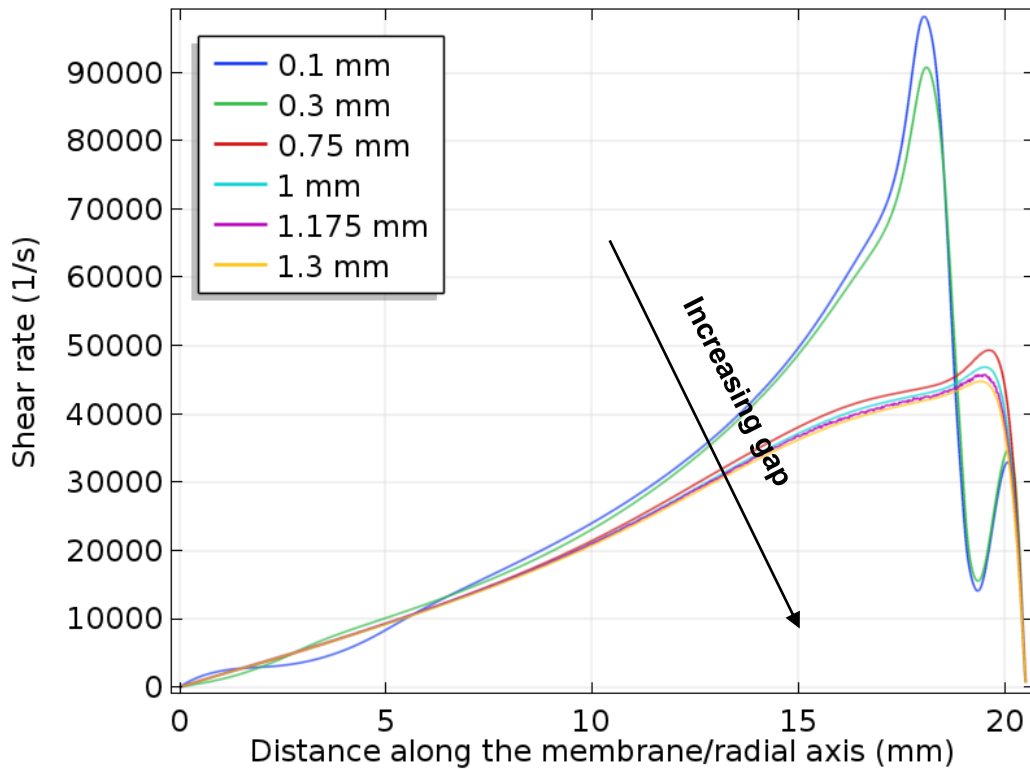
Figure 3.17 Effect of varying h_c on the shear rate distribution radially across the membrane for a 3.8° disc angle, 35 mm disc diameter and 4000 RPM disc speed.

As was the case in section 3.1.3.2.2.1, a similar trend was seen in Figure 3.17 where the gap, h_c, was varied. The change in wall shear rate profile occurred when h_c was increased from 0.3 mm and 0.75 mm, and so only these two parameters were studied in more detail. The shear rate distribution across the membrane did not vary much for gaps greater than 0.75 mm, and was not as responsive to changes in h_c compared to varying $α$. Figure 3.18 and Figure 3.19 show the 2D cut plane plot of shear rate distribution at the membrane surface, 2D arrow surface plot of the velocity field and the axial distribution of rotational velocity:tip speed.

A.

B.

C.
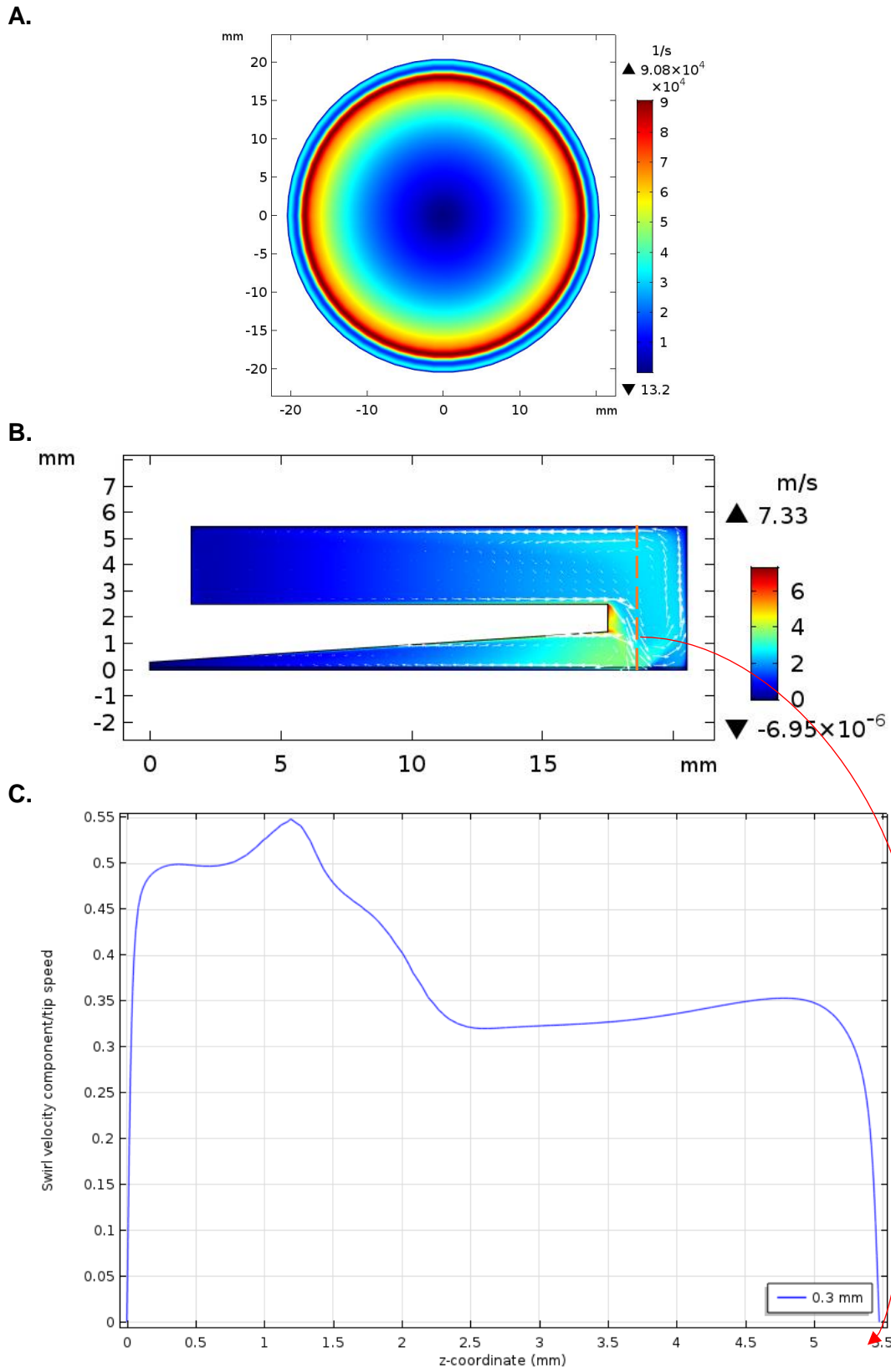
Figure 3.18 Variation of shear rate and velocity magnitudes h_c=0.3 mm. Top: 2D cut plane section of shear rates at z=0 mm, middle: 2D velocity magnitude surface plot (r-z plane) and, bottom: axial distribution of dimensionless swirl velocity at R=18 mm.

A.

B.

C.
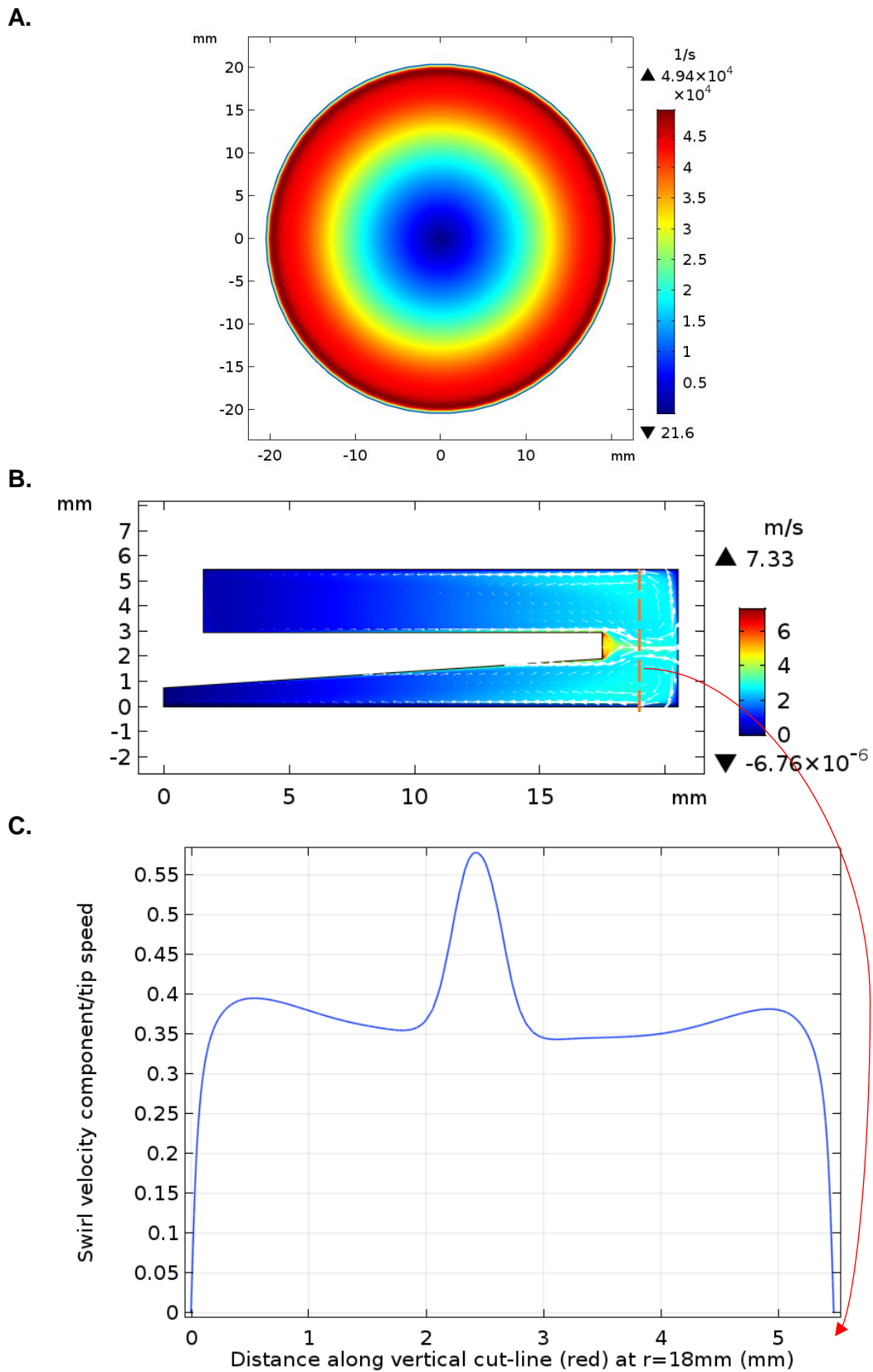
Figure 3.19 Variation of shear rate and velocity magnitudes h_c=0.75 mm. Top: 2D cut plane section of shear rates at z=0 mm, middle: 2D velocity magnitude surface plot (r-z plane) and, bottom: axial distribution of dimensionless swirl velocity at R=18 mm.

Similar to part A, the differences in wall shear rate profiles can once again be attributed to the change in flow patterns and introduction of a secondary recirculating flow. The values of $\sqrt[2]{Re_s}$ were >> 4 for all values of h_c, which indicates the flow to be in regime II again. Values of k' were estimated to be 0.5 and 0.375, for 0.3 mm and 0.75 mm, respectively. The decreasing k' value is expected because the shear rate at the membrane surface is greater when the rotating disc is closer to the membrane, *i.e.* 0.3 mm, compared to 0.75 mm gap, and hence the core fluid rotates with a relatively greater velocity.

3.1.3.2.2.3 Impact of disc diameter, D_d, on wall shear rates

The impact of changing the diameter of the rotating disc was investigated for values 25 mm, 35 mm and 40 mm, keeping h and α constant at 1.175 mm and 3.8°, respectively.
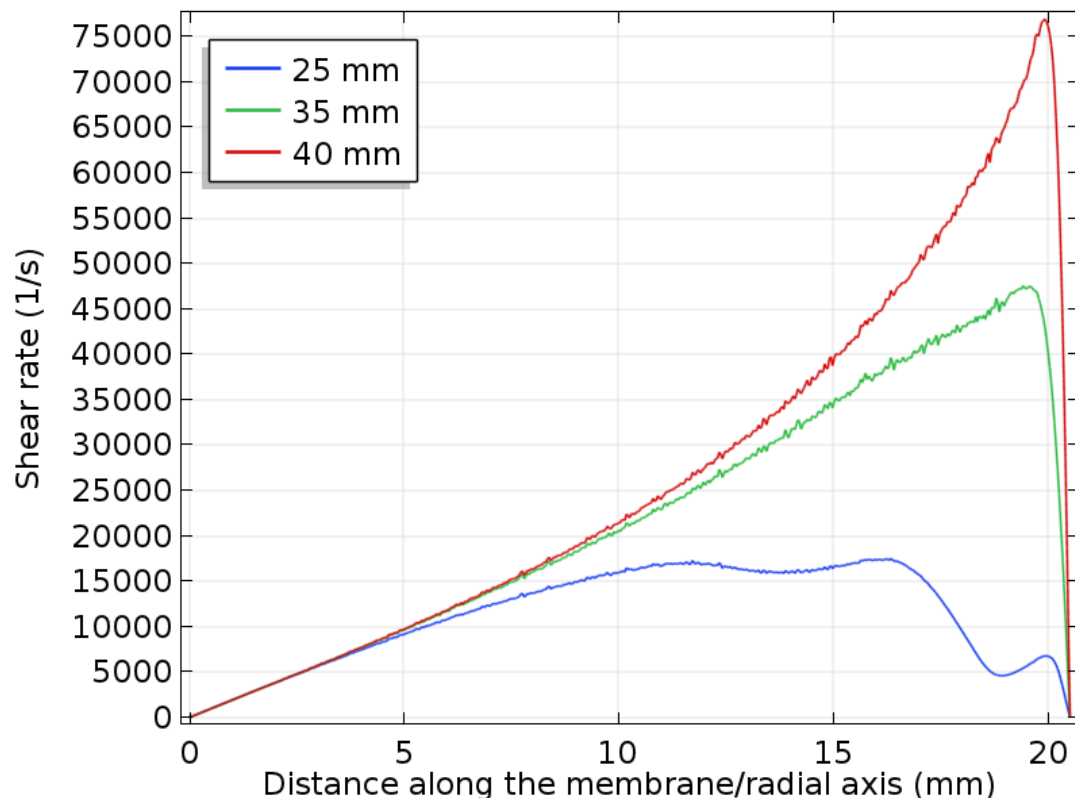
Figure 3.20 Effect of varying disc diameter on the shear rate distribution radially across the membrane for a 3.8° disc angle, 1.175 mm gap clearance and 4000 RPM disc speed. The coloured horizontal lines represent the derived average shear rates, integrated over the membrane area.

Varying the disc diameter was observed to have the greatest impact on shear rate distributions, comparing Figure 3.20 to Figure 3.17 and Figure 3.14. A significant change in shear profile was seen when the disc diameter was reduced from 35 mm to 25 mm. A disc diameter of 25 mm had the most even shear rate distribution out of all the three parameters investigated. The horizontal lines indicate the average shear rate values at the membrane surface for the three diameters. The variation and % difference between the average and instantaneous shear rate at any point on the radial axis was the least for 25 mm, followed by 35 mm, and provides a relatively accurate representation of the shear rate profile at the membrane surface. The shear distribution got worse as the diameter was increased to 40 mm, with the highest maximum shear rate. Figure 3.21 shows the shear rate distribution at the membrane surface on a 2D cut plane surface plot, 2D arrow surface plot of the velocity field and the axial distribution of rotational velocity, for disc diameters 25 mm and 35 mm, respectively.
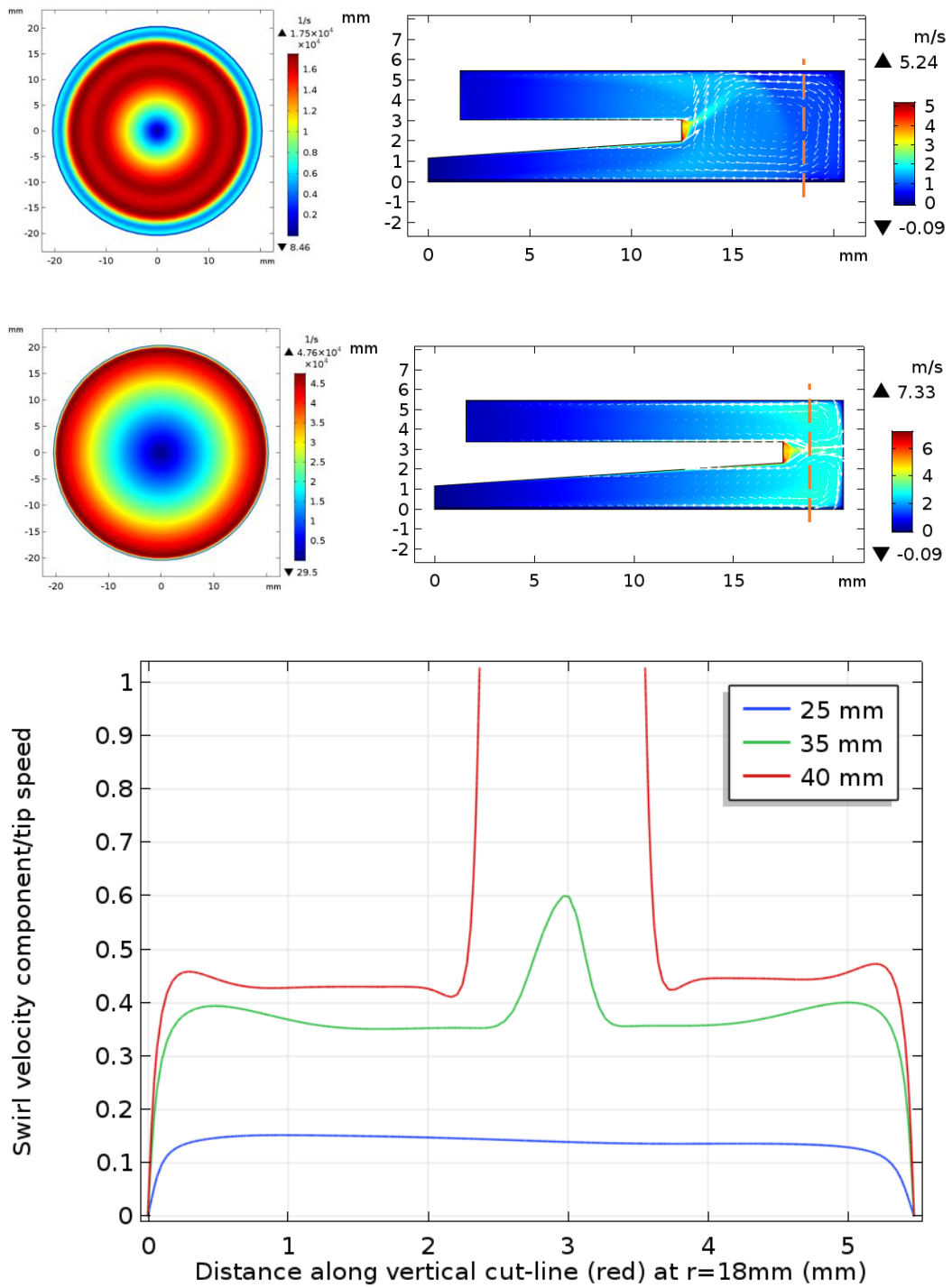
Figure 3.21 Variation of shear rate and velocity magnitudes for different disc diameters. Top: Shear rate distribution and 2D arrow surface plot for 25 mm disc diameter, middle: shear rate distribution and 2D arrow surface plot for 35 mm disc diameter, and, bottom: axial distribution of swirl velocity at R=18 mm, for 25 mm, 35 mm and 40 mm disc diameter.

As seen in Figure 3.21, the shear rate distribution for 35 mm (middle) showed a similar pattern to that seen in the earlier sections, 3.1.3.2.2.1 and 3.1.3.2.2.2, with regions of uniform shear rates accounting for ~37% of the total membrane area. However, for a disc diameter of 25 mm, this corresponding area was significantly higher, at ~67%, roughly two-thirds of the total membrane area, illustrated by the regions shaded red in Figure 3.21 (top).

In terms of flow patterns within the device, the two typical recirculating flows were observed for the 35 mm disc diameter. However, a third significant flow vortex was observed close to the rotating disc for 25 mm disc diameter, rotating at velocities very close to the tip speed as seen in Figure 3.21 (bottom), with a swirl flow velocity:tip speed ratio of 0.9. This vortex ensures good mixing of the feed and introduces unsteadiness into the bulk flow, resulting in a very flat shear rate distribution that was not seen in any of the earlier cases.

Flow regimes for all three diameters was determined to be laminar flow with two separate boundary layers, and values of *k'* calculated to be 0.5, 0.35 and 0.2 for 25 mm, 35 mm and 40 mm, respectively. *k'* was the lowest for 40 mm and is primarily because the edge of the disc was too close to the solid boundary wall (41.05 mm chamber diameter), and so the flow velocity is quickly decelerated to zero as the fluid approaches the wall. As a result, the recirculating flows have relatively smaller axial and radial velocity components, compared to the cases for smaller disc diameters with a larger clearance from the solid walls.

3.1.3.2.2.4 Impact of disc rotational speed, *N*, on wall shear rates

Disc speeds of 2000, 3000, 4000, 6000 and 8000 were simulated and corresponding wall shear rate profiles plotted in Figure 3.22.
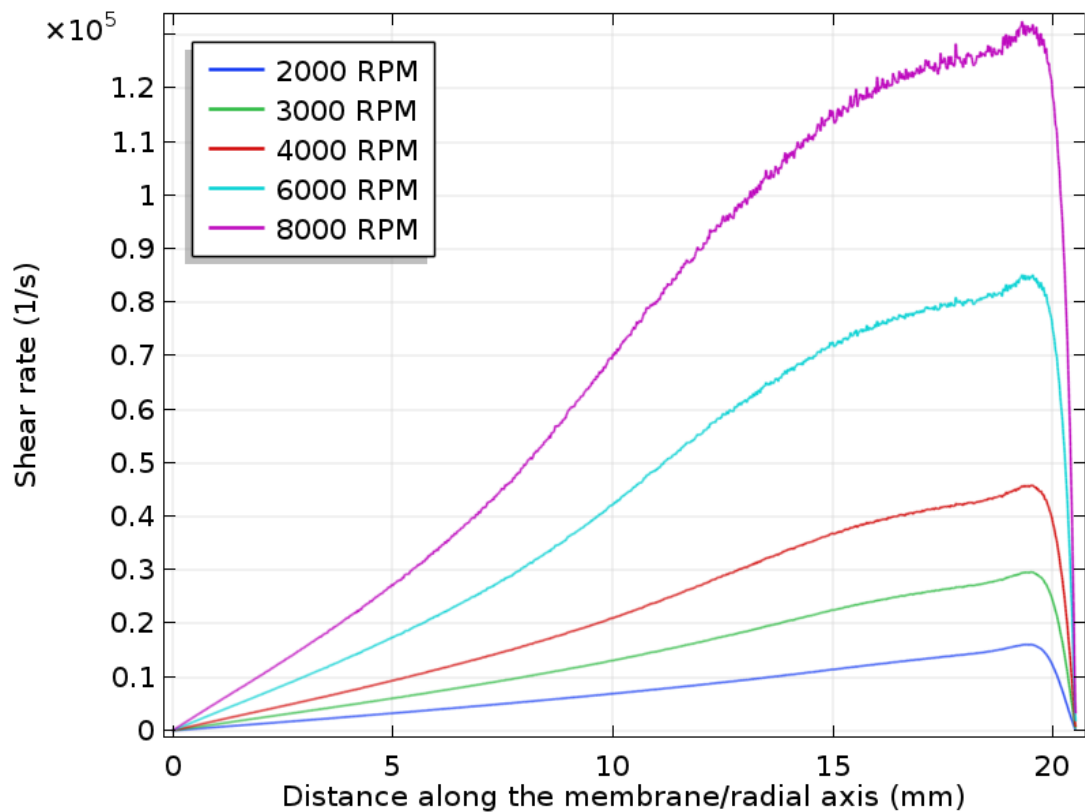
Figure 3.22 Wall shear rate profiles as a function of disc rotational speed (Hz) for 35 mm disc diameter, 1.175 mm gap and 3.8° cone angle of the disc.

The spatial non-uniformity was seen to increase significantly with increasing rotational speed of the disc, showing disproportionate increases in both maximum wall shear rates (peak of the curve) and average wall shear rates. Using higher RPMs could cause potential scale-up issues due to shear-related damage to fragile and shear-sensitive molecules and the significant spatial non-uniformity means that the area-averaged wall shear rate values tend to be non-representative of the local wall shear rates at the membrane. Charm and Wong (1981) showed that exceeding a threshold shear rate of 1×10^3 s^{-1} (>30 minutes) caused a loss of enzymatic activity, while Thomas and Dunnill (1979) observed no changes to protein structure or activity up to shear rates of $1 \times 10^5 - 1 \times 10^6$ s^{-1}. Table 3.6 lists the maximum and average shear rates in the computational domain for the various rotational speeds investigated.

Rotational speed (RPM)	Maximum shear rate (s^{-1})	Average shear rate (s^{-1})
2000	96124	1607.1
3000	1.67×10^5	2358.2
4000	2.50×10^5	3103.5
6000	4.47×10^5	4577.9
8000	6.82×10^5	6036.8

Table 3.6 Comparison of maximum and average domain shear rates for the USD computational domain. Data calculated from simulations carried out to generate Figure 3.22.

All maximum shear values were well below the 1×10^6 s^{-1} threshold, while the average domain shear were all below 1×10^4 s^{-1}. However, rotational speeds used in this thesis was 4000 RPM, as that was determined to be the maximum rotational speed that corresponds to the upper end of the typical crossflow velocity ranges in tangential flow filtration cassettes.

3.1.3.3 Screened unit cell

3.1.3.3.1 Comparison of unit cell model and 1/4th full scale geometry solutions

To verify the applicability of using smaller unit cells to model and represent phenomenon occurring in the full scale screened channel, a 3D model of full width and 4 cm path length (quarter of the entire flow length of Pellicon cassettes, was simulated and the solutions compared to those from the reduced unit cell model. Figure 3.23 shows the velocity magnitude plots of the two 3D models.
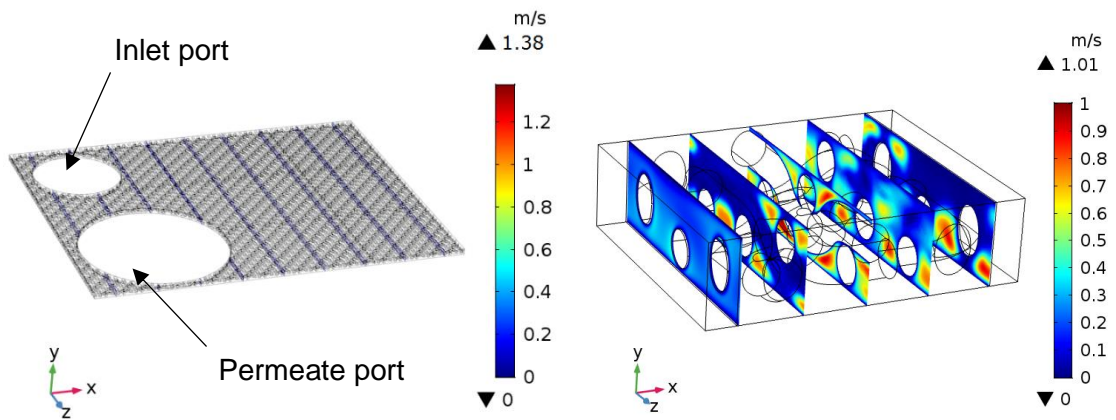
Figure 3.23 Velocity magnitude slice plots for 1/4th reduced model (left) and unit cell (right) CFD simulations for a V screen at 20 LMM feed flow rate and fluid viscosity of 0.000894 Pa.s.

Similar velocity flow fields were seen for both the 3D simulations and the average wall shear rates were calculated to be 13056 s^{-1} and 14204 s^{-1}, for the unit cell and full width model, respectively. The differences in shear rates could be attributed to the relatively coarse mesh that was used for the full width model due to memory limitations, as well as the higher local velocities in the developing flow regime near the inlet port region. Similarly, maximum velocities for the full width simulation was higher than the unit cell, which could be attributed to entrance effects near the inlet port, where the flow slowly develops and flows equally across the width of the domain, transitioning from a non-uniform flow to a full developed flow. The periodic nature of flow and thus wall shear rates are shown in Figure 3.24.
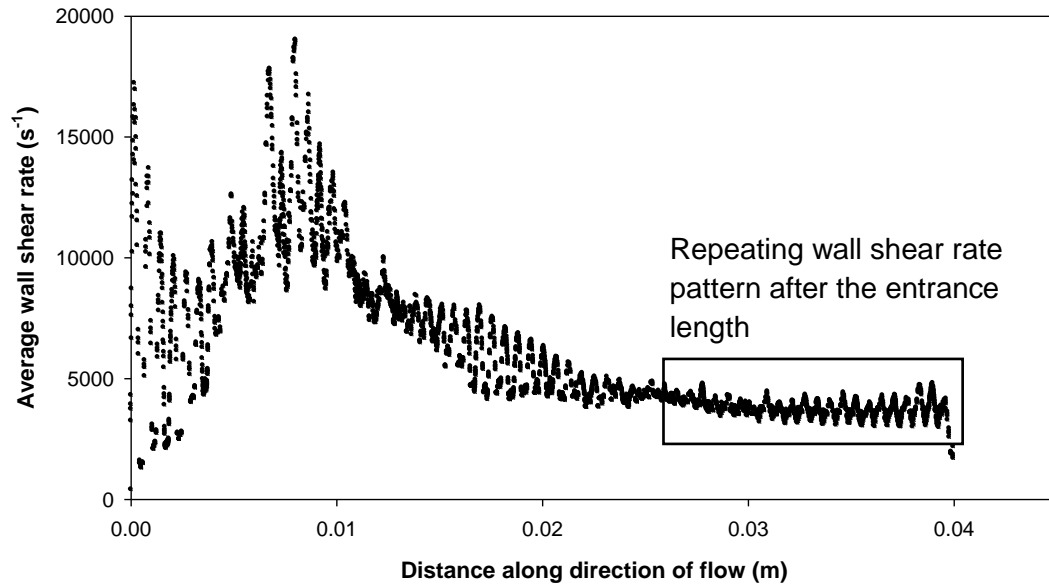
Figure 3.24 Graph showing average wall shear rate profiles for the full width 3D model and region of periodicity once flow is full established. Simulation conditions were a flow rate of 5 LMM and fluid viscosity of 0.000894 Pa.s.

As seen in Figure 3.24, once the flow was fully established (so that the velocity profile is periodic with respect to the geometry), a periodically repeated wall shear rate pattern was observed, thus validating the use of unit cells to carry out 3D analysis of flow phenomenon that is representative of the flow fields occurring in the full scale system. Although flow fields and shear rates were similar for both models, the full width model required 204 GB of RAM, even with a memory efficient memory solver like the iterative solver. As a result, the concept of unit cell was used, allowing a much greater resolution of the flow fields at a correspondingly lower memory consumption.

3.1.3.3.2 Modelling with and without extended domains for the unit cell

Extended domains were used to minimise entrance/exit effects associated with plug flow. To highlight this, a simulation with no extended domains was carried out and relative solutions in terms of wall shear rates compared in Figure 3.25.
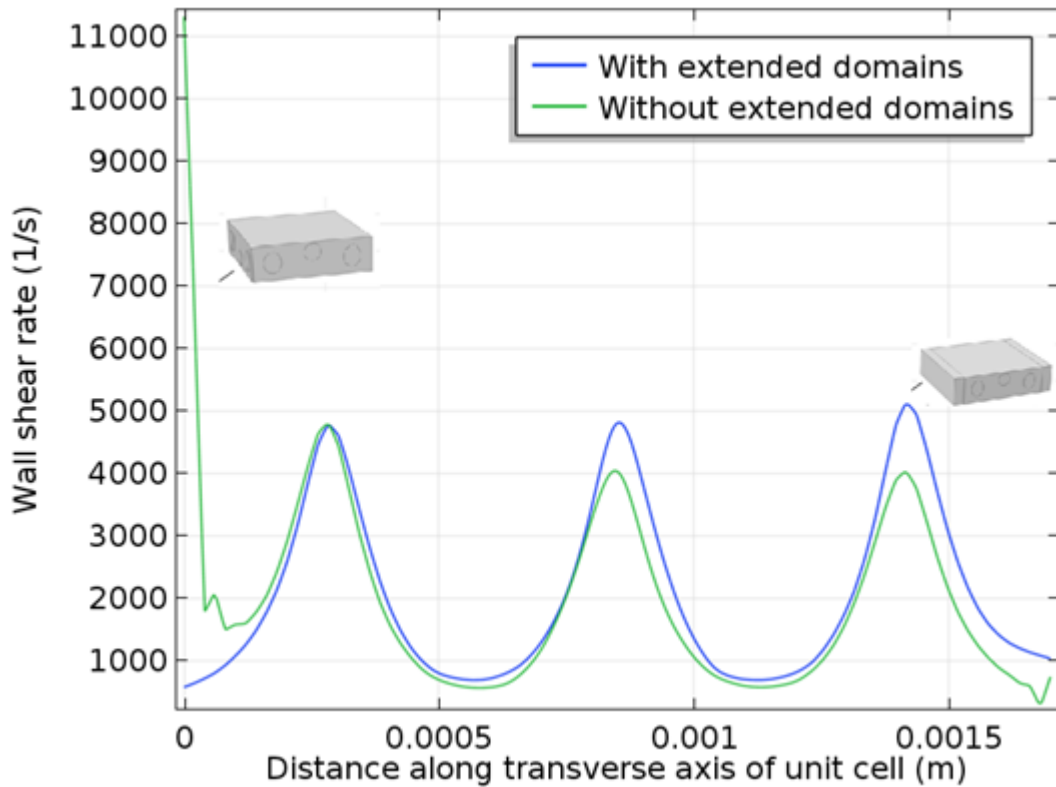
Figure 3.25 1D plot showing wall shear rates along the unit cell, for simulation conditions of 5 LMM and 0.000894 Pa.s.

In Figure 3.25, there is a large, asymptotic spike seen in local wall shear rates at the inlet region for the model without extended domains, and therefore, the arithmetic average tends to be skewed by the outlier of the asymptotic shear rate at the junction of the inlet and the no-slip wall of the unit cell. Performing the average over a greater length increases the length over which the high initial value at the inlet-wall junction is distributed; however, this is not possible in the case of unit cells, which prompted the need for extended domains at the inlet and outlet of the unit cell.

The wall shear rate profiles for both cases were similar, but the shear rates for the model with extended domains were higher than the model without. This was because the prescribed inlet velocity was calculated based on the channel width and height without accounting for the obstruction by the screen, which leads to an increase in velocity in the reduced cross-sectional area of the flow (by mass conservation). This was another reason for using extended domains, to enable the right velocities to be applied to the inlet boundary based on screen type and calculated inlet flow rates.

3.1.3.3.3 Discussion of unit cell results for A, C and V screens

For a viscosity of 0.000894 Pa.s and inlet flow rate of 5 LMM, simulated velocity magnitudes and pressures across the unit cells for A, C and V screen channels are shown in Figure 3.26. Simulation conditions for all three screens were a constant inlet flow rate of 5 LMM and a fluid viscosity of 0.000894 Pa.s. The regions of high velocity and pressure are indicated in red and the areas of low velocity and pressure in blue.

Flow velocities across the channel (in the *x*-direction) were seen to vary roughly five-fold for the V screen, and up to eleven-fold and eight-fold for the A and C screens, respectively. The bulk of the fluid travels at the average flow rate (depending on the voidage of the channel that is dictated by the characteristics of the screen), while the regions close to the screens experience localised accelerated flow and therefore greater shear rates. At a feed flow rate of 5 LMM, the maximum channel velocities were quite different for the three screens, with the tight A screen having the largest maximum velocity magnitude of 0.88 m/s and the coarse V screen with the lowest of 0.27 m/s. Figure 3.27 shows the wall shear rates and pressure as a function of the position along the direction of flow.
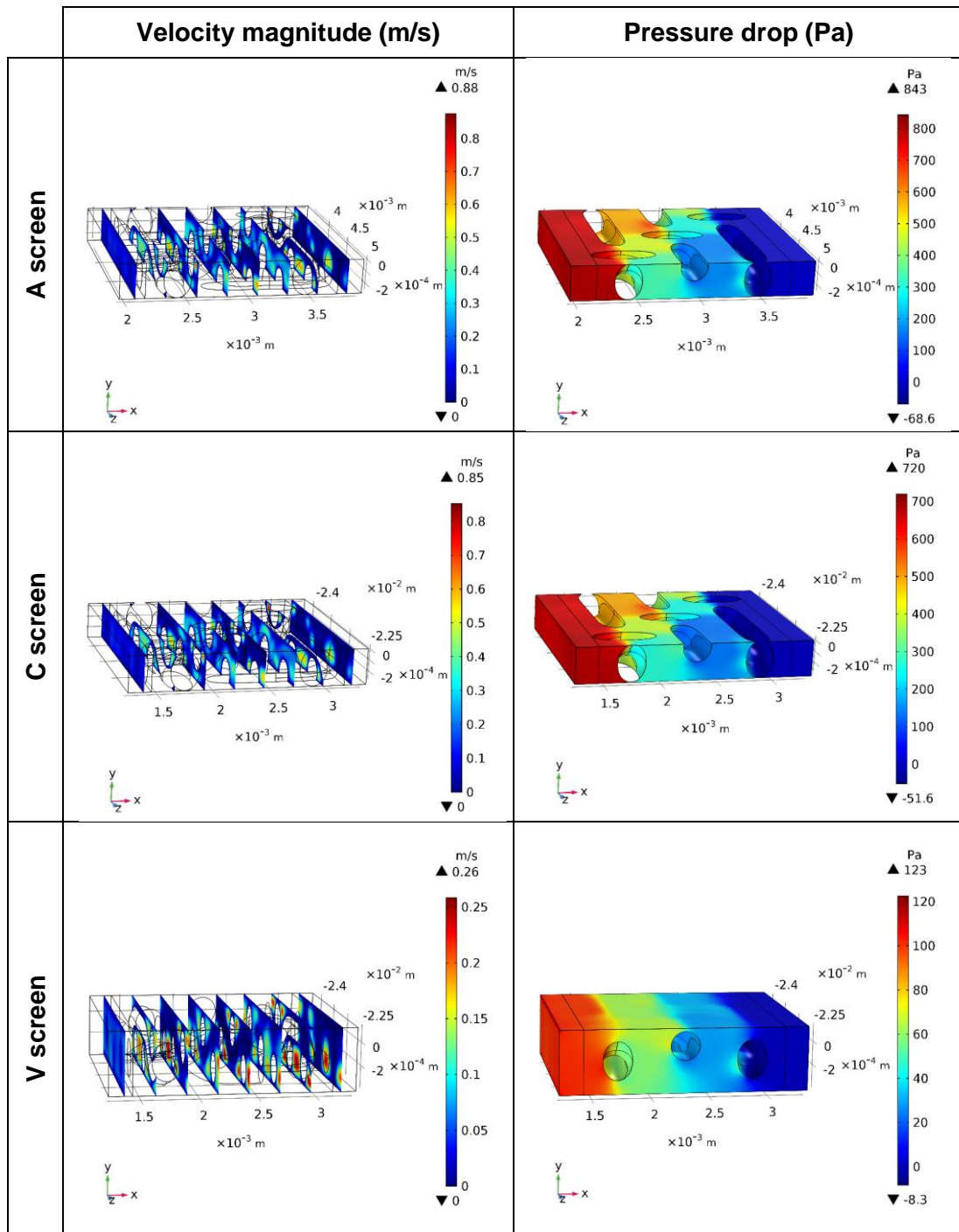
Figure 3.26 CFD simulation results for the three screened unit cells investigated (A, C and V), showing 3D velocity slice plots (left) and 3D volume pressure fields (right), along with minimum and maximum values. Direction of flow is from left to right.
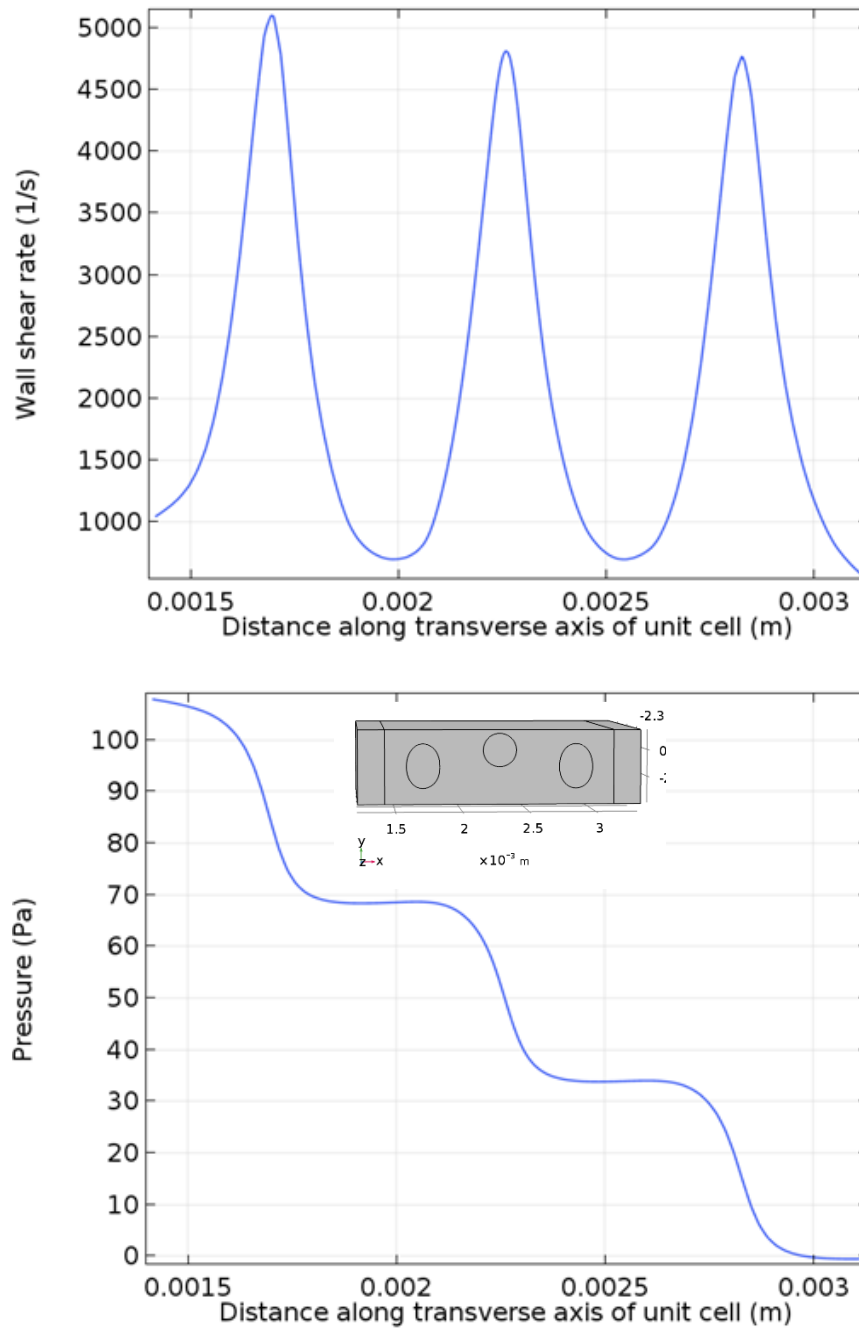
Figure 3.27 Wall shear rate (top) and pressure drop (bottom) profiles for the V screen unit cell (5 LMM, 0.000894 Pa.s). Domains before and after the unit cell were excluded. A general projection operator was used to integrate output parameters along the z-axis for the 1D plots.

By conservation of mass, there is an increase in velocity as the fluid is forced past the fibres and squeezed into the small gaps around them, and thus maximum wall shear rates occur opposite the screen fibre and wall shear rates approach a minimum where the fibres are further away from the wall. Figure 3.26 shows a relatively linear

and uniform pressure drop across the unit cell, and peak pressure drops occurring where the fibres are in close proximity to the wall, followed by a region of constant pressure in between the fibres (Figure 3.27). For a constant feed flow of 5 LMM, the tight A screen had the greatest pressure drop, followed by the C screen and V screen.

For a better understanding of flow pattern within the channel, a cross-sectional plane along the *x-y* axis (Figure 3.28) was visualised in a 2D surface plot. Oscillating vortices and stable recirculation eddies were observed close to the screen fibres, creating flow instabilities at relatively low Reynolds numbers. A steady laminar flow is seen with the formation of stable, circulating eddies (without vortex shedding) due to localised reversal of flow behind the fibres, and an unsteady flow regime at the boundary between free flow and eddies, characterised by moderate instabilities.
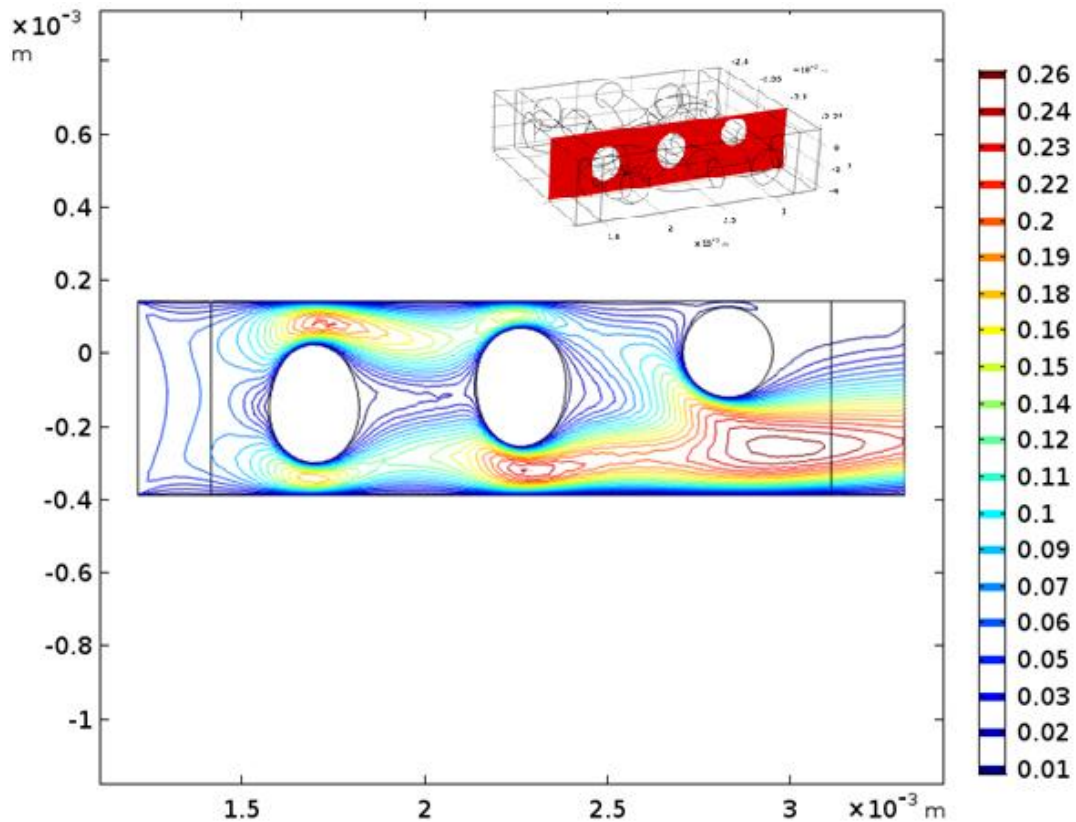
Figure 3.28 2D contour plot of velocity magnitude showing recirculation eddies (5 LMM, 0.000894 Pa.s) for a 2D cross sectional plane taken at *z*=0.24 mm from the V screen unit cell simulation.

As the fluid travels through the screened channel, eddies are formed through conservation of angular momentum, as a result of the altered fluid flow path due to

the presence of obstacles (screen fibres). This change is directly influenced by the screen characteristics such as diameter of the cylindrical fibres and mesh opening (distance between neighbouring interwoven fibres). Thus, tighter screens like the A screen force a much quicker change of direction to induce a faster rotation, which in turn creates stronger eddies that greatly enhance back-transport, albeit at the expense of greater pressure drops. Wall shear rates dominated the shear rates at the surface of the screen fibres, with ratios of wall shear:screen of 1.55, 1.5 and 0.9, for A, C and V screen, respectively.

3.1.4 Conclusions

The geometrical configuration and the resulting hydrodynamics within the system was seen to play a vital role in shear rate profiles at the membrane surface for the USD membrane device and screened channels. The change observed was due to the introduction of secondary and tertiary recirculating flow vortices that allow a greater degree of axial and radial mixing. Focusing on the importance of minimising variations of wall shear rates across the membrane surface to ensure the area-averaged shear rates are a good representative of localised phenomenon, the impact of geometric variations on wall shear profiles was studied.

The primary factor affecting the uniformity of wall shear rates was determined to be the relative position of the edge of the disc with respect to the boundary walls, and varying parameters such as disc angle, clearance between the disc and membrane and disc diameter ideally achieves this movement of the disc to the optimal central position. This optimal position generates uniform shear rate profiles due to a minimum of two circulating regions within the flow regime. Decreasing the disc diameter was observed to have the greatest impact (with relatively constant shear rates over 67% of membrane area), followed by increasing disc angle, α (~46% membrane area with uniform shear rates). Changing the clearance of the disc above the bottom plate, h, had the lowest impact, and there was no significant change in shear rate profiles or flow patterns for clearance beyond 0.75 mm. Furthermore, flow regimes simulated by CFD study were backed up and verified by the work done by Daily and Nece (1960) with regards to the $\sqrt[2]{Re_s}$ values and the expected flow regimes.

The current USD membrane device was deemed to be optimised, and even though a smaller disc diameter of 25 mm presented a uniform wall shear rate profile, the larger rotational speeds required to mimic the crossflow effect generated in large-

scale TFF cassettes and associated shear and/or energy dissipation effects make it an unattractive choice. Furthermore, higher rotational speeds were observed to worsen the uniformity of the wall shear rate distributions radially across the membrane, thus negating any potential improvements in uniformity of wall shear rate profiles.

For the unit cell model, the concept of a repeatable and simplified geometry was compared to the full scale screened channel and was found to be a good representation of the flow, wall shear rate and pressure profiles in the full scale system, provided the flow is fully developed. Wall shear rates were seen to vary periodically and dominated fibre shear rate for all the screens.

Flow within the screened channel was characterised by circulating eddies behind the fibres of the screen, and an accelerated flow and thus shear rates at regions close to the fibres. The velocity magnitudes and pressures across the unit cell were compared for the A, C and V screen cassettes at a flow rate of 5 (L/min)/m^2. Although the A screen was seen to generate the greatest pressure drop, it provided the greatest acceleration effects and instabilities near the boundary and hence the greatest mass transfer compared to the V and C screens. Velocity magnitudes were seen to vary between six and eleven-fold along the transverse axis, with little variation along the other spatial axes.

3.2 Development of wall shear rate and feed channel pressure drop correlations

3.2.1 Introduction

The previous section investigated the flow and shear rate profiles in Pellicon cassettes and the USD membrane device. In this section, CFD simulations will be used to calculate average wall shear rates for both the USD membrane device and screened Pellicon cassettes to establish a robust scale-up model. However, in the previous section for the unit cell model, flow was assumed to be fully developed and the inlet/outlet effects ignored during modelling. In this section, the hydrodynamic inlet and outlet effects were accounted for as they influence the wall shear rates and pressure drops. For a typical TFF cassette like the Pellicon device, the fluid enters through a feed/retentate port on one side of the cassette and is slowly distributed over the channel width, transitioning from plug flow (flat profile) to a fully developed parabolic flow over a certain distance known as fluid entrance length (FEL). In the case of the narrow TFF channels with spacers, the hydrodynamic entrance lengths can be significant (long) depending on the feed flow rates and type of screen used and are expected to be important.
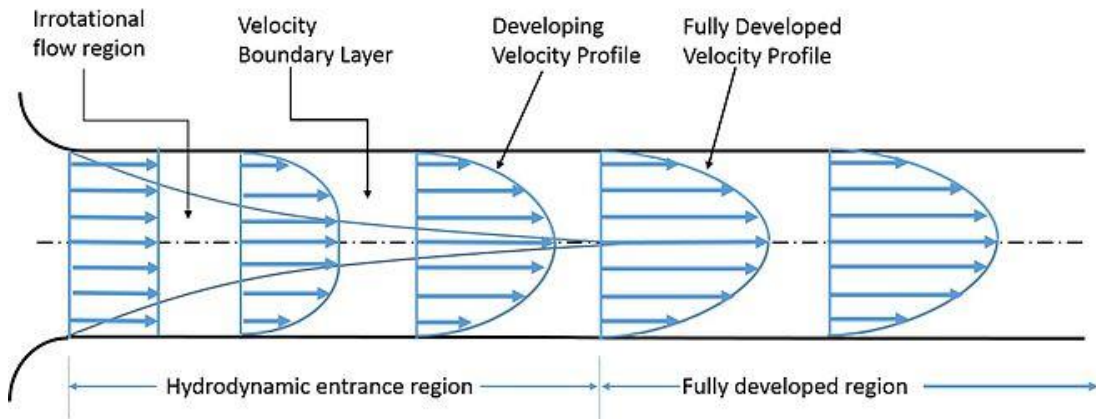
Figure 3.29 Illustration of the typical flow regime observed between two parallel surfaces, showing the transition from developing flow to fully developed flow, after the hydrodynamic entrance region (Çengel and Cimbala, 2014).

Figure 3.29 shows the typical flow regime expected between two parallel plates, as is the case in screened channels. As the flow enters the channel, the no-slip condition on the walls come into play and viscosity effects dominate the boundary layer, where

velocity builds up from zero at the wall to a uniform velocity at the centre of the channel, forming a parabolic profile for laminar flow. Within the hydrodynamic entrance length region or FEL, the flow velocity profile slowly develops and after this length, the velocity profile is said to be fully developed and does not vary in the direction of flow. Similarly, exit effects also exist in channels, where the reverse occurs, and hence needs to be accounted for to determine accurate wall shear rate and pressure drops.

FEL is a function of the Reynolds number and geometry characteristics, and for flow between parallel plates, there have been theoretical correlations developed (Çengel and Cimbala, 2014; Deen, 2011) but they do not apply to flow in screened channels. FEL in the laminar flow regime can be expressed using the dimensionless entrance length number (Bergman and Incropera, 2011), as shown in Equation 3.8.

$$\text{Entrance length number} = \frac{FEL}{d_h} = 0.06 \cdot Re$$

Equation 3.8

where FEL is the fluid entrance length (m) and d_h is the hydraulic diameter of the channel (m).

The aim of this study was to use CFD simulations to evaluate wall shear rates for different viscosities and disc rotational speeds, to develop a specific shear rate correlation for the USD membrane filtration device for both MF and UF membranes, and similarly for the three A, C and V screen devices. These wall shear rate correlations would then form the basis for scale-up to establish equivalent mass transfer rates at both scales. Furthermore, channel pressure drops for the screened channels will also be developed to help predict pressure profiles upon scale-up.

3.2.2 Methods

3.2.2.1 Model development and assumptions

In all simulations, the fluid was assumed to be incompressible and Newtonian, despite most biological solutions ideally exhibiting non-Newtonian behaviour. Majority of the biological solutions, particularly those containing cells, cell debris or macromolecules,

exhibit shear-thinning characteristics and at very high shear rates, the shear viscosity becomes independent of shear rate applied. An independent study was carried out for both unit cells and the 2D-axi model for the USD membrane device, comparing average wall shear rates for both Newtonian and non-Newtonian viscosity models, using the constant K and flow index n (results not shown). Near identical average wall shear rates were obtained in both cases, further validating the use of a Newtonian viscosity model at infinite shear rates for the feed used.

The membrane was assumed to be a smooth surface despite polymers being naturally rough materials. Although the friction coefficients are important in shear drag, especially at the walls, the influence of the friction coefficient of the membrane was considered irrelevant since the membrane type is kept constant upon scaling. Thus, the relative surface roughness of the membrane was not considered since scale-up would be achieved based on equivalent wall shear rates, rendering the surface roughness of the membrane moot. In terms of pressure losses, which is a function of form drag (due to pressure fields because of flow past the feed screen) and skin friction drag (produced as a result of surface roughness of the screen and membrane skin), Lutz (2015) demonstrated that form drag dominated skin friction and thus frictional effects could be safely ignored based on detailed expressions of the two terms and comparison to experimental data.

3.2.2.1.1 USD membrane device

The model used here was identical to that described in section 3.1.2, using the same geometry, SST turbulence model and the optimised mesh characteristics. Since the membrane was considered a part of the solid phase, the effective chamber height therefore varied depending on the type of membrane used (UF membranes are thicker than the MF membranes). Parametric sweeps were performed on the original configuration, varying two parameters, namely, the fluid viscosity, μ, and rotational speed, N. Ranges of values investigated were, μ (Pa.s): {0.000894, 0.001, 0.0012, 0.0015, 0.0018, 0.002, 0.0025, 0.003, 0.004, 0.005, 0.007, 0.01} and N (RPM): {2000, 3000, 4000, 6000, 8000}. The viscosity range selected was believed to be representative of the typical range encountered when working with biological suspensions. Although the power pack of the USD membrane device limited the rotational speeds to discrete values of 4000, 6000 and 8000 RPM only, values outside that range were also included in the study as there were options to change the

settings of the speed control unit, effectively allowing the disc to be set to any desired rotational speed.

A fixed mesh with a total of 503,086 elements was used for all the simulations.

3.2.2.1.2 Screened unit cell

To account for inlet and exit effects for the screened channels and determine FEL, a 1/4th model of the full scale geometry, similar to Pellicon cassettes, without screens, was used (Figure 3.30). A model with screens was not used due to time limitations, and since the flow regime was predominantly laminar in screened channels and FEL is a function of Reynolds number and channel height, a computational domain without screens is a good approximation to determining FEL.
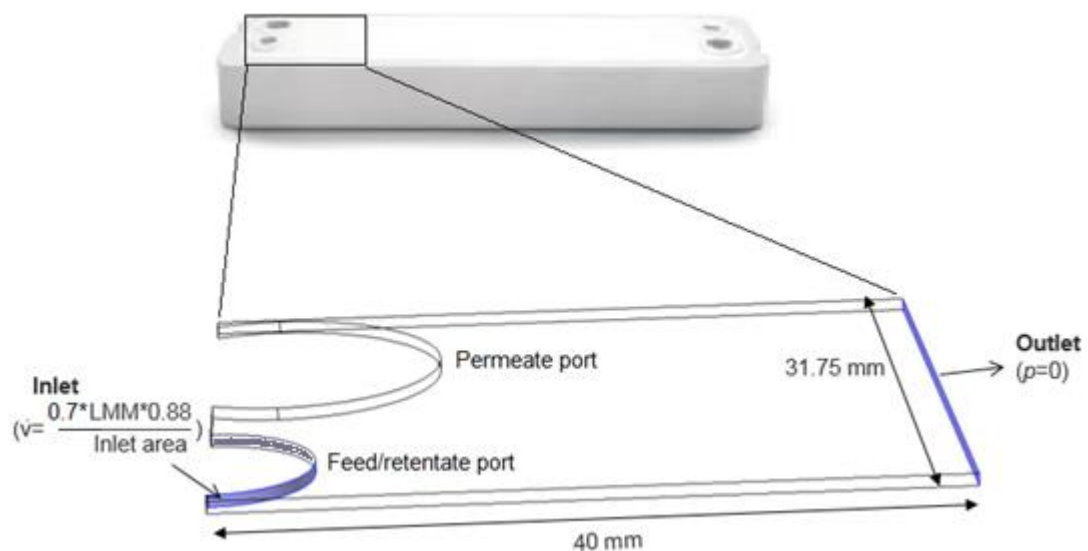
Figure 3.30 3D CFD domain developed based on the single-channel Pellicon 3 micro cassette (88 cm^2) to determine FEL. Image for Pellicon 3 micro adapted from Merck Millipore Pellicon 3 product webpage.

A 4 cm length model was used to determine FEL for a range of channel heights, flow rates and viscosities, and the prescribed inlet velocity was multiplied by a voidage factor of 0.7, to account for volume taken up by screens and determine average inlet velocity to the domain. Following that, parametric sweeps for the unit cells, by varying channel heights, feed flow rates and fluid viscosities, was carried out as shown in Table 3.7. The upper and lower limits for channel heights were determined based on

the thicknesses of Ultracel and Durapore membranes (0.1 mm) and the thicker Biomax membrane (0.3 mm) in Table 2.2, providing an estimate of the maximum allowable protrusion of the screen into the different membranes. A fixed mesh of 180,052 elements was used for all the simulations.

Parameters	A screen	C screen	V screen
Channel height, h (mm)	$0.18<h<0.30$	$0.26<h<0.50$	$0.52<h<0.58$
Feed flow rate (LMM)	3-8	4-13	5-35
Fluid viscosity (Pa.s)	0.000894, 0.001, 0.0012, 0.0015, 0.0018, 0.002, 0.0025, 0.003, 0.004, 0.005, 0.007, 0.01		

Table 3.7 Summary of parametric studies performed for the three different unit cells.

Assumptions for the model (plus those previously mentioned for the unit cell) included modelled inlet/outlet ports to be the same size as the average channel height used (excluding extra compression effects at the ports), a uniform twill weave sequence across the full system and constant channel height along the direction of flow. The model also assumes an unobstructed feed port and relatively 'clean' screens.

3.2.3   Results and discussion

3.2.3.1   Wall shear rate correlations

3.2.3.1.1   USD membrane device

Average shear rates at the membrane surface can be determined by performing a *Surface Average* calculation during post processing in COMSOL, which determines the average of the surface defined in the *r-z* plane. However, the equivalent surface integral (in 3D) was calculated by selecting the '*compute volume integral'* option. The surface integral is the more accurate representation as it includes the correct formulation of the integration by providing the correct weighting with respect to *r*, while the former solution gives the cross-sectional value without the $2\pi r$ weighting, which is a result of the Jacobian associated with the cylindrical polar coordinate system (Figure 3.31). Figure 3.32 shows the average wall shear rates versus feed flow rate and viscosity relationships generated using the CFD results for a typical MF and UF membrane, respectively.

Figure 3.31 2D-axi model (left) showing the boundary (in blue) used for average wall shear rate determination and a 3D revolution plot (right) generated from the 2D solution.
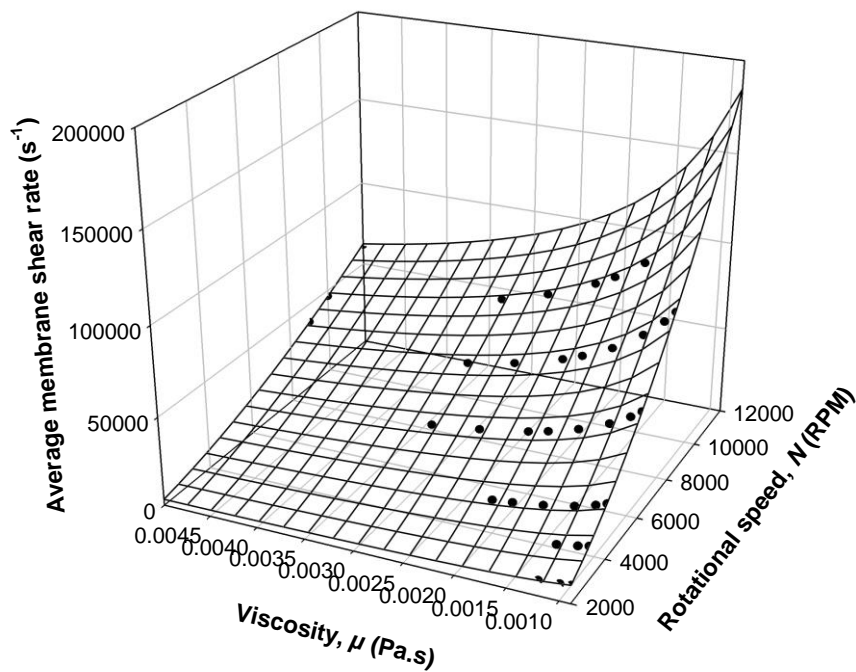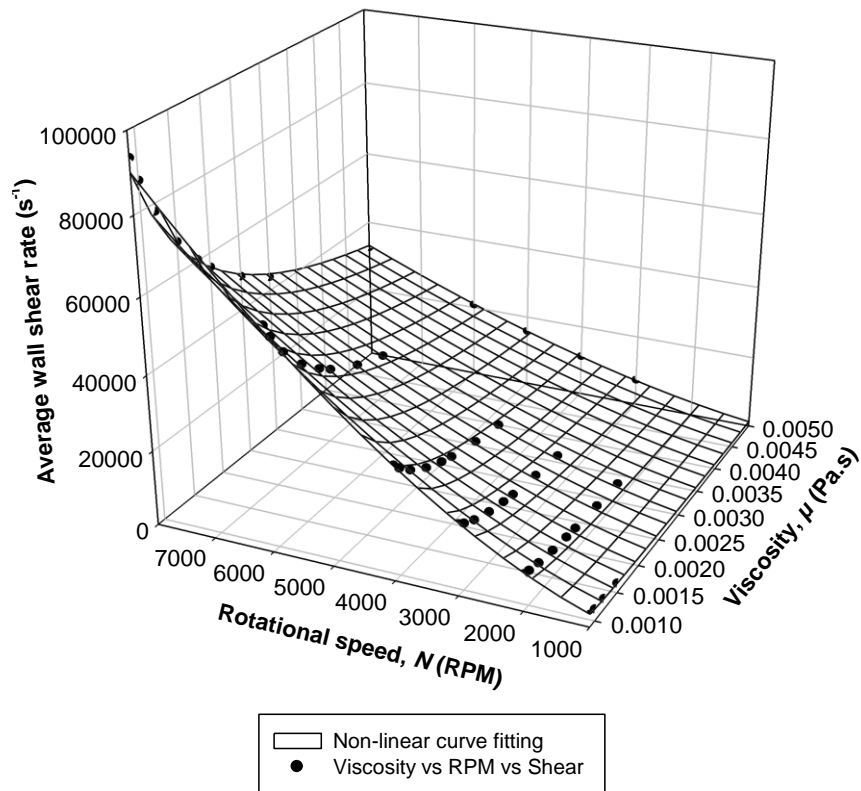
Figure 3.32 3D mesh plots of average wall shear rate as a function of fluid viscosity and rotational speed for MF membranes (top) and UF membranes (bottom). Non-linear curve fitting was done using sum of least squares method, with $R^2 = 0.99$, $\Sigma(x_i - x)^2 = 0.019$ for MF and 0.021 for UF.

The characteristic wall shear rate to be used the scaling parameter was defined as the integral surface area along the membrane radius for the USD membrane device. Using the sum of least squares method, non-linear fits were performed, resulting in the following shear rate correlations for MF (0.1 mm) and UF (0.3 mm) membranes:

$$\bar{\gamma}_{w_{USD-MF}} = 1.046 \text{x} 10^{-3} \cdot \mu^{-0.581} \cdot N^{1.579}$$

Equation 3.9

$$\bar{\gamma}_{w_{USD-UF}} = 5.194 \text{x} 10^{-4} \cdot \mu^{-0.630} \cdot N^{1.626}$$

Equation 3.10

where $\bar{\gamma}_w$ is the average wall shear rate (s^{-1}), μ is the dynamic viscosity of fluid (Pa.s) and N is the rotational speed (RPM) of the disc in the USD device.

As expected, the average wall shear rates for the thicker UF membranes have a stronger dependence on fluid viscosity and rotational speed, since the membrane is closer to the disc. The form of the CFD-derived Equation 3.9 and Equation 3.10 is comparable to the empirical equations developed by several authors for wall shear stresses in the laminar regime, namely, Schiele (1979) and Bouzerar et al. (2000a), described by Equation 3.11:

$$\tau_{w,\text{laminar}} = C \cdot \rho \cdot v^{0.5} \cdot (k' \omega)^{1.5} \cdot r$$

Equation 3.11

where $\tau_{w,\text{laminar}}$ is the wall shear stress (Pa), C is a dimensionless geometry-related constant (Schiele (1979): 1.81, Bouzerar et al. (2000a): 0.77), ρ is the density of the fluid (kg/m^3), k' is an empirical velocity entrainment factor (dimensionless), ω is the angular velocity (rad/s), r is the radius of the disc (m), and v is the kinematic viscosity (m^2/s).

Wall shear rate (γ_w), assuming Newtonian behaviour, can then be calculated using:

$$\gamma_w = \frac{\tau_{w,laminar}}{\mu}$$

<div align="right">**Equation 3.12**</div>

For the original geometry, the value of *k'* was estimated to be 0.35, from the CFD data generated in section 3.1.3.2. Using values of ρ=997 kg/m^3, μ=8.94x10^{-4} Pa.s, v=8.97 m^2/s, *N*=4000 RPM (66.6 Hz), *r*=0.0175 m in Equation 3.11:

Schiele (1979), *C* = 1.81: γ_w = <u>59,380 s^{-1}</u>

Bouzerar et al. (2000a), *C* = 0.77: γ_w = <u>25,261 s^{-1}</u>

Equation 3.9: γ_w = <u>30,359 s^{-1}</u>

The analytical model derived by Schiele (1979) outputs wall shear rates significantly higher than the average shear rates calculated by CFD simulations, while using the coefficient 0.77 by Bouzerar et al. (2000a) the wall shear rate value was closer to that calculated using CFD correlation. Furthermore, work done by Hwang and Wu (2015) confirmed that shear rates generated in RDF systems typically range between 1x10^4-1x10^5 s^{-1} for rotational speeds ranging from 1000 to 5000 RPM.

3.2.3.1.2 Screened unit cell

Area-averaged wall shear rates were computed using separate average component couplings (aveop1(spf.sr)) on the two boundaries, top and bottom of the unit cell (Figure 3.33).
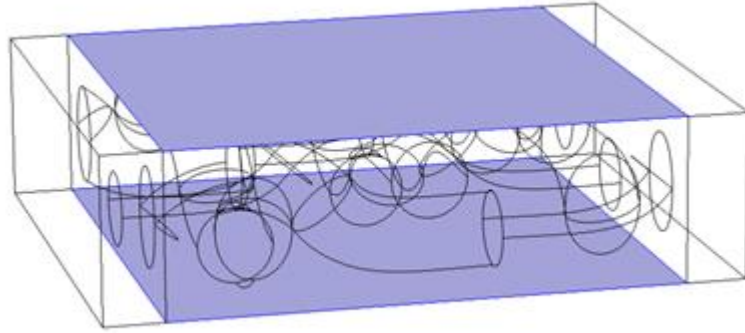
Figure 3.33 3D plot showing the boundaries selected, in blue, used to compute average wall shear rates for the unit cell model.

Results for the FEL determination are plotted in Figure 3.34; the entrance length was seen to increase with Reynolds number, but all plots showed a similar profile, transitioning from a region of non-uniform flow with higher velocities to a fully developed region with constant velocity downstream.
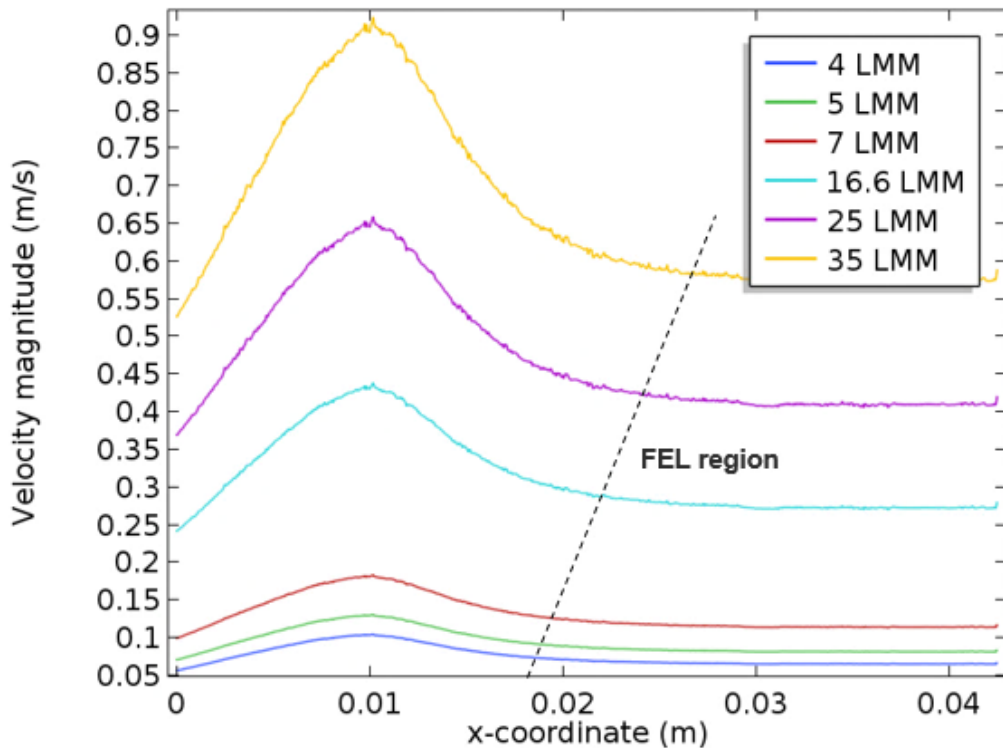
Figure 3.34 1D general projection plot of velocity magnitude in the direction of flow for the 3D FEL model (4 cm length), integrated with respect to the z-axis along the x-axis.

From the CFD simulation data, the FEL was expressed as a function of average feed channel height, fluid viscosity and feed flow rate (Equation 3.13), while the average velocity in the FEL region was expressed as a function of feed flow rate and channel height (Equation 3.14):

$$FEL = 0.0798 \cdot \left(\frac{Re}{h} \right)^{0.472}$$

Equation 3.13

$$\overline{V}_{FEL} = 0.000439 \cdot \left(\frac{Q_F}{h} \right) + 0.0226$$

Equation 3.14

where $\overline{V}_{FEL}$ is the average flow velocity magnitude in the FEL region (m/s), Q_F is the feed flow rate (LMM) and h is the average feed channel height (m).

The entrance and exit lengths were calculated using Reynolds number for the unit cells:

$$Re_{unit\ cell} = \frac{\rho \cdot u \cdot \left[\dfrac{2hw}{h+w} \right]}{\mu}$$

Equation 3.15

where Q_F is the feed flow rate (LMM), μ is the fluid viscosity (Pa.s), h is the channel height (m), w is the width of the channel (m), u is the average domain velocity from unit cell simulation data (m/s) at a given feed flow rate and h (m), and ρ is the density of the fluid (kg/m^3).

Average wall shear rates were then calculated using Equation 3.16.

$$\overline{\gamma}_{w\ \text{screened channel}} = \frac{\overline{\gamma}_{\text{unit cell, feed flow rate}}}{L - \left[2 \cdot FEL\right]} + \frac{\overline{\gamma}_{\text{unit cell, } \overline{v}_{FEL}}}{2 \cdot FEL}$$

<div align="right">**Equation 3.16**</div>

where $\overline{\gamma}_{w\text{screened channel}}$ is the weighted-average wall shear rate (s^{-1}) for a given screened cassette with average feed channel height, h (m) and channel length, L (m), operated at feed flow rate, Q (LMM). The FEL was multiplied by a factor of 2 to account for both the entrance and exit effects (assuming similar lengths for both), and 0.16 m is the length of the channel, measured from the feed port to the retentate port for Pellicon cassettes. The equation provides appropriate weighting for the wall shear rates, as the entrance and exit region only account for a part of the total channel length, and the flow is fully developed for the majority remainder of the channel length.

Equation 3.16 was used to derive the following average wall shear correlations for A, C and V screens (raw data shown in Appendix 10.2):

$$\overline{\gamma}_{w\text{A screen}} (0.18 < h < 0.32) = 126.5 \cdot h^{1.493} \cdot Q_F^{(-0.269 \cdot h) + 1.211} \cdot \mu_F^{(2.043 \cdot h^2) - (0.888 \cdot h) - 0.0204}$$

$$\overline{\gamma}_{w\text{C screen}} (0.26 < h < 0.50) = 101.9 \cdot h^{-0.72} \cdot Q_F^{(-0.521 \cdot h) + 1.428} \cdot \mu_F^{(0.433 \cdot h) - 0.356}$$

$$\overline{\gamma}_{w\text{V screen}} (0.52 < h < 0.58) = \left[(2359 \cdot h^2) - (2516.1 \cdot h) + 733.2\right]$$
$$\cdot Q_F^{(-4.849 \cdot h^2) + (4.855 \cdot h) + 0.0569} \cdot \mu_F^{(4.784 \cdot h^2) - (4.895 \cdot h) + 1.006}$$

<div align="right">**Equation 3.17**</div>

where γ_w, h, Q_F and μ_F represent average wall shear rate (s^{-1}), average feed channel height (mm), feed flow rate (LMM) and viscosity of the feed solution (Pa.s), respectively.

The main advantage of CFD simulation is the capability of modelling entrance and exit regions and associated effects, and in the case of screened channels, the FEL could be significant. The entrance/exit effects and lengths are directly proportional to the feed flow rate and so predicted wall shear rates for screened channel using

analytical/empirical equations that do not account for such effects, would only be relatively accurate at the lower limits of operating flow rates.

3.2.3.2 Feed channel pressure drop correlation

As in section 3.2.3.1, average component couplings of the inlet and outlet boundaries (highlighted blue in Figure 3.35) were used to compute inlet and outlet pressures and determine the channel pressure drop, dP, over the unit cell, which was then linearly scaled-up to the full length of the channel using Equation 3.18:

$$dP_{channel} = \left(\frac{dP}{dx} \right)_{unit\,cell} \cdot L$$

Equation 3.18

where dP is the pressure drop across the unit cell (P_{in}-P_{out}), dx is the length of the unit cell, and L is the length of the channel (0.16 m).
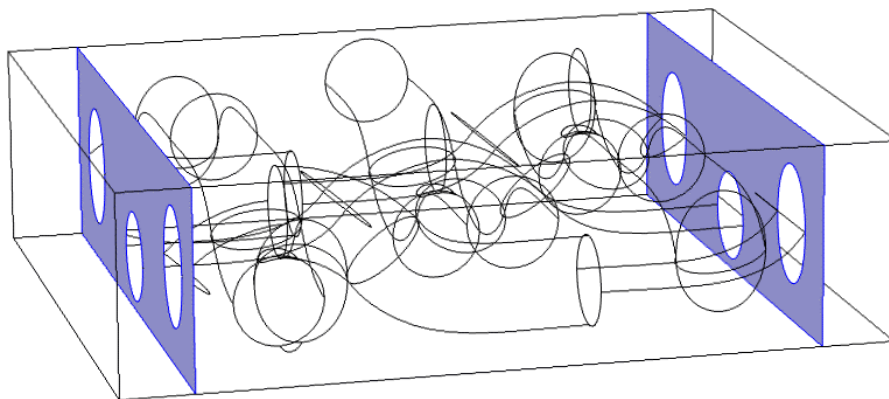
Figure 3.35 3D model for V screen unit cell highlighting regions (in blue) where the average component couplings were performed to calculate channel pressure drops.

Since the unit cell was taken in the cross-section normal to the flow and the fact that the flow velocity once fully developed, is identical to the full system, the pressure drop scales with the length in the flow direction (assuming the flow is incompressible and has a constant dP/dx), which translates to a relatively uniform and linear pressure drop in the direction of flow only. The model does not consider narrowing of the feed/retentate port due to added compression effects or blockage, which would lead

to under-predicted channel pressure drops. Equation 3.13 and Equation 3.14 were used to determine the FEL and subsequently used to develop the following feed channel pressure drop correlations for the three Pellicon cassettes:

$$dP_{A\ screen}\ (0.18 < h < 0.32) = \left[(3.525 \cdot h^{-2.763} \cdot Q_F) + (0.194 \cdot h^{-3.023}) \right] \cdot \mu_F + \left[0.0004 \cdot h^{-2.589} \cdot Q_F^{(-0.255 \cdot h) + 2.147} \right]$$

$$dP_{C\ screen}\ (0.26 < h < 0.50) = \left[(2.873 \cdot h^{-2.983} \cdot Q_F) + (0.292 \cdot h^{-4.12}) \right] \cdot \mu_F + \left[0.164 \cdot e^{-8.958 \cdot h} \cdot Q_F^{(-0.428 \cdot h) + 2.163} \right]$$

$$dP_{V\ screen}\ (0.52 < h < 0.58) = \left[(1.381 \cdot h^{-4.091} \cdot Q_F) + (240.6 \cdot h^2) - (250.3 \cdot h) + 61.678 \right] \cdot \mu_F$$
$$+ \left[0.00001 \cdot h^{-8.908} \cdot Q_F^{(4.762 \cdot h^2) - (5.719 \cdot h) + 3.592} \right]$$

Equation 3.19

where, dP, h, Q_F and μ_F represent feed channel pressure drop (bar), average feed channel height (mm), feed flow rate (LMM) and viscosity of the feed solution (Pa.s) respectively.

3.2.3.3 CFD verification studies

A comparison of computational results against experimental data is usually needed to validate the CFD models. This section looks at various experimental work carried out to validate and verify the model simulations, assessing the accuracy of the simulated results compared to the experimental data and justifications for the model assumptions used throughout the CFD modelling.

3.2.3.3.1 Drag force versus Reynolds number for the USD membrane device

2D PIV studies were not performed because of the complex curvature of the Perspex housing for the USD membrane device, time limitations and lack of appropriate camera/lens with a small enough dt to accurately capture and sufficiently resolve the timescales. Instead, the torque exerted on the rotating disc of the USD membrane device was measured using water for a range of rotational speeds, with the permeate valve closed off. Eagle Tree eLogger v10.69 was used to log the real time torque data for the USD membrane device during operation. Figure 3.36 compares the experimental and simulated drag force as a function of Reynolds number.
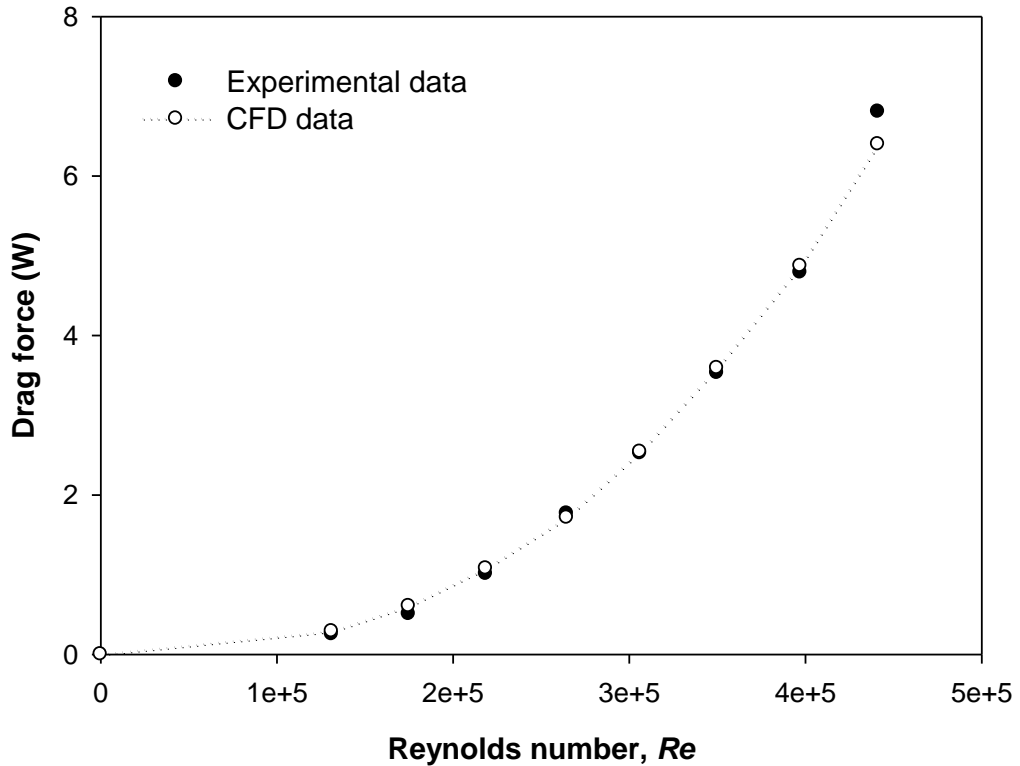
Figure 3.36 Drag force on disc of the USD membrane device versus Reynolds number. Experiments and CFD simulations were done using water.

The rotating disc experiences a drag force moving through the rotating body of water, and the simulated drag force for the USD device was computed from the velocity gradients at the boundary of the disc wall using COMSOL post-processing operations. Experimental and CFD drag force had excellent agreement, thus validating the CFD results, mesh quality and the accuracy of the SST formulation to model the physics in the USD membrane device.

3.2.3.3.2 2D-PIV

The CFD solutions and meshing strategy used to model screened channels was verified and validated by comparing CFD simulated and 2D PIV experimental velocity profiles. 2D PIV was performed using methods described in section 2.2.18 and the results are shown in Figure 3.37.
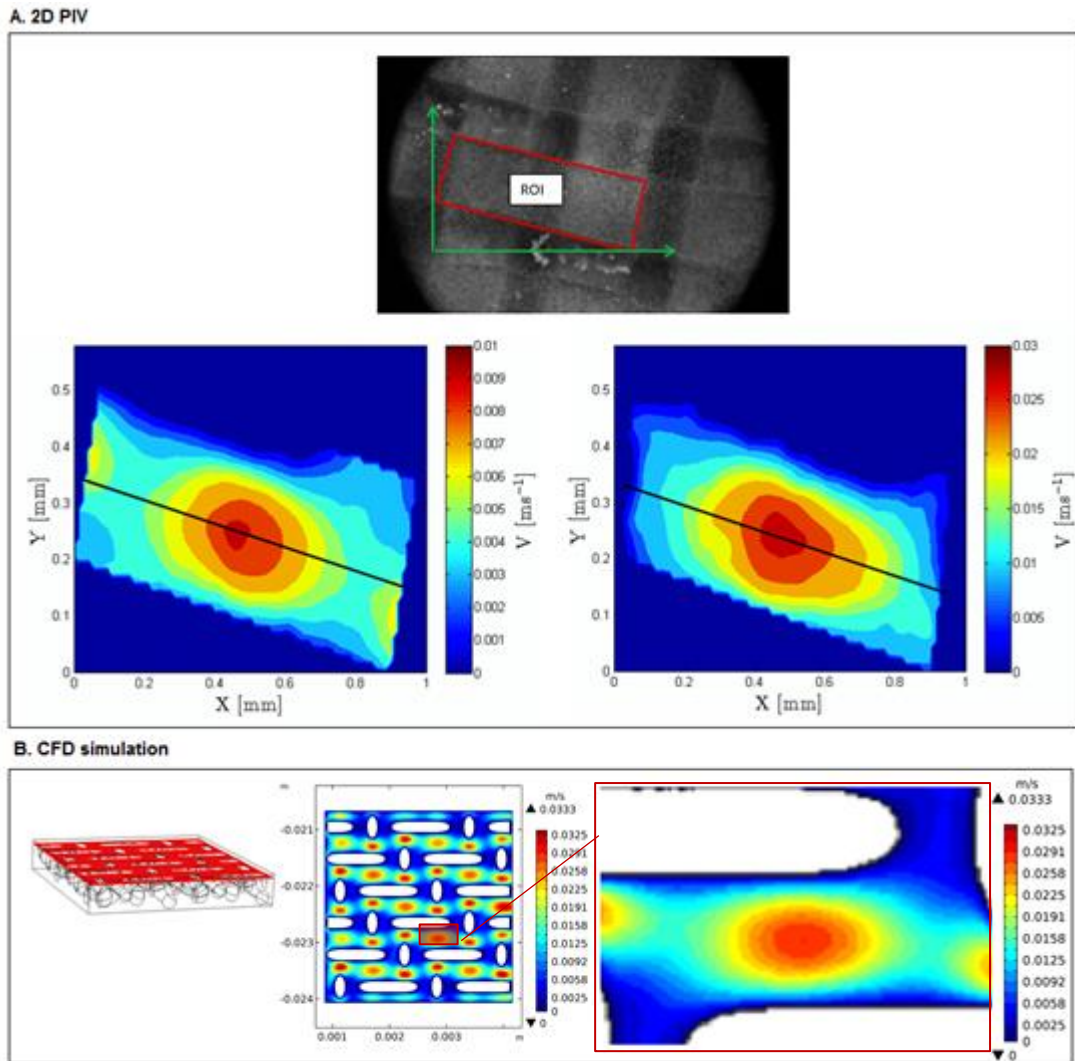
Figure 3.37 2D-PIV results. A: Snapshot of the camera view (top) highlighting the region of interest (ROI), and processed PIV velocity data for fully developed flow as 2D surface plots for pump flow rates of 2 mL/min (left) and 5 mL/min (right). B: CFD simulated velocity plot for 5 mL/min flow rate.

Figure 3.37 showed very similar velocity profiles for developed flow in both CFD simulated data and PIV experiments. In order to perform a quantitative comparison between the experimental and simulated CFD data, the respective velocity profiles along a 1D cut-line (the black line in Figure 3.37) for flow rates of 2 mL/min and 5 mL/min were plotted and compared in Figure 3.38.

174
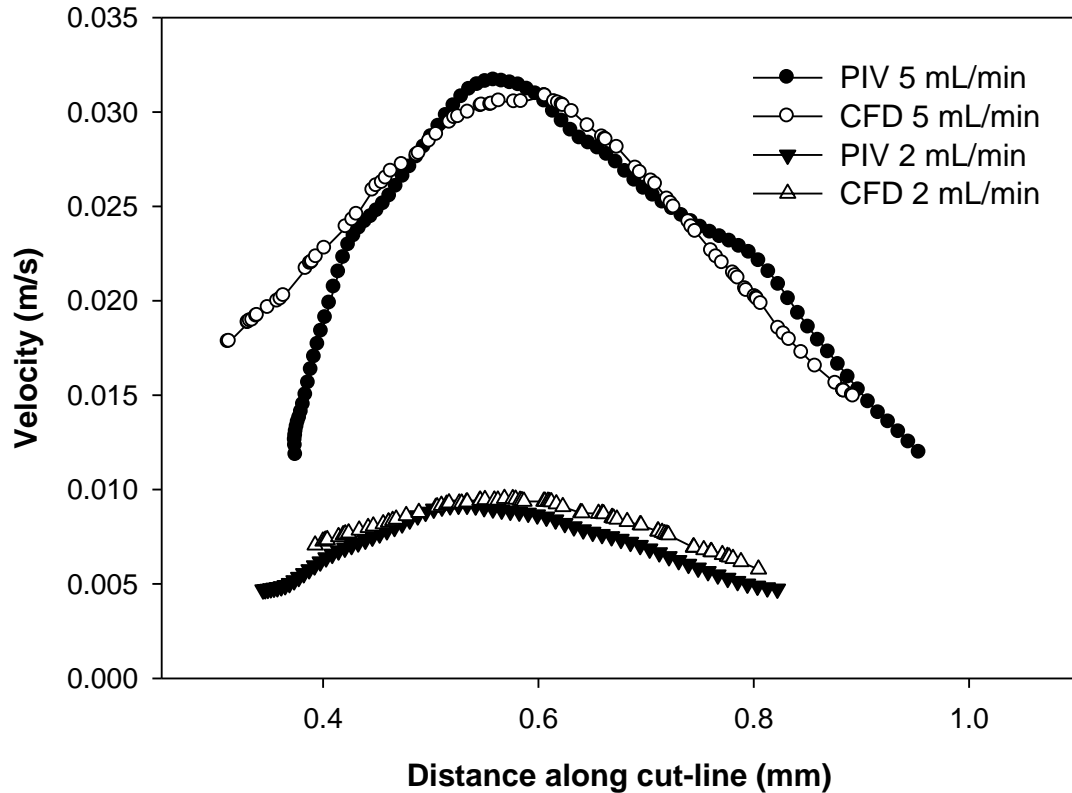
Figure 3.38 Velocity magnitude versus distance along the *x-z* cut-line at a height of 0.1 mm from the top of the unit cell, comparing CFD and experimental velocities at the flow rates tested (2 mL/min and 5 mL/min).

From Figure 3.38, a good match was seen between the experimental and CFD simulated velocities along the cut-line, with the peak velocity magnitudes nearly identical at both flow rates, within experimental errors. The velocity magnitude profile at the lower flow rate of 2 mL/min showed less divergence, whereas the difference between the simulated CFD and experimental PIV velocities were significantly larger at 5 mL/min. This could be potentially attributed to the assumption of a perfectly uniform twill weave pattern, mesh opening and alignment of fibres that provide constant flow attack angles. This is not the case for Pellicon cassettes, which have manufacturing tolerances and thus a uniform, repeatable pattern as the unit cell is not practically achievable.

Figure 3.37-A shows a still of the video during PIV measurements, where uneven mesh openings amongst neighbouring fibres and a non-uniform alignment and weave of the fibres in the test region used to carry out PIV study is observed. The PIV measurements tend to be very sensitive to the algorithms used for data processing

and parameters such as calibration factors and mesh size used, along with inherent limitations of the equipment and resolving power. Furthermore, a viscosity of 0.001 Pa.s (water) was assumed for the CFD simulations, but the test fluid for the PIV experiments was seeded with tracer particles, and the viscosity of the solution could be slightly higher as a result. Discrepancies between PIV data and CFD simulations tend to be magnified at higher flow rates, where flow velocities are more sensitive to the screen characteristics and sensitivity of the measurement methods. Thus, considering the potential limitations discussed previously in this section, the 2D PIV was deemed to have successfully verified the CFD model simulations.

3.2.3.3.3 Crossflow rate versus feed channel pressure drop tests

As a further verification study, feed flow rate versus pressure drop tests were carried out with water using Pellicon cassettes and the Sartoflow Advanced, by varying the feed flow rate starting from a maximum and recording the corresponding feed pressure drops with the permeate fully closed and retentate valve fully open. The corresponding feed channel pressure drops were recorded and plotted in Figure 3.39, along with predicted data generated using CFD pressure drop models (Equation 3.19). The average channel heights used in Equation 3.19 were determined using the feed channel hydraulic characterisation correlation (Equation 4.4), discussed in section 4.3.3.2.3.
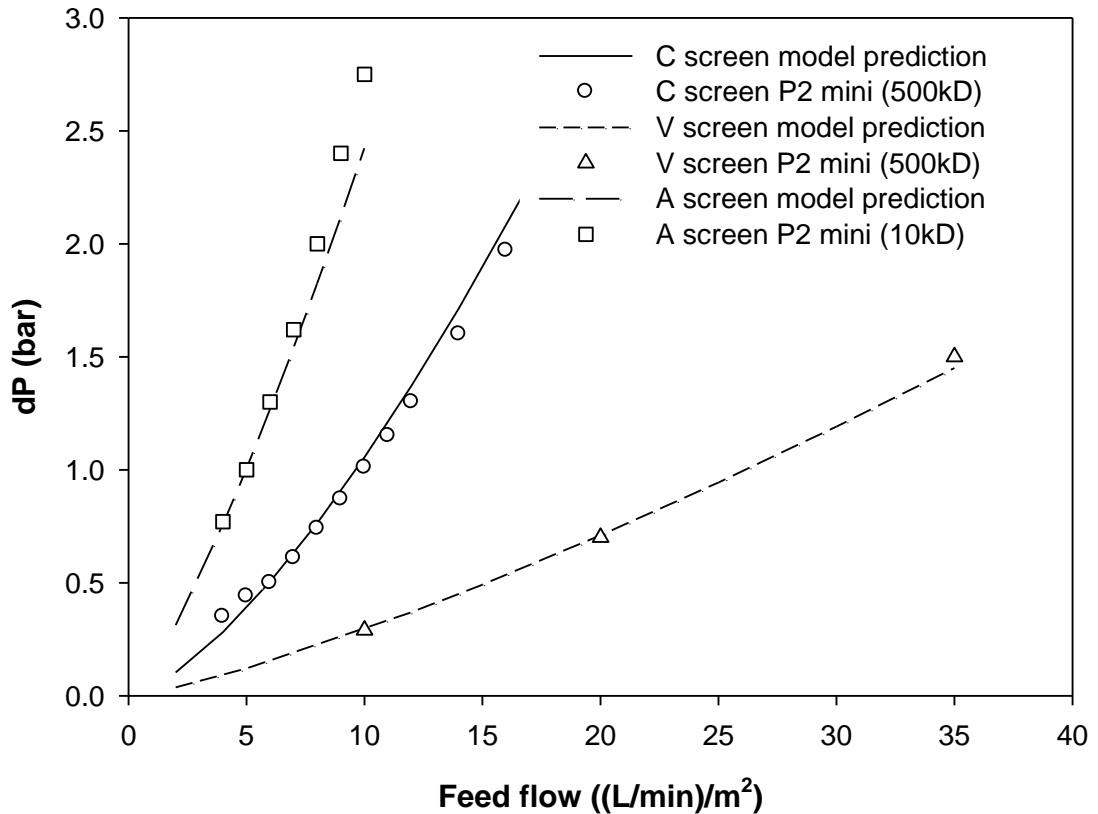
Figure 3.39 Comparison of crossflow versus dP test results for experimental Pellicon data (symbols) versus CFD predicted data (lines).

The experimental data for all three Pellicon cassettes were in excellent agreement with the CFD simulated data within experimental error. The A screen showed some divergence at higher flow rates (beyond the recommended operating flow rates), possibly because the flow transitioned into the turbulent regime and thus pressure drops increased further with feed flow rate, as well as significant system pressure losses. This verification experiment was of paramount importance, as many of the assumptions listed for the unit cell modelling and simulation are not truly the case with TFF cassettes in practice, where non-uniformities in the mesh sequence and alignment, variations in effective membrane heights along the channel length and coefficient of friction of the membrane skin exist and can contribute to significant discrepancies between simulated and experimental data. However, this was observed not to be the case based on the near perfect match between the predicted and experimental pressure drops, primarily due to the averaging effect over the full length of the channel and across multiple channels for the larger surface area cassettes, proving that the unit cell model was a good representation of the entire

screen in the feed channel and thus provided an accurate approximation of the flow velocities and pressure fields in the feed channel(s).

3.2.4 Conclusions

Accurate shear rate correlations need to be used when using shear rate as a scale-up parameter. Existing empirical and analytical models for RDF systems cannot be used due to differences in geometry between the traditional RDF systems and the USD membrane filtration device. Likewise, a lack of well-defined wall shear rate and pressure drop equations applicable to Pellicon cassettes warranted the need for a quick and robust methodology to accurately evaluate the parameters that are essential for a shear rate-based scaling.

Average wall shear rate correlations for both USD and Pellicon screened cassettes, along with feed channel pressure drop correlations for the latter, were developed as functions of flow rate (Pellicon cassette) or disc rotational speed (USD device), and fluid viscosity using the commercial CFD package, COMSOL. Wall shear rate correlations for the USD device developed using CFD was also compared to existing analytical equations, which either was found to under or over-predict wall shear rates. Furthermore, the concept of hydrodynamic entrance and exit regions was discussed and model correlations were developed, accounting for entrance and exit effects, which tend to influence the calculated wall shear rate and pressure drops. The CFD modelling results for both the USD device and Pellicon cassettes (unit cell) were successfully verified by comparing simulated results against experimental data.

Combining the wall shear rate correlations for the USD membrane device and Pellicon cassettes, an explicit relationship between the disc rotational speed in the USD device and feed flow rates (crossflow velocity) in the Pellicon cassettes were obtained based on equivalent average wall shear rates, which will be used in the next chapter to formulate the scale-up methodology and prediction model.

4 Formulation of Ultra Scale-Down methodology and prediction model for tangential flow filtration scale-up

4.1 Introduction

Development of USD system and methodology for tangential flow filtration offers many advantages, with the most useful point of USD applications in the early process development stages, where financial resources, lack of access to capital equipment and limited availability of feed stock renders extensive large scale experiments impractical and unfeasible. A robust and full scalable USD system would allow processing challenges to be solved much earlier, and combined with a DoE (design-of-experiments) methodology, generate representative data on which full scale process decisions can be based, to help develop a fully validated design space such that any process changes within this space is allowed without the need for regulatory approvals. Furthermore, since USD models aim to mimic and recreate the fundamental principles and conditions of large scale processes, a better process understanding can be derived at a fraction of the time, materials and costs. The processed feed material from a USD membrane filtration operation should be similar to that produced in a full-scale process, and so can be used as feed material for the subsequent USD downstream purification operations, allowing whole bioprocess optimisation by considering trade-offs between different unit operations, with respect to process feasibility and economics.

In the previous chapter, wall shear rate was determined to be the scale-up parameter and equivalent average wall shear rates to be the basis for non-linear scale-up from the USD membrane device to TFF cassettes at large scale. The use of equivalent average wall shear rates to scale-up tangential flow filtration from scale-down units have been demonstrated previously (Eardley-Patel, 2008; Guo et al., 2016; Ma et al., 2010). However, the large scale data looked different to data obtained from scale-down experiments due to the inherent resistance and nature of the system at large scale, which tends to skew the performance upon scale-up. The impact of different hydraulic resistances was discussed and accounted for by making TMP adjustments during scale-up.

Upon scale-up, the system itself and associated ancillary equipment are also scaled-up, which is more important for non-linear scale-up, where additional variables that

influence flow and pressure drops are introduced at large scale because of geometric dissimilarities between the two scales. These factors need to be considered and well characterised as they directly affect scale-up performance. The geometric complexity of screened channels, like the Pellicon cassettes, further compound scaling issues during non-linear scaling due to the presence of screens in the feed and permeate channels. These effects are an unavoidable consequence of the hydraulics of the screened cassettes and system components such as flow manifolds, valves, piping, pressure sensors, etc. that contribute to the overall measured pressure drops in tangential flow filtration, leading to discrepancies between expected and observed flux performances despite scaling up at constant TMP. This was highlighted in the discrepancies between measured NWP values across membrane formats, with reported NWP values of large scale cassettes being significantly smaller than those using the small scale devices (Chandler and Zydney, 2004; Eardley-Patel, 2008).

A perfect match between scales is rarely achieved upon scale-up and can be attributed to unavoidable and nuanced differences across the two scales which are not directly related to tangential flow filtration yet have a measurable impact on the overall process performance. Such differences along with other non-TFF related issues need to be adequately characterised and quantified using well-justified correction factors and scale-dependent transfer functions to enable the accurate prediction of tangential flow filtration processes at scale.

The specific aims of this chapter are to:

- Investigate and characterise phenomenon/effects associated with screened TFF cassettes at large scale, not present at small scale,
- Characterise non-TFF resistances such as system resistance and screen resistance,
- Incorporate scale and system correction factors, channel pressure drop correlations and the USD model into a robust and non-linear scale-up and prediction protocol.

4.2 Non-tangential flow filtration scale-up factors

A scale-down model is typically expected to generate TMP values that are close to the TMP measured for screened cassettes at the same permeate flux. However, this may not be the case, especially for a geometrically dissimilar scale-down device such as the USD membrane device. The reasons for this, along with observed differences in pressure drops using Pellicon cassettes at large scale are considered and discussed in section 4.2.1.

4.2.1 Differences in measured NWP

One of the key observations when comparing performances across scales is the difference in measured normalised water permeability (NWP). Discrepancies between resistances of flat-sheet discs and TFF cassettes of the same membrane material and pore size, up to factors of 20-fold, has been previously reported in literature (Chandler and Zydney, 2006; Eardley-Patel, 2008; Guo et al., 2016). In all cases, the NWP of TFF cassettes were lower than the permeability values for flat-sheet membrane discs. Table 4.1 presents the experimental NWP values at 25 °C for various membranes across different membrane formats.

Membrane	NWP (LMH/bar) @ 25 °C		
	Flat sheet disc (47 mm)	Open channel (Prostak) ± 25%[6]	Pellicon screened cassette
PLCC (5 kDa)	14.5	14.5	13.1
PLGC (10 kDa)	71.1	34.8	39.9
PLTK (30 kDa)	391.9	275.5	224.8
Biomax (500 kDa)	5252	743.1	780.2
Durapore VV (0.22 µm)	7759	742.9	915.9
Durapore DV (0.65 µm)	54200	1854	2364.1

Table 4.1 NWP comparison of flat sheet membranes and TFF modules (Pellicon and Prostak), at 0.7 bar TMP and 5 LMM feed flow/0.7 bar TMP for the disc and TFF cassettes respectively.

---

[6] Prostak maintenance guide (1991)

Even though identical membranes were used, the measured 'apparent' NWP values of the cassette format were consistently a lot lower compared to the membrane disc permeabilities. For instance, both the open Prostak and Pellicon screened cassettes had similar permeabilities for a given membrane, and both significantly smaller than the respective values for the membrane disc. Furthermore, the type of screen in the cassette did not have any significant impact on the NWP values. The observed differences in NWP can be attributed to the difference in membrane format and the resulting flow paths.

The primary characteristic of tangential flow filtration is the tangential flow of the feed liquid, which creates a crossflow effect thereby sweeping the retentate side of the membrane clean and permitting relatively larger fluxes through the membrane. However, this crossflow over the membrane has an accompanying frictional pressure drop moving from feed to the retentate, which is in the case of screened channels is significantly higher; this pressure drop is not used to drive any net flux through the membrane and is an unavoidable consequence of the inherent nature of tangential flow filtration. The overall channel pressure drop in tangential flow filtration can thus be divided into two components, namely the tangential pressure in the direction of flow drop due to frictional resistances, and the forward pressure that directly provides the driving force for filtration and contributes to the pressure-derived flux normal to the flow direction. Since average cassette TMP is typically used to characterise the total driving force in tangential flow filtration, both the pressure drop components are invariably included in the TMP value that is calculated based on the average pressure drop across the cassette rather than the actual pressure across the membrane, thereby reducing the calculated NWP value for TFF cassettes.

In the case of membrane discs like those used in the USD membrane device, the flow is in dead-end mode and so the true TMP across the membrane is equal to the forward pressure applied on the membrane, thus returning the true membrane permeability value. In the case of TFF filters, even if the flow is dead-ended, *i.e.*, retentate valve completely shut off, there is still a flow, albeit reduced, across the channel until it reaches the closed retentate side and is then forced through the membrane as permeate, generating tangential pressure drops which skew the NWP measurements; this was reflected in the measured NWP values, which showed little difference when run in either TFF or dead-end mode. Furthermore, the pressure losses incurred in the permeate channel due to the presence of the tight permeate

screen also adds to the measured TMP, which is discussed in more detail in section 4.3.3.2.4.

To validate the theory, NWP tests were performed on a 500 kDa membrane disc, roughly 23 mm in diameter, cut out from a Pellicon V screen cassette and compared to NWP values of commercial membrane discs of the same type and cut-off. Values of 4640 LMH/bar, 5410 LMH/bar and 720 LMH/bar for the coupon, membrane disc and intact Pellicon cassette (prior to being cut open) respectively, was obtained. The experimental NWP values showed a good agreement with the flat-sheet membrane disc data as expected, considering the loss of membrane permeability due to potential membrane fouling of the previously used Pellicon cassette.

The observed difference in NWP for TFF cassettes and membrane discs was seen to increase with increasing intrinsic permeability/pore size of the membranes (Figure 4.1).
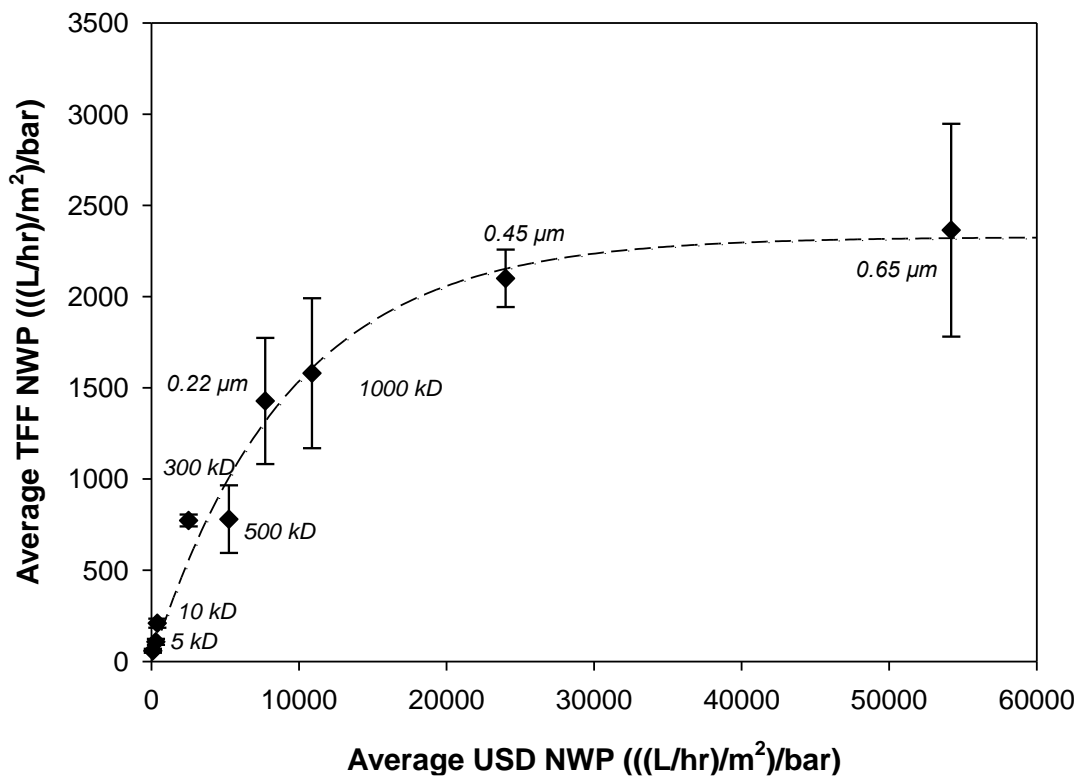
Figure 4.1 Comparison of experimental NWP values for various Pellicon cassettes (*y*-axis) and membrane discs (*x*-axis) for different membrane types and cut-offs/pore sizes. All NWP values are corrected to 25 °C.

As discussed earlier, NWP is highly dependent on the geometry and system used. The divergence between the two data across the two formats was observed to increase non-proportionately with increasing pore size/cut-off, since membranes with high intrinsic permeabilities are more sensitive and responsive to differences in the value of TMP used in Equation 2.3 to calculate NWP.

From Figure 4.1, the larger the membrane pore size, the greater the observed variability; in fact, for cut-offs >1000 kDa, the NWP can almost be considered a nonsensical figure and can be very variable due to the nature of the large membrane pores and associated pore size variability. Such discrepancies between NWP data across both scales is typically not a vital concern in the scale-up of tangential flow filtration, particularly for open membranes (>10 kDa), as they tend to equal out with process performance due to polarisation and/or caking, with NWP normally being used as a crude release test and to evaluate membrane cleanliness. However, in cases of low-viscosity process feed and/or tight membranes (<10 kDa), changes in NWP would directly correlate to process fluxes as membrane permeability, rather than osmotic pressure/polarisation, would create the more significant resistance to flow and hence NWP need to be accurately determined and considered upon scale-up.

4.2.2   System and cassette hydraulic resistances

4.2.2.1   System hydraulic resistance

Since tangential flow filtration is a pressure driven separation process, scaling across systems is done primarily based on pressure, be it at constant dP and/or TMP. One of the overriding problems with scaling up is that the one key component that cannot be kept constant, namely the tangential flow filtration system itself, along with ancillary components such as pipework, valves, flowmeters and other components in the flow path. These components create additional resistances to flow besides cassette/membrane resistance and is termed as system resistance. Since overall pressure drop is system dependent, it is difficult to translate pressure across scales and can potentially cause mismatch in operation between scales if not accounted for. The impact of system pressure drops is significant for the more open membranes, where optimum TMPs are typically very low, in the range of 0.1-0.5 bar. As a result, the real TMP across the membrane can be up to 30% smaller at large scale, resulting in drastically different fluxes despite both the pressure gauges reading the same value

(Dr. PJ Beckett, Technology Consultant - Merck Life Sciences KGaA, personal communication, 2017). This is due to the relatively large intrinsic permeability of open membranes (>300 kDa pore size), where even relatively small discrepancies (±0.05 bar) between the recorded TMP and actual TMP exerted on the membrane can significantly impact the process flux and cause it to deviate from the expected performance. This is not as much of an issue during UF, where the operating TMP is usually in excess of 1 bar, and differences of 0.05-0.1 bar in TMP across scales does not cause as significant a difference in performance.

Pumps, piping, instrumentation, tanks and mixers all change upon scale-up and offer different frictional resistances to flow and the corresponding pressure drops effectively contribute to the measured TMP value. These parasitic pressure drops between the pressure gauges and the membrane, termed as system resistance, do not contribute to the overall driving force for filtration but are an intrinsic part of the measured TMP across the system and hence cannot be ignored. Another contributing factor is the location of the pressure gauges/sensors themselves. Pressure gauges measure the backpressure of the components downstream, and thus if the pressure gauge is on the pipe leading to the cassette holder, the pressure drop in the pipe section between the gauge and the holder as well as the backpressure of the cassette will be measured, along with anything else along this flow path. The majority of small scale systems typically have the pressure gauges located within the body of the cassette holder, or at the very least, right at the feed and retentate ports of the cassette(s). However, at larger scales this is almost impossible since the holders have multiple banks and so the pressure gauges are set further back on the inlet pipe, therefore generating an extra pressure drop that could be significant depending on flow rates and viscosity of the liquid. Apart from that, the material of construction and relative roughness of the flow path could also create further resistances to flow due to wall drag.

Concerning the pressure measurements, since the pressure sensors are not in the channel itself but are in the holder port or the pipe leading to and away from the cassette, a constriction around the sensor area will seem to have a high dP when in fact the feed channel may not be compressed at all. Entrance and exit effects due to misaligned inlet and outlet ports of the cassette relative to the holder would also induce additional pressure losses in the system.

To demonstrate the impact of differences in systems and resistances between equipment across scales, independent water flux experiments were carried out on a Pellicon XL cassette (Ultracel 10 kDa) using the AKTA Crossflow and a standard Millipore lab-scale TFF system, as shown in Figure 4.2.
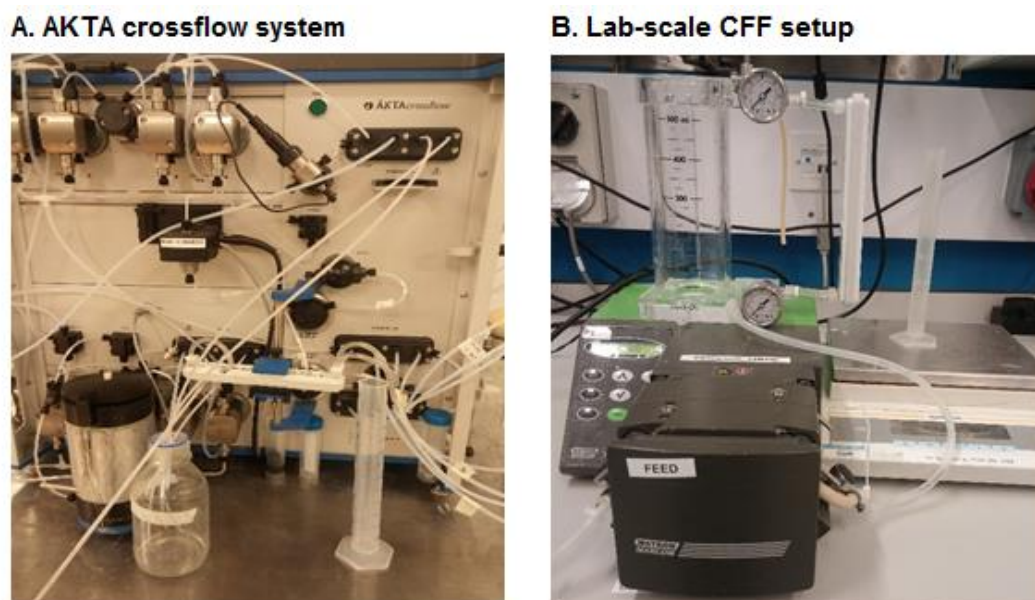
Figure 4.2 Experimental setup of the AKTA Crossflow (left) and lab-scale TFF (right) used to carry out the NWP tests for the 10 kDa Pellicon XL (PXC010C50) cassette.

The lab-scale system comprised of a Watson-Marlow peristaltic pump and a feed reservoir, with two pressure gauges, for the feed and retentate stream, and permeate flow rate was calculated by measuring the mass of permeate collected every 30 seconds using a balance. The AKTA Crossflow has on-line flow meters and pressure sensors on all three lines and hence flux and TMP data was automatically logged by the Unicorn control software. Figure 4.3 shows the results of the water flux tests at a feed flow rate of 16.4 mL/min (3.3 LMM).
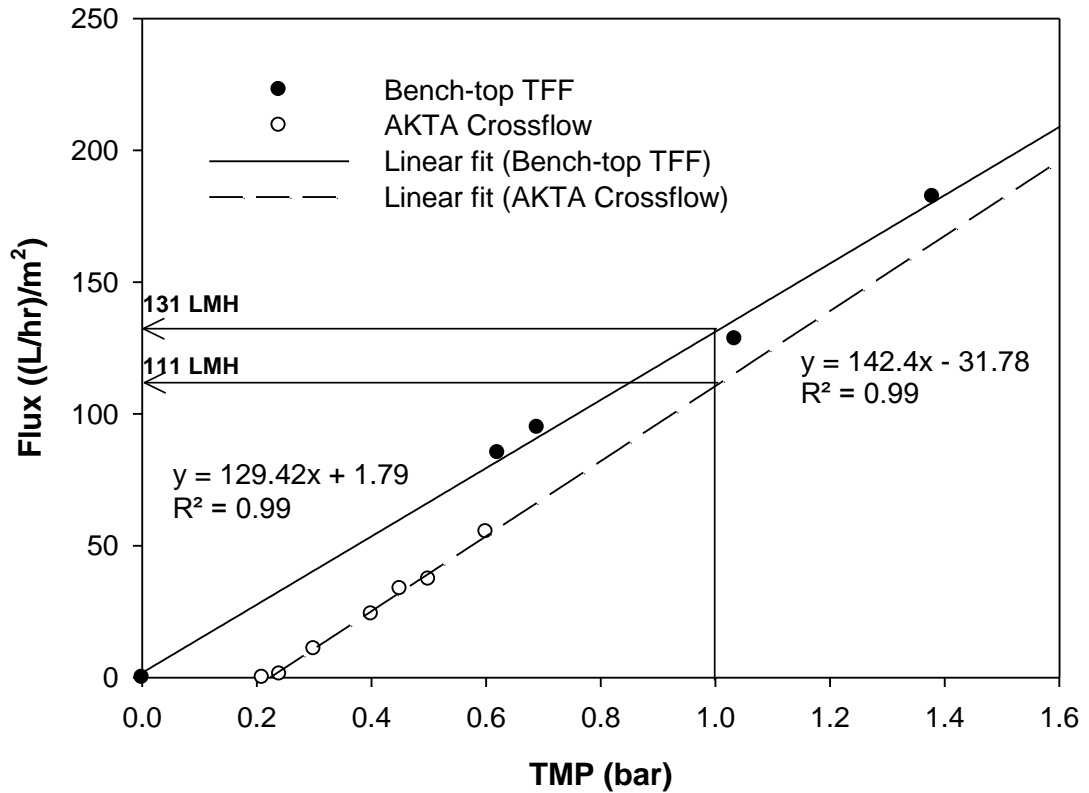
Figure 4.3 Pure water flux data for the 10 kDa Pellicon XL cassette using the AKTA Crossflow and the lab-scale TFF setup, at an inlet flow rate of 3.3 LMM and temperature of 20±1 °C.

For the same cassette, there appeared to be slightly different flux-TMP profiles for the two systems when using pure water at an identical flow rate. The membrane permeability, proportional to the gradient of the flux-TMP line, was observed to be roughly the same for both systems within experimental error, and as expected since the same membrane material/cassette was employed. However, comparing NWP values at an applied TMP of 1 bar, the lab-scale system would generate a permeate flux of 131 LMH while the AKTA Crossflow system yields a much lower flux of 111 LMH, due to an observed flow initialised pressure of 0.20 bar, below which there is no net flow out through the permeate.

The additional pressure drop of 0.20 bar observed in the AKTA Crossflow data can be attributed to the resistance in the narrow tubing, *i.e.*, sum of the components of the pressure drop of the fluid within the tubing between the cassette and the three points of measurements by the pressure sensors used to calculate TMP. This non-zero TMP at zero permeate flux increases as the viscosity of the feed increases,

which is usually the case when feed material is used instead of water, due to Hagen–Poiseuille equation, where pressure drop for an incompressible and Newtonian fluid flowing through a cylindrical pipe of constant cross section, is proportional to the dynamic viscosity of the fluid at constant flow rate. However, when the flow regime becomes turbulent because of high flow rates in the narrow tubing, the pressure drop increases in proportion to the square of the flow velocity.

4.2.2.2 Cassette hydraulic resistance

When feed flow is initialised at zero permeate flux, *i.e.*, permeate pump/valve is closed, and if the feed pressure is high enough, starling flow can occur where fluid travels from the feed channel to the permeate channel over an initial length, after which the flow is essentially reversed and permeate flows back through the membrane back into the feed channel (Lutz, 2015). This undesirable reversal of fluid flow can occur when feed pressures drop below the permeate backpressure/osmotic pressure, which is likely to occur near the retentate outlet of the flow channel when permeate flow is restricted (P_P>0 bar). However, the net permeate fluxes are often very high due to the high mass transfer rates in the initial section of the feed flow path. To illustrate the associated effects of Starling flow in TFF cassettes, a CFD simulation for a V screen flow cell (2 cm in length, 3 fibres lengthwise, representing ~1/8th of the total flow length of Pellicon cassettes), was carried out to compare pressure and permeate flow profiles with and without net permeate flux imposed (Figure 4.4).

Against common sense, when the permeate outlet is completely closed and a recirculating flow/pressure upstream of the membrane is applied, the permeate flow is not static but instead a localised permeate flow exists and the flow velocities are a function of the feed pressure applied. The feed pressure applied is thus used to overcome the combined flow resistances due to the feed and permeate screens even at zero net permeate flux, since there is a localised flow within the permeate channel(s) despite the net permeate flow being zero. Figure 4.4 shows the starling flow occurring in a typical feed channel for the no net permeate flux condition, where the first half of the feed channel had a positive permeate flow velocity (from feed to permeate), after which a complete reversal of permeate flow (negative flow velocity) back into the feed channel over the remaining path length (1 cm). The bottom graph of Figure 4.4 shows the corresponding localised feed pressures and the permeate backpressure for the no flux condition; permeate backflow occurs after 1 cm, which

is the point beyond which the upstream pressure (P_F) drops below the permeate backpressure (P_P), making the net driving force negative. With an unrestricted permeate flow however, the localised permeate flow throughout the flow channel is positive since the permeate backpressure is equal to zero and thus does not drop below the retentate backpressure at any point to reverse the flow.

Therefore, the permeate chamber can be considered as two discrete chambers: the first being the one with a positive TMP gradient (shaded blue) which generates a positive flow through the membrane and the second chamber with a negative TMP gradient, which generates a backward flow through the membrane (shaded red). Provided free communication between the two chambers exists, the pressure gradients should ideally equilibrate across the membrane (area of red region=area of blue region), cancelling each other out to generate a net TMP=0, where observed permeate backpressure equals the average feed channel pressure drop ($[P_F+P_R]/2$). However, in practice, the feed and permeate channels are not perfectly uniform and the permeate channels typically have a much tighter screen than the feed channel. The narrow permeate channel could lead to a relatively high resistance to flow which may hinder the communication between the two permeate chambers mentioned above, leading to a situation where the localised negative TMP gradients are much smaller or larger than the corresponding positive gradients in the first half of the module. Figure 4.5 shows the experimental non-zero TMPs observed with for different cassettes using water, as feed flow rate is increased with permeate closed.
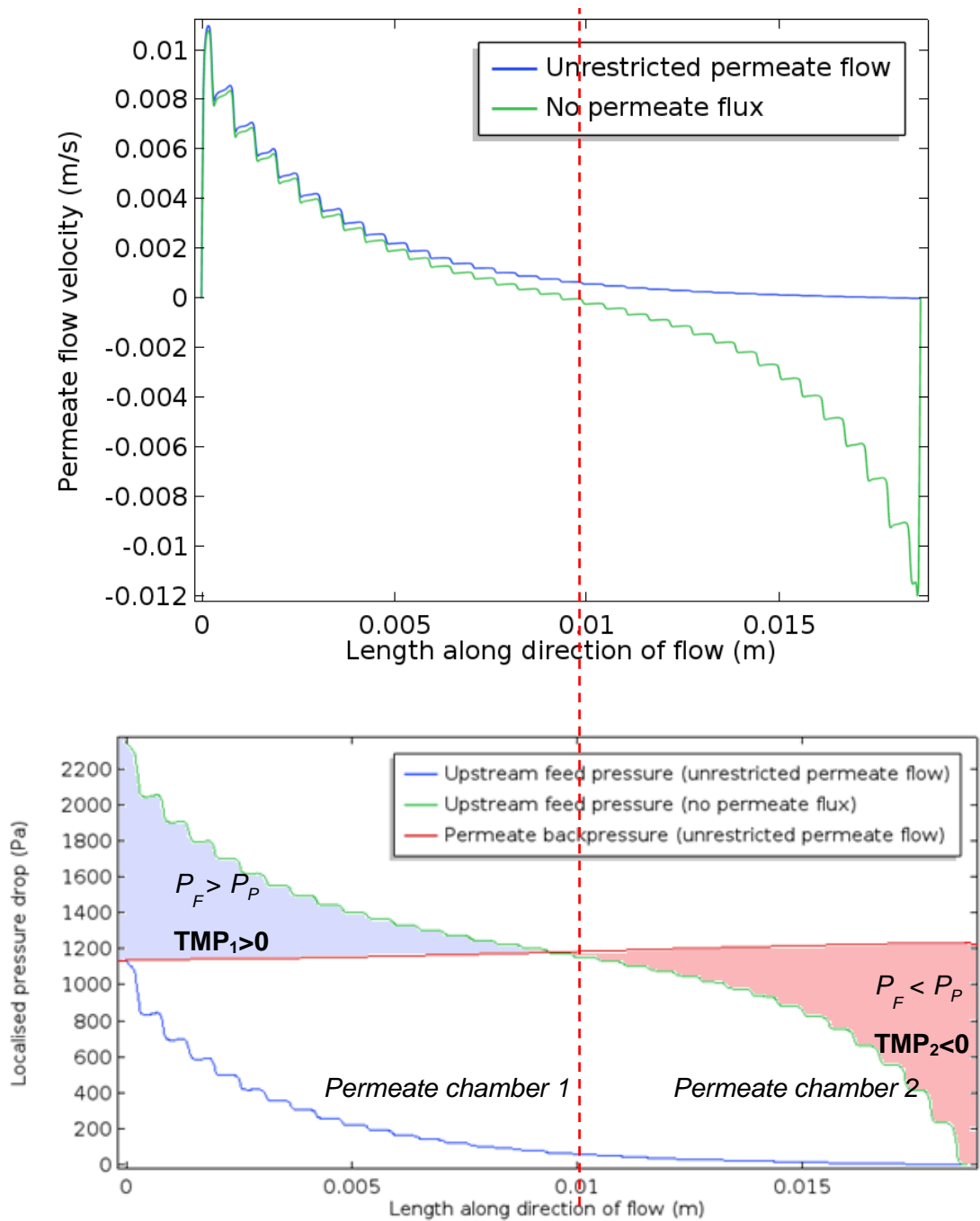
Figure 4.4 CFD simulation results illustrating starling flow in a V screen flow cell (2 cm length) for total permeate closure (0 permeate flux) and unrestricted permeate flow, at 2 LMM feed flow rate and using water as domain material. Top: permeate flow rate profiles along the transverse axis. Bottom: pressure exerted on the membrane as a function of flow channel length; for the simulation with unrestricted permeate flow, permeate backpressure was zero throughout (not shown).
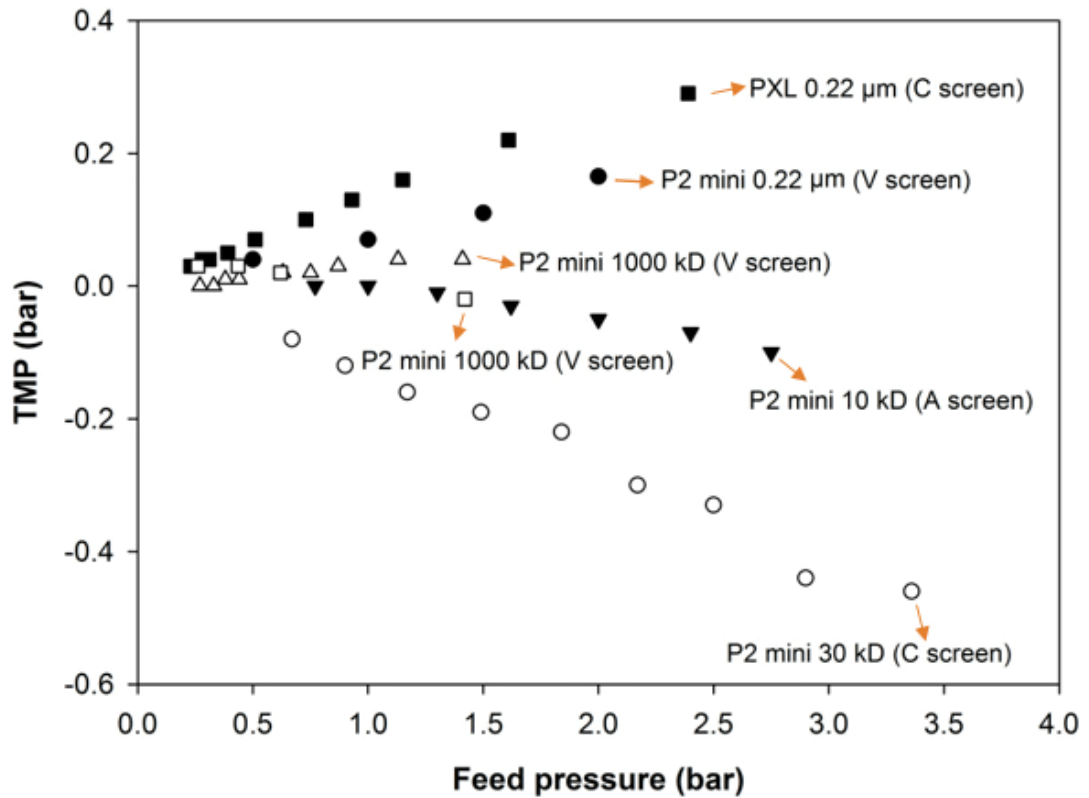
Figure 4.5 Experimental data for initial TMP versus feed pressure for different membrane cut-offs and pore sizes using water at 25 °C at zero permeate flux.

As expected, a non-zero TMP was observed in all cassettes for the range of feed pressures investigated. The impact of starling flow on the initial TMP was seen to be more pronounced at higher feed flow rates (feed pressures) and low permeability membranes like the 10 kDa and 30 kDa, where initial net TMP was observed to be less than zero and decreasing further with increasing feed pressure in a non-linear fashion. The TMP was also observed to decrease from a net positive TMP to a net negative TMP with applied feed pressure/feed flow rate for the case of 10 kDa A screen cassette. To further investigate and study the potential causes of positive and negative initial TMP with permeate closure, the concept of two independent permeate channel halves was further investigated using CFD, particularly for cases where the two permeate chamber halves are not identical in heights. Figure 4.6 shows the 2 cm CFD model setup with different heights for the permeate flow channel (0.2 mm versus 0.4 mm) and the simulation results at feed pressures of 0.1 and 0.5 bar.
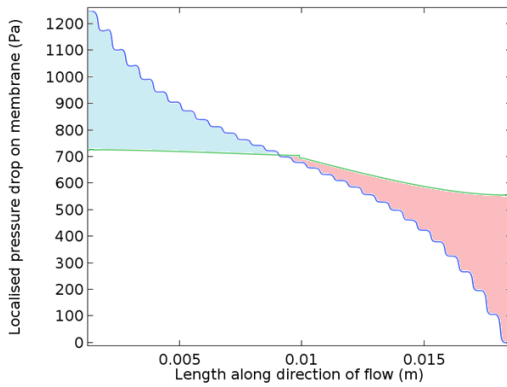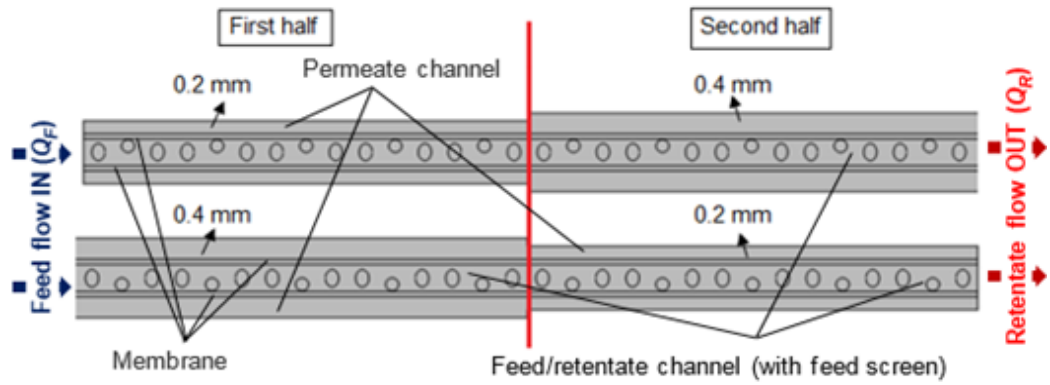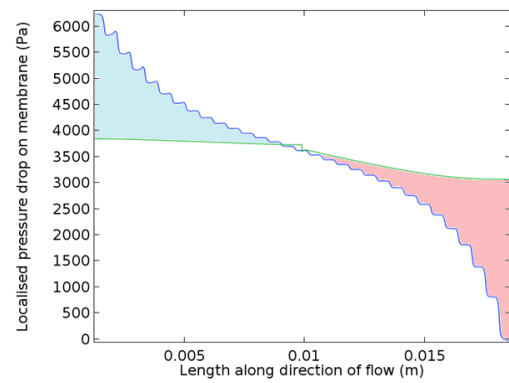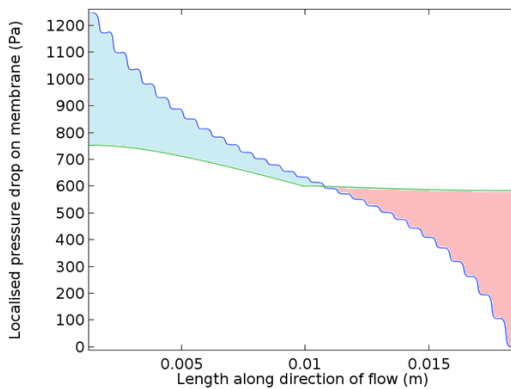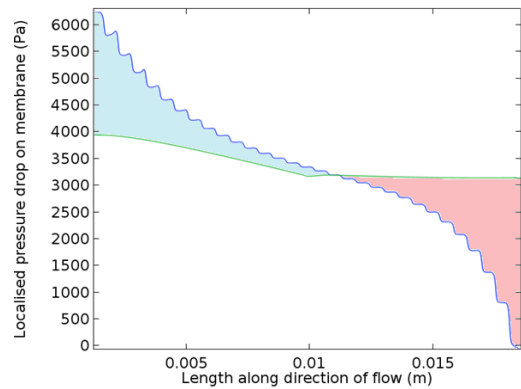
Figure 4.6 CFD model setup and results to illustrate the impact of uneven permeate channel thickness on observed net process TMP. Top: 2D illustration of the 3D CFD model (2 cm length in direction of flow using water as domain material at 25 °C and zero net permeate flux) used to investigate the two typical cases of uneven permeate channel heights along the flow path; bottom: 1D plots of the CFD simulation results showing pressure drop on the membrane (actual TMP) as a function of modelled

channel length (2 cm) at feed pressures of 0.1 bar and 0.5 bar. The blue and green lines represent the feed channel and permeate channel pressure drops across the channel length respectively. Shaded regions represent the difference between feed and permeate pressures in the two halves, where blue represents region of localised positive TMP gradient (TMP_1) and red the region of negative TMP gradient (TMP_2).

When the permeate flow is restricted (particularly for open membrane operations with low optimal TMPs), or in the case of total permeate closure (at the start of the operation), there is a significant positive permeate backpressure exerted on the membrane and the height of the permeate channel comes into play, which is not the issue in the case of unrestricted permeate flow. The permeate backpressure responds directly to the upstream pressure applied and is a function of the permeate channel hydraulics; the backpressure is dictated by the extent of the permeate flow velocity restriction due to the limited height of the permeate channel. Ideally, the permeate backpressure at zero net permeate flux should be constant and equal to half the axial pressure drop applied across the feed channel, provided the permeate channel is of uniform thickness throughout. However, variations in permeate channel heights along its length (due to uneven weave of the permeate screen, fibre diameter, etc.) creates a non-uniform permeate pressure profile across the cassette, as opposed to the relatively constant permeate pressures seen in Figure 4.4.

At a given feed pressure, a variable permeate backpressure profile across the cassette can be generated because of the variations in the heights across the permeate chamber halves which directly impacts the observed net TMP. This phenomenon can be seen in the CFD simulated results illustrated in Figure 4.6. In the first case, where the first chamber is larger than the second half, the area shaded blue is smaller compared to the area shaded red which means that the overall TMP is likely to be negative since the localised negative TMP gradients in the second half of the channel dominates the positive TMP gradients that exist in the former half. The opposite effect is seen when the first half is smaller than the second half, as can be seen in the bottom images of Figure 4.6. To quantify these effects, the areas of the shaded regions were evaluated and net TMPs calculated as shown in Table 4.2.

CFD simulation conditions		P_F - P_P for P_R=0 (Pa)		
		TMP$_1$ (1st half of flow channel)	TMP$_2$ (2nd half of flow channel)	Net TMP (Half 1+Half 2)
P_F = 0.1 bar	Permeate chamber 1: 0.4 mm Permeate chamber 2: 0.2 mm	129.43	-130.26	-0.83
	Permeate chamber 1: 0.2 mm Permeate chamber 2: 0.4 mm	133.13	-128.54	4.59
P_F = 0.5 bar	Permeate chamber 1: 0.4 mm Permeate chamber 2: 0.2 mm	107.17	-109.18	-2.01
	Permeate chamber 1: 0.2 mm Permeate chamber 2: 0.4 mm	113.31	-107.5	5.81

Table 4.2 Impact of permeate channel height distribution on localised and net TMP values for a CFD simulated channel length of 2 cm (proportional to area of the shaded regions in Figure 4.6), determined using the open-source image processing package ImageJ 1.52a.

Table 4.2 shows that the initial TMP is less than zero when the second permeate chamber is smaller compared to the first permeate chamber resulting in TMP$_1$<TMP$_2$, and vice versa. These net TMPs are larger at higher applied feed pressures due to proportionately larger local permeate flow velocities in the permeate channel, despite no net permeate flow exiting the cassette (Figure 4.7).
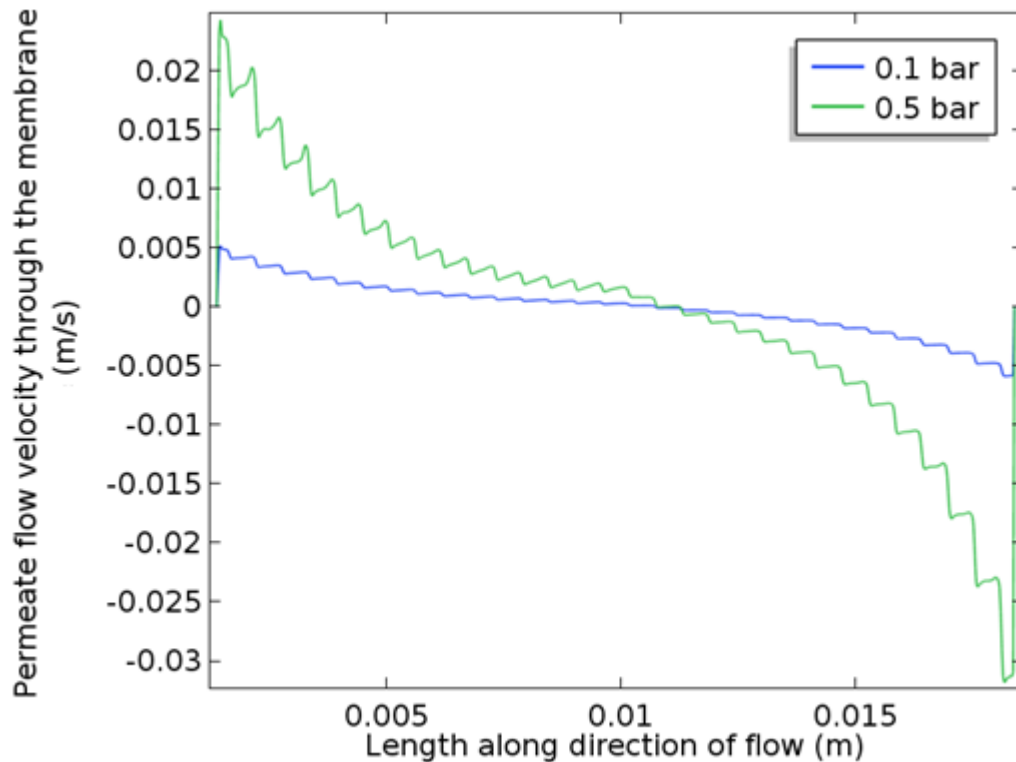
Figure 4.7 1D line plot of localised permeate velocity profiles for two feed pressures for [0.4 mm, 0.2 mm] permeate channel heights for water at 25 °C.

The higher the feed pressure, the greater the upstream recirculating flow velocities in the feed channel which translates to larger flow velocities through the membrane and into the permeate channel, illustrated by the larger velocity magnitude profiles at 0.5 bar feed pressure compared to 0.1 bar in Figure 4.7. Higher permeate velocity means a correspondingly larger pressure drop in the narrow permeate channels (when permeate flow is closed) and this effect is exasperated for tighter membranes with feed material, where additional permeate pressure is required in the second half of the channel to drive flow back into the feed channel through the low permeability membrane by overcoming retentate osmotic pressures.

Although water was used for all experiments and simulations, *i.e.*, no polarisation or caking effects, the flow initialised TMP was seen to respond to applied feed pressures in a power-law fashion, indicating the influence of a combination of the system and permeate channel hydraulic resistances of the TFF cassette. The presence of air pockets in the permeate channel(s) could also affect the pressure equilibration across the membrane since trapped air cannot go through the membrane if the pressure is below the bubble point pressure, particularly for tight membranes (<100 kDa). Apart

from that, there could be other complex cassette-specific effects that could cause deviations from the ideal scenario of a zero TMP at zero net permeate flux. This is primarily the case when using single feed channel cassettes such as the Pellicon XL and Pellicon 3 micro, where the feed and permeate channels are likely to undergo extreme deformation to generate very unusual and unexpected flow within the cassette flow path due to uneven channel thicknesses due to the narrowing of the flow channels along the channel length. This effect is ironed out in cassettes with larger surface areas (multiple channels) and there is an overall averaging effect and the permeate channels do not undergo as much compression and deformation (apart from the first and last channels) as the single feed channel cassettes.

The real-life consequence of starling flow in TFF cassettes can be observed in flux excursion data for microfiltration. For a standard tangential flow filtration system, without permeate restrictions and no retentate backpressure, the minimum operating TMP is equal to dP/2. However, if a permeate flow restriction is used, which is generally desirable for open membranes to generate low TMP, the flux-TMP plot may not be correct when TMP<dP/2, since the permeate pressure would be higher than the retentate pressure leading to unusual flows in the latter half of the cassette.

Figure 4.8 shows process optimisation data at three crossflow rates using a 500 kDa hollow fibre, showing inaccuracies in TMP data points where the minimum TMP(=dP/2) rule was not satisfied.
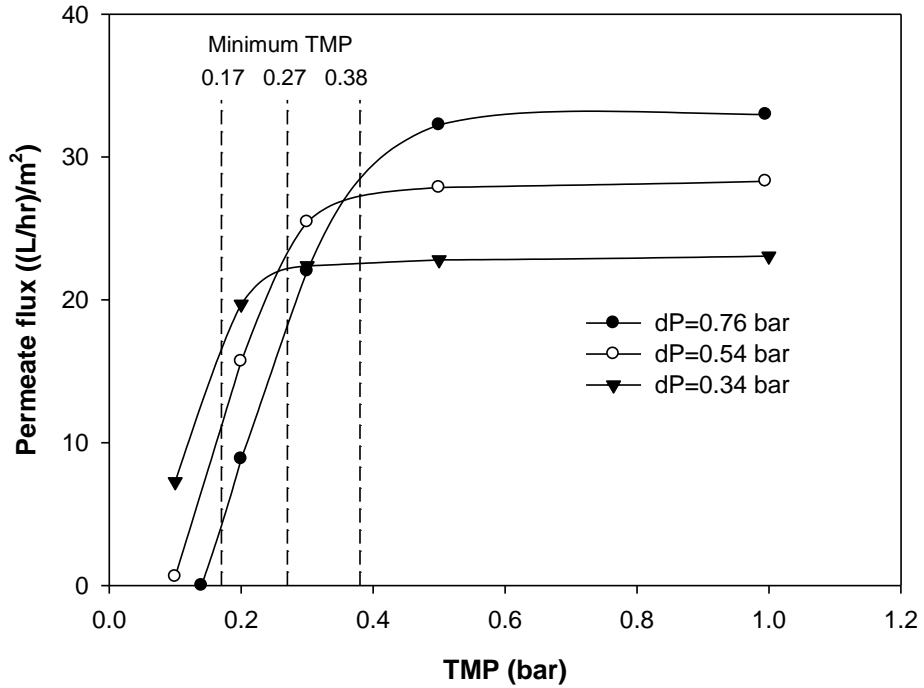
Figure 4.8 Process optimisation data (permeate flux versus TMP) for clarified allantoic fluid using a 500 kDa hollow fibre for three crossflow rates. Data courtesy of JP Neff (personal communication, GE Healthcare Life Sciences, 2018).
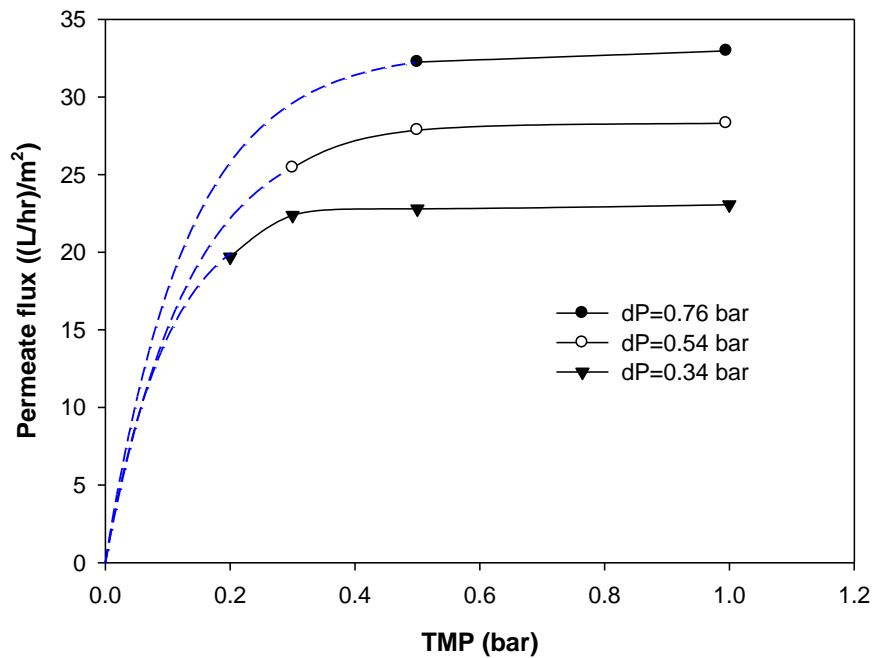
Figure 4.9 TMP corrected data from Figure 4.8, showing only valid data points where TMP>dP/2 (minimum TMP) criteria is met, and backward interpolation to (0,0) shown as blue, dashed lines.

In Figure 4.8, the flux-TMP curves was seen to not go through the origin (0,0) and this could not be due to any osmotic pressure related effects since a very open and permeable membrane was used, which prevents the formation of any significant concentration gradients across the membrane. At zero net TMP, all extrapolated permeate flux values were less than zero, indicating an overall reverse flow filtration where localised negative TMP gradients further down the channel was decidedly greater than the positive TMP gradient near the inlet. As expected and discussed previously, the initial TMP values at zero flux was seen to increase with the feed flow rate, which generated larger driving forces for filtration and thus larger permeate velocities, leading to greater permeate backpressures and correspondingly larger negative TMP gradients in the second permeate chamber. Consequently, a much greater applied TMP was required to overcome the initial reverse flow filtration and drive a net positive flux through the module as feed flow was increased.

Figure 4.9 shows the corrected flux-TMP plots with all data points where TMP was higher than dP/2. An extrapolation of this data showed that the curves seemed to go through zero, or very close to zero, depending on the system resistance. The discrepancy in data at TMPs below the minimum operating TMP highlights the consequences of partial reverse flow filtration, which leads to a part of the membrane area not being effectively utilised for filtration thus skewing the observed performance. The relatively higher localised negative TMP gradients at the end of the flow path due to starling flow adds to the flow resistances through the membrane and prompts the need for the extra pressure to drive a net positive flow through the membrane. When the applied TMP is greater than the average upstream pressure, a net positive flux through the membrane is achieved.

Thus, the resistance of the system and cassette cannot be simply characterised by taking ratios of resistances across scales and adjusting TMP to generate identical permeate fluxes upon scale-up, due to the non-linear relationship of initial TMP with feed flow rate and impact of the cassette and cut-offs and so cannot be assumed to be constant for a given system. Furthermore, the non-zero initial TMP becomes more pronounced with viscous feed and cannot be accurately predicted by using a TMP correction factor based on NWP values across scales alone. As a result, it is imperative to recognise the impact of feed viscosity and system and cassette-related factors on the overall resistance to flow through the membrane in tangential flow filtration, and needs to be experimentally determined for process feed, membrane cut-off and all feed flow rates investigated.

4.2.3   Sources of variations affecting TMP and flux

Although the manufacture process and cassette assembly and sealing are controlled to tight specifications, there are still variations observed amongst cassettes. Sources of variation include manufacturing tolerances for the feed screens, batch-to-batch variations impacting membrane thickness and porosities and applied compression to the cassettes that affect channel hydraulics and consequently mass transfer and pressure drops.

4.2.3.1   Membrane surface area

The potting compounds and resin, for instance silicone, used to seal the feed and permeate channels together penetrates the perimeter of the cassette to a certain depth and effectively reduces the membrane surface area to flow. This has consequences that are more prominent in the case of single feed channel TFF cassettes due to a much lower available membrane area, which means minor variations could take up a relatively significant area compared to larger cassettes. There are small variations in usable area between the cassette types (hence the 0.5 m^2 for Pellicon 2 mini and 0.11 m^2 for Pellicon 3 mini cassettes), but in reality, it falls within the acceptable experimental error of ±20% associated with scalability (Millipore, 2018a).

The major factor impacting the available surface area for filtration is the membrane embossing, which is not serious unless the cassette is over-compressed and is indicated by a steep increase in pressure drop at a certain feed flow rate. The screens present in the feed channels tend to emboss themselves into the membrane when compressed, as can be evidently seen in Figure 4.10, illustrated by the etched marks. As a result, the feed screen fibres essentially block off part of the membrane and could lead to divergence between the actual membrane area available for filtration compared to the nominal areas reported by manufacturers, impacting the flux calculation for permeate flow and consequently flux based scale-up performance. The single feed channel cassettes with smaller membrane areas (50 cm^2 and 88 cm^2) are more vulnerable to this, while the larger cassettes tend to be more resistant to membrane embossing effects due to compression because of the overall averaging effect over multiple channels. However, this becomes more pertinent when scaling up from flat membrane discs to screened cassettes, where the former has no screen-related occlusion of the membrane.
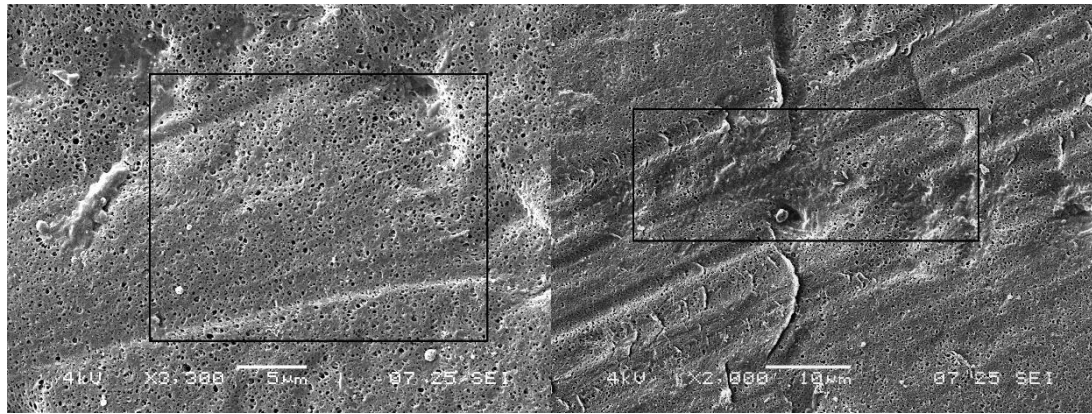
Figure 4.10 SEM images of a 500 kDa Biomax membrane, cut out from a Pellicon V screen cassette, showing indentations on the surface where the fibres of the screen made contact with the membrane, highlighted in black, compared to flat sheet membranes shown in Figure 4.11.

4.2.3.2　Membrane thickness and uniformity of pores

The active layer of the membranes, especially for UF membranes, which are cast on a solid substrate for support, is also variable and specifications for Millipore cassettes are reported to have a variability of 20-30% standard deviation for the average reported thicknesses, depending on the membrane. The membranes being compressible polymers, also vary with pressure applied and the porosity can be effectively reduced under pressure, and thus even small variations in the membrane thickness could directly affect flux.

The pore size of filtration membranes are not uniform across the membrane because of the typical nature of current manufacturing processes for polymeric membranes. Currently, the cut-offs for UF membranes are typically characterised based on rejection of mixed dextran R_{90} up to 300 kDa, while the more open MF membranes are tested using porosimetry based on bubble point tests that detect the largest pore size across the membrane. The latter is impossible to hit on tight membranes and used more as a specification release test, rather than a direct characterisation of the pore size distribution for MF membranes. The impact of pore size distribution variability is reflected in the wide range of measured NWPs for a given membrane/cassette lot, as can be seen by the magnitude of the error bars in Figure 4.1; this error increases significantly with increasing cut-off/pore size of the membrane.

Figure 4.11 shows the SEM images of 500 kDa and 0.45 µm membrane discs and pore sizes can be seen to significantly vary in both cases, more so for the 0.45 µm membrane, where pore sizes were seen to get as large as 4 µm, an increase of almost ten-fold compared to the reported average pore size specification. The 500 kDa UF membrane had a relatively tighter pore size distribution, but still exhibited a relatively large pore size distribution. Although the permeability relates to pore size, the variability is usually not an issue since the polarisation layer effectively controls process fluxes, due to its resistance being a lot higher than the intrinsic membrane resistance. This is because the primary barrier to flow through the membrane with a feedstock containing larger molecules (relative to membrane pore size) is the polarisation layer. Although the intrinsic membrane permeability does affect permeate flux through the membrane, minor changes within a single membrane cut-off is usually negligible compared to the effect of the polarisation layer. For example, even though the NWP of a 30 kDa Biomax PES TFF cassette is approximately three-times larger compared to an Ultracel Cellulose 30 kDa (150 LMH/bar versus 410 LMH/bar), the process fluxes with biological feedstock are usually very similar. Zahka and Leahy (1985) investigated the effect of membrane pore size on the permeate flux for processing *Escherichia coli* cell broth. They observed that a 100 kDa UF membrane and 0.2 µm MF membrane showed very similar permeate flux profiles, *i.e.,* exponential decay over time when run at a constant TMP. However, the 10 kDa membrane had relatively lower initial permeate fluxes and showed a very steady decline over time. The latter observation was due to the polarisation layer having a greater permeability than the 10 kDa membrane itself, and thus the primary barrier to flow though the membrane was the membrane itself, rather than the polarisation layer in this case.

Variations in pore size are not an issue for membranes with large surface areas since the average pore size/cut-off is more representative of the distribution over a much larger area. However, variability in cut-offs for tighter membranes could have an impact on particle transmission/rejection, if pore size distributions are significantly different upon scale-up, for instance, when scaling from small membrane discs with relatively small membrane areas where such variabilities would be accentuated and thus need to be accounted for.
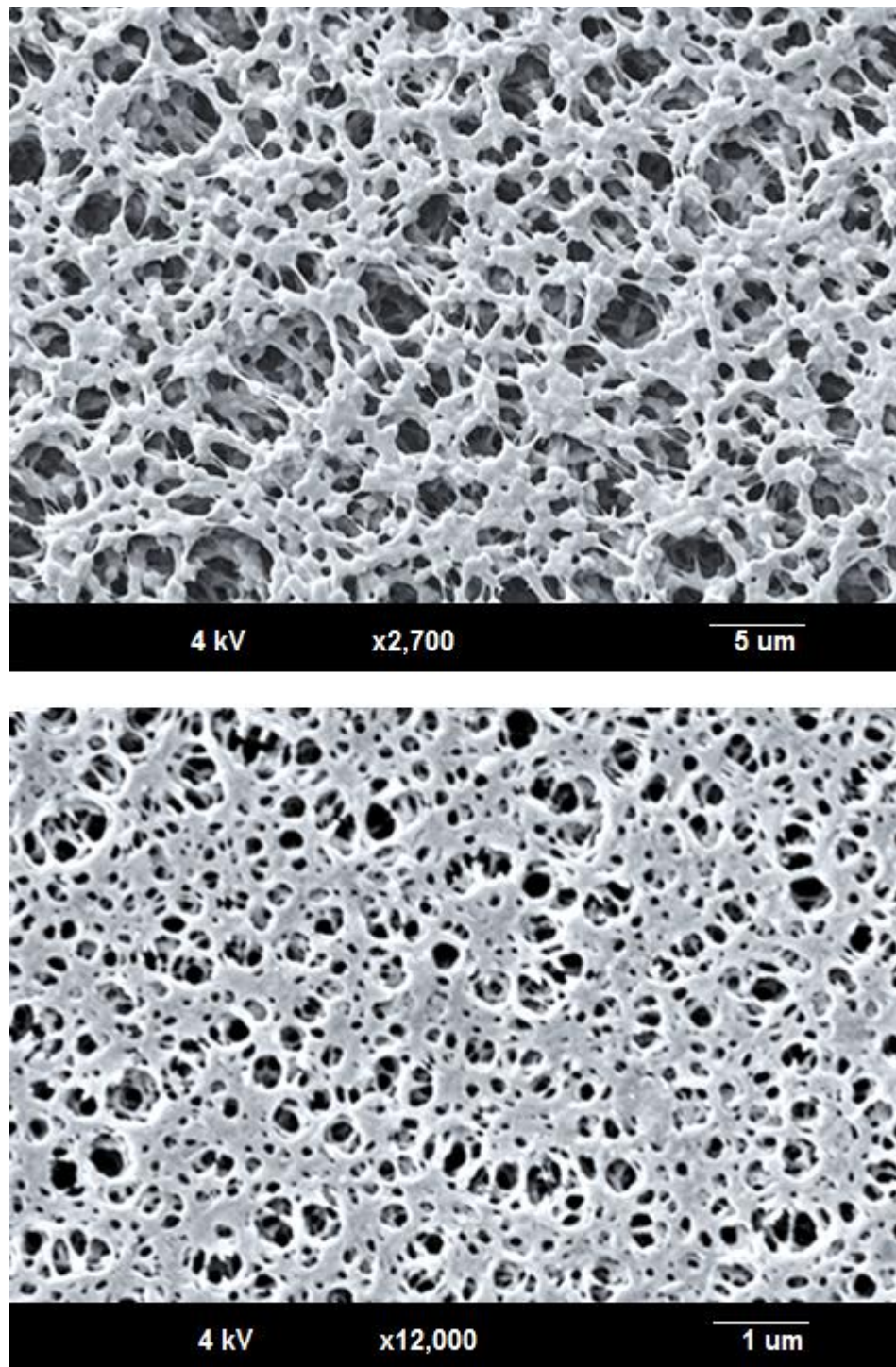
Figure 4.11 SEM images of 47 mm membrane discs. Top: 0.45 μm Durapore membrane. Bottom: 500 kDa Biomax (500 kDa cut-off roughly translates to a pore size of 0.02 μm).

4.2.3.3 Variation in feed channel hydraulics

The feed channel height, determined by a multitude of factors such as screen type, membrane embossing as a result of feed channel compression, is key to achieving the required wall shear rates across the channel and associated pressure drops at a given feed flow rate upon scale-up. The extent of membrane embossing into the screen which directly impacts effective feed channel height, depends on the physical deformability of the membrane, screen and gaskets and membrane thickness in response to the compression applied; variations in feed channel height can have a significant impact on the mass transfer rates and consequently the accuracy of the scale-up performance. The height of the feed channel is typically defined as the screen size since the membrane layers are malleable. As a result, cassettes can potentially have different crossflow velocities across the channel at a specified feed flow rate depending on the compression/torque applied and the resulting feed channel height and thus cross-sectional areas available to flow, resulting in drastically different process flux performances than expected upon scale-up.

For TFF cassettes that require a minimum compression to achieve proper sealing of the urethane encapsulations around the feed and permeate ports, as is the case for Pellicon 2 and 3 cassettes, the torque is an important factor that can affect effective channel height. The resulting compression at an applied torque is a function of friction coefficient between the spacers, threaded tie rods, nuts, and their respective states (lubricated, dry or damaged) and temperature. As a result, a cassette can have significantly different channel heights and thus process performances during operation despite having the same torque across different holders, which have different size/type of components and characteristics such as pitch, thread angle, nut diameter, etc., or even for the same holder, depending on the parameters mentioned above. The compressive force applied to the cassette directly influences the level of membrane embossing which affects the active layer and thus feed channel height due to compressible nature of the feed screen and membranes. A greater applied torque generally decreases the effective channel height, depending on the material properties of the screen. For example, polypropylene screen (26 mm commercial spacer for spiral-wound modules) was found to compress greatly under pressure and the effective feed channel height of the screened channels was found to decrease significantly (up to 100 µm) with increasing pressure applied to the module (Karabelas et al., 2018). Apart from that, the flexibility of the jacket material used to house the channels within the TFF cassette also affects the feed channel compression at an

applied torque. For instance, the Pellicon 3 jacket made of solid polypropylene is much more rigid than the Pellicon 2 made of polyurethane, which is relatively more compressible and makes effective compression more important in its operation. In comparison, the Sartorius TFF cassettes are housed in silicone, a wobbly, soft material that is very responsive to changes in compression and could change the feed channel height greatly depending on the compression applied. Furthermore, the compressibility of the spacer themselves could be a potential issue, depending on the material of construction and its properties.

Another key source of variation is the associated tolerance and specifications of the manufacturing and molding process itself. As mentioned previously, the membrane thicknesses can vary to an extent where filtration performances are adversely affected due to reduction in overall thickness and porosity under pressure. The compression however does not affect the feed channel height significantly unless greatly over-compressed, way beyond the recommended specifications, and is usually reflected in a spike in pressure drop. However, since the feed channel is only supported on the inside by the feed screen (and spacers in the case of V screen cassettes), the channels tend to balloon up and expand as far as the device allows when pressure is applied. This makes it difficult to determine the channel height accurately during operation and as a result, the feed channel height is usually defined as the thickness of the screen/spacer. Apart from that, the V screen tends to be relatively more compressible due to the presence of spacers, adding more complexity to the accurate determination of feed channel height during operation.

The variations in the screen characteristics itself due to manufacturing tolerances also plays a key part in the effective feed channel height and tends to vary from cassette to cassette; the release specifications for the different screened cassettes are based on a feed channel pressure drop window since the feed channel height cannot be realistically controlled within such tight specifications. For instance, the nominal diameter of the Pellicon 2 C screen fibre is reported to vary between 215 µm and 360 µm, with an average thickness of 270 µm (Ngan et al., 2014), highlighting the relative wide distribution of fibre diameters and consequently overall thickness of the woven feed screen. Figure 4.12 illustrates the non-uniformity of a C screen, cut out from a PXL cassette, and the CFD simulated flow velocity profiles across the channel compared to a theoretically uniform mesh.
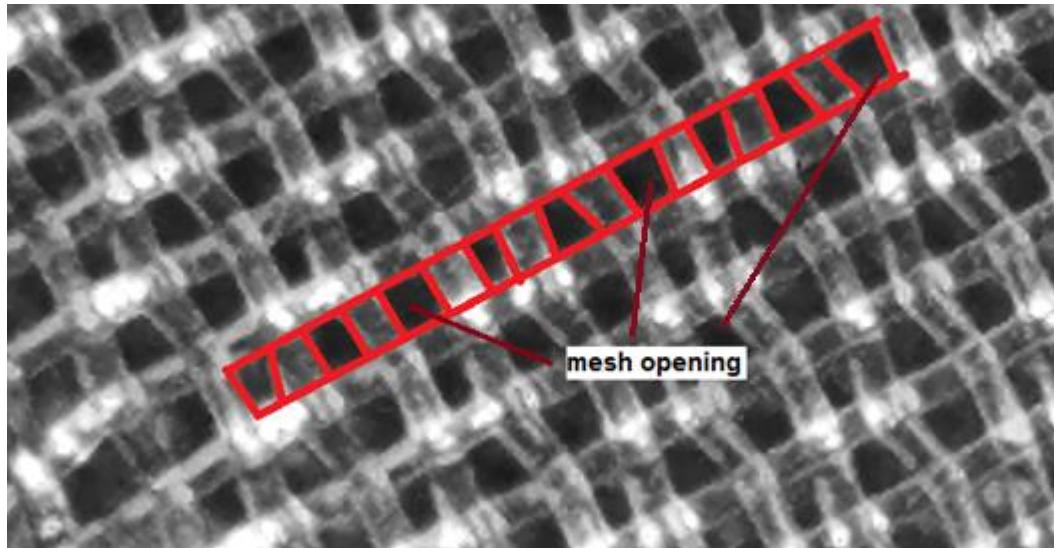
A. Non-uniform weave in a typical TFF cassette
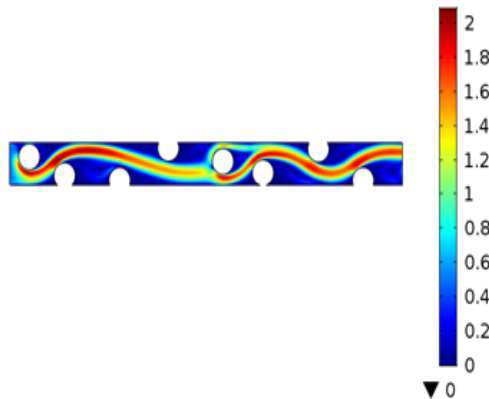
B. Uniform weave sequence
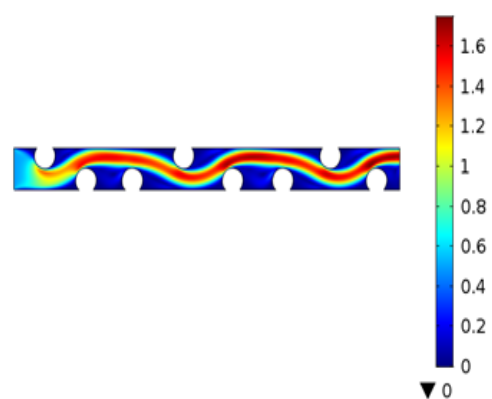
Figure 4.12 Illustration of the impact of non-uniformity in screen characteristics due to manufacturing tolerances on flow patterns through the feed channel. Top: 2D image of a C screen cut out from a Pellicon XL cassette showing regions of uneven weave sequence and variable mesh openings across the mesh (highlighted in red). Bottom: 2D CFD simulation results (0.5 m/s inlet velocity, using water as domain material at 25 °C) highlighting the impact of variable twill weave sequence and mesh opening (A) on flow velocity profiles within the channel in comparison to a uniform mesh and twill weave sequence (B). Maximum domain flow velocities are highlighted in red.

Both the fibre diameter and mesh opening tend to vary along the small section of the C screen investigated. The non-uniform weave sequence, expected in TFF cassettes, generates a maximum velocity of 2.09 m/s, compared to 1.75 m/s for the theoretically uniform weave at the same inlet velocity of 0.5 m/s. Furthermore, the flow pattern for

the non-uniform weave tends to be more random and generates a correspondingly larger pressure drop than expected/predicted values calculated based on uniform weave and mesh characteristics, which could lead to significant discrepancies between CFD predicted and experimental pressure drops if the correct feed channel height during operation is not known/used during scale-up. Figure 4.13 shows the feed channel pressure drops as a function of feed flow rate for the different Pellicon screened cassettes, determined experimentally using water. All experiments were run at the highest feed flow rate first to remove any trapped air, in descending order to the lowest flow rate; maximum and minimum pressure drops as part of the Pellicon release specifications are shown as solid black lines.

V screen experimental dP values

C screen experimental dP values

(Plot: Feed channel pressure drop, dP (bar) vs Feed flow rate, Q_F ((L/min)/m²), with High specification limit and Low specification limit curves)

Legend:
- Ultracel 30 kD PXL
- Ultracel 30 kD P2 mini
- 0.22 µm PVDF PXL
- Biomax 500 kD P2 mini
- Biomax 10 kD PXL

A screen experimental dP values

(Plot: Feed channel pressure drop, dP (bar) vs Feed flow rate, Q_F ((L/min)/m²), with High specification limit and Low specification limit curves)

Legend:
- Biomax 10 kD P3 micro
- Biomax 5 kD P2 mini
- Biomax 10 kD P2 mini

Figure 4.13 Experimental feed channel pressure drops (dP) as a function of feed flow rate (with permeate closure) for various A, C and V screen Pellicon cassettes, carried out at the recommended torque of 24 Nm and using water at a temperature of 25±1 °C.

From Figure 4.13, at all feed flow rates tested, a range of feed channel pressure drops were observed for a given cassette type/screen. Since the tests were carried out at a fixed axial compression across the cassettes, the difference in dP across the feed channel was deemed to be primarily created by variations in crossflow velocities because of small changes in the feed channel geometry due to manufacturing tolerances. These variations in the channel pressure drops would also contribute to the variability in apparent NWPs observed across cassettes of the same membrane and screen type, since the axial/tangential pressure drop forms an integral part of the measured TMP used to calculate NWP. Thus, changes in channel pressure drops could lead to significant variability during NWP measurements across TFF cassettes, despite the actual membranes within them having potentially very similar intrinsic permeabilities.

4.2.3.4 Material of construction and relative surface area of membrane housing

Within a TFF cassette under compression, the product of interest has direct contact with not only the membrane material (skin/substrate), but also system materials such as the membrane housing and components such as the silicone gaskets, internal polyethylene seals, and the feed and permeate screens. Adsorption of product to the membrane material is typically moot as the same type of membrane is use upon scale-up/-down, and the loading maintained such that the membrane area scales linearly with the volume of feed to be processed. However, with the system material, there is a possibility of non-specific adsorption of feedstock to these materials during TFF and the extent of this interaction depends on the surface area of the housing/screens, their material of construction and associated surface roughness, composition of the feedstock along with the mass of the material available for adsorption. Apart from that, operating conditions such as temperature, contact time and flow rate (static versus dynamic systems) have also been observed to affect the rate and extent of adsorption of various proteins to different surfaces (Duncan et al., 1995; Dutta Sinha et al., 2015; Santos et al., 2003).

For linear scaling of TFF cassettes, factors such as material of construction and feed volume:housing surface area ratio do not significantly affect performance since the internal surfaces such as membrane material also scale linearly and are invariably constant, provided the feed volume:membrane area ratio is kept constant upon scaling. Furthermore, the relative area of membrane housing compared to the

membrane surface area and surface area of the feed screen within TFF cassettes is significantly small. However, during non-linear scaling between the USD device and TFF cassettes, this can potentially introduce additional variables that could affect the TFF performance across scales if not accounted for. For example, the USD device does not have any permeate/feed screens or any adhesives such as polyurethane, and the system setup has a different configuration to that of traditional TFF rigs.

In the USD device, there is product contact with the stainless steel disc and the acrylic walls of the membrane housing/chamber, while for the Pellicon 2 TFF cassettes, the polyurethane housing and polypropylene screens in the feed/permeate channels come into contact with the product. In both cases, there are solid, rough surfaces available for adsorption of feedstock depending on the material of construction and available surface area. The USD device has a relative membrane housing to membrane surface area ratio of 3:1, compared to Pellicon TFF cassettes that have a ratio of approximately 150:1 per channel (two membrane flat sheets separated by a PP feed screen). The internal surface area of the housing in contact with the product is very limited in TFF cassettes, compared to the membrane and feed screen; for instance, a typical Pellicon feed channel has a feed screen[7]:membrane surface area ratio of 14800 cm^2:88 cm^2. With respect to the material of construction, both polypropylene and acrylic exhibit relatively low non-specific adsorption of proteins. These materials are widely used in the biopharmaceutical industry and are biocompatible materials; PP, acrylic and SS have been reported to have non-specific protein binding of 0.027 mg/cm^2, 0.012 mg/cm^2 and 0.001 mg/cm^2, respectively (Chandrasekaran et al., 2013; Duncan et al., 1995; Schmidt-Traub et al., 2012). Therefore, the USD membrane device is expected to exhibit relatively lower amounts of protein adsorption to the non-membrane surfaces compared to the Pellicon cassettes, due to both the material of construction with lesser protein binding and smaller surface areas available for protein interactions. However, it is important to note that the protein binding values listed above are generic and the extent of any protein-surface interactions would depend on the type of protein and its properties such as surface charge, size, etc. (Chandrasekaran et al., 2013).

Considering the three different materials that come into product contact exhibit low levels of non-specific adsorption, the loss of yield due to this adsorption is generally

---

[7] Surface area of PP screen fibers determined from the CAD model of the 3x3 unit cells used in CFD modelling in section 3.1.2 for C screen

insignificant, despite the large surface areas of the screens in TFF cassettes. This is seen with actual process data where yields of >95% are easily achievable during TFF processes, with majority of the losses usually occurring due to hold-up losses and membrane binding (Millipore, 2007). Since the adsorption to surfaces is non-specific and primarily driven by a concentration gradient, the protein comes back off the surfaces (screens, walls) when the bulk concentration crashes during a buffer flush step carried out to recover the protein in the system, and thus majority of the product is usually recovered with a buffer flush in TFF processes. Yields of >99% were obtained using Pellicon cassettes with different membranes and feed screens, across different molecules such as BSA, human gamma globulin and bovine gamma globulin (Kinzlmaier and Goodrich, 2016; Millipore, 2018a, 2016, 2003).

Considering the relatively low binding of proteins to the system materials of both devices, combined with the high recoveries achieved during processing, any adsorption of protein to non-membrane surfaces should therefore be negligible and feed composition in contact with the membrane for both the USD device and Pellicon cassettes would be nearly identical. However, reversible non-specific adsorption of proteins to surfaces can have an impact on the product quality when carrying out non-linear scale-ups between dissimilar geometries that have different materials of constructions and associated surface roughness. Previous work have shown that surface roughness of stainless steel has a direct correlation with the aggregation of mAb molecules due to interfacial shear effects (Bee et al., 2010; Biddlecombe et al., 2007; Gispert et al., 2008). Even though there were no signs of cloudiness when processing feedstock using the USD device and Pellicon cassettes in section 5.2.2 indicating no discernible protein aggregation, future work to compare the feedstock before and after processing to compare ratio of monomeric versus aggregated proteins in the USD membrane device is required. This is discussed as future work in section 8.2, as well as work to investigate effect of long processing times and relatively higher average shear rates in the USD device on product quality.

4.3 Development of the scale-up methodology

This section investigates the scaling rules required to develop a robust and predictable scale-up model that allows non-linear scale-up from the USD membrane device to tangential flow filtration and the different non-dimensional parameters that need to be maintained and kept constant upon scaling.

4.3.1 Determination of Reynolds number

To study the hydrodynamics of any system, the Reynolds number is a good dimensionless number that is often used to perform scaling regardless of geometric similarity. To that effect, the Reynolds number for both the USD membrane device and screened channels for typical operating conditions were determined and compared. It is particularly important because if the average wall shear rate is to be used as the scaling parameter, which is a strong function of the hydrodynamics and flow regimes occurring at the two scales, similar flow regimes need to be established across both scales to enable a successful scale-up.

Reynolds number is typically used to define the flow regime within a fluid flow system, however, determining Reynolds number for screened channels can be quite challenging and complex, with no set criteria or limits that allow the flow regime to be accurately characterised and determined to be laminar, transitional or turbulent. Tangential flow filtration processes are typically operated at high pressures, which generate circulating eddies that can create microscale turbulence at relatively low Reynolds numbers and as a result, standard Reynolds number equations cannot be used to accurately determine the flow regime in the screened TFF cassettes and the USD membrane device, where large rotational speeds can create significant flow instabilities and increase the Reynolds number from laminar to turbulent regime.

In the case of tangential flow filtration, which is a pressure and mass transfer-controlled process, the dimensionless mass transfer group, namely Sherwood number, is a better alternative to Reynolds number to determine flow regimes. The Sherwood number (Sh) represents the ratio of convective mass transfer (k) to the rate of diffusive mass transport (D/L) can be expressed as a function of Reynolds number; the coefficients and exponents are specific for a given module geometry and feed material. Table 1.2 lists the various Reynolds number exponents for the different filtration modules and flow regimes, and can be used to accurately determine the flow

regime if the Reynolds number exponent can be empirically determined by plotting permeate fluxes in the mass transfer-controlled region using process feed (to have membrane polarisation and hence mass transfer driven flux) as a function of operational module Reynolds number. Limiting flux was used as the dependent parameter since the limiting permeate flux is solely a function of mass transfer and is controlled by the shear rates that govern the rate of back-transport of particles away from the membrane surface and provides a good approximation to the Sherwood number.

Experiments with 20 g/L *Saccharomyces cerevisiae* in total recycle mode were conducted for three different TFF module configurations and permeate fluxes incrementally stepped up to their respective limiting fluxes for each operational condition. Figure 4.14 shows the plots of limiting permeate flux versus Reynolds number for the USD membrane device, P2 mini V screen cassette and an open unscreened channel. The single unscreened feed channel cassette, 0.55 mm in thickness, was fabricated (UCL Biochemical Engineering workshop) to represent slit flow in an open channel, to allow a direct comparison of flow regimes in screened and unscreened TFF channels.
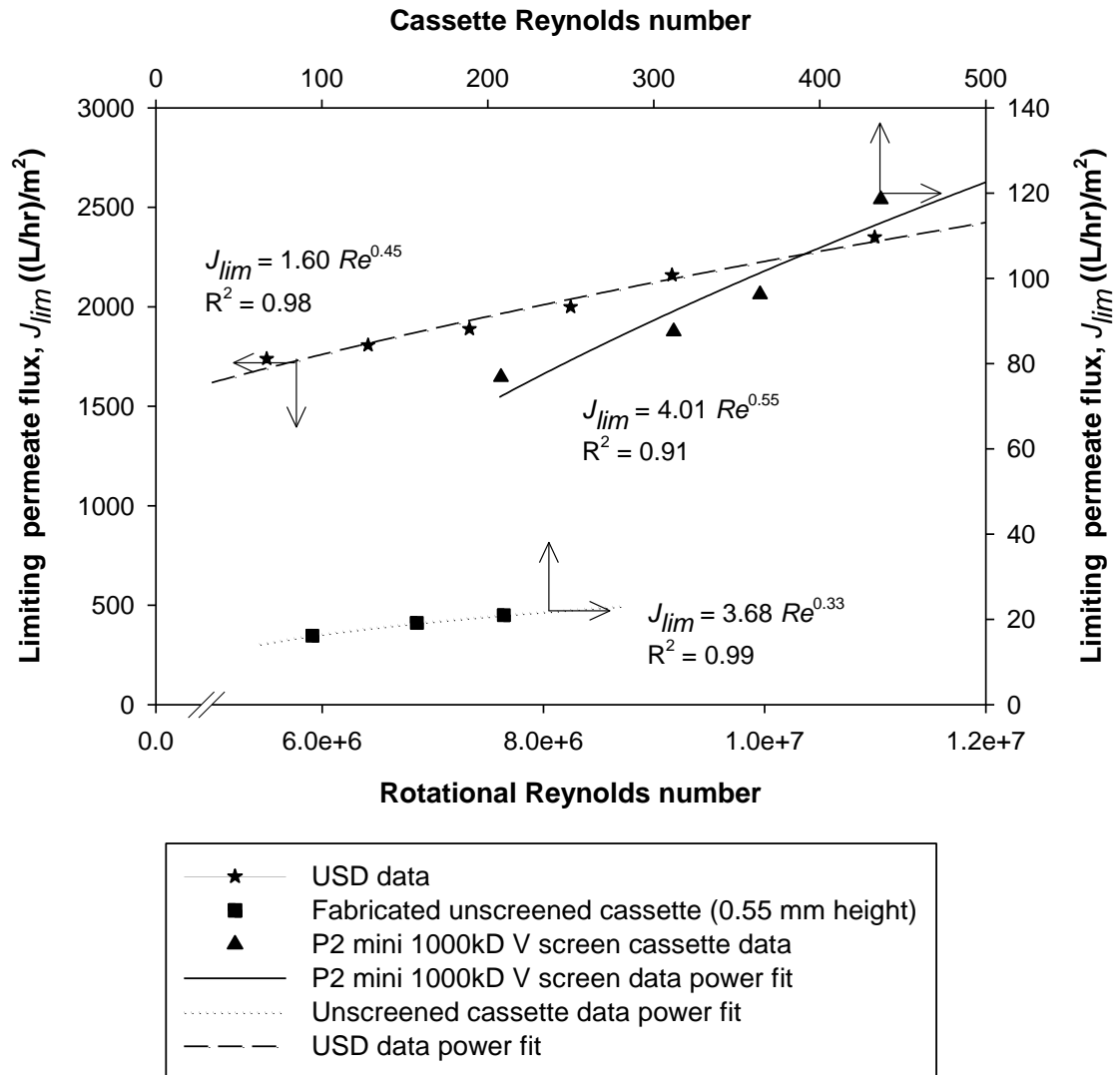
Figure 4.14 Experimental results of limiting permeate fluxes versus Reynolds number for the USD membrane device, 1000 kDa Biomax Pellicon 2 mini (V screen) and the in-house fabricated open channel cassette, used to determine fluid flow regime for operating conditions: 3000-6000 RPM (USD membrane device), feed flow rates of 16.5-35 LMM (V screen) and 9-20 LMM (0.5 mm open feed channel cassette). Feed material used was 20 g/L *Saccharomyces cerevisiae* in 0.1% (w/v) PBS at 25±1 °C, and experiments carried out in total recycle mode.

Within experimental errors and for the range of typical operating conditions explored, the calculated exponents proved the flow regime to be predominantly laminar in all the TFF modules. The Reynolds exponents for the screened channel, open channel and USD membrane device were evaluated to be 0.55, 0.33 and 0.45 respectively, which were close to the laminar flow exponent values for screened channel, slit flow and stirred-cell units with Reynolds exponents of 0.50, 0.33 and 0.55 respectively

(Table 1.2). This is particularly useful information since Cheryan (1998) suggests that screened TFF cassettes typically operated within the turbulent regime based on the relationship between channel pressure drops and feed flow rate, and the corresponding power exponent (n) of the feed flow rate in the pressure drop equation (n=1 for pure laminar flow and n=1.5 for turbulent flow). Due to the presence of screens in Pellicon cassettes, the power exponent n is around 1.3-1.5 depending on the screen type and hence would appear to be turbulent. However, the experimentally determined Reynolds exponent in the mass transfer coefficient correlation, which provides a more accurate definition of the flow regime created within the cassettes, proved the flow to be laminar when operated within the recommended feed flow rates for the Pellicon range.

4.3.2   Operational parities across scales

To have similar performances across scales, certain key operational conditions need to be maintained constant upon scale-up, as discussed in this section.

4.3.2.1   Identical membrane loading

For a standard TFF microfiltration process such as concentration, the process is terminated when a rapid and sudden increase in TMP occurs or a predefined maximum TMP limit is reached. This process endpoint is typically characterised as volumetric loading capacity or solids loading capacity. Volumetric loading is the total volume of liquid that passes through the membrane as permeate (expressed as L/m^2), while the solids/membrane loading refers to the concentration of solids that the membrane is exposed to (expressed as g/L of feed per m^2 membrane surface area).

The solids loading influences the level of cake build-up on the membrane; microfiltration with particulate heavy feeds are extremely dependent on the $g/L/m^2$ parameter, as the dirty feed accumulates and builds up on the membrane rapidly giving the membrane a limited "capacity" like a depth filter or normal flow membrane filter, even with permeate flux control. The solids and volumetric loading limits on the membrane restrict the microfiltration process. For UF processes, there is a bit more leeway since the process is more steady-state and the membrane fouls much slower, provided sensible flow rates and TMPs are used. As a result, the volume does not matter too much for UF, but in the case of TFF-MF, there is a variable capacity on the

membrane, in L/m^2, (at a given TMP, initial solids loading and feed flow rate) that can be processed through the membrane before the solids loading capacity of the membrane is reached and an uncontrollable rise in TMP is observed.

The membrane loading, *i.e.*, the effective load of solids on the membrane, dominates the maximum capacity of the membrane sizing at the selected operating conditions. Processing 100 L of 20 g/L is not the same as processing 10 L of 200 g/L despite the membrane seeing the same load, due to the mechanics of polarisation and how the membrane reacts to different concentrations of feed material. The membrane loading assumes the same feedstock is used upon scale-up and thus, as long as the same feedstock is used (same concentration), the membrane loading should remain constant upon scaling. Volumetric loading (volume:membrane area) in L/m^2 is normally used and maintained constant upon scale-up as it is easier to deal with volumes rather than mass, despite both parameters defining and characterising the same phenomenon.

The membrane loading capacity limit, *i.e.* maximum solids loading, is solely dependent on the characteristics of the feedstock (such as particle sizes, morphologies, etc.), particle-membrane interactions (pore size, membrane material) and the operating conditions (permeate flux, feed flow rate) as demonstrated by Pattnaik et al. (2014). For a particular feedstock, membrane type and operating conditions, the solids loading capacity of the membrane will be constant upon scale-up while volumetric capacity is inversely proportional to the operating conditions as well as the initial solids loading. Consequently, for concentration microfiltration applications, the initial concentration and composition of the feedstock should be identical at both scales and the feed volume to membrane surface area ratio should be kept constant and not exceeded upon scale-up, which ensures similar cake dynamics and processing times across scales. The capacity is also an issue when performing diafiltration operations with particulate heavy feed, where feed concentration remains constant for a constant volume diafiltration.

This membrane loading constraint does not apply to flux/TMP excursion experiments since they are run in total recycle mode and a pseudo steady-state is reached where the feed concentration and thus solids loading is constant throughout the process. Apart from that, the relatively small operational times needed for flux excursions mean that the initial pore blocking of the membrane by smaller particles in the feed is limited and kept to a minimum without affecting the process greatly, hence *pseudo* steady-

state. Therefore, the volumetric loading ratios do not necessarily need to be maintained upon scale-up when carrying out flux excursions, provided that the feed volume used is larger than the total hold-up volume of the filtration system to prevent introduction of air into the system and potentially avoid any localised concentration of particles on the membrane surface when the volume of liquid in the feed tank drops significantly to prevent good mixing, leading to an inhomogeneous feed solution with higher than average bulk concentration being pumped into the cassette.

4.3.2.2 Identical hydrodynamic conditions and membrane polarisation

The polarisation layer formed due to the accumulation of rejected particles dictates the performance of the filtration process and thus maintaining the polarisation layer by controlling the hydrodynamics across systems is vital for a robust and accurate scale-up. This was demonstrated by Zahka and Leahy (1985) for the harvest of *Escherichia coli*, where 1000 kDa UF and 0.2 μm MF membranes gave similar flux decline performances when operated at the same initial TMP, highlighting the significance of membrane polarisation in controlling process performance despite significant differences in pore sizes and membrane permeabilities. Since the polarisation layer controls tangential flow filtration, a poorly controlled polarisation layer can cause irreversible build-up of cake on the membrane and have drastic consequences on resulting fluxes.

Membrane polarisation layer is a function of the operating temperature (affects viscosity), crossflow across the membrane (controls rate of back transport away from the membrane, k) and permeate flux (controls rate at which particles are transported towards the surface of the membrane). Thus, for a given feed material, the polarisation layer is most directly affected by the crossflow rate and net permeate flux, and so can be regulated using a two-pump system with a feed/retentate pump and permeate pump, as discussed earlier in section 4.2.3.2.

The crossflow across the cassette can be controlled by regulating feed flow rate, retentate flow rate or dP across the cassette, but they have their advantages and disadvantages as discussed below:

- Feed flow rate: this is the simplest method and gives a constant wall shear rate, however pressure may increase over time as the membrane fouls. A constant feed flow control will lead to a drop in retentate flow rate along the

length of the channel thus leading to a membrane polarisation pattern moving from feed to retentate. As permeate fluxes are increased, retentate flow rate drops and as long as the permeate conversion is small, dP remains relatively constant which indicates a constant wall shear rate and a relatively uniform polarisation layer thickness.

- Retentate flow rate: retentate flow rates can be controlled using a pump or a flowmeter on the retentate line, which feeds back to the feed pump and is regulated by a PID controller to maintain constant retentate flow. The key issue occurs, for instance, when permeate fluxes are increased during flux excursion experiments for process optimisation, a constant retentate flow control will lead to an increasing feed flow (and thus wall shear rates) which in turn changes the membrane polarisation pattern on the feed side of the channel as a greater number of particles are brought into the feed channel, as well as increasing the feed pressure due to higher feed flow rate, which results in an observable increase in TMP.

- dP: controlling the polarisation dynamics using constant dP and TMP is not entirely scalable and requires complex setups to control flow and/or a pressure control valve on the permeate side. Historically, this is how it was done; however, it can lead to problems. As the concentration proceeds, the feed gets more viscous and the dP increases, and the feed pump responds by dropping the feed flow rate to control the dP within the pre-set range, thus thickening the polarisation layer. The increased polarisation then causes a further increase in dP and a positive feedback loop is generated. Furthermore, the dP at a given feed flow rate can vary across cassettes depending on the feed channel geometry and would generate different permeate fluxes; however, using a permeate pump to regulate permeate flow makes variances in dP moot, since the polarisation layer formation is influenced by the convective forces of the permeate flow as much as the skin drag from the feed channel tangential flow.

Manipulating the applied TMP and the feed flow rate from the feed pump, *i.e.*, the two primary drivers for flux across the membrane, allows direct control of the polarisation layer and this method is fully scalable. Using the TMP provides a good indication of what is happening on the membrane itself rather than just the pressure losses through the system, and it can be controlled by adjusting the retentate valve, or more

217

commonly for open membranes, using a combination of the permeate pump and the retentate valve.

4.3.3 Development of the USD model

4.3.3.1 Scale-up rules

To obtain identical performances upon scale-up, there are key scaling rules that need to be followed, to ensure the operational parities mentioned previously in section 4.3.2 are achieved across scales. The following parameters are to be constant when scaling-up from the USD membrane device to the screened Pellicon cassettes:

- Identical feed characteristics (homogeneity, composition, solids concentration).

- Identical feed channel/path length (constant across the Pellicon cassette range).

- Constant membrane loading (g/L/m2, V/A).

- Constant operating temperature (controlled to ±2 °C).

- Identical membrane type and cut-off/pore size.

- Constant averaged wall shear rates across scales (RPM of disc in USD membrane device corresponding to the feed flow rate for Pellicon cassettes to generate similar wall shear rates).

- Permeate pump/valve control for open membranes (>300 kDa) to regulate permeate flux.

- Low permeate conversion ($Q_F/Q_P \leq 30\%$) to have relatively constant feed flow/wall shear rates, average bulk concentration and mass transfer across the feed channel(s).

- Identical volumetric concentration factor (VCF), number of diavolumes (N).

- Minimum operating volume must be greater than the sum of system and cassette hold-up volume to avoid introduction of air into the system and formation of localised concentration gradients.

- Integrity of USD membrane discs and Pellicon cassettes must be checked by comparing against water flow rate tests (or NWP) and pressure drop data in the release specification, respectively, for the membrane used.

4.3.3.2 Development of prediction protocol

This section focuses on formulating a robust scale-up model that allows prediction of scale-up performance, going from the USD membrane device to large scale screened TFF cassettes, where TMP is expressed as a function of the permeate flux imposed, along with a multitude of other system and cassette-related components.

4.3.3.2.1 Determination of USD model coefficients and viscosities

The first step is to carry out the small scale experiments using the USD membrane device at a given disc rotational speed (RPM) to characterise the filtration/fouling performance using the given feed material, and for a flux excursion/optimisation experiment, the flux-TMP data can be modelled and fit to a first-order increasing to maximum exponential equation:

$$J = \alpha \cdot \left(1 - e^{-\beta \cdot TMP}\right)$$

Equation 4.1

The coefficients α (LMH) & β (1/bar) are feedstock-membrane specific parameters that can be determined experimentally. Rearranging Equation 4.1 to make TMP the subject of the formula yields:

$$TMP = \frac{\ln\left(1 - \dfrac{J}{\alpha}\right)}{-\beta}$$

Equation 4.2

Coefficient α, the limiting permeate flux of the process, is a strong function of the wall shear rate, while β is dependent on both the wall shear rate and the specific interactions between the membrane and the feed material used, and represents the rate of transition from the pressure-driven flux to the mass transfer-driven flux.

The viscosity of the feed and permeate streams from the USD experiments also need to be accurately determined since the prediction model relies on the accuracy of the measured viscosity values, particularly for non-Newtonian liquids such as protein and particulate containing feed material, where the apparent viscosity of the solution varies with the shear rate applied.

4.3.3.2.2 Establishing system pressure drop correlations

The pressure losses across the system and its flow path needs to be accurately characterised, as they are an integral component of the measured TMP across the cassettes and cannot be isolated. The system pressure drops would effectively add to the pressure limits of the cassette and system in use, and for processes with low optimum TMP, could cause significant discrepancies between actual and measured TMP.

The dP at different feed flow rates and viscosities of test solution for the AKTA Crossflow and Sartoflow Advanced was measured using the protocol described in section 2.2.20. Part of the results are shown in Figure 4.15.
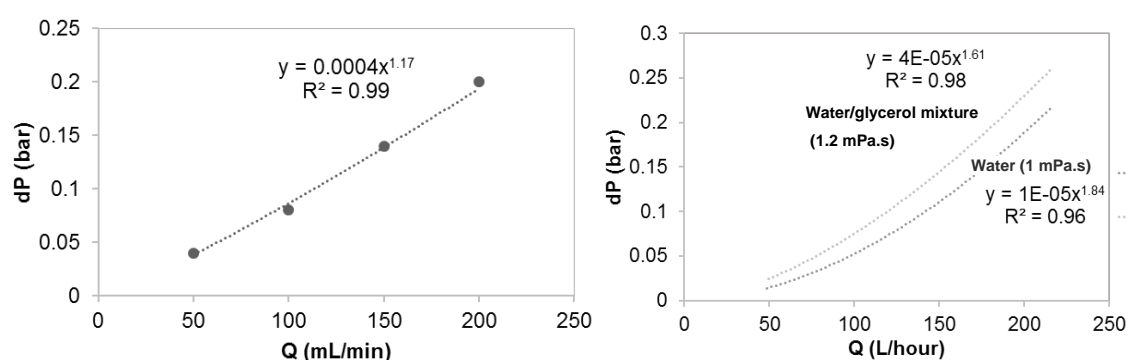
Figure 4.15 Experimental system dP as a function of operating feed flow rates for the AKTA Crossflow (left) and Sartorius Sartoflow advanced system (right).

The system pressure drop correlations for the two systems were determined to be:

$$\text{System } dP_{\text{AKTA Crossflow}} = 3.95 \times 10^{-3} \cdot \left(Q_F - \frac{JA}{120} \right)^{1.165} \cdot \mu_F^{0.33}$$

$$\text{System } dP_{\text{Sartoflow Advanced}} = 5 \times 10^{-3} \cdot \left(Q_F - \frac{JA}{120} \right)^{1.823} \cdot \mu_F^{0.69}$$

Equation 4.3

where Q_F is the feed flow rate (LMM), J is the permeate flux (LMH), A is the total membrane surface area (m^2) and μ_F is the dynamic viscosity of the feed (Pa.s). Since all dP versus feed flow rate tests were conducted at zero permeate flux, the average feed flow $\left(Q_F - \frac{Q_P}{2} \right)$ is used instead of feed flow rate (Q_F) in the correlations when net permeate flux exists (J>0).

4.3.3.2.3 Feed channel hydraulic characterisation

As the feed screen embosses into the membrane surface, the effective average channel height is primarily dictated by the compressive force applied to the cassette, the compressibility of the membrane/feed screen and uniformity of the weave pattern (which depends on manufacturing tolerances). As a result, the effective feed channel height cannot be directly assumed equal to the spacer thickness and assumed constant across cassettes of the same screen/membrane type. Furthermore, both the flow profiles and the pressure drops across the screened channel are a function of the screen variables such as weave pattern, wire diameter, mesh count, mesh opening, overmolding and orientation of the wires (Da Costa et al., 1994). These screen characteristics are prone to vary between individual cassettes of the same manufacturing lot and can influence the observed channel pressure drops at a particular feed flow rate.

Consequently, a method to determine the average channel height during operation, taking in account varying degrees of membrane embossing due to the spacer, cassette-to-cassette variations due to manufacturing tolerances and potential

deformability/expansion effects upon initiation of feed flow through the cassette is required, which can only be achieved by experimental tests to obtain accurate results.

In order to accurate characterise the feed channel hydraulics for Pellicon cassettes, a feed flow rate versus average feed channel height correlation was derived from the CFD simulation results (section 3.2.3.2) to characterise and account for any potential variations of feed screen characteristics and torque applied to the cassette. The feed flow rate required to generate a dP of 1 bar using water (25 °C), at zero net permeate flux, can be used to determine the average feed channel height for a given Pellicon cassette:

$$h\,(\text{A screen}) = 0.163 \cdot Q_{F_{dP=1\,bar}}^{0.366}$$

$$h\,(\text{C/V screen}) = 0.129 \cdot Q_{F_{dP=1\,bar}}^{0.452}$$

Equation 4.4

where h is the average height of the feed channel (mm) and Q_F is the feed flow rate recorded at 1 bar channel pressure drop (LMM).

The correlations in Equation 4.4 were experimentally validated by comparing physically measured thicknesses of the feed channel against the CFD predicted heights for four different Pellicon cassettes using Equation 4.4. The actual feed channel heights were determined by cutting open the cassettes and measuring the total thickness of the embossed feed channel and subtracting the combined thicknesses of the respective screen and membranes. The results are shown in Table 4.3; all measured thicknesses were reported to ±0.1 mm due to the sensitivity of the vernier caliper used, as well as the compressible nature of the membranes, which introduced certain degree of uncertainty associated with the measurements. The results also show the potential variability in feed channel heights across different cassettes of the same membrane type and screen and consequently, the importance of accurately characterising the average feed channel height for a given cassette used in operation.

		P3 micro A screen (10 kDa Biomax)	PXL C screen (10 kDa Biomax)	PXL C screen (300 kDa Biomax)	PXL C screen (30 kDa Ultracel)
Measured quantities	Membrane thickness, T_m (mm)	0.30-0.32			0.10-0.12
	Total thickness of 2 membranes and feed screen, T_T (mm)	0.91-0.92	0.89-0.91	0.99-1.01	0.51-0.53
	Effective feed channel height (mm) = T_T - $2T_m$	0.31±0.02	0.30±0.02	0.38±0.02	0.30±0.02
Eq. 4.4	$Q_{F_{dP=1bar}}$ (LMM)	5.7	5.33	8.5	6.9
	h (mm)	0.28	0.30	0.36	0.33

Table 4.3 Comparison between physically measured channel heights versus predicted heights using the semi-empirical model (Equation 4.4) for different Pellicon cassettes.

As mentioned previously in section 4.2.3.3, the feed pressure drops can be quite variable depending on the average feed channel height of the particular cassette in operation (Figure 4.13) and could result in drastically different performances both in terms of flux and TMP, since the average wall shear rates and channel pressure drops would be different depending on the effective feed channel height at a given feed flow rate across different cassettes. This is particularly important for concentration experiments where the viscosity of the retentate increases as the concentration proceeds and the observed dP would directly depend on the viscosity of the retentate as well as the average height of the feed channel used in the TMP prediction model.

Once the average feed channel height is determined, Equation 3.17 can be used to calculate the feed flow rate required to achieve USD-equivalent average wall shear rates in the Pellicon cassettes, and to predict channel pressure drops for the feed material at the calculated operating feed flow rate.

4.3.3.2.4 Permeate channel hydraulic characterization

When feed flow is initialised and net permeate flux exists, there is an additional pressure drop incurred as the permeate stream is forced past the tight permeate

screen and out the permeate outlet. Assuming a low permeate conversion (<30%) and a low water-like viscosity of the permeate, the pressure drop across the permeate channel (ΔP_{Ps}) was modelled using CFD (3x3 unit cell, 2/1 square twill right-hand weave, 0.165 mm fibre diameter, overall channel height of 0.32 mm and 27.6 strands/cm)(Steen, 2015) for a range of low viscosities (0.001-0.003 Pa.s) and permeate fluxes (10-500 LMH). The simulation results were subsequently used to develop a permeate pressure drop correlation as a function of permeate flux and permeate viscosity. Figure 4.16 shows the CFD simulated pressure drops as a function of permeate viscosity and permeate flux, curve fit using a linear regression model in Equation 4.5.
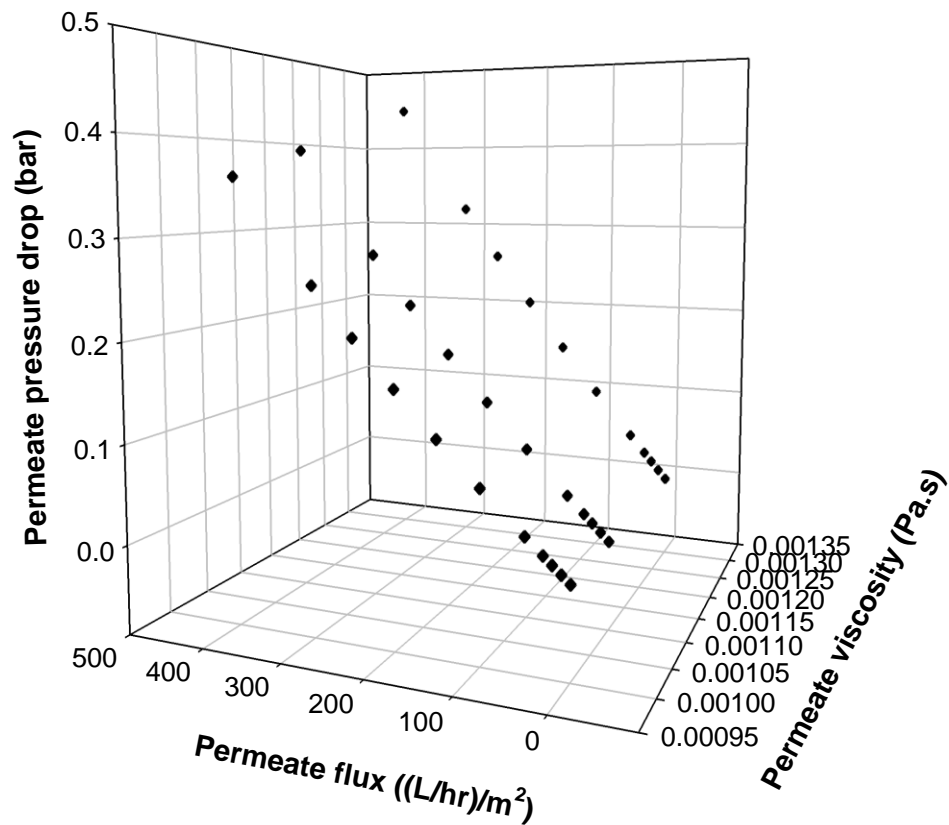
Figure 4.16 3D scatter plot of pressure drop due to permeate screen versus permeate flux versus permeate viscosity determined using CFD simulations for a constant permeate channel height of 0.32 mm.

$$\Delta P_{Ps} = -0.033 + \left(0.000965 \cdot J \right) + \left(26.39 \cdot \mu_P \right)$$

Equation 4.5

where μ_P is the permeate viscosity (Pa.s) and J is the permeate flux (LMH).

The permeate channel height of 0.32 mm was assumed constant for all cases despite known variations observed in overall permeate channel heights that result in non-zero TMP observed at zero net permeate flux (section 4.2.2.2). However, since the term TMP' incorporates that variation and its consequence on net TMP at a given flux, the minimum height of 0.32 mm for the permeate channel (equal to the woven permeate screen thickness in Pellicon cassettes) was considered to be a good approximation. The pressure loss due to permeate flow in the narrow screened permeate channel is reflected in the addition feed pressure/measured TMP which is required to overcome this resistance to flow without effectively contributing to pressure-driven flux. The pressure drop incurred in the permeate channel due to the tight screen (compared to the feed screens for the Pellicon devices, as seen in Table 1.1) creates a significant resistance to permeate flow that is not measured by the pressure gauge on the permeate line, since the gauge measures pressures downstream. Thus it is vital to accurately account for this pressure drop component as it would contribute to a higher feed pressure when there is a net positive permeate flux through the membrane, without contributing to the pressure derived flux component of the measured TMP.

To confirm the theory, permeate pressure drop in a Pellicon cassette was measured by pumping water through the permeate channel and blocking off the feed channel. Experiential data was compared against CFD simulated data for a permeate channel height of 0.32 mm. Figure 4.17 shows the permeate pressure drop as a function of permeate flux (or the feed flux into the permeate port in this case). >> can see that for a moderate conversion of feed to permeate (< 30%) and moderate fluxes of 100 LMH on average, the model predicted permeate pressure drop is similar to the experimental pressure drops. The experimental data starts to deviate from the model at higher permeate flow rates, but it could be attributed to the more compressed singular permeate channel present in the smaller P3 micro devices which is narrower than the 0.32 mm channel height assumed for the CFD modelling. Furthermore, permeate fluxes of greater than 200 LMH is seldom achieved during operation, due to high rates of fouling that accompany high permeate fluxes.
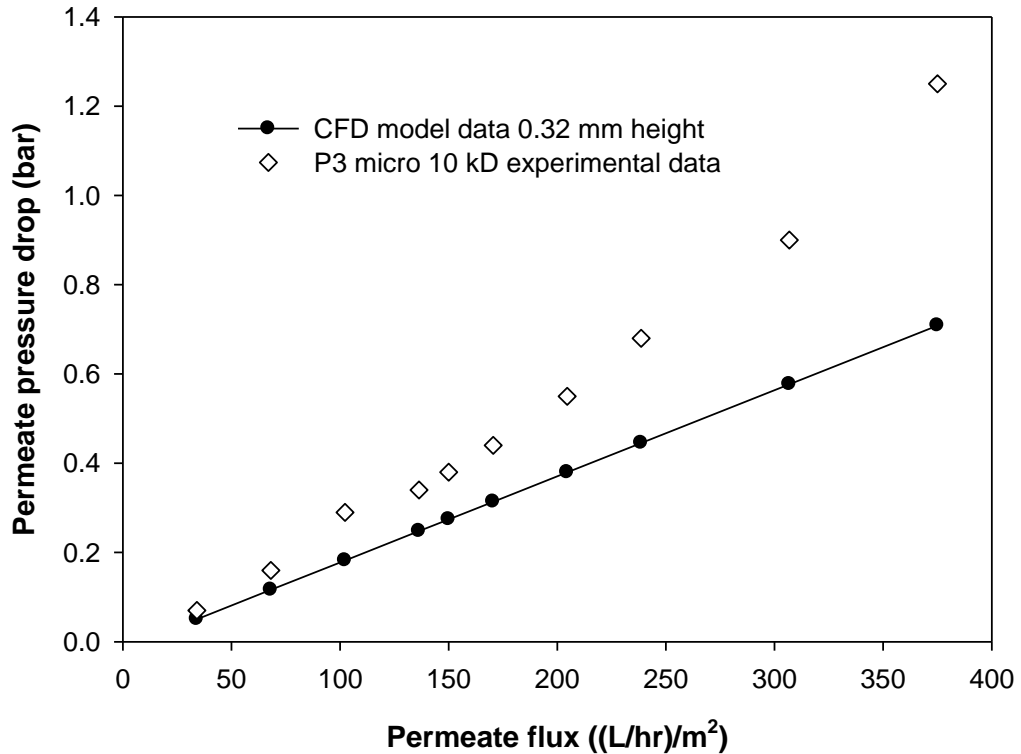
Figure 4.17 Experimental versus CFD simulated permeate channel pressure drops. A Pellicon 3 micro cassette (10 kDa) was used, with water flowing through one permeate port out to the other, and both feed and retentate ports closed off. CFD simulation carried out for a permeate channel unit cell model of fixed height (0.32 mm thick) and viscosity of 0.000894 Pa.s (water at 25 °C).

The effect of this permeate pressure drop due to the permeate screen is observable in water flux experiments for the Pellicon cassettes and flat sheet discs for 500 kDa Biomax membrane, as shown in Figure 4.18. The permeate screen channel pressure drop is particularly important for open membranes (>300 kDa) where higher permeate flux is achieved. When the TMP was corrected by accounting for pressure losses in the permeate channel, the NWP value of 3857 LMH/bar (equal to the gradient of the flux versus TMP linear plot) gets much closer to the flat-sheet membrane disc NWP of 3770 LMH/bar, compared to the 829 LMH/bar without any TMP corrections. Accounting for system pressure drops and channel pressure drop components would not make a significant impact and would merely translate the linear plot to the left and reduce the y-intercept value without affecting the gradient and thus the NWP value would be unchanged.
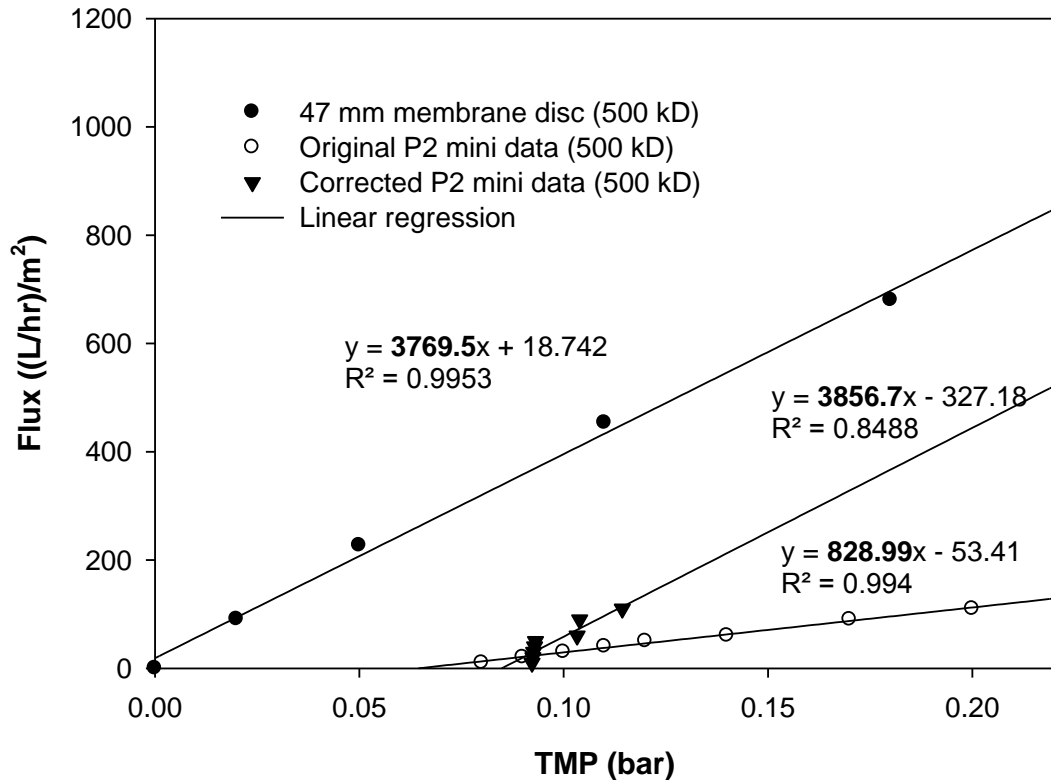
Figure 4.18 Experimental flux versus TMP plots for 500 kDa Biomax membrane in the USD membrane device and P2 mini V screen cassette using water at 25 °C. Gradient of the lines are highlighted in bold and equal to the NWP at 25 °C. P2 mini TMP values were corrected by subtracting the pressure losses due to the permeate screen at a given flux and a viscosity of 0.000894 Pa.s.

4.3.3.2.5 Calculation of flow initialised TMP (TMP') at zero permeate flux

The corresponding TMP value at the empirical 1 bar dP-feed channel height test can be used to determine the effect of the permeate channel hydraulics on the resulting TMP with permeate closed. Due to complexities of the flow in tangential flow filtration with regards to measured TMP versus actual TMP acting on the membrane, Ma et al. (2010) proposed an alternative definition for the measured module TMP. TMP can be split into its two pressure drop components, namely the tangential pressure drop component (dP) which does not actively contribute to the driving force for filtration and the applied pressure drop (ΔP_A), the difference between the feed and permeate pressures and is proportional to the actual TMP that drives liquid through the membrane:

$$TMP = \Delta P_A - \frac{dP}{2}$$

<div align="right">**Equation 4.6**</div>

Variations in permeate channel thickness across the flow path will influence the value of ΔP_A, where it becomes larger or smaller than the average feed channel pressure drop component (dP/2) at a given flow rate, leading to an overall net positive or negative TMP at zero permeate flux. ΔP_A is a function of the average feed flow rate ($\overline{Q_F}$) across the channel and viscosity of the feed solution, μ_F:

$$\overline{Q_F} = \left(Q_F - \frac{JA}{2} \right) = \left(Q_F[\text{LMM}] - \frac{J[\text{L/m}^2/\text{hr}] \cdot A[\text{m}^2]}{120[\text{min/hr}]} \right)$$

<div align="right">**Equation 4.7**</div>

For a given feed viscosity (at 25 °C), the applied pressure drop increases with the power of the average feed flow rate across the channel:

$$\Delta P_A = \frac{dP}{2} + TMP = C \cdot \left(\overline{Q_F} \right)^n$$

where,

$$C = 1120 \cdot \mu_F \cdot 10^{\log\left(0.5 + TMP_{dP=1\,bar} - (n \cdot \log(Q_{F_{dP=1\,bar}})) \right)}$$

$$n_{\text{A screen}} \; (0.18 < h < 0.32) = 7.67 \cdot h^3 - 7.01 \cdot h^2 + 1.95 \cdot h + 1.10$$

$$n_{\text{C screen}} \; (0.26 < h < 0.50) = -1.22 \cdot h^2 + 0.51 \cdot h + 1.43$$

$$n_{\text{V screen}} \; (0.52 < h < 0.58) = -1.0523 \cdot h + 1.8474$$

<div align="right">**Equation 4.8**</div>

The exponent n was determined from the CFD-derived pressure drop models in Equation 3.19 by plugging in the viscosity of water at 25 °C (0.001 Pa.s) and a dP=1 bar and rearranging pressure drop as a simple power law model. The range for average feed channel heights h stated were based on the values used in the CFD simulations and based on back-calculating the heights from the feed pressure specification lines for the three screens (Figure 4.13) to obtain typically expected maximum and minimum heights for a given feed screen.

TMP' at any permeate flux, for a given feed flow rate and feed viscosity (at infinite shear rate for non-Newtonian liquid), can then be calculated using Equation 4.9, once parameters coefficient *C*, power exponent *n* and average feed channel height *h* are determined:

$$TMP'(J) = \Delta P_A - \frac{dP}{2} = 1120 \cdot C \cdot \left(\overline{Q_F}\right)^n - \frac{dP(\overline{Q_F})}{2}$$

Equation 4.9

where $dP(\overline{Q_F})$:

$$dP_{A\ screen}\ (0.18 < h < 0.32) = \left[(3.525 \cdot h^{-2.763} \cdot \overline{Q_F}) + (0.194 \cdot h^{-3.023})\right] \cdot \mu_F + \left[0.0004 \cdot h^{-2.589} \cdot \overline{Q_F}^{(-0.255 \cdot h) + 2.147}\right]$$

$$dP_{C\ screen}\ (0.26 < h < 0.50) = \left[(2.873 \cdot h^{-2.983} \cdot \overline{Q_F}) + (0.292 \cdot h^{-4.12})\right] \cdot \mu_F + \left[0.164 \cdot e^{-8.958 \cdot h} \cdot \overline{Q_F}^{(-0.428 \cdot h) + 2.163}\right]$$

$$dP_{V\ screen}\ (0.52 < h < 0.58) = \left[(1.381 \cdot h^{-4.091} \cdot \overline{Q_F}) + (240.6 \cdot h^2) - (250.3 \cdot h) + 61.678\right] \cdot \mu_F$$
$$+ \left[0.00001 \cdot h^{-8.908} \cdot \overline{Q_F}^{(4.762 \cdot h^2) - (5.719 \cdot h) + 3.592}\right]$$

4.3.3.2.6 Prediction protocol

A prediction protocol that highlights the steps needed to carry out a prediction of large scale tangential flow filtration using flux-TMP data from the USD membrane device, along with scale-dependent parameters and correlations introduced to account for the phenomenon discussed in the earlier sections, was created and is shown in Figure 4.19.

Develop system pressure drop correlation for TFF rig using water and glycerol/water mixtures, as a function of feed flow and viscosity **(Equation 4.3)**

↓

Determine feed (μ_F) and permeate viscosity (μ_P), along with USD model parameters *α*, *β* (**Equation 4.1**)

↓

For the TFF cassette, record the feed flow rate, $Q_{F_{dP=1\,bar}}$ ((L/min)/m²) and corresponding TMP (bar) needed to generate P_F or dP=1 bar (P_R=0) at zero permeate flux using water at 25 °C

↓

Determine average feed channel height, h, from the $Q_{F_{dP=1\,bar}}$ using **Equation 4.4** and evaluate TMP' using **Equation 4.9**

↓

Predict the flux versus pressure drop relationships at large scale with *α*, *β*, **TMP'**, **permeate screen pressure drop** and **system pressure drop** using **Equation 4.10**

↓

Verify model prediction against large scale experiment data, following the scale-up rules outlined in **4.3.3.1**

Figure 4.19 Flowchart highlighting the chronological steps of the prediction protocol to predict TMP at large scale using USD inputs and other parameters.

The TMP for a given permeate flux can be predicted using Equation 4.10:

$$TMP(bar) = TMP'(J) + \underbrace{[-0.033 + (0.000965 \cdot J) + (26.39 \cdot \mu_P)]}_{\text{Pressure drop due to permeate screen}} + \underbrace{\frac{\ln\left(1 - \dfrac{J}{\alpha}\right)}{-\beta}}_{\text{USD model}} + \underbrace{system\,dP_{\overline{Q_F}}}_{\text{Pressure losses due to system}}$$

where TMP'(J) is the Feed and permeate channel pressure drops.

Equation 4.10

At a constant feed flow rate, $\overline{Q_F}$ is a function of the permeate flux, J, and thus all the pressure drop components can be expressed as functions of J. The resulting net TMP for screened TFF cassettes therefore is a combination of system pressure drops, feed and permeate channel resistances, plus the actual driving force required to force the feed through the membrane at a given permeate flux.

4.3.3.3 Model assumptions

The assumptions for the developed prediction model (Equation 4.10) are:

- Low permeate conversion (<30%) such that concentration, flow velocity, feed viscosity and mass transfer rates across the feed channel are relatively constant.

- Feed pressures <2.5-3 bar for A and C screen and <1.5-2 bar for V screen cassettes, to avoid plugging of the narrow feed channel(s)/feed port and compression of the active layer of the membrane (reference).

- No initial particle deposition/cake formation, particularly near the inlet of the feed port/channel where local TMP maxima exist.

- Relatively clean and unobstructed feed screen with no particles trapped within screens and flow path of the feed flow.

- Membranes with similar NWP across scales, and are not fouled to an extent where the membrane permeability drops below the permeability of the polarisation layer.

- A properly compressed cassette, with all internal seals correctly applied and no extreme deformation of the feed channel.

- No significant differences in the composition of the feed material and the operational temperature throughout the experiments.

4.4 Conclusions

The key differences between tangential flow filtration and small scale stirred dead-end filtration systems were discussed and a scale-up methodology and model was developed to bridge these differences across scales. Firstly, factors that do not influence the tangential flow filtration process itself, namely the cassette and feed/permeate channel-related factors, yet form an intrinsic component of the overall measured TMP at large scale and can affect scale-up if not accounted for, were discussed and characterised. These factors can generate additional pressure drops and resistances to fluid flow without contributing towards any pressure-derived flux through the membrane. The non-TFF scale-up factors, along with other potential sources of variations such as available membrane surface area and variability in feed channel height, were further discussed and considered during the development of the scale-up model. Discrepancies in measured NWP across device formats and the non-zero TMPs observed at the start of the process at zero permeate flux when feed flow is initialised was investigated using CFD. The permeate channel can be assumed to be two discrete halves, and differences between the heights of these two permeate chambers can lead to an imbalance between localised positive and negative TMP gradients across the cassette that can result in non-zero TMP values at zero net permeate flux. Finally, the unusual reversal of permeate flow, typical of microfiltration operations with low optimum TMPs, and its consequences on the pressure drops achieved at the start of the filtration with no net permeate flux were discussed.

CFD modelling was used to characterise the feed and permeate channel hydraulics in Pellicon A, C and V screen cassettes to develop pressure drop models, expressed as functions of the feed flow rate, fluid viscosity and average channel height that can be empirically determined by crossflow tests at 1 bar dP using water with the

permeate closed off. The concept of applied pressure drop, the difference between feed and permeate pressures, was introduced and characterised using an empirical power model (Equation 4.8) that allows initial TMPs to be predicted, for different feed flow rates, viscosities and screen type. Finally, pressure losses due to the permeate screen when net flux is imposed was also modelled using CFD and a linear correlation developed as a function of permeate flux and permeate viscosity.

Accounting for the various resistances that exist during a typical TFF operation, a TMP prediction model that can accurately predict large scale performance was developed. The prediction model uses a combination of USD-based model inputs to characterise the fouling/polarisation profiles for a given feedstock-membrane combination, system-specific pressure drop correlations and feed and permeate screen resistances that can be easily determined using the CFD-derived equations. Finally, the rules of scale-up were established where key operational parities like the overall flow hydrodynamics and membrane loading (V:A) are required to be maintained constant upon scaling, as well as operating within specified feed pressure limits for a given screened cassette to prevent anomalous observations and deviation from model predicted data.

5 Validation of scale-up methodology and model for USD tangential flow filtration

5.1 Introduction

The aim of this section is to use different biological feedstock to validate the accuracy and robustness of the scale-up methodology and prediction model developed in the previous chapter. To confirm the potential and suitability of the USD membrane device to successfully mimic and replicate the TFF performance at scale, flux excursion experiments, as described in section 2.2.5, were performed. The permeate flux was incrementally increased until an unsteady and rapid rise in TMP was observed, which marks a clear transition from the pressure dependent region to the uncontrolled mass transfer-controlled region. The flux excursion experiments in total recycle mode are helpful in characterising the filtration process at both scales since constant feed conditions are maintained throughout the process and thus comparisons can be made under pseudo steady- state conditions upon scale-up. The current acceptance criteria in industry for truly linear scalability for Pellicon TFF cassettes is a difference of <20% in average process fluxes upon scale-up (Millipore, 2018a), and thus the accuracy of the non-linear scale-ups carried out in this chapter will be judged against this acceptance criterion.

Flux excursions at both scales were performed without any replicates deliberately for a couple of reasons. Firstly, since membrane polarisation effective controls TFF performance as discussed in section 4.2.3.2, provided the conditions of the feedstock prior to the experiments are well controlled, *i.e.*, only thawed before each experiment, kept well mixed and homogenous throughout by gentle mixing and most importantly, temperature controlled within ±2 °C, the characteristics of the different feedstock used in this chapter should remain largely unchanged and within acceptable feed variations. Secondly, since this chapter aims to validate the USD methodology and prediction model, the robustness of the model can be validated by using data without repeats and thus eliminating any additional uncertainties in the model validation part that could be attributed to potential variations in feedstock, which could be as large as ±10% depending on the nature of feedstock used. Finally, NWP tests were done on the membrane discs used in the USD device and compared against expected values and the release specification provided by Millipore to check the integrity of the membrane before use.

5.2   Results and discussion

5.2.1   Compression tester results

For commercially available large scale cassettes like the Pellicon range, apart from the Pellicon XL devices, that are not pre-compressed, the compression is another variable that needs to be accounted for upon scaling. The axial compressive force exerted in the cassette holder is essential to get the cassettes to work and function correctly; if the internal seals within the device are not enforced correctly, the feed flow would bypass the membrane entirely and end up in permeate directly. The recommended torque values for the Pellicon cassettes was between 20-22.5 Nm, but they apply to a Pellicon cassette holder only. Differences between cassette holders such as diameter of the tie rods, size and material of construction of the nuts, thread characteristics, etc. would generate different axial forces across holders at a set torque. Since a Sartorius slice holder was used to house the Pellicon 2 mini cassettes, a compression versus applied torque experiment was performed using the Sartocon slice holder and Millipore cassettes to determine the correct axial compression to be applied as per the Millipore recommendations, shown in Figure 5.1.
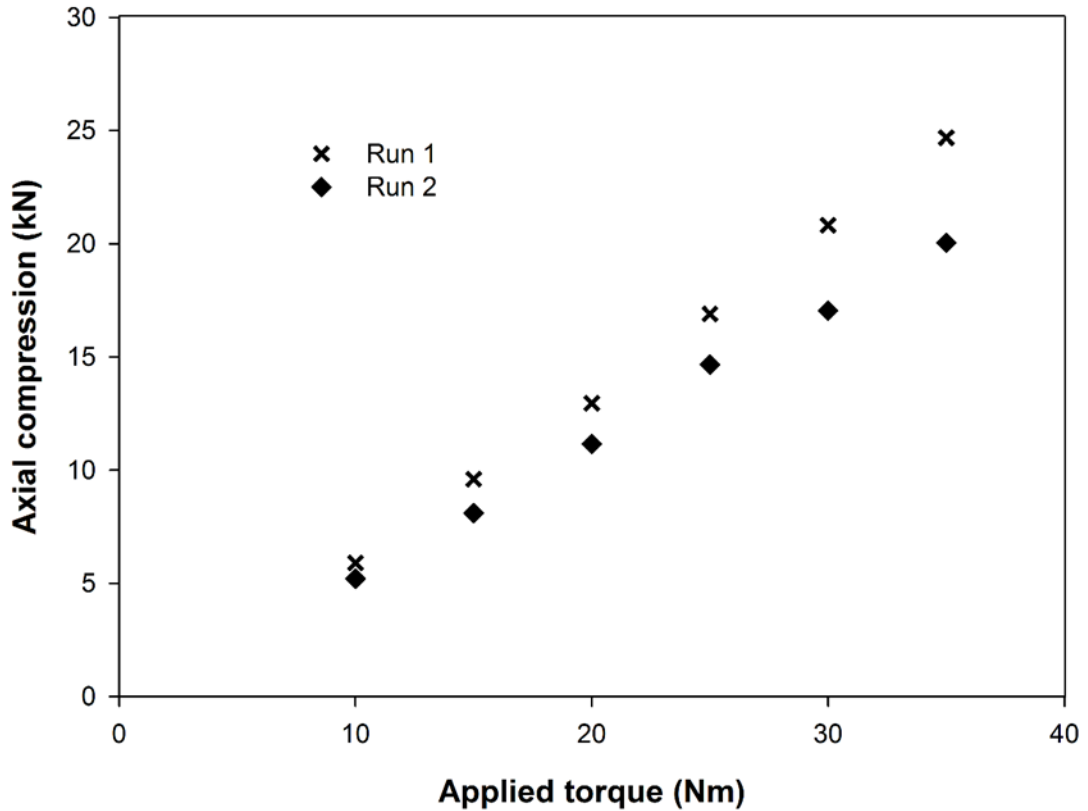
Figure 5.1 Torque versus axial compression data generated using the compression tester.

Millipore cassettes require a minimum axial compressive force of 13.8 kN to work as intended. From Figure 5.1, the average axial force at a constant temperature can be expressed as a linear function of the torque applied:

$$\text{Compressive force (kN)} = 0.58 \cdot \text{Torque (Nm)}$$

Equation 5.1

For the Sartocon slice holder, Pellicon cassettes need to be tightened up to 23.8 Nm, compared to the recommended torque of 22.5 Nm for Pellicon cassettes to ensure adequate compression using a Pellicon holder. The equation assumes that both tie rods are equally tightened and the temperature variations are kept to a minimum (±1 °C).

5.2.2 Flux versus TMP prediction for non-linear scale-ups from USD membrane device to screened Pellicon cassettes

To verify the predicted TMP data, flux excursion experiments were carried out using different biological feedstock and experimental versus predicted flux-TMP curves were plotted and compared. All flux excursion experiments were done in total recycle mode and operating temperatures controlled to 25±1 °C. Identical initial feed concentration (similar to the feed used in the USD experiments) and minimum feed volumes of 0.7 L and 75 mL for the Sartoflow Advanced and AKTA Crossflow systems, respectively, was used for each flux excursion experiment to maintain solids loading on the membrane upon scale-up and overcome the total system hold-up and ensure an appropriate level of feed/retentate was maintained in the feed vessel. The following sub-sections highlight the key variables and parameters that were evaluated/measured and used to predict TMP at large scale (Pellicon cassettes) using the prediction protocol and compare experimental versus model predicted flux-TMP data for different biological feedstock. All reported permeate flux values were normalised to a temperature of 25 °C.

For tight cut-off membranes (<300 kDa), only TMP values ≥dP/2 were explored and plotted since the optimum TMPs are typically much higher than for open membranes; the permeate flow was left unrestricted and so the permeate pump restriction was not required to operate at low TMP, unlike for the more open membranes.

5.2.2.1 Uni-variate globular protein (BSA)

A simple, single component protein feed was initially used to assess the predictability and accuracy of the scale-up model, and BSA being a model solution that is readily and cheaply sourced, it was considered an ideal feedstock as the starting point for validating the prediction model. An Ultracel regenerated cellulose membrane with a 30 kDa cut-off was used to retain the 67 kDa BSA (at 20 g/L concentration) in the retentate stream and provide high fluxes with minimum binding of the protein to the membrane surface. Table 5.1 lists the various parameters and measured viscosities required for the prediction model. The operating flow rates required to generated USD-equivalent average wall shear rate of 22900 s^{-1} (at 3500 RPM) were calculated to be 10.6 LMM and 9.7 LMM for the PXL and P2 cassettes, respectively.

Viscosity measurements (25 °C)	μ_F	0.001	Pa.s
	μ_P	0.0009	
USD exponential model parameters (Equation 4.1)	Rotational speed, N	3500	RPM
	α	252.5	LMH
	β	0.647	1/bar
	Average wall shear rate, $\overline{\gamma}_{wall}$	22875.2	s^{-1}

	Cassette (screen)	PXL (C)	P2 mini (C)	
1 bar dP test with water, 0 permeate flux (Equation 4.4)	$Q_{F, dP=1\ bar}$	6.3	5.3	LMM
	$TMP_{dP=1\ bar}$	-0.05	-0.15	bar
	Average feed channel height, h	0.32	0.30	mm

Applied pressure drop equation parameters (Equation 4.8)	n	1.46	1.47	-
	C	0.030	0.031	bar/LMM^n

	Operating feed flow rate, Q_F	10.6	9.7	LMM
Predicted pressures at t=0 (0 permeate flux)	Feed flow rate, Q_F, to generate USD-equivalent wall shear rate (Equation 3.17)	0.0409	0.00874	bar
	dP	2.04	2.15	
	ΔP_A	0.94	0.84	
	TMP'	-0.078	-0.237	

Table 5.1 Summary of the various parameters needed for TMP prediction and predicted initialised pressures at zero flux for BSA solution using 30 kDa Ultracel Pellicon XL and P2 mini cassettes.

A. USD membrane device (3500 RPM, 0.0013 m^2)
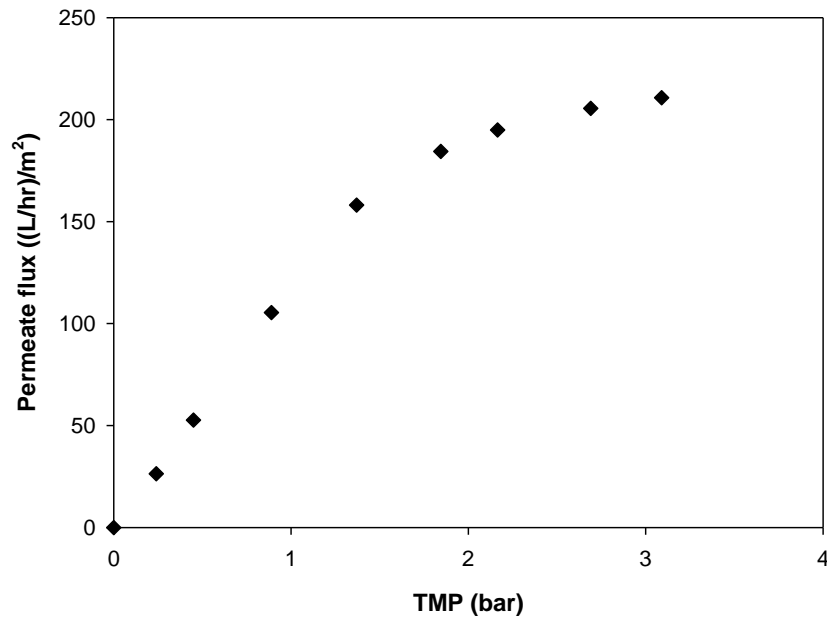
B. Pellicon XL C screen (50 cm^2)
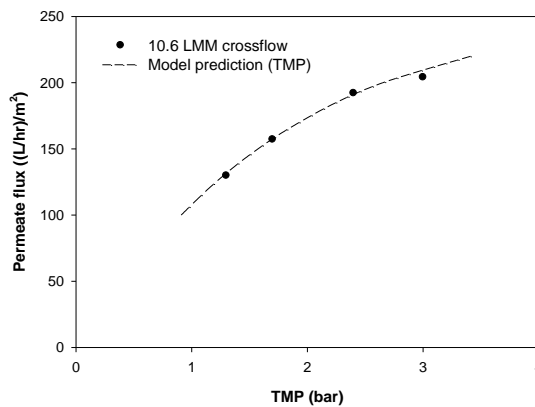
C. P2 mini C screen (0.1 m^2)
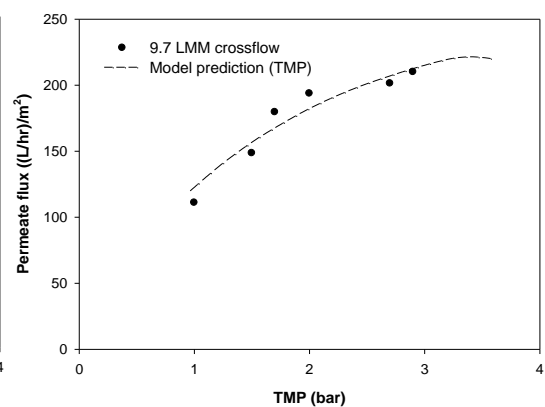
Figure 5.2 Flux excursion curves for 20 g/L BSA and 30 kDa Ultracel membrane. A. USD membrane device (3500 RPM), B. Pellicon XL C screen (10.6 LMM) and C. P2 mini C screen (9.7 LMM). Solid data points represent experimental TMP values whilst dotted line is the model predicted TMP for the range of permeate fluxes investigated at 25 °C.

From Figure 5.2, a very good agreement (<5% deviations) between predicted and experimental flux versus TMP data was observed for both the single feed channel Pellicon XL device and the larger P2 mini cassette, indicating true scalability of this method. The first-order exponential model parameters that were empirically determined using the USD membrane device was proven to accurately mimic the

filtration process and fouling dynamics that would occur in TFF cassettes, represented by excellent predictions of the limiting process flux when the membrane is fully polarised and the region between the pressure-dependent and pressure-independent region, where the critical point lies. These two parameters, amongst others, are essential to optimising any given TFF process and the USD model characterises the specific feed-membrane interactions occurring during the filtration process and provides useful scale-up data for process simulation and prediction.

The single feed channel cassettes like the Pellicon XL and Pellicon 3 micro devices demonstrate a lot more variability due to the absence of flow averaging effects that occur across multiple feed channels in the other devices with larger nominal surface areas. However, since this scale-up methodology empirically characterises the feed and permeate channel hydraulics, the predicted flux versus TMP values showed excellent agreement even for the Pellicon XL cassette using BSA. The importance of using applied pressure drops to account for the initial non-zero TMP effect seen in TFF cassettes and discussed in section 4.2.2.2 can be seen in Table 5.1, where at the feed flow rates used, the PXL and P2 mini cassettes had flow-initialised TMP of -0.08 bar and -0.24 bar at zero net flux, respectively. Thus, if the applied pressure drop correlation was not used, all predicted TMP values would be offset by 0.08 bar and 0.24 bar for the two flux versus TMP data. Furthermore, even if considering a simpler, linear scale-up from the Pellicon XL C screen cassette to the larger P2 mini C screen device, it can be seen from Figure 5.2 that different feed flow rates were required (10.6 LMM versus 9.7 LMM) to obtain the same process flux performance. This is contrary to the recommended method of maintaining the normalised feed flow rate (LMM) when performing linear scale-up, due to differences in effective feed channel heights that need to be accounted for to have a fully scalable performance. As a result, the typical discrepancies between predicted and experimental data observed upon scale-up can be attributed to differences in feed channel hydraulics across cassettes and the specific configuration and height of the permeate channels which affects the flow-initialised TMP values.

5.2.2.2 Long-chain polymeric protein (PVP-40)

PVP-40, a long chain polymer, of 10 g/L concentration was next used as feedstock to investigate the impact of differently shaped protein compared to BSA, which is a globular protein and reacts differently under pressure to PVP-40, to help further validate model prediction for UF membranes with relatively 'clean' protein feed. The membrane and cut-off used also changed to a 10 kDa Biomax PES, which would have different interactions with the solutes in the feed solution, and the process was scaled-up from the USD membrane device to C and A screen Pellicon cassettes.

Table 5.2 and Figure 5.3 summarise the prediction model parameters and resulting flux versus TMP data for the various cassettes. The operating flow rates required to generated USD-equivalent average wall shear rate of 20094 s^{-1} (at 3500 RPM) were calculated to be 15.6 LMM , 9.9 LMM and 7.9 LMM for the PXL, P3 micro and P2 cassettes, respectively.

Viscosity measurements (25 °C)	μ_F	0.001		Pa.s
	μ_P	0.00091		
USD exponential model parameters (Equation 4.1)	Rotational speed, N	3500		RPM
	α	172.9		LMH
	β	1.12		1/bar
	Average wall shear rate, $\overline{\gamma}_{wall}$	20093.7		s^{-1}

	Cassette (screen)	PXL (C)	P3 micro (A)	P2 mini (A)	
1 bar dP test with water, 0 permeate flux (Equation 4.4)	$Q_{F,\ dP=1\ bar}$	11	6.5	5.0	LMM
	$TMP_{dP=1\ bar}$	0.04	0.05	-0.05	bar
	Average feed channel height, h	0.39	0.30	0.27	mm

		PXL (C)	P3 micro (A)	P2 mini (A)	
Applied pressure drop equation parameters (Equation 4.8)	n	1.44	1.27	1.27	-
	C	0.034	0.051	0.058	bar/LMM^n

		PXL (C)	P3 micro (A)	P2 mini (A)	
	Operating feed flow rate, Q_F	15.6	9.9	7.9	LMM
Predicted pressures at $t=0$ (0 permeate flux)	Feed flow rate, Q_F, to generate USD-equivalent wall shear rate (Equation 3.17)	0.065	0.073	0.006	bar
	dP	1.92	2.01	1.97	
	ΔP_A	1.00	0.95	0.80	
	TMP'	0.036	-0.067	-0.18	

Table 5.2 Summary of the various parameters needed for TMP prediction and predicted initialised pressures at zero flux for 10 g/L PVP-40 solution using the 10 kDa Pellicon cassette(s).
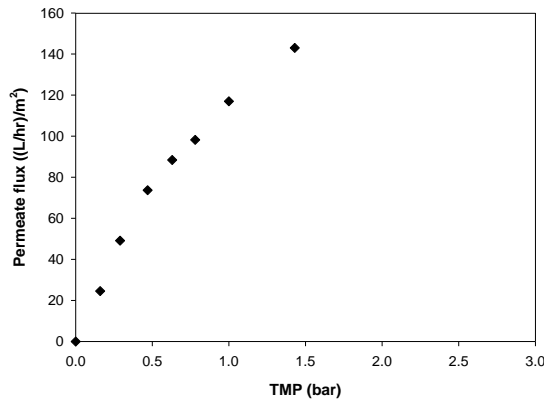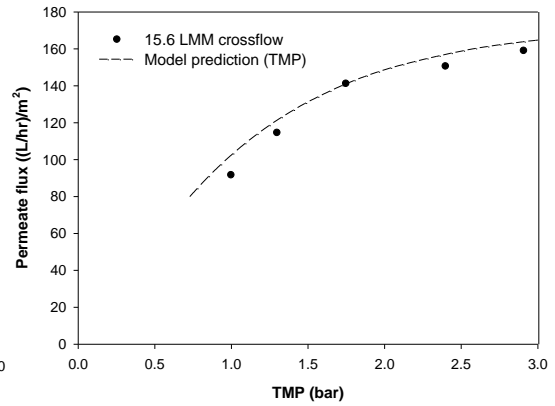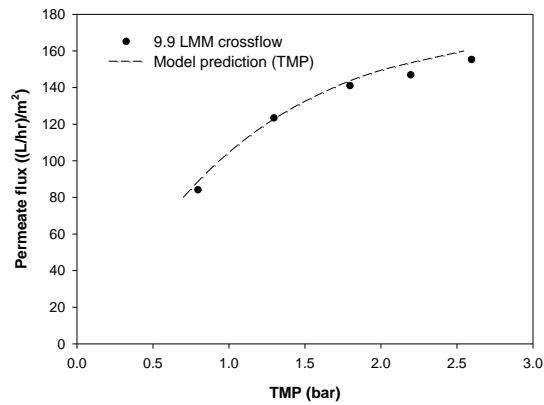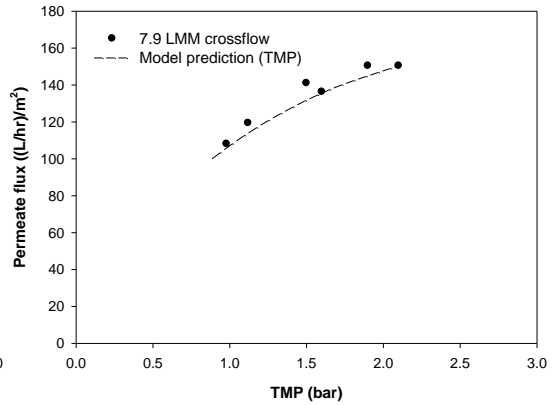
Figure 5.3 Flux excursion curves for 10 g/L PVP-40 and 10 kDa Biomax membrane using, top left: USD membrane device (3500 RPM), top right: Pellicon XL C screen (15.6 LMM), bottom left: Pellicon 3 micro A screen (9.9 LMM) and bottom right: P2 mini A screen (7.9 LMM). Solid data points represent experimental TMP values whilst dotted line is the model predicted TMP for the range of permeate fluxes investigated at 25 °C.

The predicted TMP at all fluxes were in good agreement with the experimental TMP for both C screen and A screen cassettes. This further validated the TMP prediction model using averaged wall shear rates as a scale-up parameter, which allows non-linear scaling not only from the USD membrane device to screened TFF channels but also across different screen types, which proved the robustness of the scale-up methodology and prediction model. Like the previous section with BSA as feed, experimental TMP values matched the predicted TMP through the linear region all the way to the pressure-independent region of the curve. The cassettes required

different feed flow rates to generate an identical average wall shear rate and have similar process fluxes, with the A screen cassette requiring a much lower crossflow rate than the C screen cassette since the former has a narrower feed channel due to the presence of the relatively tight A screen. It was also seen from Figure 5.3, that at any given TMP, the permeate flux was different across the different screened cassettes, which can be attributed to the variations in the effective feed channel heights for a given screen or different channel heights for different screens, the system pressure drop at the operating feed flow rate and the initial TMP value at zero flux; all these factors actively contribute to the measured TMP across the cassettes. As a result, although a constant TMP was applied, the actual driving force on the membrane was effectively different across the cassettes which led to different permeate fluxes.

5.2.2.3 Multicomponent, multivariate feed *(Escherichia coli* homogenate*)*

70 g/L *Escherichia coli* homogenate was used in this section to represent a complex, multicomponent feedstock that would be typically used in the biopharmaceutical industry. The variability of the homogenate was a good validation test of the scale-up and prediction model due to the different components such as cell debris, HCP, Fab', DNA, and proteins amongst others, all of which have different interactions with the membrane and with each other, making it harder to characterise and model their dynamics. Biomax PES membrane with a 500 kDa cut-off was used instead of regenerated cellulose as it can cope with a more concentrated and viscous material and is relatively easier to clean, and scale-up performed using C and V screen Pellicon 2 cassettes. The operating flow rates required to generated USD-equivalent average wall shear rate of 12083 s^{-1} (at 3500 RPM) were calculated to be 11.1 LMM and 21.2 LMM for the C and V screen cassettes, respectively, as shown in Table 5.3.

Viscosity measurements (25 °C)	μ_F	0.0026	Pa.s
	μ_P	0.001	

USD exponential model parameters (Equation 4.1)	Rotational speed, N	3500	RPM
	α	63.2	LMH
	β	12.43	1/bar
	Average wall shear rate, $\overline{\gamma}_{wall}$	12082.5	s^{-1}

	Cassette (screen)	P2 mini (C)	P2 mini (V)	
1 bar dP test with water, 0 permeate flux (Equation 4.4)	$Q_{F,\ dP=1\ bar}$	10	26.6	LMM
	$TMP_{dP=1\ bar}$	0.01	0	bar
	Average feed channel height, h	0.38	0.54	mm

		P2 mini (C)	P2 mini (V)	
Applied pressure drop equation parameters (Equation 4.8)	n	1.44	1.28	-
	C	0.053	0.022	bar/LMM^n

		P2 mini (C)	P2 mini (V)	
	Feed flow rate, Q_F, to generate USD-equivalent wall shear rate (Equation 3.17)	11.1	21.2	LMM
Predicted pressures at t=0 (0 permeate flux)	System pressure drop at operating Q_F	0.022	0.072	bar
	dP	2.23	1.37	
	ΔP_A	1.74	1.08	
	TMP'	0.63	0.39	

Table 5.3 Summary of the various parameters needed for TMP prediction and predicted initialised pressures at zero flux for 70 g/L *Escherichia coli* homogenate using the 500 kDa P2 mini cassettes.

A. USD membrane device (3500 RPM, 0.0013 m^2)

B. P2 mini (0.1 m^2)

- 21.2 LMM crossflow (V screen)
- 11.1 LMM crossflow (C screen)
- Model prediction (V screen)
- Model prediction (C screen)
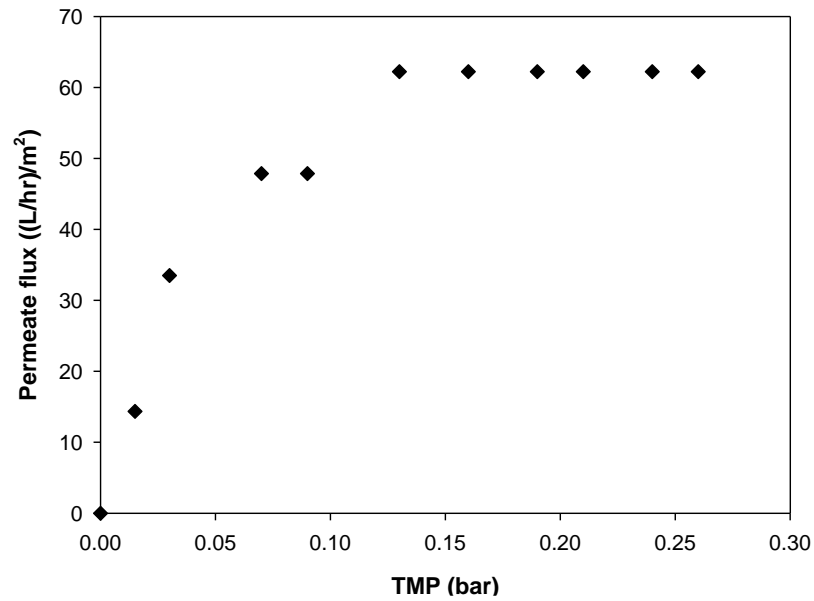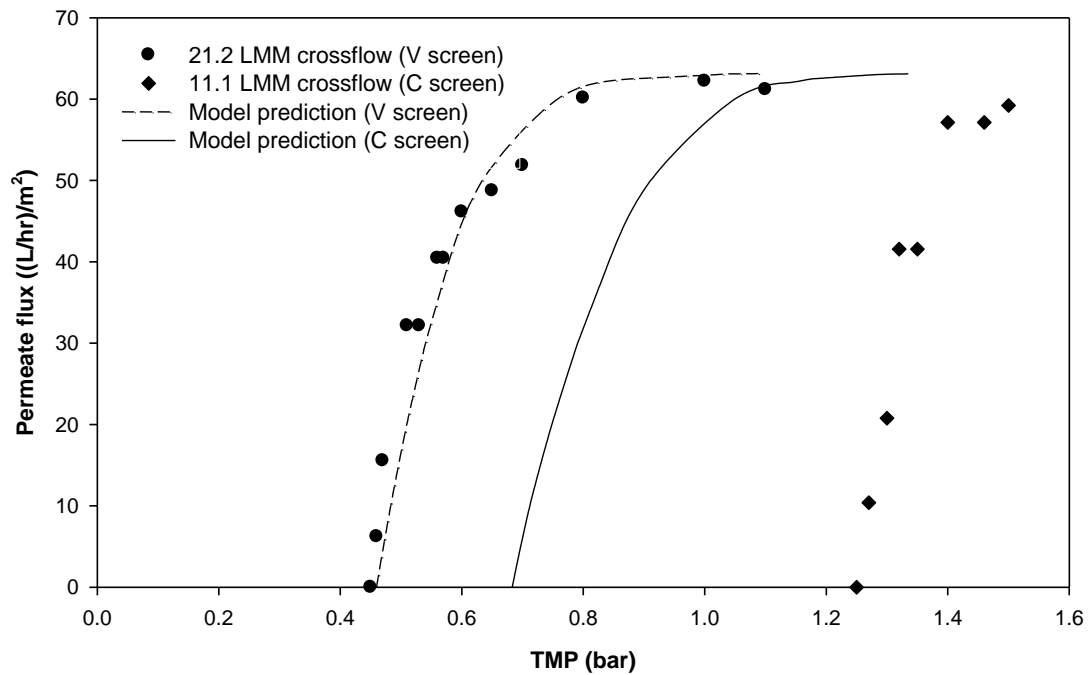
Figure 5.4 Flux excursion results for 70 g/L *Escherichia coli* homogenate and 500 kDa Biomax membrane using, A. USD membrane device (3500 RPM) and B. P2 mini C screen (11.1 LMM) and V screen device (21.2 LMM). Solid data points represent experimental TMP values whilst dotted line is the model predicted TMP for the range of permeate fluxes investigated at 25 °C.

The model predicted data for the V screen showed excellent match with the experimental data at all fluxes, unlike for the C screen cassette. The C screen

predicted results were significantly off because of the large feed flow rate (11.1 LMM) that was used to generate the required USD-equivalent average wall shear rate, which generated a significant pressure drop therefore warping the results; the model predicted dP of 2.2 bar was a lot lower than the 3.6 bar dP observed during the experimental run. The failure of the prediction model in this case could be due to a number of potential factors. Firstly, the excessive feed pressure of 3.6 bar generated during the process was much larger than the 3 bar feed pressure limit suggested for the USD prediction model in section 4.3.3.1. High feed pressures are likely when processing particulate-heavy and fairly viscous feed such as homogenates, lysates or even large proteins through a tight screen like the A and C screen devices at relatively large flow rates required to achieve the USD-equivalent wall shear rates in this experiment. Using high feed flow rate/crossflow across the cassette comes at the expense of higher pressure drops that can counteract the potential benefits of having a larger mass transfer coefficient and compact the polarisation layer to create a greater resistance to flow, generating unexpected and anomalous process data with much higher TMP need to generate an expected permeate flux. The response of permeate flux to feed pressures (proportional to the feed flow rate) for a microfiltration cassette using typical biological feedstock at constant TMP is shown in Figure 5.5.
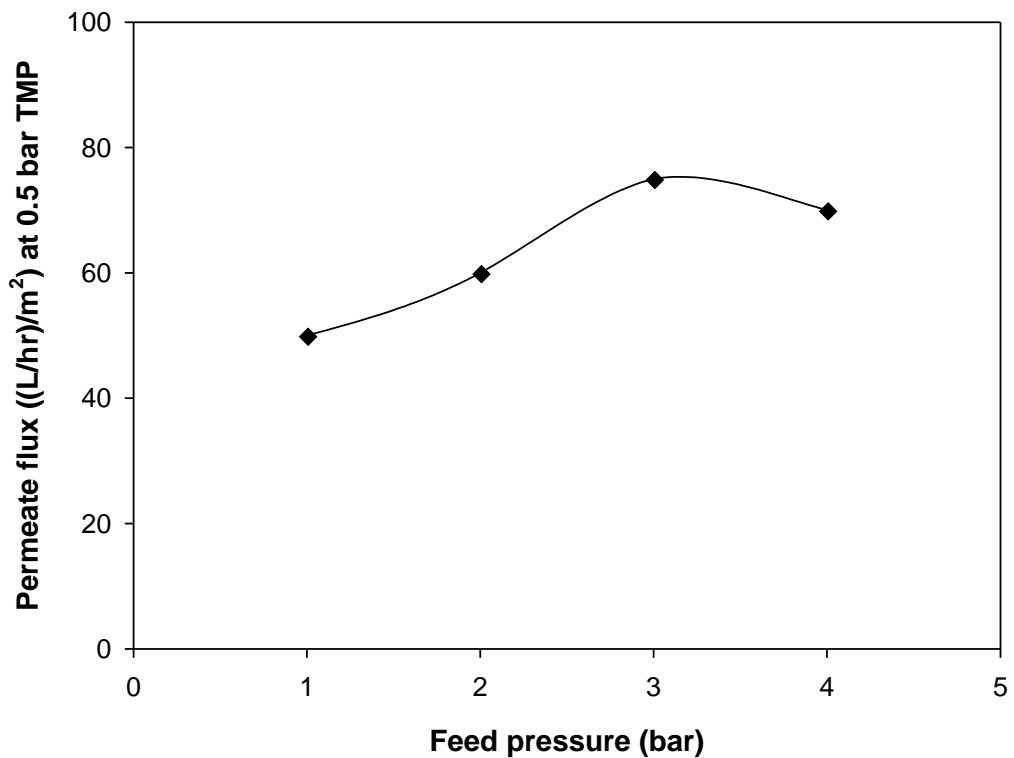
Figure 5.5 Graphical illustration of the typical results expected for permeate flux (at 0.5 bar TMP) versus feed pressure/dP experiments for a screened TFF-MF cassette, carried out in total recycle mode. Graph adapted from Iverson (2003).

From Figure 5.5, for all other parameters such as TMP, feedstock and temperature held constant, there is no increase in permeate fluxes observed above feed pressures of 3 bar. Under normal circumstances, a higher feed flow rate leads to greater sweeping effect across the membrane to reduce fouling and enhance process fluxes at a given TMP. However, the associated increase in feed pressures can result in a very rapid fouling of the membrane as well as potentially crushing the active layer of the membrane, thereby negating the advantages of a higher crossflow. Even though a higher mass transfer coefficient is achieved at higher feed flow rates, the correspondingly large feed pressure generated, combined with the permeate backpressure generated by the permeate pump/valve in TFF-MF operations, can crush the polarisation layer across both sides of the membrane and increase the hydraulic resistance to flow through the membrane. For example, to generate a TMP of 0.5 bar, a feed pressure of 2 bar requires a permeate backpressure of 0.5 to maintain that TMP, compared to a 1 bar permeate backpressure when the feed pressure is 3 bar. For the latter case, the permeate flux is likely to be lower due to

high pressures on both sides of the membrane which alters the dynamics of the polarisation layer and thus flow through it.

As a result, there exists an optimum crossflow rate at any given TMP (corresponding to ~2-3 bar feed pressure typically, depending on the particular cassette and screen type) beyond which, any further increase in feed flow rate does not lead to higher permeate fluxes and could instead have a negative impact on permeate flux (Gabler and Ryan, 1985; Iverson, 2003). The excessively high pressures upstream of the membrane forces the particles on to the membrane to such an extent that it dominates the increased mass transfer due to the higher crossflow, which plugs the membrane further. Once the membrane starts plugging and/or the polarisation layer is thickened, the permeate flux tends to decline until nothing goes through anymore (at constant TMP), or for constant flux, a much higher TMP is needed to obtain a desired permeate flux. This optimum feed flow rate is dependent upon the feedstock used and its properties such as particle diameter and size distribution; for instance, a lysate may have a much lower optimum flow rate compared to a whole cell feed such as *Pichia pastoris*. In the case of UF concentration using relatively small proteins/dissolved solutes, the optimum crossflow is likely to be extremely high and unfeasible to hit during operation.

The other factor could be attributed the high solids concentration of particles in the homogenate feedstock used. This could have an impact on both the accuracy of the viscosity measurement, as well as the quantity of particles within the feed channel that can make the boundary layers less defined and lead to some degree of membrane fouling compared to the USD device (Postlethwaite et al., 2004). The viscosity measurement greatly depends on the geometry, gap size and concentration of solids, which could lead to inaccurate measurements for polydisperse and particulate-rich feedstock (Faitli, 2001). There is also likely to be a critical solids concentration for TFF cassettes with screens where too high a solids concentration can induce other phenomenon in the feed channel and adversely affect pressure drops. Therefore, there is a need for further work on the viscosity model to consider the effects of solids concentration and diameter on the effective viscosity of suspensions.

All predicted TMP values for the C screen cassette were off by 0.57 bar in comparison to the experimental data. As the permeate flux was controlled as opposed to TMP (in Figure 5.4), the added hydraulic resistance was reflected in the additional TMP requirement to maintain the permeate flux imposed. The USD membrane device does not have this limitation since the pressure and shear are decoupled and thus independently controlled. A possible explanation could be the plugging of the narrow feed channel and feed ports of the Pellicon cassette but was extremely unlikely since there was no observable spikes in pressure drops during the course of the experiment.

Although the model failed in accurately predicting the TMP values for the C screen, a comparable flux versus TMP profile to the experimental data was seen. Therefore, the model is capable of providing key process-related data such as the maximum attainable TMP and permeate flux values (where the process is mass transfer controlled), and thus is still useful for purposes such as large scale process simulations and subsequent process design. The identical limiting permeate fluxes seen in Figure 5.4 proved that the average mass transfer rates were very similar across the three devices, which successfully validated the average wall shear rate based scale-up part of the model.

As well as flux excursions, experiments to study the transmission (concentration of Fab' in permeate:retentate) of 46 kDa Fab' through the 500 kDa membrane were carried out by performing constant volume diafiltration at a constant permeate flux of 30 LMH up to 8 diavolumes using the USD membrane device, V screen and C screen cassettes. Transmission or retention of species is another important performance metric for tangential flow filtration besides the throughput and flux. The retentate volume (equal to one diavolume) was set to a minimum of 0.4 L for the Pellicon 2 mini cassettes used (0.1 m^2) to maintain equal V/A loading across scales. In the case of the USD membrane device, the transmission was determined by measuring the Fab' concentration in the permeate stream and using mass balance to calculate the concentration in the retentate, *i.e.*, the feed held within the shear chamber of the USD membrane device. The experimental transmission data for all three devices is shown in Figure 5.6.
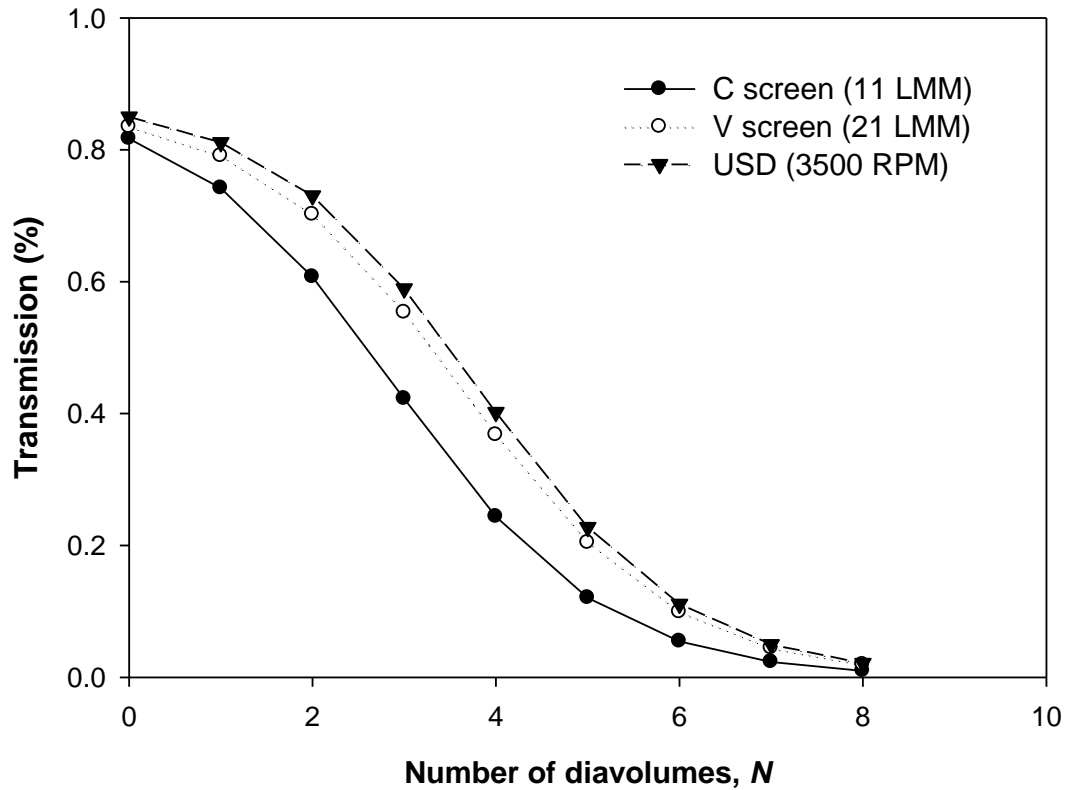
Figure 5.6 Fab' transmission data for the USD membrane device (3500 RPM) and P2 mini C and V screen (11 and 21 LMM respectively), at a constant permeate flux of 30 LMH and temperature of 25 °C. 1 diavolume=0.4 L.

Once again, the Fab' transmission data from the three devices showed relatively good comparability with each other. Both the V and C screen transmissions were lower than the USD membrane device, which suggests other extraneous factors that could be responsible for this observation. Firstly, since the V and C screen TFF cassettes have higher upstream pressures than those in the USD membrane device, the effective permeability of the polarisation layer formed could be relatively lower in the screened TFF cassettes despite the three devices having identical polarisation layer thicknesses in theory due to the same averaged wall shear rate and permeate flux used. A compacted polarisation layer/cake would have a smaller effective pore size than the membrane that can hinder the transmission of Fab' particles through it and lower the transmission, seen in the lower transmission at all diavolumes for the V and C screen cassette. Furthermore, variability in the membrane and any fouling of the reusable Pellicon cassettes could cause different retention/transmission characteristics compared to the clean, single-use membrane discs used in the USD device.

Apart from that, there is a possibility of the feed composition being dissimilar across the USD device and Pellicon cassettes, due to non-specific binding surfaces besides the membrane such as feed/permeate screens or interactions between various components such as other proteins and cell debris in the homogenate feed under pressure. Losses due to adsorption is unlikely as previous processing data using the Pellicon devices have shown close to a 100% recovery of product in the permeate using whole cell and lysate feedstock using open membranes, albeit at relatively modest TMP of less than 0.4 bar (Millipore, 2018b). Similarly, Guo et al. (2016) and Ma (2009) have observed very good agreement for Phage T7 and Fab' transmission using *Escherichia coli* whole cell and lysate respectively, at TMP less than 0.3 bar, between lab-scale Pellicon and custom-built USD devices. Consequently, the high TMP of 0.5 bar used in this transmission experiment (compared to < 0.1 bar in the USD device), coupled with the interaction of the Fab' molecule with other components in the feedstream could cause the lower transmission observed for the Pellicon devices. Homogenates contain significant amounts of large macromolecules, proteins and cell debris, which can bind the Fab' molecule depending on the ionic strength and pH of the solution thereby reducing the amount of free Fab' molecules available for transmission (Novais et al., 2001; Ripperger and Altmann, 2002; Ujam, 2007). Since the transmission was calculated using a mass balance derived concentration of the retentate, the amount of unbound Fab' in the retentate could be much lower resulting in a lower calculated transmission.

The phenomenon observed in this section warrants further work such as carrying out control experiments to determine the impact of the volume of feedstock:surface area of the housing ratio on the amount of free protein molecules available for filtration, as well as the potential influence of surface roughness and material of construction on product quality and aggregation. Thus, the next section looks at scaling between the two Pellicon devices with different screens, to eliminate any potential possibility of non-specific interaction and differences in the composition of the feed in contact with the membrane surface, and using a diluted feedstock and operating at lower feed pressures.

5.2.2.3.1 Scaling from C to V screen cassette (25 g/L homogenate)

The experiment with *Escherichia coli* homogenate was repeated at a much lower cell concentration (25 g/L, 0.0016 Pa.s viscosity) to avoid excessive feed pressures (<3 bar), as the viscosity is proportional to the cell concentration. The USD membrane device was not used in this section, but instead scale-up was carried out between the two Pellicon 2 cassettes, scaled up directly from a C screen (at 6 LMM feed flow rate) to a V screen. For the C screen data, the initial TMP value of 0.28 bar when feed flow was initialised (at zero permeate flux) was subtracted from all recorded TMP values, to obtain TMP corrected values, which was then fit to the first-order exponential model to obtain the coefficient α and exponent β, shown in Table 5.4. Furthermore, the permeate screen pressure drop component in the TMP prediction model was set to zero since the TMP corrected data used to generate the exponential model incorporated the permeate screen pressure losses at all the fluxes explored and hence was not required in this TMP prediction.

A comparison of the flux versus TMP corrected data for both V and C screen is shown in Figure 5.7.

Viscosity measurements (25 °C)	μ_F	0.0016	Pa.s
	μ_P	0.001	
Exponential curve fit for P2 C screen data (6 LMM) (Equation 4.1)	α	122	LMH
	β	6.537	1/bar
	Average wall shear rate, $\overline{\gamma_{wall}}$	8019.1	s^{-1}

	Cassette (screen)	P2 mini (V)	
1 bar dP test with water, 0 permeate flux (Equation 4.4)	$Q_{F,\,dP=1\,bar}$	25	LMM
	$TMP_{dP=1\,bar}$	0.07	bar
	Average feed channel height, h	0.53	mm
Applied pressure drop equation parameters (Equation 4.8)	n	1.29	-
	C	0.014	bar/LMM^n

	Operating feed flow rate, Q_F	13.3	LMM
Predicted pressures at t=0 (0 permeate flux)	Feed flow rate, Q_F, to generate C screen-equivalent wall shear rate (Equation 3.17)	0.026	bar
	dP	0.63	
	ΔP_A	0.41	
	TMP'	0.092	

Table 5.4 Summary of the various parameters needed for TMP prediction along with predicted initialised pressures at zero flux for 25 g/L *Escherichia coli* homogenate using the 500 kDa P2 mini V screen cassette.
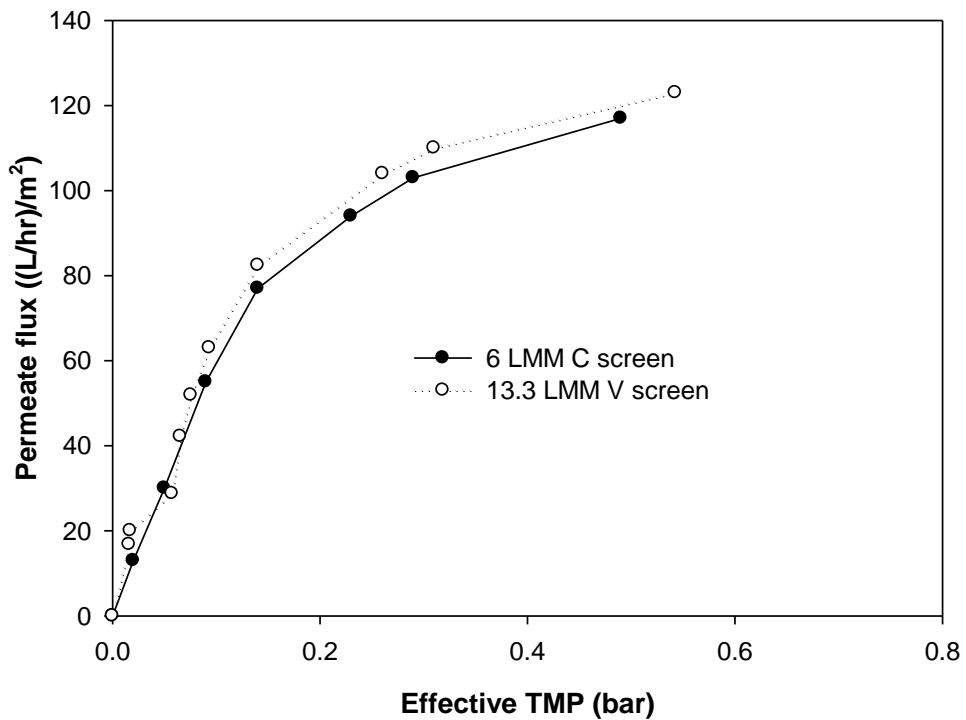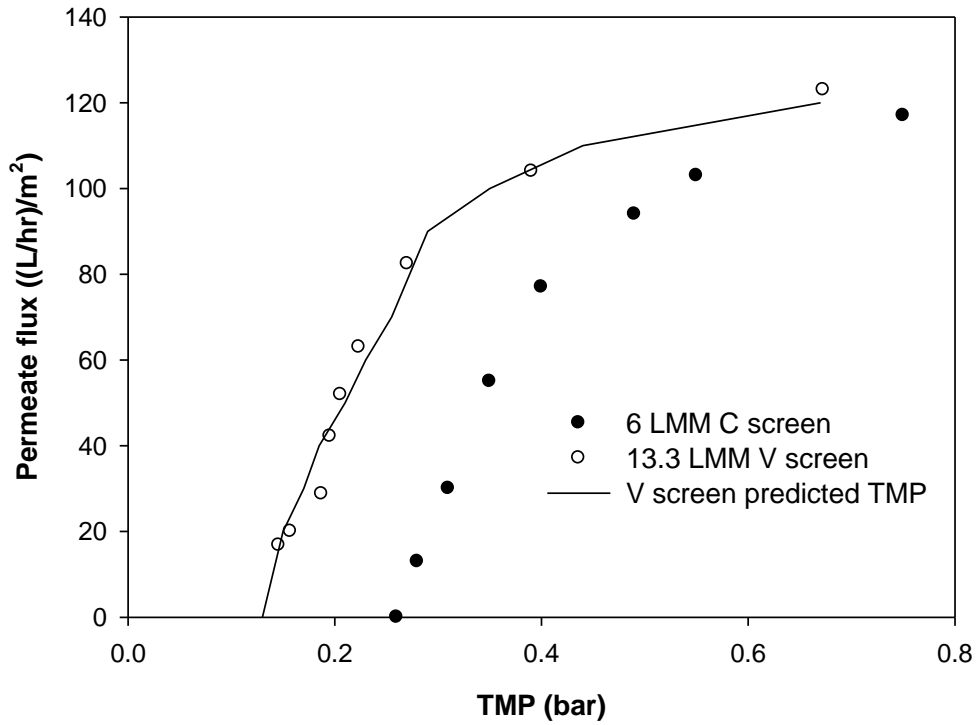
Figure 5.7 Experimental versus predicted flux-TMP data for *Escherichia coli* homogenate. Top: flux excursion curves for 25 g/L *Escherichia coli* homogenate and 500 kDa Biomax membrane using P2 mini C screen (6 LMM) and P2 mini V screen (13.3 LMM). Solid data points represent experimental TMP values whilst solid line is

the model predicted TMP for the range of permeate fluxes investigated at 25 °C. Bottom: TMP corrected data for the two cassettes.

The predicted data shown in Figure 5.7 (top) was a very good overlay of the experimental values for the V screen cassette at all points. The effective TMP versus permeate flux for the two also showed excellent agreement with each other (<10%), which validated the non-linear scale-up methodology and demonstrated a robust, predictable scale-up between different screen cassettes provided the scale-up rule of maintaining low feed pressures is implemented.

5.2.2.4 Whole cell feed (*Pichia pastoris*)

Since the previous section using *Escherichia coli* homogenate successfully validated the applicability and robustness of the scale-up methodology and prediction model, this section looks at using 30 g/L *Pichia pastoris* feedstock to generate a USD model expressed as a function of averaged wall shear rates (function of fluid viscosity and RPM of the disc in the USD membrane device). This model would allow the prediction of TMP versus flux relationships for any desired operating feed flow rate at large scale using the same prediction model with a slightly modified approach. 0.22 μm Durapore PVDF membrane and disc rotational speeds of 3000, 3500 and 4000 RPM (corresponding to average wall shear rates of 12300, 15790 and 19620 s^{-1} respectively) were used to carry out flux excursions. The corresponding α and β values for the first-order exponential model fit to experimental data plotted against average wall shear rate, as shown in Figure 5.8 (top). This section looks to take the model one step further and expand the USD model to expressing average wall shear rates as a function of disc RPM, which can then allow large scale predictions for any desired feed flow rate and allow simulation of process scale data using USD data and the prediction model.

Viscosity measurements (25 °C)	μ_F	0.00185	Pa.s
	μ_P	0.00115	
USD exponential model parameters (Figure 5.8, top)	α	$0.0045 \cdot \overline{\gamma_{wall}} - 18.856$	LMH
	β	$16.2 \cdot e^{-0.0000153\overline{\gamma_{wall}}}$	1/bar

	Cassette (screen)	PXL (C)	
1 bar dP test with water, 0 permeate flux (Equation 4.4)	$Q_{F,\,dP=1\,bar}$	12.7	LMM
	$TMP_{dP=1\,bar}$	0.117	bar
	Average feed channel height, h	0.41	mm

Applied pressure drop equation parameters (Equation 4.8)	n	1.43	-
	C	0.034	bar/LMM^n

	Operating feed flow rate, Q_F	14	18	LMM
	Average wall shear rate to mimic, $\overline{\gamma_{wall}}$	17272.8	19929.9	1/bar
Predicted pressures at *t*=0 (0 permeate flux)	Feed flow rate, Q_F, to generate USD-equivalent wall shear rate (Equation 3.17)	0.069	0.092	bar
	dP	1.82	2.62	
	ΔP_A	1.46	2.09	bar
	TMP'	0.55	0.78	

Table 5.5 Summary of various parameters needed for TMP prediction and initialised pressures at zero for 30 g/L *Pichia pastoris* using 0.22 µm Pellicon XL cassette. Average wall shear rates at feed flow rates of 14 and 18 LMM were calculated using Equation 3.17 (C screen) for feed viscosity of 0.00185 Pa.s.
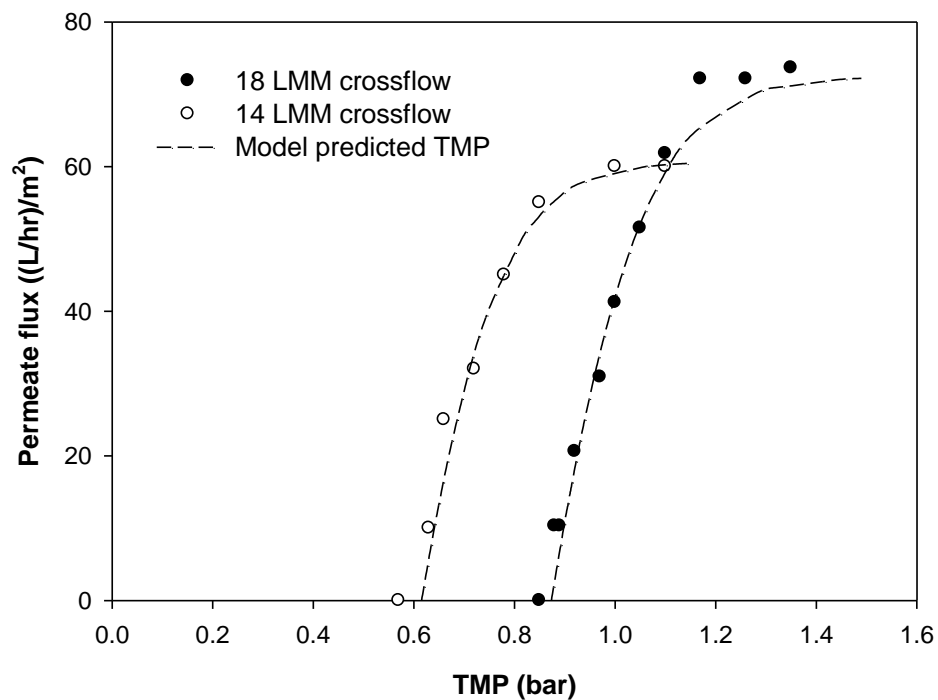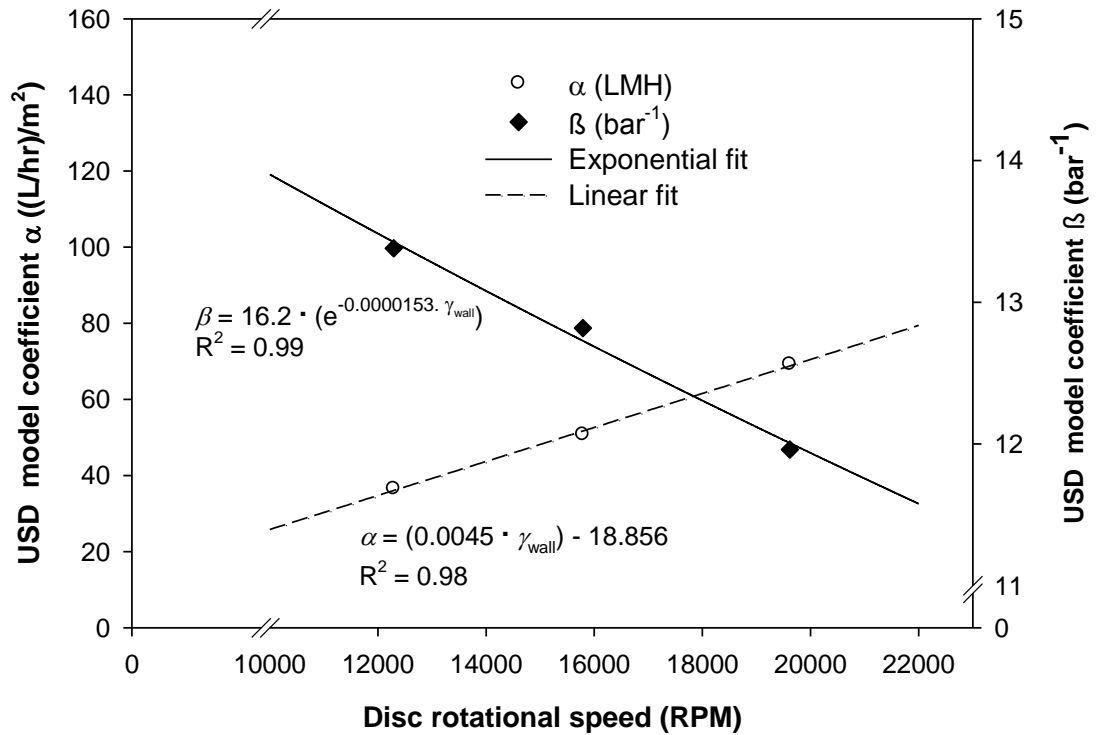
Figure 5.8 Experimental results for 30 g/L *Pichia pastoris* feed and PVDF 0.22 μm membrane; Top: First-order model coefficient *α* and exponent *β* versus average wall shear rate in the USD membrane device, bottom: flux versus TMP data for Pellicon XL C screen at operating flow rates of 14 LMM and 18 LMM. Solid data points represent experimental TMP values whilst the dashed line is the model predicted TMP for the range of permeate fluxes investigated at 25 °C.

The predicted TMP at 14 LMM and 18 LMM for the Pellicon XL device closely matched the experimental values at all fluxes, including the initial TMP value at zero net flux. By expressing the USD model parameters as a function of the RPM/average wall shear rates in the USD membrane device, the flux versus TMP profiles can be accurately predicted for any desired operating flow rate using the TMP prediction model without the need for repeating the parameter-determining experiments using the USD device each time the operating feed flow rate is changed. This further consolidates the robustness of the proposed first-order exponential model to characterise the fouling dynamics and interactions for a specific feedstock and membrane combination, and the potential application of the USD membrane device to successfully mimic filtration processes at scale and enable large scale process simulations and predictions for a wide range of operating conditions that enable and help accelerate process development and optimisation with minimal number of large scale experiments. The parity plot (Figure 5.9) shows the extremely good fit between predicted and experimental TMP and thus validating the USD methodology and more importantly, the model used to extrapolate and predict performances for any desired feed flow rate for the large screen cassettes.
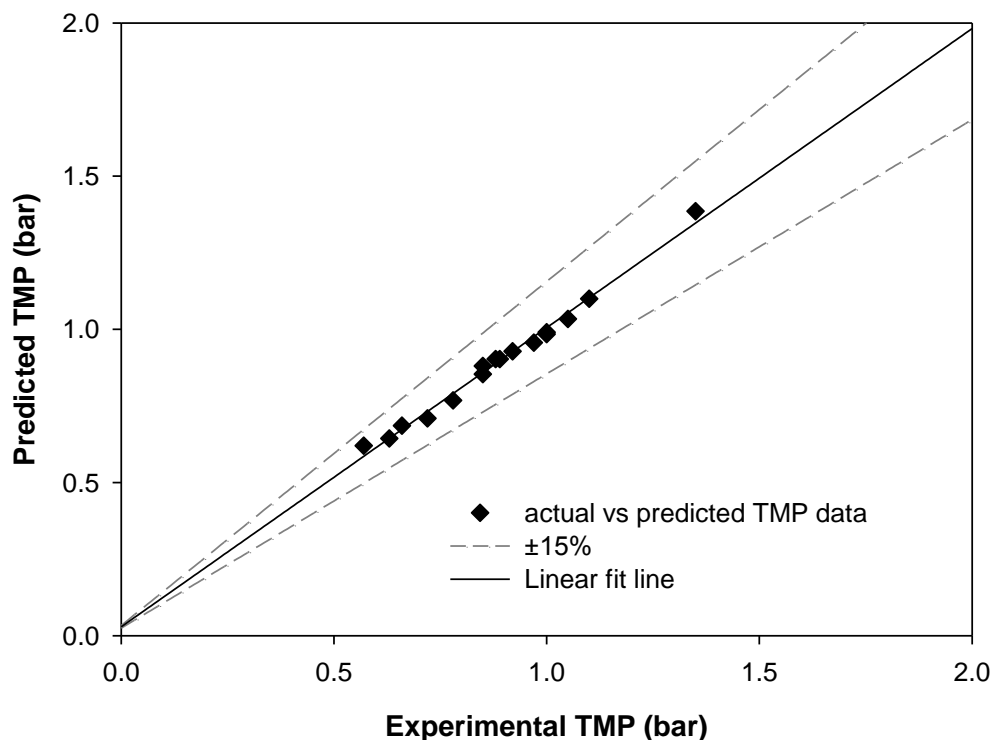
Figure 5.9 Parity plot showing all predicted versus experimental TMP values for PXL C screen data using *Pichia pastoris*. Data taken from Figure 5.8.

5.3 Conclusions

The non-linear scale-up data from the comparative flux excursion experiments at large scale using Pellicon cassettes showed excellent agreement with the ultra scale-down model predicted data with a variability of ≤5% on average, which was about less than half the acceptance criteria for true linear scalability (15-20%) typically employed in industry. Various feedstock representative of industrial/process scale manufacturing were used to verify both the USD-based scale-up method and TMP prediction model, ranging from simple proteins such as BSA to complex, multivariate feed like *Escherichia coli* homogenate and *Pichia pastoris.* Experimental flux versus TMP profiles at large scale showed excellent agreement with the predicted data (across the different feedstock) generated using the TMP prediction model, which made allowances for the system, feed and permeate channel pressure drops to improve the accuracy of the prediction model. Furthermore, scaling between different feed screens, namely V and C screen, was demonstrated along with transmission performance upon scale-up for *Escherichia coli* homogenate feed containing 46 kDa Fab'. Both TMP and transmission data showed a good match to the USD data considering inherent uncertainties such as experimental errors, differences in membrane permeabilities across scales and the multivariate nature of the homogenate feedstock, all of which are difficult to model accurately. However, the quality of the product across both scales using different material of construction is something that needs to be further investigated, and forms part of the future work.

The empirical USD model coefficients derived using the USD membrane device proved to be an accurate representation of the filtration process and phenomenon occurring for the specific feedstock-membrane combination used, indicated by the nearly identical predicted versus experimental data for limiting permeate fluxes and the transitional critical point region at large scale across all the different feedstock investigated. The coherence of predicted and experimental large scale data successfully validated the suitability of the USD membrane device as a mimic for tangential flow filtration, as well as the basis of using averaged wall shear rates as the scaling parameter, for both linear and non-linear scaling.

The importance of following the scale-up rules was demonstrated in the case of C screen using 70 g/L *Escherichia coli* homogenate, where high feed pressures (>3 bar) was seen to greatly distort the flux versus TMP experimental data, causing the prediction model to be thrown off and thus the model was found to significantly

underpredict the process TMP at all permeate fluxes. In theory, larger feed flow rates across the cassette would result in a better performance; however, there is a trade-off against high pressure drops that occur because of the high crossflow rates. Thus, there exists an optimal crossflow rate and any further increase beyond the optimal crossflow rate, for all else equal, would not increase permeate flux and was instead found to decrease the permeate flux (at constant TMP). For microfiltration tangential flow filtration using particulate-rich feed, the TMP was found to be more dominating than the crossflow rate, with regards to its impact on the permeate flux. The issues were resolved and the model behaved as expected when the experiment was repeated with a diluted feed concentration of 25 g/L. The final part investigated a modified approach where USD parameters are expressed as a function of disc rotational speed in the USD device, allowing the prediction of any feed flow rate at large scale by determining wall shear rates at the desired operating feed flow rate and calculating the semi-empirical USD parameters. This was successfully validated using *Pichia pastoris* and a parity plot was generated to prove the model accuracy and its potential applications.

To conclude, the prediction model was able to accurately predict all TMP values ranging from the linear, pressure-dependent region through to the mass-transfer controlled region, at any desired feed flow rate (by using USD model parameters expressed as functions of USD-averaged wall shear rates). The excellent agreement observed between the single-set experimental data for the USD device and the smallest Pellicon cassette with a single feed channel successfully validated the model robustness. Therefore, the USD membrane device combined with the relatively simple scale-up methodology and TMP prediction model, can provide valuable information such as optimum TMP for a process, transmission/retention characteristics and process throughputs, thus accelerating early stage process optimisation by reducing the number of verification runs required at large scale.

6 Case studies for novel USD-based bioprocessing applications

The previous sections looked at establishing the USD scale-up methodology and prediction model, which was successfully validated by the flux excursions using a wide range of biological feedstock, membrane types and cut-offs, including different feed screens. As the USD membrane device was verified to be able to accurately mimic the performance of equivalent large scale equipment using millilitre quantities of material, this section discusses two such case studies to showcase the potential applications of the USD membrane device combined with the validated prediction model to optimise tangential flow filtration microfiltration (TFF-MF) processes. The true potential of USD, aligned with the QbD initiative, lies in its ability to rapidly generate small scale data to provide key and valuable processing-related information, such as throughputs, feed-membrane interactions, transmission and membrane fouling in the case of tangential flow filtration. USD tools aim to provide a more thorough understanding of the relationship between the process variables (inputs) and product-related parameters (outputs) therefore reducing complexity, as well as information regarding the interactions between operating conditions upstream and downstream and trade-off between upstream optimisation versus impact on the subsequent operations downstream. Thus, USD technologies provide a more attractive and cost-effective option for screening, process characterisation and optimisation by high throughput experimentation, allowing to effectively de-risk a process through increased process understanding.

6.1 Characterisation of capacity limits for TFF microfiltration of *Saccharomyces cerevisae*

6.1.1 Introduction

The previous chapter successfully verified the scale-up protocol and prediction model for both UF and MF membranes when conducting flux excursions. However, for open membranes used in microfiltration, the process is generally required to be able to handle particulate containing feed such as whole cells, cell debris, suspensions, etc., which tends to have a much higher fouling propensity than dilute feed containing soluble species used in UF. Microfiltration processes differ from ultrafiltration processes as they are also characterised by a maximum achievable throughput or a capacity limit, and consequently the optimisation approach for a MF process is different from a standard UF concentration.

MF operations are typically operated using a two-pump control system, the feed pump and permeate pump; the latter regulates the permeate flux through the membrane and helps limit and control membrane fouling at the start of the operation due to the high intrinsic permeability of open membranes. However, even with permeate flux control and operating at fluxes below the critical flux, there is a maximum volume of feed that can be processed as permeate through the membrane at a specific feed flow rate and TMP/flux, before the membrane plugs and the TMP (at constant flux) rises rapidly. This phenomenon occurs even when performing diafiltration operations using a MF membrane with particulate-heavy feed where feed concentration remains unchanged.

The volumetric throughput limit poses an additional constraint in the microfiltration process, apart from the low optimum TMPs of microfiltration processes. The volumetric capacity or throughput (typically expressed in L of permeate/m^2) is a pore plugging issue caused by the presence of small colloidal particles, similar to the pore plugging issues observed in normal flow filtration. The four key mechanisms of membrane fouling (Figure 6.1) are gradual pore plugging, complete pore plugging, cake formation and hybrid (a combination of the other three mechanisms). With a standard protein feed like BSA or mAbs, the fouling mechanism is primarily dominated by gradual pore plugging caused by the proteins sticking to the inside of the pores and gradually blocking them over time. Gradual pore plugging is slow and thus the capacity is relatively large, and provided the process is optimised correctly, would

take extremely long processing times to be able to hit the capacity limit under normal operation. In the case of particulate-containing feed typically used in MF, the mechanisms of membrane blocking are gradual pore blocking, followed by complete pore blocking and finally cake formation. This occurs since particles sizes in the feed are comparable to the pore sizes of the microfiltration membrane and these particles block the membrane pores and accumulate over the blocked pores forming a cake layer over time and thus the capacity for a MF process is a lot lower than UF.

FOULING SCHEMATICS
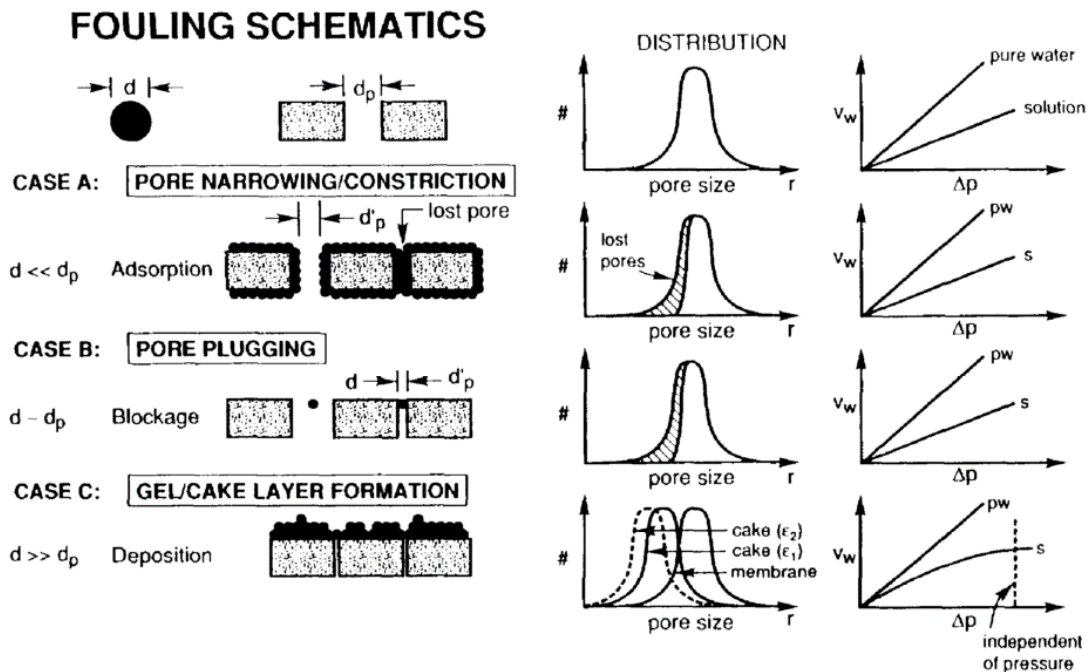
Figure 6.1 Schematic illustrating the various fouling mechanisms observed in filtration processes (Belfort et al., 1993).

Some of the key fouling mechanisms include:

- Pore narrowing/constriction: This is when particles/solutes are adsorbed, both direct and long-term, to the membrane; even without any flux through the membrane, a monolayer of particles and solutes can be formed. As a result, the internal resistance of the membrane increases.

- Pore blocking: When particle sizes are comparable to the average pore diameter of the membrane, these particles can plug the pores resulting in a loss of permeate flux due to a decrease in the total number of pores available.

264

- Deposition/gel formation: In cases where the solute or particles are significantly larger than the pores of the membrane, particles and solutes deposit and form layers at the membrane surface, and can grow, creating a significant additional resistance to flow.

- Hybrid: This is when more than one fouling mechanism occurs concurrently or sequentially, such as combined pore plugging and caking.

For non-Newtonian fluids operating in dead-end mode, all blocking laws can be generalised into the following empirical equations (Hermia, 1982):

$$\frac{d^2 t}{dV^2} = K \left(\frac{dt}{dV} \right)^n$$

Equation 6.1

for constant pressure filtration and

$$\frac{d(\Delta p)}{dV} = K \, (\Delta p)^n$$

Equation 6.2

for constant filtrate rate filtration.

Where V is the cumulative permeate volume (L) collected over time, t (s), K is a system specific decay constant, and the exponent, n, is a mechanism specific constant and describes the rate of blocking.

Table 6.1 summarises the various values of the constant, K, and exponent, n for the different filtration laws.

Mechanism	K	n
Cake filtration	$K_c = \dfrac{\alpha \cdot \gamma \cdot s}{A \cdot R_0 \cdot Q_0 \cdot (1 - ms)}$	0
Intermediate blocking	$K_i = \dfrac{\sigma}{A}$	1
Standard/gradual blocking	$K_s = \dfrac{2C}{\delta_m \cdot A} \cdot Q_0^{1/2}$	1.5
Complete pore plugging	$K_c = u_0 \cdot \sigma$	2

Table 6.1 Parameter expressions for the various blocking filtration laws for dead-end filtration.

For tangential flow filtration, the blocking laws discussed above can be modified to include a back diffusion term for TFF-MF, as described by Field et al. (1995) for constant k and index n:

$$-\frac{dJ}{dt} = K \cdot (J - J^*) \cdot J^{(2 - n)}$$

Equation 6.3

Where J and J^* are the instantaneous and critical permeate fluxes expressed in LMH, respectively, and the index n are similar to that for dead-end flow mentioned in Table 6.1.

This volumetric throughput limit presents additional constraints when optimising microfiltration processes, and is impacted by several key factors, namely the initial feed concentration (initial solids loading), feed flow rate (dP across the cassette) and the permeate flux; the permeate flux and feed flow rate effectively control the polarisation and fouling dynamics at the membrane surface, and thus are vital parameters that define and control the observed capacities. The endpoint for a microfiltration process with permeate flux control is usually indicated by the increase in observed TMP to a pre-defined maximum pressure or an increase in retention or decrease in transmission through the membrane. Therefore, the aim of this chapter is to use the small scale capacity data generated using the USD membrane device

and apply it to the TMP prediction model to predict performance at large scale, using Pellicon 2 mini V screen cassette and *Saccharomyces cerevisae* as feedstock to verify the model and predicted capacity.

6.1.2 Results and discussion

To determine the volumetric throughput limits for 25 g/L *Saccharomyces cerevisae*, 10-fold fed-batch volumetric reduction experiments were conducted using Durapore 0.65 µm flat-sheet membrane. A constant permeate flux of 50 LMH was used as the critical flux at 250 g/L *Saccharomyces cerevisae* suspension was experimentally determined to be roughly 100 LMH (Figure 6.2), and thus 50% of the critical flux value was used as the permeate flux for the subsequent concentration experiments.
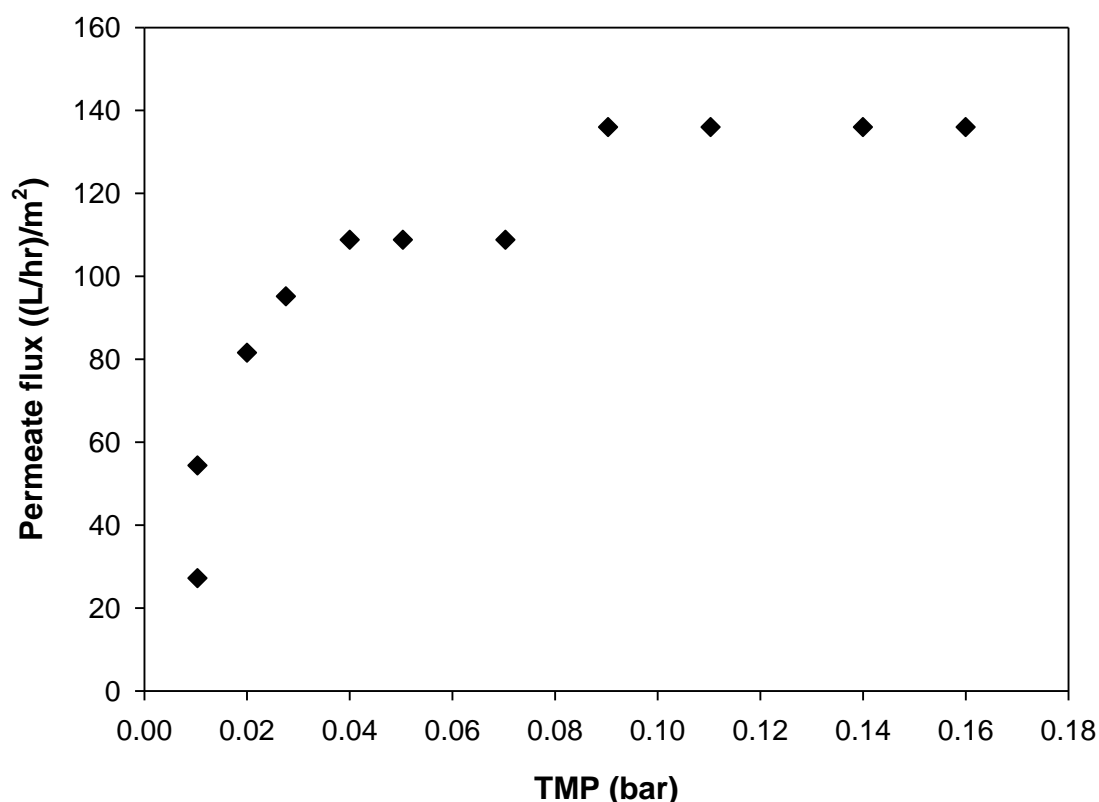
Figure 6.2 Flux excursion data for 250 g/L *Saccharomyces cerevisae* using the USD membrane device at 4000 RPM.

The small scale concentration data generated using the USD membrane device is shown in Figure 6.3. Disc rotational speed of 4000 RPM was used for the USD membrane device because the viscosity varies during the concentration run, and for the current speed control unit, a minimum disc speed of 4000 RPM was required to

allow the dynamic feedback loop to function effectively. The feedback loop allows the disc to rotate at a constant speed of 4000 RPM regardless of the liquid viscosity by continuously adjusting the power supplied to the motor based on the feedback. Even though the RPM selected for the USD device could typically be back-calculated from the average wall shear rates that correspond to the operating feed flow rates for TFF cassettes at scale, this was purely a limitation of the type of motor used. The recommended operating rotational speed range for the motor ranged from a minimum of 4000 RPM to speeds in excess of 10000 RPM, and the feedback control required a minimum of 4000 RPM to be used as the set point.
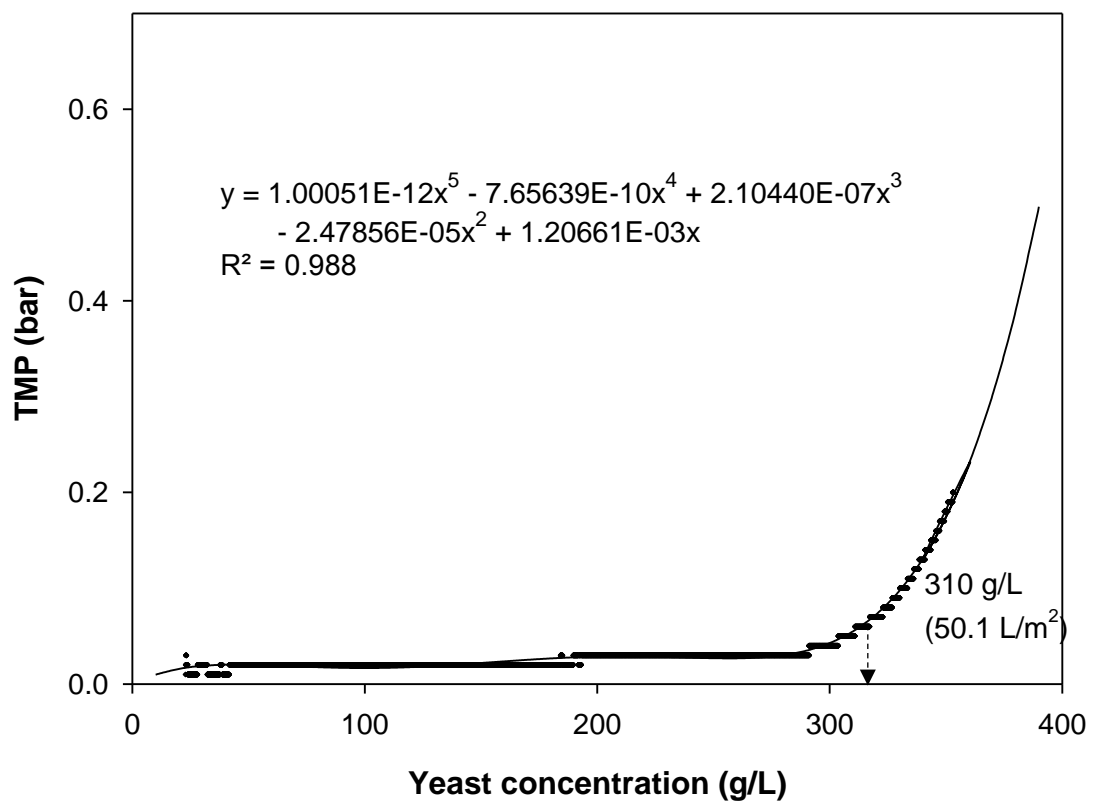
Figure 6.3 TMP versus concentration of *Saccharomyces cerevisae* generated using the USD membrane device at 4000 RPM and constant permeate flux of 50 LMH, starting from an initial concentration of 25 g/L. Solid black line represents the polynomial curve fit to the experimental data.

From Figure 6.3, the TMP was observed to rise exponentially at around 310 g/L, which corresponded to a total permeate volume of 66.2 mL (~50 L/m^2), indicating a maximum volumetric permeate throughput of around 50 L/m^2 that can be processed for a *Saccharomyces cerevisae* concentration of 25 g/L, 4000 RPM and flux of 50

LMH. A maximum volumetric throughput of 50 L/m^2 and solids loading capacity of 310 g/L means that at the average wall shear rates for 4000 RPM, 25 g/L *Saccharomyces cerevisae* and a permeate flux of 50 LMH, a maximum permeate volume of 50 L per m^2 of available membrane surface area can be processed. Beyond this point, the maximum solids loading of 310 g/L would be breached, indicated by a rapid increase in TMP. The volumetric capacity and solids loading limit are constant for a given feedstock-membrane combination, operated at a given average wall shear rate (RPM and feed flow rate) and permeate flux.

The prediction model was employed once again to predict TMP profiles for the Pellicon 2 cassette. However, since viscosity of the retentate stream effectively increases with cell concentration during the experiment, viscosity was measured at different concentrations of *Saccharomyces cerevisae* and expressed as a function of cell concentration at an applied shear rate of 1500 s^{-1} and 25 °C, as shown in Figure 6.4.
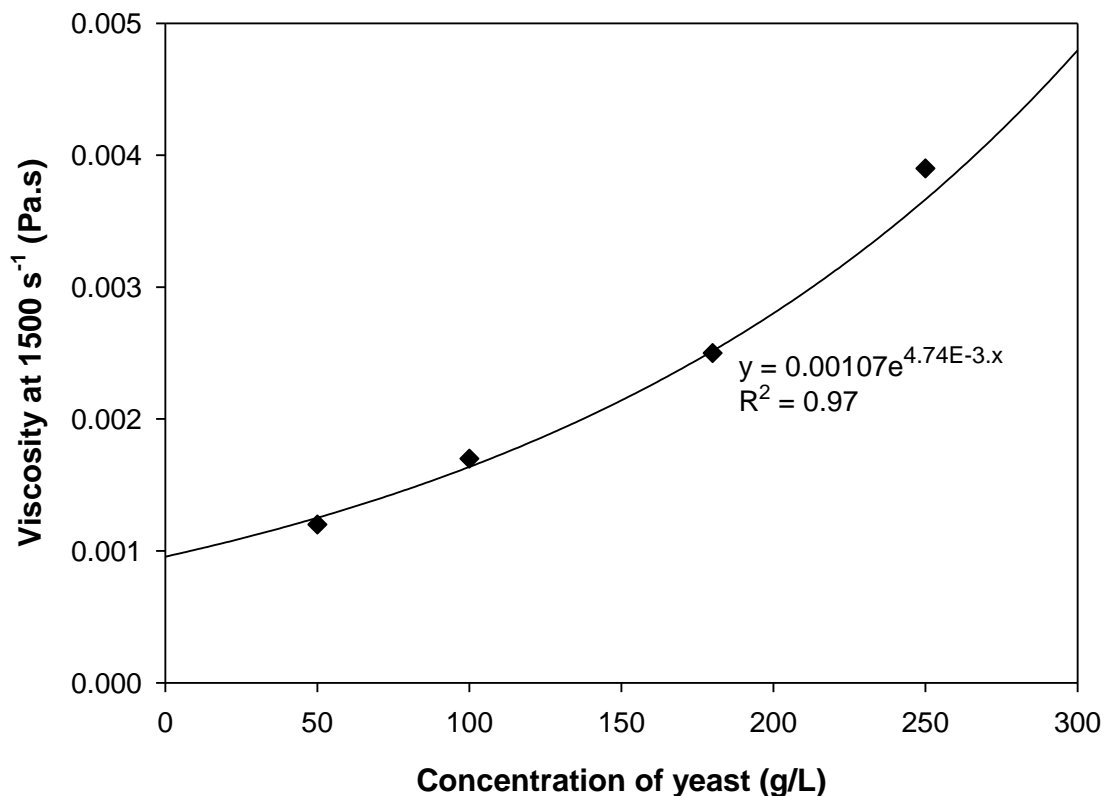
Figure 6.4 Viscosity of *Saccharomyces cerevisae* at a shear rate of 1500 s^{-1} at 25 °C.

The average wall shear rates at the final desired concentration 250 g/L (VCF=10) was used to determine the appropriate feed flow rate required for the Pellicon cassette, since the wall shear rates, at a constant feed flow rate, would decrease with increasing concentration of the feed/retentate (due to the increase in feed viscosity with cell concentration). In terms of choosing the average wall shear rates to be used as the scaling parameter, either the average wall shear rates at the start (VCF=1) or the desired endpoint (VCF=10) could be evaluated and used to determine operating feed flow rates. However, since wall shear rates are more sensitive to cake formation, likely to occur towards the end of the concentration (as particles accumulate and form a cake/polarised layer whose thickness is directly influenced by the wall shear rate/feed flow rate used), a feed viscosity of 0.003 Pa.s corresponding to the final desired concentration (250 g/L) was used to calculate the average wall shear rates. Table 6.2 lists the various experimental and USD parameters, as well as expressing feed viscosity as a function of cell concentration and initial predicted pressure drops at t=0 with no permeate flux.

Viscosity measurements (25 °C)	$\mu_F=f$(cell concentration, x)	$0.00107e^{4.74E-3x}$	Pa.s
	μ_P	0.0009	
USD model parameters	Rotational speed, N	4000	RPM
	Average wall shear rate at 250 g/L (0.003 Pa.s), $\overline{\gamma}_{wall,VCF=10}$	15893.4	s^{-1}
	TMP=f(cell concentration, x)	$1.00051E-12x^5 - 7.65639E-10x^4 + 2.10440E-07x^3 - 2.47856E-05x^2 + 1.20661E-03x$	bar

	Cassette (screen)	**P2 mini (V)**	
1 bar dP test with water, 0 permeate flux (Equation 4.4)	$Q_{F,\,dP=1\,bar}$	33.3	LMM
	$TMP_{dP=1\,bar}$	-0.03	bar
	Average feed channel height, h	0.59	mm
Applied pressure drop equation parameters (Equation 4.8)	n	1.23	-
	C	0.0064	bar/LMM^n

	Feed flow rate, Q_F, to generate USD-equivalent wall shear rate (Equation 3.17)	30	LMM
Predicted pressures at t=0 (0 permeate flux)	System pressure drop at operating Q_F	0.079	bar
	dP	0.92	
	ΔP_A	0.55	
	TMP'	0.092	

Table 6.2 Summary of the various parameters needed for TMP prediction and predicted initialised pressures at zero flux for *Saccharomyces cerevisae* solution using 0.65 μm Durapore Pellicon 2 mini cassettes.

The TMP profile for the large scale concentration using Pellicon 2 V screen cassette can then be predicted using Equation 6.4:

$$TMP(x) = TMP' + \text{system } dP + \text{permeate screen } dP + TMP_{USD}$$

Equation 6.4

where:

$$TMP' = \Delta P_A - \frac{dP}{2} = (1120 \cdot \mu_F(x) \cdot C \cdot \overline{Q_F}^{-n}) - \frac{1}{2}(dP(x))$$

$$TMP_{USD} = (1.00051\text{E-12} \cdot x^5) - (7.65639\text{E-10} \cdot x^4) + (2.10440\text{E-07} \cdot x^3)$$
$$\quad - (2.47856\text{E-05} \cdot x^2) + (1.20661\text{E-03} \cdot x)$$

$$\Delta P_{Ps} = -0.033 + (0.000965 \cdot J) + (26.39 \cdot \mu_P)$$

$$\text{System } dP_{\text{Sartoflow Advanced}} = 5\text{x}10^{-3} \cdot \left(Q_F - \frac{JA}{120}\right)^{1.823} \cdot \mu_F^{0.69}$$

$$\mu_F(x) = 0.001 \cdot e^{4.74\text{E-3} \cdot x}$$

$$x = VCF_t \cdot x_0 = \frac{V_T}{V_R} \cdot x_0$$

In the equations above, all pressure components (TMP, TMP', ΔP_{Ps}, system dP) are in units of bar, μ_F is the feed viscosity (Pa.s), x and x_0 are the cell concentrations in g/L (DCW) at time t and at the start (t=0) respectively, J is the permeate flux (LMH), A is the available filtration area (m^2), Q_F is the feed flow rate (LMM), VCF_t is the volumetric concentration factor at time t in the process (-), V_T and V_R represents the total feed volume (5 L) and average retentate volume (0.5 L) respectively, and μ_P is the permeate viscosity (Pa.s).

To verify the model predicted data, a large scale fed-batch volumetric concentration study using Pellicon 2 mini V screen cassette and 25 g/L *Saccharomyces cerevisae* at a constant permeate flux of 50 LMH was carried out. The retentate volume in the tank was kept constant at 0.5 L in the feed vessel of the Sartoflow to maintain the same initial solids loading on the membrane compared to the USD device, with fresh feed being fed to the tank at the same rate as permeate flow rate out (5 L/h). Concentration was carried out until a VCF=10 or a TMP= 0.7 bar was achieved, whichever occurred first. The USD results, large scale experimental data and the model predicted data are all shown in Figure 6.5.
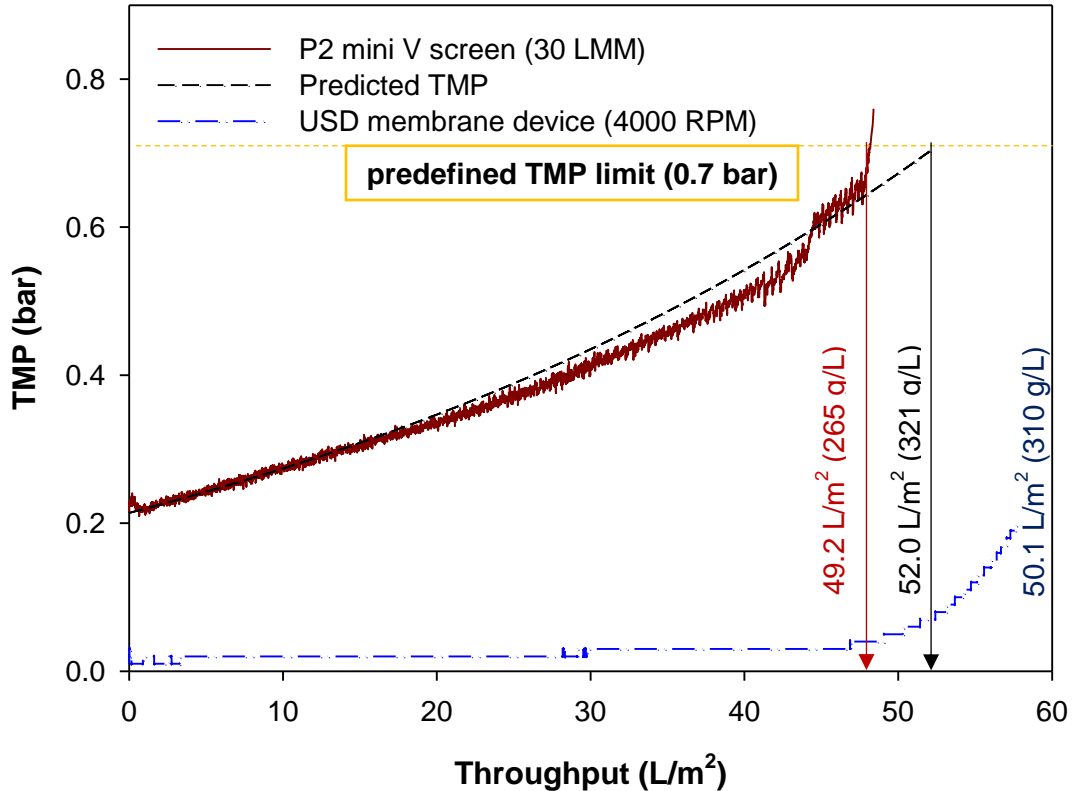
Figure 6.5 TMP versus volumetric throughput data for USD device (4000 RPM), P2 mini cassette (30 LMM feed flow rate) and predicted model using 25 g/L *Saccharomyces cerevisae* at a constant permeate flux of 50 LMH.

Although a fed-batch concentration was carried out, it was a good representation of a typical batch concentration step, since the ratio of total volume of feed to be processed (~5 L) to the retentate volume in the tank (0.7 L, including hold-up) was 7:1. This was close to the recommended fed-batch ratio of 5:1 (Dr. P.J. Beckett, Technology Consultant - Merck Millipore Life Sciences, personal communication, 2018), to avoid any potential pump related damage to the feed plus other processing time related issues that are likely to occur and cause deviations in the observed performance. As a result, a fed-batch and a batch concentration would both have similar concentration and consequently TMP profiles, assuming the product/cells are not damaged and do not influence membrane fouling.

Similar profiles for the predicted and experimental TMP profiles were observed in Figure 6.5 and the volumetric capacities (at 0.7 bar TMP) were determined to be 52.0 L/m^2 and 49.2 L/m^2 from the predicted and experimental data respectively; both sets of results demonstrated a successful and predictable scale-up performance. However, the model predicted TMP was not a complete overlay to the experimental

data, particularly near the region where the exponential increase in TMP was observed (around 45 L/m^2). The importance of volumetric loading limits can be seen, where the large scale Pellicon cassette reached a final concentration of 265 g/L compared to the 310 g/L achieved in the USD device before their respective TMP spikes, despite using similar operating conditions (permeate flux of 50 LMH (50% of critical flux at 250 g/L) and initial concentration of 25 g/L *Saccharomyces cerevisae*).

There are a few plausible explanations for the discrepancies between the solids loading capacity (265 g/L versus 321 g/L). Firstly, as the concentration proceeds, the dP across the cassette rises and at a certain point, the 1.5-2 bar feed pressure limit for V screen Pellicon cassettes was exceeded and the experimental TMP profile started to deviate from the model because of the atypical interactions and fouling dynamics that are likely to occur at high feed pressures and localised TMPs at the beginning of the feed channel. The experimental versus predicted dP across the cassette is shown in Figure 6.6.
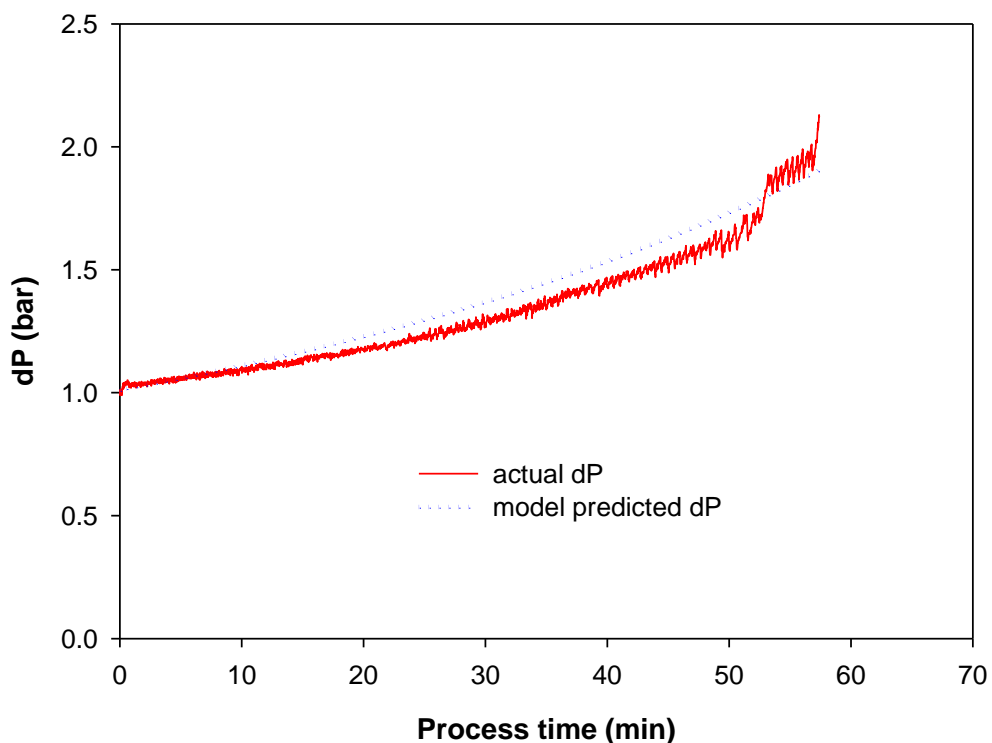
Figure 6.6 Feed channel pressure drop (dP) profiles for the concentration run using *Saccharomyces cerevisae* and Pellicon 2 V screen cassette at 50 LMH flux and 30 LMM feed flow rate. Experimental dP is shown as solid line, while the predicted dP (combination of dP, system pressure drop and permeate screen pressure drop) is shown as dashed line.

Similar to the optimum feed flow rate discussed in chapter 5.4.3.1, there is also an optimal feed flow rate/feed pressure/dP with respect to capacity; at the optimum feed flow rate and constant permeate flux, the volumetric loading limit reaches a maximum and beyond it, the capacity can be seen to decrease. Figure 6.7 illustrates this effect for a typical MF concentration operated at two different permeate fluxes. The volumetric capacity, for both permeate fluxes, can be seen to increase with feed pressures up to a point, beyond which the capacity starts to decline. The increase in TMP at a lower volumetric throughput for the Pellicon cassette compared to the USD device (at constant flux of 50 LMH) could be attributed to the relatively large feed flow rate of 30 LMM (that was required to generate USD-equivalent average wall shear rates) exceeding the optimal crossflow for the process (corresponding to pressures >2 bar).
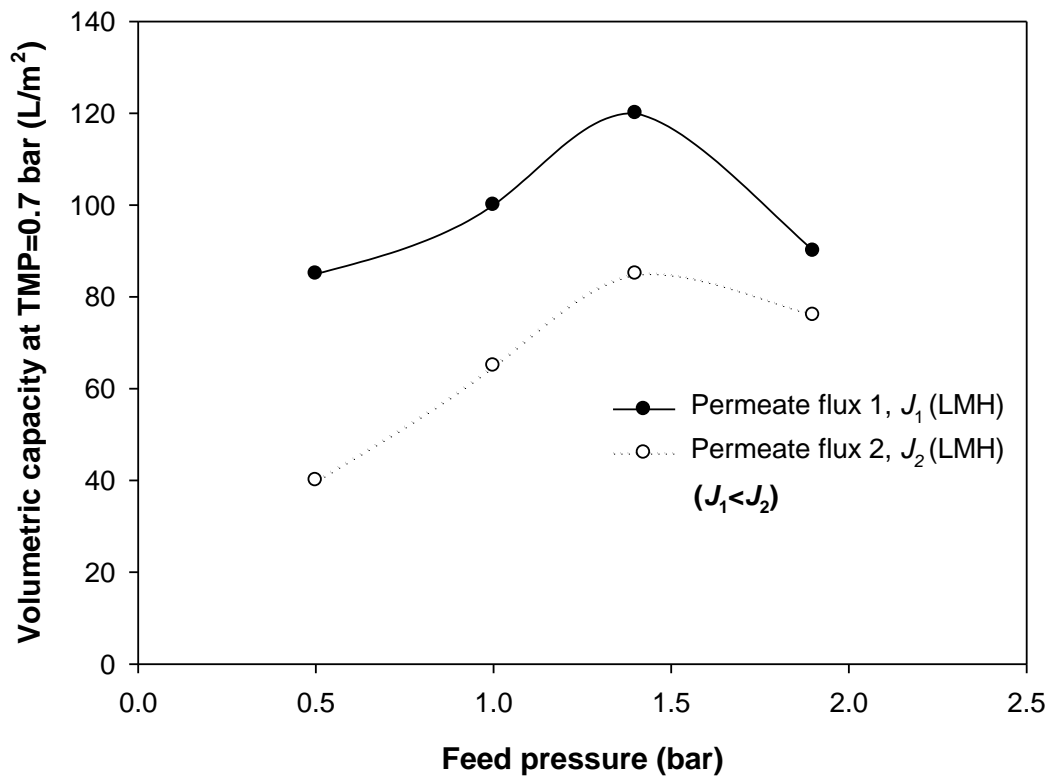
Figure 6.7 Illustration of the concept of optimum crossflow rate/dP during MF, highlighted by the expected relationship between volumetric capacity of the membrane (L/m^2) and the feed pressure/dP for a typical MF process.

Another plausible explanation could be the differences in NWP across membranes in general depending on lot-to-lot and batch variation; for Millipore membranes, NWP

variability across membranes was calculated to be ±25% on average (from Figure 4.1). The relationship between NWP and capacity, in theory, should be inversely proportional since the NWP describes the state of the membrane and how dirty the membrane pores are, while the capacity limits indicate the point at which the membrane starts to foul to such an extent where the permeate flow is restricted. Thus, there is likely to be a causal relationship between the two, wherein a membrane with lower initial NWP is likely to register smaller empirical throughputs and vice versa, for all things equal. Apart from that, the differences in predicted and experimental dP could also be due to potential inaccuracies of the viscosity model used, since the feed pressures are very sensitive to small changes in fluid viscosity due to the very narrow flow channels within screened cassettes. The TMP at which membrane capacity is determined also plays a key role and needs to be taken into consideration; for example, the capacity at 0.7 bar, 49.2 L/m^2 is much higher than the capacity at 0.5 bar, 40 L/m^2. Ideally, the membrane loading limits can be taken at the first point where the TMP is seen to increase rapidly, which indicates the onset of membrane fouling, but it is subject to human error and not as quantifiable or comparable to when using pre-defined TMP limits.

Although the predicted data was observed to deviate from the experimental curve at higher feed pressures, it was deemed close enough to be very useful for simulation and preliminary process optimisation purposes rather than testing the actual process at scale. Considering the high feed pressure issues (>2 bar) towards the end of the process, the small differences between the predicted and experimentally determined capacities at large scale can be assumed to be well within experimental errors, and as a result, the prediction model was considered sufficiently validated, provided it is operated within predefined rules. There are no existing models for simulating volumetric capacities for TFF-MF processes to date, and the work presented here showcases one of the many applications of the USD membrane device and the developed prediction model, which was able to accurately predict the capacity of the membrane at a given permeate flux, which is information that is generally obtained empirically using large scale runs.

6.1.3 Conclusions

The optimisation of microfiltration TFF operation is more complex than a standard ultrafiltration process since the microfiltration with particulate feed is also limited by a maximum permeate throughput (capacity) that can be achieved at a particular feed flow rate, permeate flux and feed concentration. This capacity limit is determined by the feed characteristics such as particle size and type, as well as the specific interactions between the membrane and particles in the feed stream.

A non-linear scale-up method and TMP prediction protocol for the microfiltration concentration application was demonstrated. In order to determine and subsequently predict the volumetric capacity limits for a typical microfiltration process, 25 g/L *Saccharomyces cerevisae* was used to carry out a 10-fold volumetric reduction experiment using the USD membrane device and a 0.65 µm Durapore PVDF membrane. The device was operated at a disc speed of 4000 RPM and a constant permeate flux of 50 LMH (50% of the critical flux at the desired endpoint).

An equivalent large scale validation run was performed using a Pellicon 2 mini V screen device, operated at USD-equivalent averaged wall shear rates, identical initial concentration of *Saccharomyces cerevisae* and permeate flux. A combination of the modified USD model (capacity versus concentration), variable viscosity model and the flow initialised TMP' (as a function of feed concentration/viscosity) was used to predict the TMP profiles as a function of volumetric throughput at large scale for the Pellicon 2 mini V screen device. Good agreement was seen between the predicted and experimental TMP versus throughput profiles, as well as the maximum achievable volumetric throughputs, with values of 49 L/m^2 and 50 L/m^2 for the large scale and USD runs respectively, for the given operating conditions.

The concept of optimum feed flow rate/feed pressure with respect to maximum volumetric capacity was discussed, where feed pressures greater than 1.5-2 bar for the V screen cassette was found to be counter-productive with regards to the observed capacities; increasing crossflow beyond the optimal value reduced the volumetric throughput capacity, for all things equal. The volumetric capacity limit dictates the endpoint for a microfiltration process (due to rapidly rising TMPs beyond the maximum throughput) and is a very useful performance parameter (besides process flux and feed flow rate) that directly impacts process area sizing and thus is a vital part of the process development approach with respect to the optimisation of

microfiltration TFF processes. The USD membrane device, combined with the scale-up methodology and TMP prediction model, was found to successfully simulate the TMP profiles at large scale and predict volumetric throughput limit accurately, something which is typically determined empirically in industry.

6.2 USD study of the relative fouling propensities and subsequent development of an efficient dewatering strategy for microalgae suspensions

6.2.1 Introduction

Over the last few years, algal biomass has been increasingly recognised as having significant potential to be a sustainable and renewable energy source for biofuel production (Zhang et al., 2010). Microalgae is considered as an economical and attractive source of raw material because it can be grown in saline water or otherwise non-productive land (can also be grown in photobioreactors), exhibits short growth period and a high growth rate with more high-lipid precursors than food crops (Chen et al., 2009; Lakaniemi et al., 2011; Weyer et al., 2009; Chisti, 2008).

One such model organism is the unicellular, thermo-tolerant freshwater alga *Chlorella sorokiniana* (UTEX 1230). A lot of work and growth optimisation studies have been carried out over the years and *Chlorella* is currently a widely used model algae feedstock and extensively researched for the generation of biodiesel and high value products (Moronta et al., 2006; Chen et al., 2011; Vonlanthen et al., 2015; Hongjin and Guangce, 2009; Kumar et al., 2014; Li et al., 2013; Rosenberg et al., 2014). One of the key advantages is its ability to be grown up to relatively high cell densities with rapid doubling times compared to other microalgal strains, typically ranging between 4 to 6 hours, and can be grown phototrophically, heterotrophically or mixotrophically. Studies have further shown that maximum growth rates and lipid yields are generated when *Chlorella sorokiniana* is grown mixotrophically, with strong preferences for simple sugars like glucose or sucrose (Ngangkham et al., 2012; Ratha et al., 2013; Wan et al., 2012). Furthermore, recent work has also demonstrated the ability of *Chlorella sorokiniana* to be successfully grown phototrophically using wastewater and exhaust gases, with both biomass and lipid yields comparable to those grown in BBM-minimal media (Lizzul et al., 2014).

The lipid composition is another key factor when selecting the right microalgal species. Polar and neutral lipids tend to be preferred and the *Chlorella* genus has been identified to successfully produce those lipids, up to 50% of their dry cell weight (Sharma et al., 2011). Triacylglycerol (TAG) is one of the more preferred sources of renewable oil since it has a good ratio of hydrogen to carbon and can be extracted from algal biomass with relative ease and subsequently transesterified into biofuels.

Furthermore, if heterotrophic substrates can be cheaply and sustainably derived from sources such as cellulosic biomass or wastewater streams, conversion of organic substances in to lipids could present a viable option for the production of algal biofuel (Rosenberg et al., 2014).

The majority of current microalgal production and harvesting methods are based on a combined flocculation-centrifugation step, which tends to be energy intensive and amounts to a major proportion of the total energy requirements of the overall process (Molina Grima et al., 2003), significantly reducing the net energy output, especially if the microalgae is used for biofuel production. Membrane technology is a relatively cheaper alternative and is generally not as energy intensive; it can achieve close to 100% recovery of algal biomass, along with the potential disinfection by filtering out protozoa and viruses (Judd, 2006). Filtration also offers the option of recycling the media and re-using it for subsequent cell cultures. Zhu et al. (2013) recently demonstrated the successful cultivation of microalgae (*Chlorella zofingiensis*) by using the water that is generated post- algal biomass harvest. This research provided a method where the harvest water could be recycled twice to re-grow algal cells, thus improving the overall efficiency and economy of the harvesting process.

However, even when employing the use of membrane technologies, harvesting *Chlorella sorokiniana* biomass is not cost-effective as the energy requirements and costs associated with processing large volumes are significantly high. The initial harvest step alone accounts for more than 30% of the total production cost from microalgae to biodiesel (Chini Zittelli et al., 2006; Horiuchi et al., 2003). Low cell concentrations in the algal fermentation media (0.5–5 g/L) and relatively small particle sizes (typically 3–10 μm in diameter) render the harvest of algal cells quite challenging, and since generation of biodiesel is not possible from such dilute cultures, the initial harvest step typically involves a volume reduction of up to 50 to 200-fold (Al Hattab et al., 2015). In addition to that, shear-induced damage/shear stress to microalgal biomass due to increased number of cycles through the feed pumps and valve flashing could break the cells into smaller particles and/or enhance the release of exopolymeric substances (EPS). These particles are known to be severe biofouling agents and can enhance pore blocking and promote biofilm/cake layer formation on the membrane surface and is a major bottleneck when using filtration technology (Babel and Takizawa, 2010; Ladner et al., 2010).

Malériat et al. (2000) studied the fouling phenomenon and the vital role that polysaccharide adsorption plays during filtration processes. Many microalgae strains produce an extracellular matrix that projects outwards from the cell wall. This matrix constitutes of extracellular polymeric substances such as polysaccharides, proteins, lipids and humic substances and serves as a scaffold where algal cells can adhere to the membrane surface and each other to form a biofilm. These biofilms can block the feed channels or clog the membrane pores, resulting in increased energy requirements and a lower permeate flux at a particular TMP. In addition, the exocellular polysaccharides (sheath) can form cross-links between the cells (illustrated in Figure 6.8) to further compact the deposit on the membrane surface, thereby increasing resistance to flow and decreasing mass transfer across the membrane. Inter-particle interactions in mixed species environments have the potential to change the characteristics such as resistance of the foulant layer, even for simple model systems (Le-Clech et al., 2006).
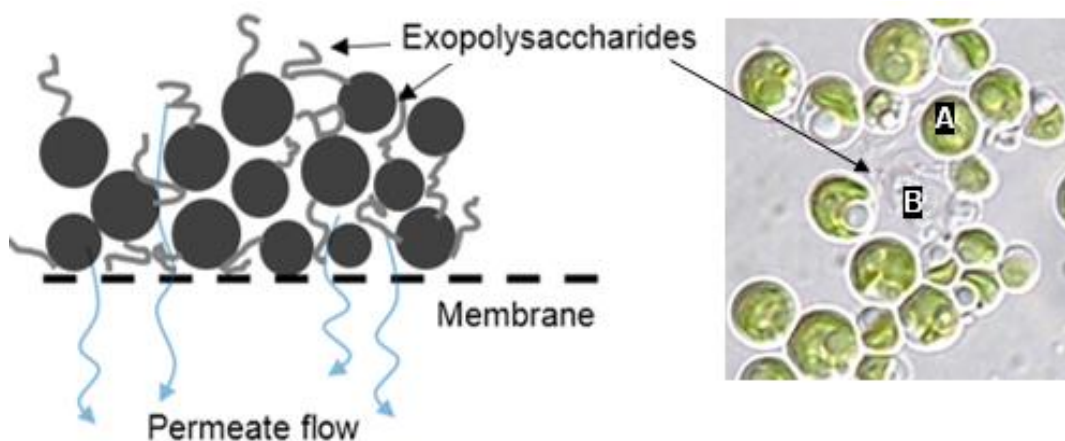
Figure 6.8 Illustration of extracellular sheath network formed between neighbouring algal cells. Left: Theoretical representation of algal cells deposited at the membrane surface, showing the linkages formed between cells. Right: 50x optical imaging of *Chlorella sorokiniana* cells in TAP minimal media; A: *Chlorella sorokiniana* cell, B: extracellular sheath primarily made of polysaccharides.

Morineau-Thomas et al. (2002) observed the significant role soluble compounds in the culture medium can play on limiting the permeate flux. The interaction between algal cells and the soluble components was also identified as one of the significant contributors to fouling. Apart from the extracellular sheath matrix between cells, membrane fouling by algae is thought to be caused by various factors, namely

membrane properties, media formulation and components, growth conditions and mainly, algal secretions which are commonly referred to as extracellular polymeric substances (EPS). EPS are sticky, organic substances that are typically secreted by algae, diatoms or cyanobacteria, and can either exist as an extracellular matrix around cells, herein referred to as EPS, or as discrete, colloids in solution that are classified as transparent exopolymeric particles (TEP) (Passow and Alldredge, 1994). TEP can form from dissolved organic matter such as bacterial cells present in a symbiotic relationship with algae and other organic debris released into the media upon cell senescence, and can be present in various molecular weights/sizes. Villacorte et al. (2009) reported TEP as small as 0.05 µm based on membrane fouling studies, and other studies have reported a wide range of particle size and distribution for particles classified as TEPs (Discart et al., 2013; Passow and Alldredge, 1994; Xiao and Zheng, 2016). The main mechanism of fouling by TEP is suggested to be a combination of pore blocking (by the carbohydrate and protein constituents) and cake formation by enhancing biofilm formation as a result of the inherent sticky nature of TEP, which serves as a cross-linking scaffold for cells and other foulants (Meng and Liu, 2013). Babel and Takizawa (2010) have demonstrated that membrane fouling during the dewatering of *Chlorella* species was greatly influenced by the amount of extracellular organic matter present in the media, which can coat the surface of the membrane and potentially alter the physio-chemical properties of the membrane itself. TFF microfiltration of *Chlorella sorokiniana* was performed by Wicaksana et al. (2012) using direct microscopic observation technique to study fouling and protein transmission. The deposition of cells was seen at low permeate fluxes, although the observed TMP remained low and only increased when the degree of fouling worsened. Increased transmission of extracellular polymeric substances was achieved at higher crossflow rates at the cost of increased membrane fouling rates.

Extracellular organic matter (EOM) is secreted by both bacteria and phytoplankton, as part of cell death (organic debris), detachment from cell surface (mucus/cell coating) or the direct release of organic material into the extracellular fluid (Passow, 2002). EPS and TEP are similar in composition, *i.e.*, mainly consisting of acidic polysaccharides and other polysaccharide-like substances, and the primary difference between them is that the former exists as a gel-like matrix around the cells while the latter exists as discrete particles of EPS in solution in various forms (filaments, colloids) and sizes (0.01-200 µm) (Berman and Passow, 2007). Microalgal-derived EPS have different characteristics compared to other abiotic organic matter (Henderson et al., 2008) and could cause severe fouling issues if not

characterised properly. In the case of non-axenic *Chlorella sorokiniana* cultures, the amount of TEP, for a given algae cell concentration, would be relatively higher due to the extra organic matter secreted by the symbiotic bacteria. Colloidal/soluble TEPs are known fouling agents in membrane filtration, with higher concentrations of TEP in solution positively correlated to lower critical fluxes during tangential flow filtration (Fan et al., 2006).

The fouling propensity of microalgal feedstock during tangential flow filtration (MF/UF>300 kDa) could be influenced by the concentration of the EPS per volume of algal cell along with characteristics such as composition (hydrophobicity, net charge at media pH), molecular weight distribution, all of which depend on the media, time of harvest and culture growth conditions. Apart from that, Zhang et al. (2012) found that the fouling propensity increased with the time of harvest of *M. aeruginosa* cultures, with stationary phase producing the highest fouling AOM consisting of proteins, polysaccharides and humic-like substances. Techniques such as scanning electron microscopy (SEM), Fourier-transform infrared spectroscopy (FT-IR) and direct observation through the membrane (DOTM) using microscope-based observations have identified proteins, polysaccharides and organic matter to be the major foulants during MF processes involving microalgal feedstock (Bacchin et al., 2006; Bilad et al., 2014; Charcosset, 2012; Chen et al., 2004; Fane, 2012; Jepsen et al., 2018; Kwon et al., 2007; Zhang et al., 2010). Plenty of fouling studies using microalgae have been carried out over the years, however, the fouling mechanism have not yet been well understood nor characterised. Understanding the nature and characteristics of the foulants, in addition to the fouling dynamics, is equally important to optimising a TFF-MF process.

The aforementioned issues multiply as feed concentration increases, becoming more viscous, leading to greater pressure drops across the membrane. Microalgae exhibit some highly unusual rheological properties, typically exhibiting non-Newtonian behaviour with pseudoplastic characteristics, which makes it significantly complicated to characterise and predict their behaviour. Furthermore, other factors such as the negative surface charge of the cells, culture age, and type of membrane, media components and temperature might also have an impact on the filtration process and its efficiency. For processing of low feed volumes (<2000 L/day), tangential flow filtration might be a more cost-effective option compared to centrifugation. However, the constant recirculation of feed, costs of replacing membranes and frequent backwashing as a result of fouling are high and thus for larger production scales

(>20,000 L/day), centrifugation may be the more economic method for dewatering microalgae (MacKay and Salusbury, 1988).

To tackle the issues of membrane fouling when processing large volumes of algal feedstock, different approaches have been used over the years, ranging from flocculation techniques (microbial, auto, bio, electrolytic), pre-treatment of the feed to remove identified fouling components or operational strategies such as periodic backflushing of the membrane, to the use of dynamic membrane systems to generate high wall shear rates to disrupt the polarisation layer (Bilad et al., 2012, 2013; Drexler and Yeh, 2014; Al Hattab et al., 2015; Higgins and VanderGheynst, 2014; Liu et al., 2013; Molina Grima et al., 2003; Poelman et al., 1997). However, they all have their limitations such as the introduction of extra 'contaminants' in the feed stream that need to be removed in the subsequent steps, increased costs associated with the addition/removal of flocculants and the increased buffer usage. Furthermore, practical limitations of achieving periodic backflushing and potential integrity breach of the membrane due to the backflush are some of the key considerations. More importantly, all the approaches mentioned above generally fail to resolve and improve the cost-effectiveness and sustainability issues associated with using membrane technologies for the harvest of dilute algal cultures.

Therefore, sustainable and economical methods to harvest large volumes of microalgae (with near complete biomass retention) are needed, which could potentially take us a step closer to solving the global energy crisis and further the biopharmaceutical use of microalgae to develop and extend into new areas, provided the issues of fouling and consequences on throughputs are solved. Considering the numerous challenges and cost-effectiveness issues associated with tangential flow filtration as an initial harvest and dewatering step for microalgal feed, the aims of this section are to evaluate the biomass growth kinetics of *Chlorella sorokiniana* using three different media and growth conditions, characterise fouling dynamics using the USD membrane device and subsequently develop a high throughput flux-control methodology for efficient harvest of microalgae. The specific objectives are to:

- Investigate the impact of using different media and growth conditions for *Chlorella sorokiniana* cell cultures and the impact on filterability and membrane fouling using the USD membrane device,
- Investigate relationships between upstream cell culture conditions and its impact on subsequent tangential flow filtration harvest step downstream,

- Compare the relative membrane fouling propensities and establish a correlation between foulants and degree of irreversible fouling of the membrane,

- Use the ultra scale-down membrane device to help optimise process conditions for the dewatering of *Chlorella sorokiniana* for the chosen media/condition, by minimising membrane fouling whilst still achieving high volumetric throughputs,

- Develop and demonstrate the application of a novel USD-based dynamic flux step-down methodology with relatively higher filtration efficiencies and minimal fouling rates compared to established optimisation methods, and verify it with large scale experimental data.

6.2.2 Results and discussion

6.2.2.1 Impact of media and culture conditions on *Chlorella sorokiniana* biomass yield and growth rates

The first set of experiments were designed to determine the influence of culture conditions on the growth of *Chlorella sorokiniana*. The impact of three different media, namely TAP, 3N-BBM+V and EG:JM (grown autotrophically, heterotrophically and mixotrophically), on biomass and growth rates was investigated and the results are shown in Figure 6.9. The optical density measured at 750 nm was converted to biomass using the empirically determined relationship:

$$DCW \text{ (g/L)} = 0.1723 \cdot OD_{750nm}$$

Equation 6.5

From Figure 6.9, all growth curves followed the characteristic sigmoidal '*S*'-shaped profile with a relatively short lag phase, which meant little to no time was required by the cells to acclimate to the fresh growth media since the inoculum used was harvested at the end of their exponential growth phase, where the metabolism was already well adjusted to using both light and simple sugar as their source of carbon. The autotrophic cell cultures across the three different media investigated had the smallest growth rates and the least biomass generated overall, compared to the heterotrophic and mixotrophic growth conditions; the 3N-BBM+V culture yielded the

greatest autotrophic biomass due to a combination of extra nitrogen (3N) and vitamins present in the media that facilitated growth.

TGP media supplemented with 10 g/L glucose generated the greatest biomass concentration of 5 g/L, followed by the heterotrophic 3N-BBM+V cells with biomass concentration of 3.5 g/L. Heterotrophic cultures are typically expected to yield relatively greater biomass since the organic carbon source selectively enhances the production of biomass over the synthesis of pigments such as chlorophyll (Miao and Wu, 2006), which leads to chlorosis as was observed by the light green/pale yellow colour of the heterotrophic cell cultures (Figure 6.11). However, the more complex EG:JM media had very similar biomass growth profiles for both heterotrophic and mixotrophic cultures, with a maximum biomass concentration of ~3 g/L by the end of the exponential phases. This suggested that the light intensity could have been the growth limiting factor for the mixotrophic culture, whilst the availability of rich minerals and nutrients in the complex, undefined EG:JM media (from the *Saccharomyces cerevisae* extract) resulted in heterotrophic assimilation of the carbon source dominating carbon fixation.
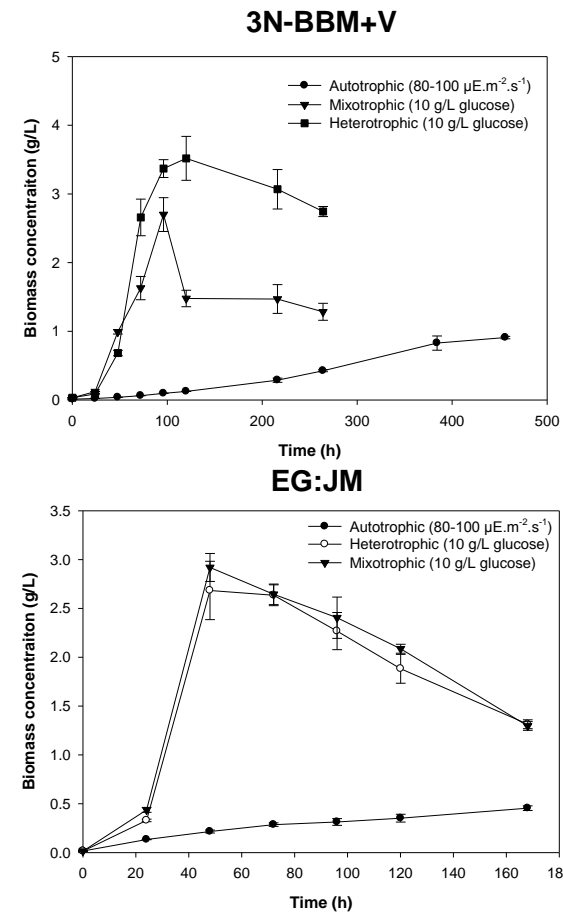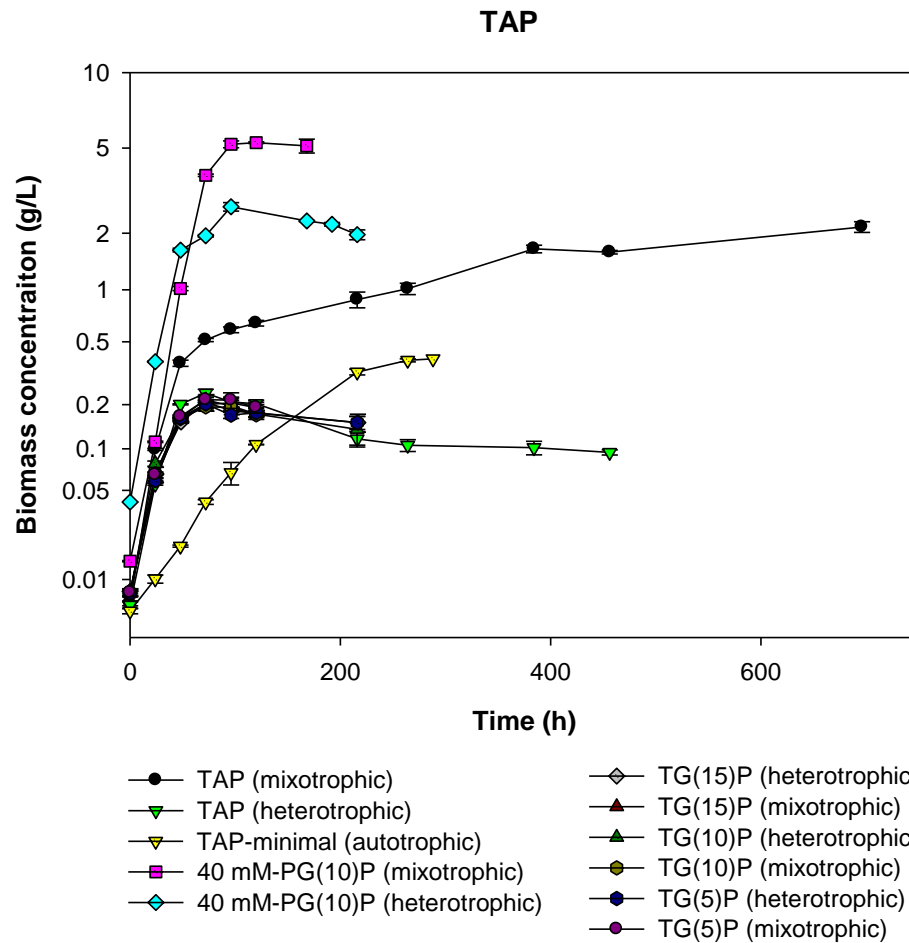
Figure 6.9 Cell growth profiles for *Chlorella sorokiniana* in different culture media under autotrophic, heterotrophic and mixotrophic conditions. Autotrophic and mixotrophic cultures were illuminated at a light intensity of 80-100 µE.m^{-2}.s^{-1}, while the carbon source used for heterotrophic and mixotrophic cultures was either acetate or *D*-glucose. PG(*x*)P, PIPES-Glucose (x g/L)-Phosphate; it represents the altered TAP formulation, where the Tris buffer was replaced by a 20 or 40 mM PIPES buffer and glucose (concentration of *x* g/L) instead of 17.4 mM acetate as the carbon source. All data shown are presented as the average±1 SD of two independent repeats.

The differences in the nitrogen sources present in the TAP, 3N-BBM+V and EG:JM media, NH_4Cl, $NaNO_3$ and *Saccharomyces cerevisae* extract respectively led to different specific growth rates observed across the different media; the maximum specific growth rates ($\ln(\Delta c)/\Delta t$) in the exponential phase were calculated to be 0.054 h^{-1}, 0.0038 h^{-1}, 0.080 h^{-1} and 0.033 h^{-1}, for mixotrophic PGP, TAP, EG:JM and 3N-BBM+V cultures respectively. *Chlorella sorokiniana* readily assimilates nitrogen preferentially in the form of ammonium over nitrates and others nitrogen containing compounds, which need to be subsequently reduced to ammonium by reducing enzymes prior to assimilation. EG:JM had the highest specific growth rate due to the 10-12% nitrogen containing compounds present in the *Saccharomyces cerevisae* extract, along with additional 10 g/L glucose, both of which are readily taken up by the cells and assimilated for cell growth. TAP acetate grown mixotrophically had the smallest specific growth rate and least generation of biomass because of the basic constituents of the TAP media formulation which provided the basic and minimal micronutrients and elements required for algal growth; however, it showed continued and sustained growth over extended time periods, suggesting a switch in cell metabolism to adapt to purely phototrophic metabolism after all the initial acetate was consumed.

However, when the acetate was replaced with glucose, the growth of *Chlorella sorokiniana* was seen to cease after 40-50 hours and entered the death phase at very low cell densities, for different concentrations of glucose and growth conditions investigated, as can be seen in Figure 6.9. To further investigate this phenomenon, the pH of the culture media was measured and recorded over time and the pH profiles are shown in Figure 6.10.
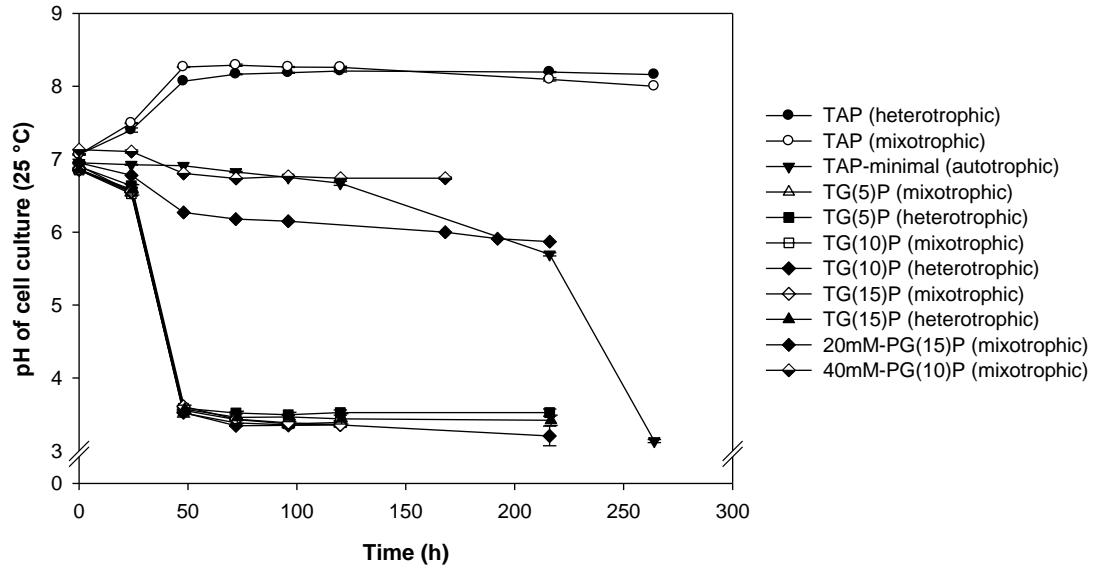
Figure 6.10 pH profiles measured at 25 °C for TAP, TGP and PGP formulations used to grow *Chlorella sorokiniana*, with 5, 10 and 15 g/L glucose as the carbon source.

Chlorella sorokiniana grows best at an optimal pH range between 7-8 (Moronta et al., 2006) and from Figure 6.10, all TAP cultures supplemented with 5, 10 and 15 g/L glucose grown both heterotrophically and mixotrophically was seen to have a drop in pH to around 3-3.5 within the first 50 hours, which was detrimental to the growth of microalgae. For autotrophically grown cells in TAP minimal media (without acetate), there pH decline was seen to occur at a much later stage around the 200 hour mark. In both cases, the drop in pH coincided with the culture time at which biomass concentration was around 0.3-0.4 g/L, suggesting a correlation between increasing biomass and the start of the observed drop in pH. However, in the case of TAP acetate, the pH was observed to remain constant after an initial increase in pH over the first two days, which helped sustain growth over extended periods.

There are two reasons for the drop in pH observed in TAP media containing glucose and ammonium as the nitrogen source. Firstly, the uptake of NH_4^+ ions into the cells is facilitated by exchanging H^+ ions within the cell with NH_4^+ ions (1:1 ratio) in the growth media to maintain cell neutrality (Eustance et al., 2013). In the case of nitrate ions, the nitrate is exchanged with an OH^- ion, which has the opposite effect and alkalises the media. Secondly, in the presence of simple sugars such as sucrose and glucose, *Chlorella sorokiniana* cells, the glucose is transported into the cell via the hexose/H^+ symport system which translocated a H^+ ion into the growth media for

every glucose molecule; in the case of acetate as the carbon source, the acetate ion is exchanged with a chloride ion and over time, the pH can be seen to increase from 7 to 8 once all the acetate is utilised and the buffering capacity of Tris-phosphate buffer is maximised at a pH of 8 (pH=pKa), which prevents further changes in the pH of the media. The net movement of protons into the growth media as a result of glucose and ammonium ion uptake acidifies the media, and in the case of a batch shake-flask culture without pH control, the Tris-phosphate buffer (with a pKa of 8.1 at 25 °C) in the TAP media can be easily overwhelmed at high cell densities and fails to effectively buffer the media at low pH which leads to the observed decrease in pH over time. Apart from that, the relatively higher respiration rates when using glucose as a carbon source (Eustance et al., 2013) could lead to a scenario where respiration (rate of CO_2 production) > rate of photosynthesis (rate of CO_2 consumption), further compounding the media acidification issues in a system without a proper pH control or sufficient buffering.

As a result of the pH decline observed due to insufficient buffering capacity when using a combination of glucose and ammonium, the standard 20 mM Tris buffer in TAP media was replaced with 40 mM Piperazine-1,4-bis(2-ethanesulfonic acid) (PIPES) buffer, which has a pKa of 6.8 and thus has a greater buffering capacity around physiological pH. With PIPES as buffer, the 10 g/L PGP media was seen to generate the greatest biomass yield of 5 g/L when grown mixotrophically with a relatively constant pH of 7, while the heterotrophic maximum biomass was around 2.5 g/L. The lower biomass generated under heterotrophic conditions can be explained by the slight pH decline to ~6 seen in Figure 6.10, where rate of respiration was potentially dominating rate of photosynthesis in the absence of a light source. However, it is also important to note that despite reaching relatively high biomass densities in heterotrophic cultures using glucose, the concentration of chlorophyll was lower compared to phototrophic/mixotrophic cultures, indicated by the pale/yellow colour of the culture as opposed to a green/dark green colour and can be seen in Figure 6.11. Differences in the observed colour intensities can also be attributed to the cell concentration at day 7, with autotrophic cultures yielding the smallest biomass concentrations and thus were a lighter shade of green compared to the heterotrophic and mixotrophic cells.
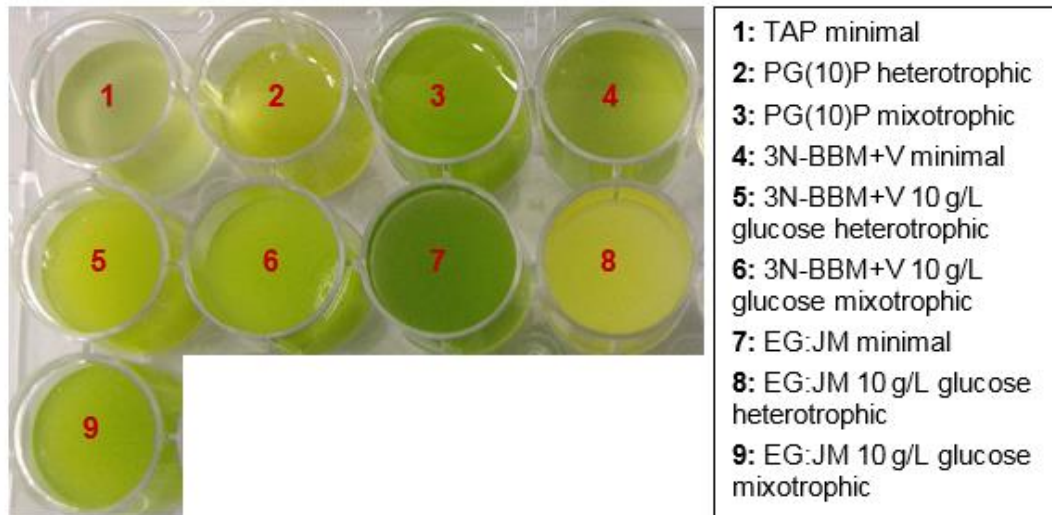
Figure 6.11 Photos of day 7 cell cultures for all three media (PG(x)P, 3N-BBM+V, EG:JM) investigated, grown under auto-, hetero- and mixo-trophic conditions. All heterotrophic and mixotrophic culture media was supplemented with 10 g/L glucose.

Growth curves are essential to a cell culture/fermentation because it allows the optimisation of biomass and yields of desired products as a function of culture time and provides information like the optimal harvest time where maximum product yield and minimal contaminants are obtained, thereby reducing the burden on the subsequent purification operations downstream. Since the aim of this chapter was to develop a novel dewatering strategy for the recovery of algal biomass, the harvest point was chosen to be the end of exponential phase where the cells are typically healthy and in a rapidly dividing state. The cells harvested at the end of the exponential phase across the three different media (40mM-PGP, 3N-BBM+V and EG:JM) were used for subsequent filtration and fouling optimisation studies in the following section.

6.2.2.2   Impact of growth conditions on fouling and filterability

In this section, experiments to determine the fouling propensities of the *Chlorella sorokiniana* grown in different media under different conditions were carried out by performing flux excursions using Durapore 0.45 µm PVDF membrane in the USD membrane device at 4000 RPM. A 0.45 µm membrane was used as the membrane pores were small enough to reject the microalgal biomass but not too large where high permeate fluxes and consequently rapid membrane fouling would occur. Apart from that, PVDF membranes have low fouling and protein absorption characteristics.

The algal feed was held within the shear chamber of the USD device and prefiltered feed (*i.e.* spent culture media) fed in and continuously recycled as permeate back to the USD device via the feed reservoir. Cells were grown in the three different media under auto-, hetero- and mixo-trophic conditions (10 g/L glucose was used as the organic carbon source for hetero- and mixo- trophy growth) and subsequently harvested at the end of their respective exponential growth phases.

To ensure a truly comparative study, the algal feedstock were all corrected to a pH value of 8±0.1 and a cell concentration of 1 g/L, before being frozen at -20 °C. Concentrated algal feed was diluted using spent media to avoid the introduction of variables such as media composition and its physio-chemical properties that could give rise to differences in the membrane-feed interactions and filtration characteristics. The age of the culture media also plays a vital part in the secretion of EPS and humic-like substances that cause fouling of the membrane; cultures in early exponential phase was observed to have a lower concentration of exopolymeric substances and hence degree of membrane fouling was lower than cells harvested in their stationary growth phase (Zhang et al., 2013). Moreover, the pH was also an equally important parameter to control since a pH>9 could damage the hydrophilic layer on the surface of the *m*PVDF membranes, thus dramatically altering the membrane permeability and the fouling behaviour. The pH can also influence aggregation and other interactions between the macromolecules and particles in the algal feed, which can introduce additional feed-related variabilities if the pH is not kept constant across the different feed. All feed was thawed and allowed to reach room temperature (~25 °C) before each experiment and the results of all the flux excursions are shown in Figure 6.12:
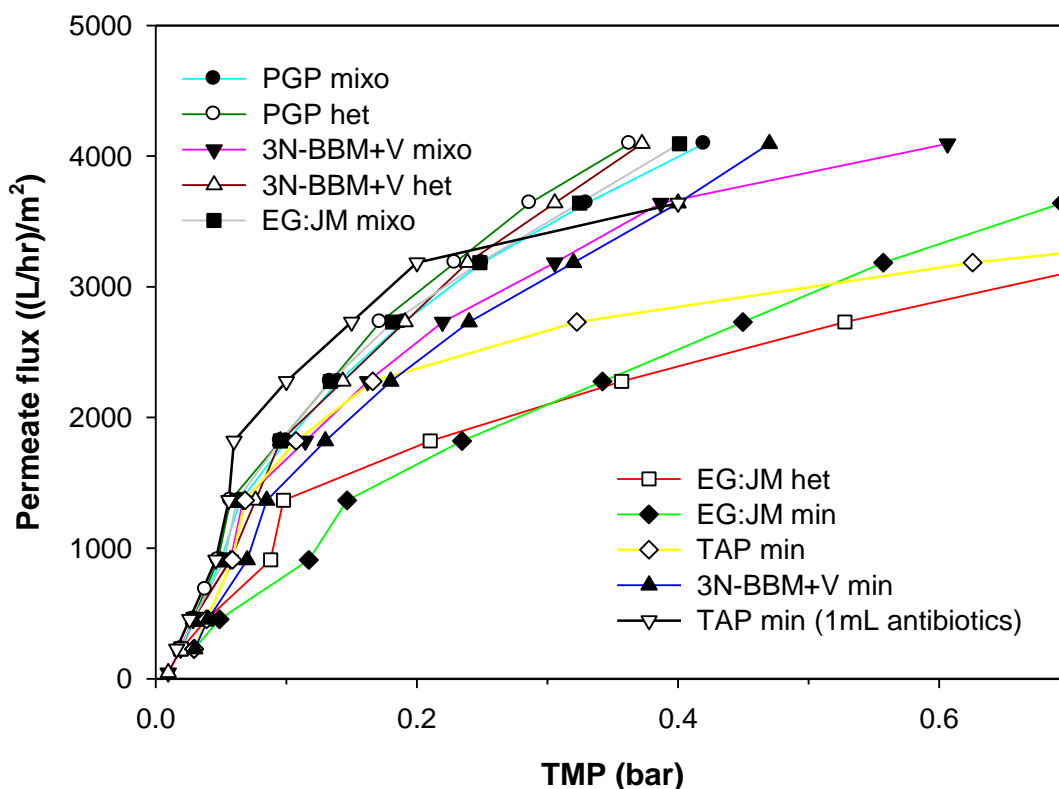
Figure 6.12 Flux excursion curves (0-4000 LMH) generated using the USD membrane device (0.45 μm PVDF membrane, 4000 RPM) for 1 g/L *Chlorella sorokiniana* cells grown auto-, hetero- and mixotrophically in 40mM-PG(10)P, 3N-BBM+V and EG:JM media at pH 8 and 25±1 °C. Heterotrophic and mixotrophic cultures were supplemented with 10 g/L glucose, and a constant illumination of auto- and mixotrophic cultures at an intensity of 80-100 μE/(m^2.s). All fluxes reported are temperature corrected to 25 °C and averaged values reported (*n*=2) with <5% standard deviation; error bars were excluded to preserve image clarity but are shown in Table 6.3.

Figure 6.12 illustrates the impact of growth conditions and media used on the flux excursion curves and consequently, its filterability. MATLAB 2016 was used to process the flux versus TMP raw data and the temperature corrected flux data fitted to the first-order exponential curve; critical fluxes was determined to be the point where TMP_F:TMP_i ≥ 1.5:1. The limiting permeate fluxes, fouling dynamics and rate of fouling all differ based on the growth conditions and media of the cells. To compare the severity of fouling across the different feed samples, the NWP before and after the flux excursion experiments were measured and the % drop in permeability along with critical fluxes reported in Table 6.3.

Sample	J_{crit} (LMH)	Mean drop in $NWP_{25\,°C}$ (%)
TAP minimal	2067.6 ± 35	60 ± 0.3
TAP min PIPES+1ml antibiotics	2324.7 ± 19	21 ± 1.1
PGP heterotrophic	3073.3 ± 42	21 ± 0.3
PGP mixotrophic	2851.7 ± 58	9 ± 0.3
3N-BBM+V minimal	3192.0 ± 11	34 ± 0.8
3N-BBM+V heterotrophic	3267.3	29 ± 0.4
3N-BBM+V mixotrophic	2614.3 ± 21	29 ± 1
EG:JM minimal	3282.1 ± 9	62 ± 0.4
EG:JM heterotrophic	2123.2 ± 87	17 ± 3
EG:JM mixotrophic	2844.0 ± 44	23 ± 0.3

Table 6.3 Experimentally determined critical fluxes and average % drop in NWP at 25 °C post-run (for the various *Chlorella sorokiniana* (1 g/L) feedstock investigated. Values reported to 1 standard deviation about the mean (*n*=2).

No strong correlation was observed between % drop in NWP and the observed critical fluxes, which suggests other factors that can influence fouling and critical fluxes that were not controlled during the experiment. The % decrease in NWP reflects the degree of fouling that took place during the flux excursions, with TAP and EG:JM minimal experiments exhibiting largest drop in membrane permeability. Factors that are influenced by growth conditions (media, pH, carbon source) include variations in cell morphologies (which impacts cake resistances based on aspect ratio of cells and effective packing of the cake layer), biomass/lipid yields and concentration of fouling agents such as EPS. Detailed studies and investigations of the effect of cell size and morphology on filtration has been done by using polymorphic microorganisms (Foley et al., 2005; McCarthy, 2002; McCarthy et al., 1999, 1998); the experimental results strongly indicated that the specific cake resistance and cake compressibility is a function of cell morphology, more specifically the mean aspect ratio of the cells. It has also been reported that the physiological state of the algal culture and extracellular organic material (EPS/TEP) determines the rate of fouling (Babel and Takizawa, 2011; Wicaksana et al., 2012). To investigate the impact of media and growth conditions on the cell morphology of *Chlorella sorokiniana*, SEM imaging and particle size distribution (PSD) analysis was carried out for the different cell cultures and are shown in Figure 6.13 and Figure 6.14, respectively.

TAP minimal

PGP heterotrophic

PGP mixotrophic

3N-BBM+V minimal

3N-BBM+V heterotrophic

3N-BBM+V mixotrophic

EG:JM minimal

EG:JM heterotrophic

EG:JM mixotrophic

TAP minimal (+1 mL antibiotics)

Control (membrane only)
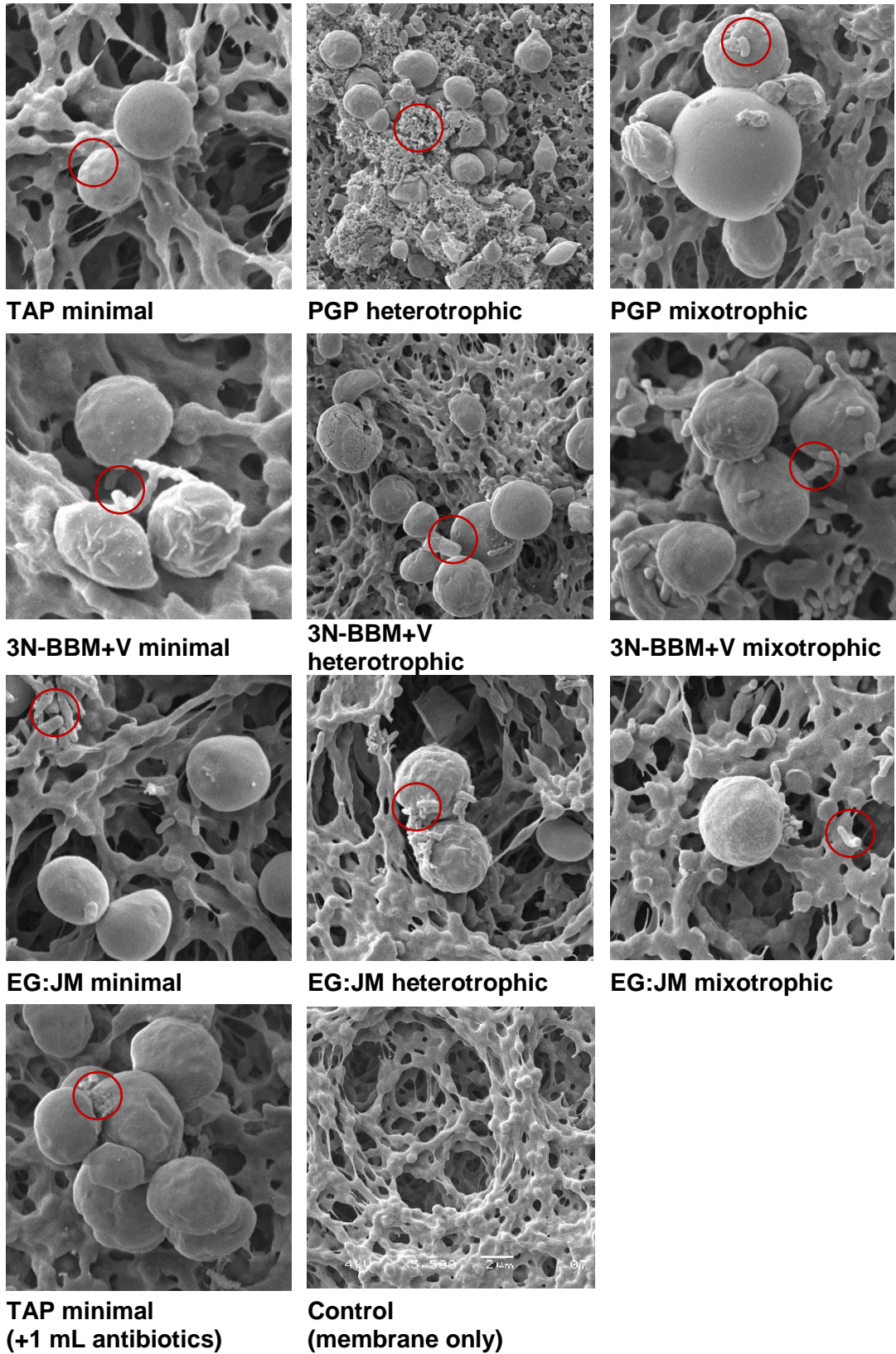
Figure 6.13 SEM images (4 kV, 10000x magnification and working distance of 5 mm, cells filtered on to 0.45 μm Durapore membrane discs) of *Chlorella sorokiniana* cells grown in different media and growth conditions (all hetero- and mixo- trophic cultures

were supplemented with 10 g/L glucose). 0.45 µm Durapore membrane wetted with water and critical point dried was used as a negative control. Bacteria are highlighted by red circles. Size bar was not included as the individual images were zoomed in to clearly show microalgal and bacterial populations, including cell morphology.
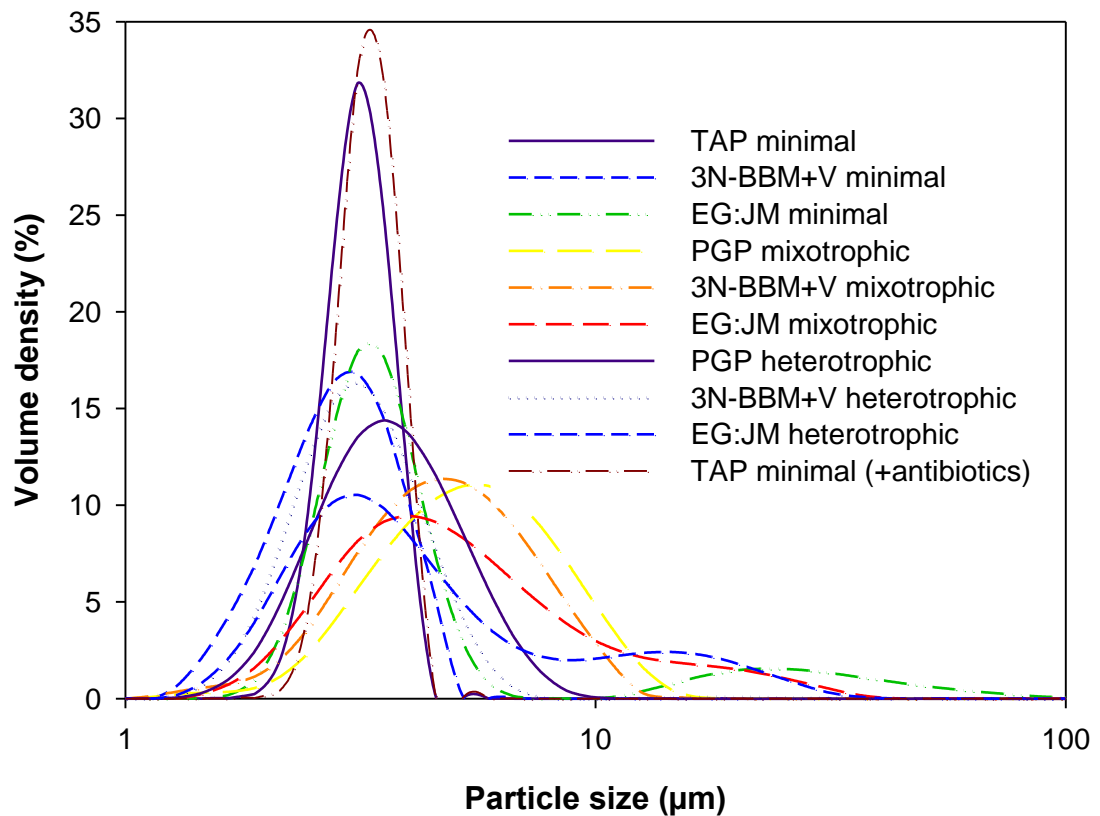
Figure 6.14 Impact of growth conditions and media formulation on particle size distributions (PSD) of *Chlorella sorokiniana* cells. Measurements were performed in triplicates and size distributions averaged and presented as a volume-based distribution. No submicron particle sizes or particles larger than 100 µm was observed and thus the *x*-axis scale adjusted to show data between 1-100 µm.

From Figure 6.13 and Figure 6.14, both the morphology and the range of particle sizes was observed to vary depending on the growth conditions and media, which are expected to have an influence on the extent and dynamics of membrane fouling, when a cake/polarised layer forms during filtration. Apart from that, the range of particle sizes present in the feed solution would also dictate properties such as the compressibility and permeability of the cake layer. The average particle size (D_{50}) of *Chlorella sorokiniana* cells across the different media was determined to be around 3.51±0.56 µm, suggesting a relatively large variability of particle size distribution,

which could explain the differences in flux excursion data observed in Figure 6.12. Furthermore, despite observing a significant bacterial population co-existing with the microalgal cells from the SEM images, the PSD curves did not show peaks that would correspond to the typical sizes for rod-shaped bacteria (1-2 µm). The reasons for this include the use of refractive index and properties used to carry out the PSD experiments that were specific to microalgae, and the aggregation of bacteria seen from the SEM images, which correspond to particle sizes in the 10-100 µm region.

For a given growth media, average particle size (D_{50}) was seen to increase in the order of mixotrophic>heterotrophic>autotrophic conditions, suggesting the cells grew to a larger size on average when supplemented with both light and a carbon source, rather than either on its own. During tangential flow filtration, larger particles tend to be swept away from the membrane surface, and thus the polarised/cake layer is usually made up from a finer fraction of the particle size distribution with a relatively higher specific resistance. The increase in specific cake resistance with increasing crossflow velocity can be explained based on mass transfer mechanisms. At a given crossflow velocity, there exists a maximum particle size that can deposit on to the surface of the membrane, and with increasing crossflow velocity, this cut-off diameter decreases thus allowing smaller particles to form a cake layer (Le-Clech et al., 2006); Keskinler et al. (2004) found that the specific cake resistance of *Saccharomyces cerevisae* cells was inversely proportional to the crossflow velocity, all else being equal. In contrast, Lee and Clark (1998) observed no such stirring speed associated effects on the specific resistance values during the membrane filtration of monodisperse latex particles, suggesting the compressible nature of biological cells which have variable morphologies and particle size distributions.

Apart from the observed variability in cell morphologies and sizes across the different growth media and culture conditions, a significant bacterial population was also observed in close proximity to the algal cells in the SEM images, attached either to the algae cells themselves or around them, marked red in Figure 6.13. The degree of bacterial contamination (*i.e.* population of bacterial species) was seen to be proportional to the concentration of *Chlorella sorokiniana* cells, with greater bacterial counts observed for heterotrophic and mixotrophic cultures. Microalgae are known for their symbiotic relationship with certain bacteria, and *Chlorella sorokiniana* has been observed to have pro-symbiotic relationship with certain species of bacteria and fungi; Jones et al. (1973) observed typical large scale *Chlorella sorokiniana* cell cultures to be significantly infected with bacteria, namely *Pseudomonas*,

Acinetobacter, *Flavobacterium* and *Bacillus* even when grown at extreme temperatures of 39 °C. Bacteria such as CSSB-1 and CSSF-1 tend to adhere directly to the surface of *Chlorella sorokiniana* cells, whilst other species like CSSB-2 and CSSB-3 was found to populate the extracellular sheath matrix excreted by the microalgae (Watanabe et al., 2005). Higgins and VanderGheynst (2014) investigated and compared axenic *Chlorella minutissima* and *Escherichia coli-Chlorella minutissima* co-cultures and found the latter to generate significantly greater biomass yields in a shorter time period with relatively higher intracellular lipid concentrations, proving a symbiotic relationship between the two species. Axenic microalgae cell cultures are difficult to obtain and maintain in practice, and generally require addition of antibiotic and antifungal cocktails in the growth media, and Szaub (2013) reported no difference in growth rates between autoclaved and un-autoclaved growth media (grown autotrophically and heterotrophically).

However, despite no competition for resources and space between microalgae and bacterial populations in non-axenic cultures, the presence of bacteria could compound biofouling challenges when using tangential flow filtration for the initial harvest step. This was evident in the flux excursion data for TAP minimal cultures where cultures supplemented with an antibiotic mix yielded greater permeate fluxes (at a given TMP) as well as a much lower drop in NWP, compared to the non-axenic culture. Microalgae secrete extracellular organic material into the media which are taken up by bacteria, which then provide the microalgae with growth promoting factors in a mutually beneficial relationship (Miao and Wu, 2006). The SEM images show the presence of an extracellular sheath matrix around the cells, which serve as a scaffold and mediator role in symbiotic associations for inter-cellular communication; the extracellular matrix can be observed in some of the images in Figure 6.13, and is typically composed of polysaccharides, lipids and inorganic components (Watanabe et al., 2006). This sticky, gel-like matrix can enhance cell aggregation and biofilm formation at the membrane surface during filtration.

Thus, to better understand the relationship between the concentration of these fouling species and corresponding irreversible fouling via pore constriction/pore blocking, colorimetric absorption experiments were conducted to quantify the relative quantities of soluble TEP <0.2 µm in size (since the average pore size of the membrane used was 0.45 µm), as well as the total soluble carbohydrates and protein concentrations across the different cell cultures. The degree of irreversible fouling was determined by calculating the % drop in NWP post-experiment, after a quick water flush to get rid

of any unbound/loosely bound foulants and any cake/polarised layer formed at the membrane. On the other hand, the amount of foulant remaining on the membrane and/or within its pores was determined by making use of a mass balance approach; it was determined to be equal to the difference between the colorimetric absorbance of the feed and permeate samples (conversion to concentration was not required as the % decrease would be relative). The processed data expressed as g/L concentration (by using appropriate empirical calibration curves), as well as previous PSD (D_{10}), NWP and J_{crit} data, are shown in Table 6.4.

The empirical fouling metrics in Table 6.4, namely the % loss in NWP and the critical fluxes across the different conditions tested, provide a semi-quantitative indication of the degree of irreversible fouling by pore blocking/constriction (indicated by the proportion of recoverable NWP relative to the initial NWP) and the properties of the deformable cake formed at the membrane surface which corresponds to the point where the TMP starts to rise uncontrollably, *i.e.*, critical flux, respectively. Irreversible fouling can be characterised as the *internal* fouling that occurs and requires aggressive chemical cleaning to dissolve the foulants adhered to the membrane and/or pores to restore initial membrane permeability. On the other hand, reversible fouling such as cake formation is an *external* fouling and is largely reversible by gentle backflushing or low crossflow across the cassette (with permeate closed) using pure water (Crittenden et al., 2012). It is important to note that the nature of cake formed is different for normal dead-end filtration versus tangential flow filtration; the former generates a cake whose thickness depends solely on the pressure applied, whereas for tangential flow filtration, the limiting cake thickness is determined by both upstream pressure and the crossflow velocity (Tarleton and Wakeman, 1993).

The morphology of the cake layer, which depends on the nature and the size of the particles forming the cake layer, is a vital parameter that directly affects process fluxes in tangential flow filtration. Thus, for a fixed crossflow rate (4000 RPM), same permeate flux, same feed concentration, the properties and thickness of the cake formed will depend on the particle size distribution of the feed particles. For a given crossflow and a standard Gaussian-distribution of the feed particles, the larger particles are more likely to be driven back into solution via inertial lift and shear-induced back diffusion, whilst the much finer particles would be back-transported from the membrane by Brownian diffusion alone, which is the slowest transport mechanism out of all (Shankararaman Chellam and Wiesner, 1997). Huisman et al. (1999) claimed that the finer particles in a polydisperse feed would influence the critical flux,

as the smaller particles (0.2-2% of the sizer distribution) would be the first to predominantly deposit on the membrane to form a cake and define the overall cake permeability. This was further backed up by experiments carried out by Tarleton and Wakeman (1993), who found the median particle size, D_{50}, was a poor indicator for membrane fouling via cake formation/pore plugging, and the 10th percentile (D_{10}) of the cumulative feed particle size distribution was a better representative measure with their microfiltration experiments with calcite suspensions. Thus, the D_{10} values, *i.e.* the diameter at which 10% of the feed is made of particles with size $<D_{10}$, from the PSD curves in Figure 6.14 was also included in Table 6.4 to provide a quantitative measure.

Feed	% decrease post-filtration			C*P*T	% drop in NWP	D_{10}	J_{crit} (LMH)
	C	P	T				
TAP minimal	100%	96%	91%	87.4%	60 ± 0.3	2.88	2067.6 ± 35
TAP minimal (axenic)	100%	6%	0%	6.0%	21 ± 1.1	2.96	2324.7 ± 19
PGP heterotrophic	100%	65%	83%	54.0%	21 ± 0.3	2.82	3073.3 ± 42
PGP mixotrophic	53%	13%	64%	4.4%	9 ± 0.3	3.22	2851.7 ± 58
3N-BBM+V minimal	100%	86%	99%	85.1%	34 ± 0.8	1.99	3192.0 ± 11
3N-BBM+V heterotrophic	91%	74%	101%	68.0%	29 ± 0.4	2.54	3267.3
3N-BBM+V mixotrophic	80%	63%	93%	46.9%	29 ± 1	2.86	2614.3 ± 21
EG:JM minimal	100%	37%	84%	31.1%	62 ± 0.4	2.66	3282.1 ± 9
EG:JM heterotrophic	92%	21%	79%	15.3%	17 ± 3	2.58	2123.2 ± 87
EG:JM mixotrophic	100%	15%	73%	11.0%	23 ± 0.3	2.74	2844.0 ± 44

Table 6.4 Summary of average critical fluxes, particle diameter D_{10} (from Figure 6.14) and concentrations of carbohydrate, protein and soluble TEP (relative to the initial concentrations of the species) retained by the membrane for 1 g/L *Chlorella sorokiniana* cells in different media/conditions. J_{crit} and % drop in NWP values are reported to ±1 SD about the mean (*n*=2). C-carbohydrates, P-protein, T-soluble TEP.

One of the key observations from Table 6.4 was the impact of using antibiotics to obtain axenic cultures and compare experimental flux and fouling data to non-axenic

cultures. The TAP minimal with antibiotics feed showed no observable retention/decrease of soluble TEP or proteins by the membrane compared to the media without antibiotics, which proved the source of both soluble TEP and proteins to be microbial-derived, and the use of antibiotic mix stopped the growth of bacterial and thus keeping production/secretion of soluble EPS and its precursors to a minimum. The axenic TAP minimal feed showed a ~67% decrease in the degree of irreversible fouling (% losses in NWP) compared to the non-axenic TAP minimal cells (drop from 60% to 21%). However, the associated increase of ~250 LMH in critical flux was not considered statistically significant to establish a correlation between critical flux and amount of soluble TEP, due to the large observed variabilities in particle size distributions, which impacts critical fluxes observed between the axenic and non-axenic cultures. In terms of critical fluxes, there was a clear trend observed within subgroups of data, *i.e.* for a given media, the critical flux was observed to be proportional to the D_{10} value, supporting the previously discussed hypothesis of the critical flux being relatively more sensitive to the finer particles present in the feed stream and overall cake permeability being predominantly dependent upon the deposition of the smaller particles on the membrane surface. This observation suggests that increasing the effective particle diameter by reducing the proportion of the finer particles in the feed (D_{10}) could effectively result in a greater critical flux, for all else equal.

For the irreversible fouling, as mentioned previously, the extent of fouling and dynamics are directly affected by factors such as the molecular weight distribution and relative hydrophobicity of the foulants (EPS, carbohydrates, proteins), as well as the ratio of the three foulants to each other (protein:carbohydrate:EPS), which was found to affect observed cake resistances and fouling rates for a 100 kDa UF process (Arabi and Nakhla, 2008). Furthermore, the initial concentrations of the three species are highly variable, mainly with respect to carbohydrates and proteins, which would be typically higher in the nutrient-rich media such as the 3N-BBM+V and EG:JM, which contains extra nitrate/vitamins and *Saccharomyces cerevisae* extract to supplement growth respectively, despite the feed concentrations being diluted and normalised to 1 g/L before the experiments. Because of that, plus the lack of quantitative data for the molecular weight distribution of the foulants investigated here, it was difficult to draw up a conclusive correlation between % decrease in individual foulant quantities and the % drop in permeability post-operation.

However, despite the issues discussed above, some degree of comparison and trends could still be observed by using all the data in Table 6.4, where a combined fouling factor (C*P*T) was calculated and used, rather than looking at them independently. Figure 6.15 shows the data on a scatter plot that was subsequently used to establish a relationship between the variables.
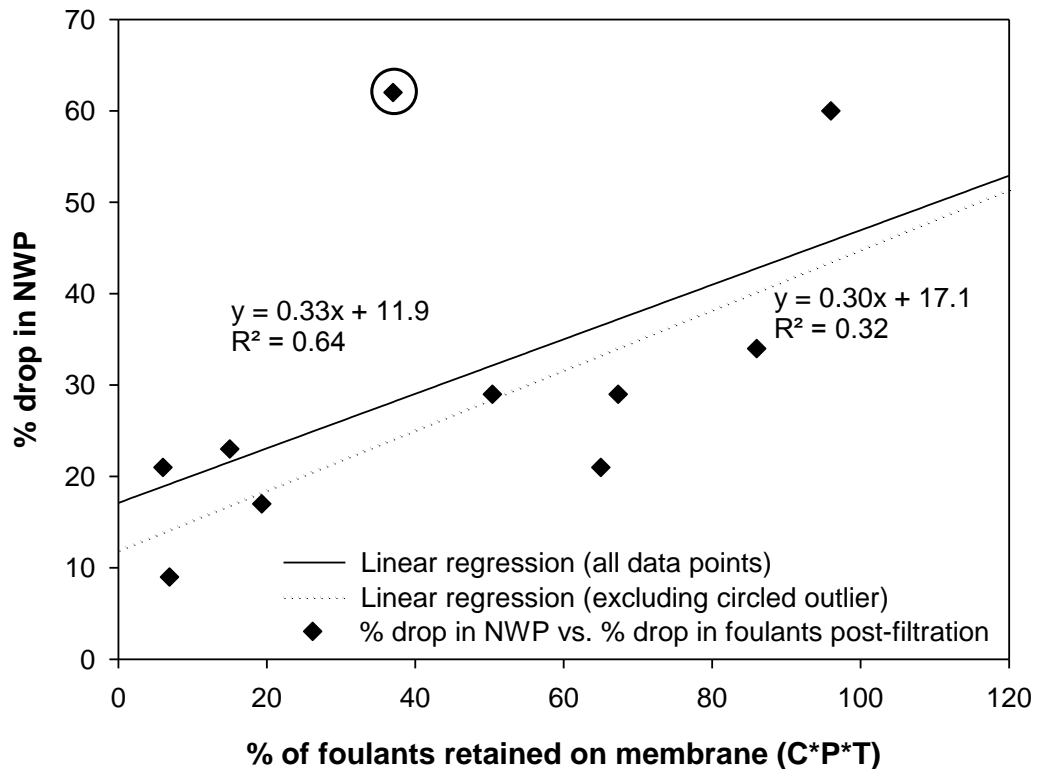
Figure 6.15 Scatter plot of the degree of irreversible fouling (quantified by % drop in NWP) versus combined fouling factor (overall % drop across all three fouling components) post-filtration for all the different growth conditions and media used for *Chlorella sorokiniana.*

A weak positive correlation with the data points fairly dispersed around the regression line was seen for the different media, for all things equal and assuming a similar molecular weight distribution and specific properties of the fouling species. It is generally difficult to establish a conclusive relationship for the individual foulants and observed fouling since there is likely to be additional interactions, both amongst the fouling species themselves and the biomass. The proportion of foulants being retained by the membrane was observed to be proportional to the extent of irreversible fouling. The correlation was improved by excluding the potential outlier (circled black), almost doubling the R^2 value from 0.32 to 0.64. The positive correlation

established could be further improved by considering the molecular weights of the fouling species, the hydrophobicity/hydrophilicity and affinity of the particles towards PVDF membranes, and quantifying EPS particles >0.2 µm in size. However, considering the many sources of variations, and the mass balance approach limitations where some of the foulants were lost in the wash/rinse step before the NWP measurement post-experiment, the regression value of 0.64 proved the positive correlation to be statistically significant and established causality.

The observation of pore plugging/constriction and cake formation is in good agreement with work done previously by Qu et al. (2012), who identified pore plugging and cake formation to be the main mechanisms for membrane fouling during the ultrafiltration of *Microcystis aeruginosa* using negatively charged PES membranes, with EPS sizes ranging between 100 kDa and 0.45 µm to be the major foulants. In another independent study by Rickman et al. (2012), a constant-flux stepping stirred-cell filtration of *Chlamydomonas* algal suspensions in total recycle mode was carried out to gain a better insight into the fouling mechanisms for UF/MF membranes. The critical flux, fouling rates and possible fouling reversibility was determined; at high fluxes, high rates of irreversible fouling was observed with the smaller membrane pore sizes (50 kg/mol UF and 0.22 µm MF), while a 5 µm pore size had little fouling and changes in overall resistance, although the whole cells were rejected and deposited on the membrane surface as cake. Submicron particles, proteinaceous substances and humic-like particles present in the 5 µm MF permeate stream were identified to be the primary fouling agents responsible for the flux decline and fouling irreversibility. These smaller colloids were deemed to form cakes with increased resistances (UF and 0.22 µm MF) and/or block the membrane pores (0.22 µm MF), rather than the macromolecules or the algal biomass cake. To further investigate and determine the dominant fouling mechanism between caking and pore plugging/constriction by particulates and soluble species in the liquor, 1 g/L TAP minimal cells (grown autotrophically) was spun down twice in an Eppendorf 5810R centrifuge (Eppendorf AG, Germany) for 30 minutes at 4,000 RPM (10 °C) to generate two isolated streams; namely, the liquor containing soluble species and the cell paste, which was resuspended in 0.1 M PBS solution to generate the resuspended solids (RSS) component. Flux excursions using the USD membrane device (4000 RPM, 0.45 µm) was carried out for the liquid supernatant, RSS and the mixed liquor (original TAP minimal feed), and the results are shown in Figure 6.16.
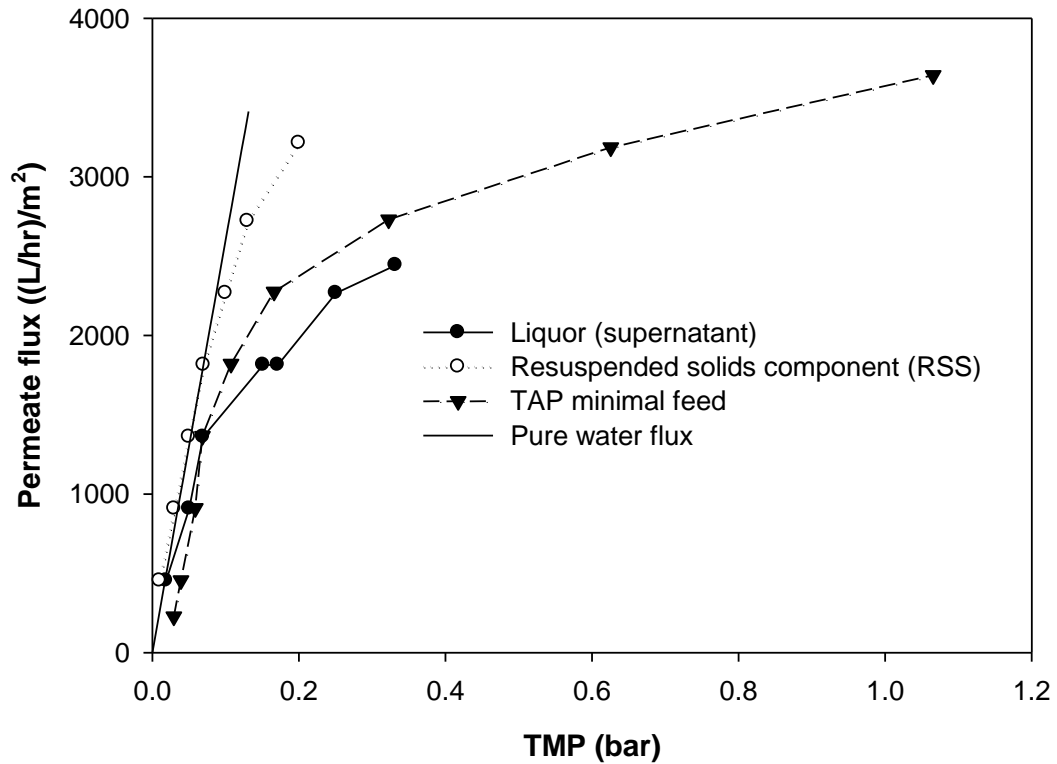
Figure 6.16 USD flux excursion data (0.45 μm Durapore PVDF membrane at 4000 RPM and 25 °C) for: 1 g/L *Chlorella sorokiniana* in TAP minimal media (pH 7), resuspended solids component (spun-down paste$_{4000\ RPM}$ resuspended in 0.1 M PBS) and liquor component (supernatant$_{4000\ RPM}$). Solid line represents the normalised pure water flux data included as the baseline for unfouled process performance. All permeate flux data reported are corrected to 25 °C.

The flux versus TMP data for the RSS stream showed little deviation from the pure water flux line with no membrane fouling), indicating little/no contribution to membrane fouling from the biomass itself, in terms of cake formation at higher pressures (> 0.1 bar); the TMP profile followed the typical linear rise in pressure (*n*=0 from Table 6.1) for a cake composed of undeformable, rigid particles. Microalgae cells are generally more rigid and robust than most biological cells due to the presence of the cellulosic cell wall, with *Chlorella* possessing a cell wall that is primarily 80% carbohydrates (Rodrigues and da Silva Bon, 2011). The rigid and undeformable nature of the *Chlorella sorokiniana* cells made severe membrane fouling via pore blocking and subsequent cake formation unlikely to occur at lower pressures, since the membrane pore size (0.45 μm) was much smaller than the average cell diameter (*D$_{50}$*=4.3 μm average diameter from the PSD curves in Figure 6.14).

On the other hand, pore constriction by the soluble components in the liquor was the dominant fouling mechanism and caused much more rapid increase in TMP ($n \geq 1$) with increasing flux, leading to the conclusion of complete pore plugging at higher fluxes. The TAP minimal flux versus TMP curve was dominated by the pore plugging from the liquor which offers the greatest resistance and consequently irreversible fouling, rather than the resuspended solid stream; Mukherjee (2014) reported a similar observation during the microfiltration of proteins, where internal fouling (pore constriction/plugging) was found to dominate cake formation primarily due to the much more open pores of MF membranes compared to UF.

Spinning down the algal feed suspension causes the cells along with other suspended particles/colloids to separate and settle down into a cell paste, however, the supernatant could still contain smaller colloids/particles that cannot be separated via centrifugation at the *g* force applied, compared to membrane separation. As a result, the primary foulants were identified to be soluble components such as proteins, EPS (<0.4 µm) and carbohydrates present in the liquor, as opposed to the EPS that exist attached to the cell surface (bound-EPS or the biomass itself, similar to the findings previously (Babel and Takizawa, 2010; Discart et al., 2013; Fane, 2012; Jepsen et al., 2018; Xiao and Zheng, 2016). Furthermore, it was highly unlikely to be discrete particulates in the sub-micron range that could have contributed to gradual and complete pore blocking, since the PSD data showed no population of particles with sizes <0.1 µm.

Optimisation of media formulation with regards to foulant concentrations can be performed after such USD experiments, with regards to overall biomass/lipid yields at the lowest EPS and protein secretion to avoid rapid membrane fouling. The main issue highlighted here was the complexity associated with MF processes, particularly when using complex feed with a wide array of foulants, whose specific properties are dependent upon a multitude of factors, thus making it difficult to model and/or optimise the concentration process to achieve high sustainable fluxes while minimising membrane fouling. However, special care must be taken when using this approach because the data generated above only applies to *Chlorella* cultures grown in shake flasks (with poor temperature, pH, light and CO_2 control) and harvested at the end of stationary phase. Cells grown in shake flasks are likely to experience different stresses at the micro-scale level compared to large fermenters with agitators and online control of parameters that can generate different metabolite and foulant profiles. Furthermore, the concentration of solids influences the potential of cake

formation, while the EPS trapped within the algal cakes can significantly increase the specific cake resistance compared to cake formed at lower cell concentrations (Yeh and Drexler, 2014). The research done here highlights the fact that downstream processes can be optimised by considering not only process-specific parameters, but also considering optimising the growth conditions upstream. Since the media and growth conditions were seen to affect both biomass production along with the amounts of foulants secreted into the liquor, there is a potential trade-off to be considered. Thus, tangential flow filtration downstream can be optimised in a couple of different ways, making use of the USD-derived information regarding product yield versus filterability. Few such examples include optimising the growth media to minimise or completely eliminate the secretion of the polysaccharide foulant species as well as soluble EPS (which can be achieved with maintaining axenic culture conditions), pre-filtering the cell suspensions using a depth filter to reduce the population of the smaller particulate matter (D_{10}) or modifying the growth media/conditions to minimise the production of low molecular weight contaminants that could cause rapid membrane fouling. Apart from that, as previously mentioned, factors such as culture age, point of harvest or even the choice of carbon source (glucose versus glycerol versus acetate) could potentially influence the excreted metabolite profiles, which could be optimised based on their relative fouling potential, which can be evaluated using the USD membrane device.

Therefore, the next section looks at an USD-based optimisation approach for the dewatering of *Chlorella sorokiniana* cells grown mixotrophically in 3N-BBM+V media, which was chosen due to its rapid growth rates and biomass yields generated. Furthermore, mixotrophic growth conditions have been proven to be extremely effective for *Chlorella* cell cultures, capable of generating and sustaining relatively high biomass concentrations and high lipid productivity, by limiting the impact of lower biomass generation during the dark respiration phase and providing a good mixture of organic and inorganic carbon sources for sustained biomass growth (Brennan and Owende, 2010). The mixotrophic condition allows the cells to initially grow and replicate on the organic carbon source (glucose in this case), and once the initial glucose in the media is depleted, the cells are then able to switch their metabolism to primarily assimilate inorganic carbon to sustain continued growth.

6.2.2.3 USD-based optimisation of *Chlorella sorokiniana* microalgae concentration process

The traditional and widely accepted approach for optimising a concentration process, not dissimilar to the *Saccharomyces cerevisae* case study in section 6.1, is to determine volumetric capacity throughputs and optimise the MF process based on both volumetric throughput limits and critical flux. Section 6.2.2.3.1 looks at the established approach used in industry for a typical MF concentration process, which is then compared to the novel USD-based concentration methodology that enables higher throughputs to be achieved with minimal membrane fouling.

6.2.2.3.1 Optimisation using volumetric capacity limits

As discussed previously in section 6.1.1, microfiltration operations involving particulate-rich feed also have volumetric capacity limits, and consequently, the operating fluxes for MF processes typically require to be optimised with respect to both volumetric capacity limits and critical fluxes. 0.5 g/L *Chlorella sorokiniana* grown mixotrophically in 3N-BBM+V media was used to carry out flux excursions using the USD membrane device (4000 RPM) to determine the critical flux, and the results are shown in Figure 6.17. Large scale experiments to verify USD data were not done since the previous section 6.1 proved the accuracy and robustness of the scale-up/prediction model with respect to volumetric capacity and critical fluxes.
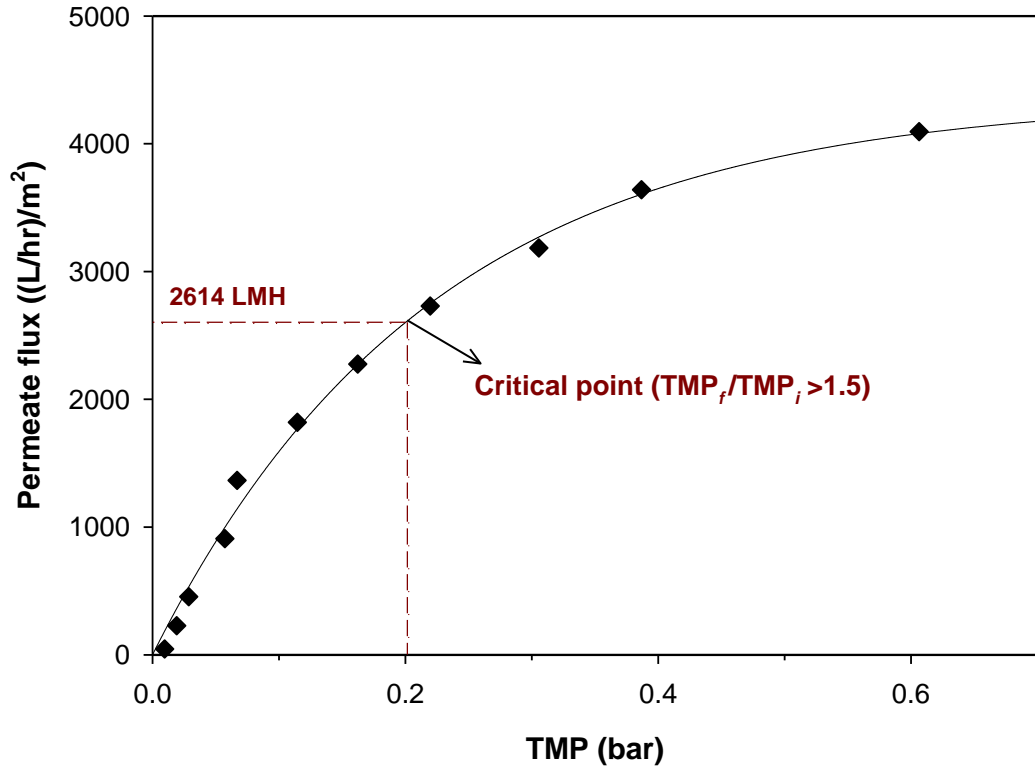
Figure 6.17 Evaluation of critical flux for 0.5 g/L *Chlorella sorokiniana* (3N-BBM+V, 10 g/L mixotrophic culture, pH 8) from steady-state flux excursion data generated using the USD membrane device (4000 RPM, 25 °C) in total recycle mode.

To determine maximum throughput (volumetric capacity) as a function of permeate fluxes, range of permeate flux values below the critical flux (2600 LMH) at the initial cell concentration of 0.5 g/L was used to carry out volumetric reduction experiments. Concentration experiments were carried out a constant RPM of 4000 RPM and fluxes ranging between ~50 LMH and 350 LMH. The process endpoint (maximum throughput) was predefined as 0.2 bar maximum TMP (well below the recommended maximum forward pressure of 0.7 bar for open membranes, i.e., >100-300 kDa (Ultrafiltration Membranes Operating Manual, 2011)) or when a rapid increase of TMP was observed. The final concentration at the end of the experiment was calculated by VCF achieved and verified using OD_{750} measurements in Equation 6.5 to calculate dry cell weight concentration.
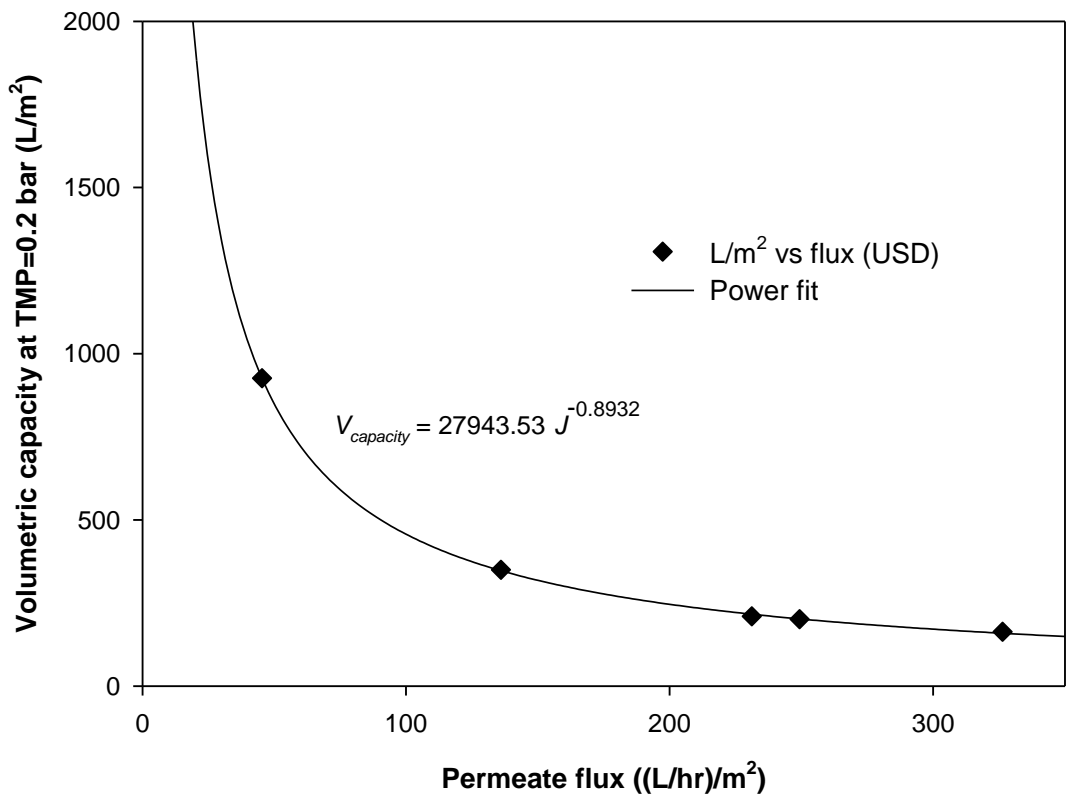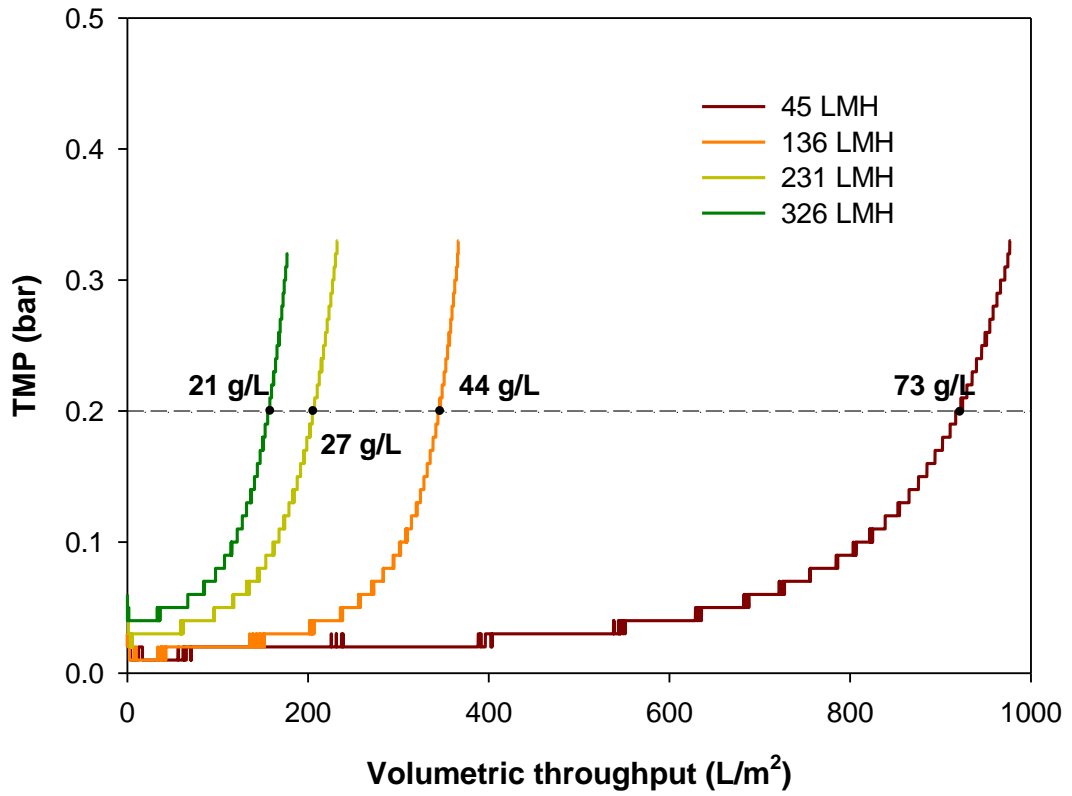
Figure 6.18 Volumetric reduction experiment results for 0.5 g/L *Chlorella sorokiniana* (3N-BBM+V, mixotrophic) using the USD membrane device at 4000 RPM and 25 °C.

Top: TMP versus volumetric loading at different permeate fluxes, bottom: volumetric throughput limit (at 0.2 bar TMP) as a function of permeate flux, with solid line representing a power fit with R^2=0.99.

At constant crossflow rate and initial solids concentration, both the volumetric capacity through the membrane and final achievable cell concentration was seen to decrease with increasing permeate flux (Figure 6.18) and there was a trade-off between processing time versus volumetric capacity. As expected, there was a typical asymptotic behaviour seen as the permeate flux approached zero since there would be minimal fouling/cake formation (for screened TFF cassettes, there is some degree of polarisation occurring at zero net flux due to upstream pressures on the membrane). As permeate flux increases, the capacity decreases since the crossflow effect is diminished and overwhelmed by the greater convective forces depositing particles on to the membrane, causing build-up of cake which fouls the membrane and thus there is a limited amount of feed that can be processed before a catastrophic fouling feedback loop is reached and the TMP (at constant flux) rises uncontrollably.

At a given permeate flux, there is a maximum volume of feed that can be processed and a corresponding maximum solids concentration that can be achieved. The increase in TMP during concentration experiments is not dissimilar to the concept of critical flux, where at operating fluxes beyond the critical flux (for a given set of operating conditions) results in rapid irreversible fouling of the membrane and a corresponding rise in TMP. The maximum achievable concentration at a given permeate flux could be related to the critical flux at the final concentration, and an uncontrollable increase in TMP is seen when the operating flux exceeds the critical flux value for a specific solids concentration. To verify and further understand this relationship, flux excursions were carried out for different concentrations of 3N-BBM+V mixotrophic cells to determine critical fluxes as a function of cell concentration. The critical fluxes at different cell concentrations, along with permeate fluxes used for capacity determination experiments, are shown in Figure 6.19.
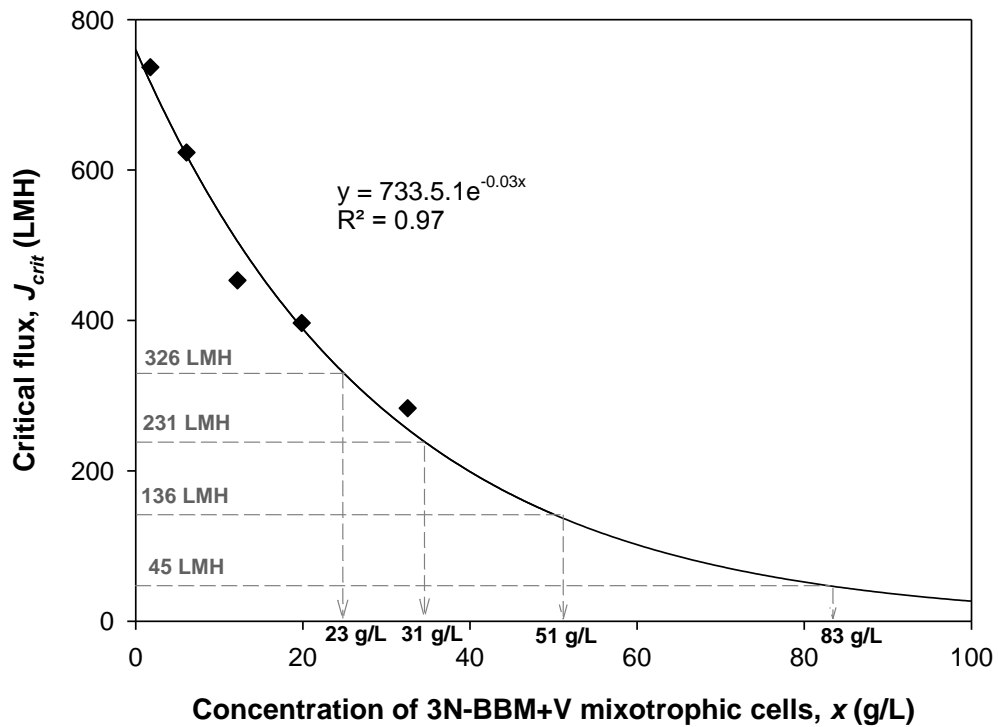
Figure 6.19 Critical fluxes as a function of concentration for *Chlorella sorokiniana* cells. Permeate fluxes used for capacity determination experiments and the corresponding concentrations at which operating flux=critical flux (shown as grey dotted arrows). Solid line represents exponential decay curve fitting to experimental data.

From the critical flux data above, critical flux was found to be inversely proportional to the cell concentration and observed to decrease exponentially as the feed gets concentrated. For the various permeate fluxes used for capacity determination, the corresponding concentration was calculated from the non-linear empirical relationship (equation of solid line in Figure 6.19) and compared to final concentrations achieved in the concentration experiments (Table 6.5).

Permeate flux (LMH)	Final concentration (g/L)	
	Capacity experiment (Figure 6.18)	Critical flux (Figure 6.19)
45	83	90
136	51	54.3
231	31	37.3
326	23	26.2

Table 6.5 Comparison of final concentrations achievable derived from capacity and critical flux experimental data.

Both sets of final concentration data at different permeate fluxes showed good agreement within experimental errors, particularly the errors associated with extrapolation of concentration (Equation 6.5) and more importantly, using critical fluxes for cell concentrations >35 g/L that lies outside the data set (Figure 6.19). This proves the relationship between observed final concentration with regards to capacity and the critical flux, with the TMP increasing rapidly once the operating flux exceeds the critical flux for the concentration at that given point in time during the concentration. Thus, critical fluxes can be used to evaluate the final achievable concentration at any given permeate flux for MF operations. A lower operating flux allows a greater final concentration to be achieved at the expense of greater processing time.

However, in practice, operating fluxes are typically optimised based on critical fluxes at the initial feed concentration and capacity experiments operated at fluxes <50-75% of the critical flux. For instance, carrying out flux excursions for *Chlorella sorokiniana* at the desired final concentration would require a preliminary volumetric reduction experiment to concentrate the feed to the final concentration. Assuming the use of a 0.1 m^2 Pellicon 2 or 3 mini cassette for lab-scale optimisation and a desired VCF of 40, an initial feed volume of ≥4 L would be required (minimum working volume of 100 mL for a 0.1 m^2 cassette), a significant volume of feedstock that may not be readily available nor cheap to source at the early stages of process development. The use of the USD membrane device, requiring only millilitre quantities of feed material, allows such optimisation to be rapidly carried out in a cost-effective manner by generating key process-related data such as critical fluxes, which can be used to further optimise the TFF process to maximise throughputs whilst keeping membrane fouling to a minimum.

Once the critical fluxes and capacities for sub-critical operation fluxes have been determined, the permeate flux/throughput for the MF process can then be optimised such that membrane area requirements are kept to a minimum while achieving relatively high throughputs with little/no membrane fouling. Membrane area required for a given feed volume can be calculated in two ways, based either on capacity limits or on flux-time considerations:

- Capacity based:

$$A_{capacity}, A_1 \left[m^2 \right] = \frac{V [L]}{V_{capacity} \left[L \Big/ m^2 \right]}$$

Equation 6.6

- Flux-time based:

$$A_{flux\text{-}time}, A_2 \left[m^2 \right] = \frac{V [L]}{J [LMH] \cdot t [hr]}$$

Equation 6.7

where V is the volume of feedstock to be processed, J is the permeate flux and t is the desired processing time.

In terms of an example processing scenario for *Chlorella sorokiniana*, the optimum flux can be determined using the USD capacity data generated in the previous section along with Equation 6.6 and Equation 6.7, assuming the following processing criteria and information:

- Batch volume post-fermentation, V: 1000 L

- Maximum processing time, t: 3 hours

- Membrane: Durapore 0.45 µm PVDF

- VCF=50 (0.5 g/L to 25 g/L)

Using the processing information above and Equation 6.6 and Equation 6.7 to determine capacity and flux-time based areas, the optimum operating point can be determined by plotting the two areas against permeate flux, shown in Figure 6.20.
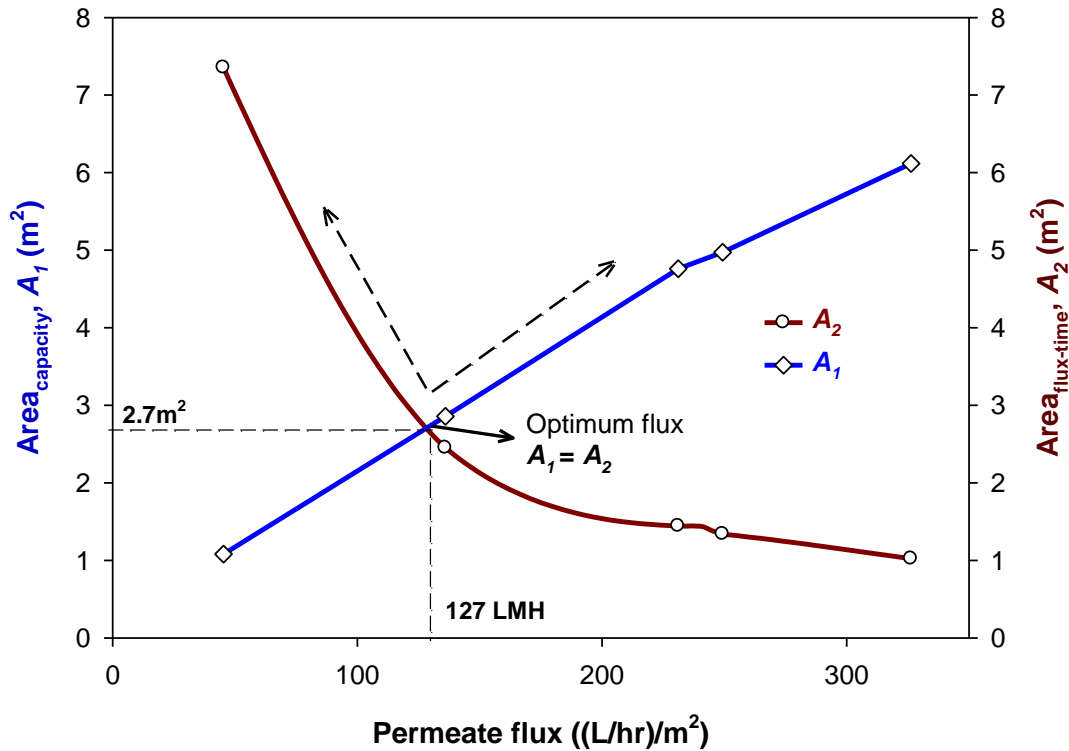
Figure 6.20 Capacity and flux-time based areas versus permeate flux plots used to determine optimum operating flux and membrane area requirements for concentrating *Chlorella sorokiniana* cells grown mixotrophically in 3N-BBM+V media. The short-dashed arrows (V shaped) show the region of the graph where both area requirements are satisfied.

The capacity-based area (A_1) was seen to increase with permeate flux (since $V_{capacity}$ decreases with increasing flux), while flux-time area (A_2) decreased with increasing fluxes. The area above the red and blue lines represent the area where the MF process satisfies the process constraints, both in terms of capacity limits as well as flux-time requirements. The optimum process sizing (membrane area) is the point where areas calculated using Equation 6.6 and Equation 6.7, *i.e.*, the point of intersection between the two plots where $A_1=A_2$. The optimum operating conditions to process 1000 L of microalgal feed in under 3 hours was determined to be a permeate flux of 127 LMH and a total membrane area of ~2.7 m^2. It is important to use both area calculations (A_1 and A_2) to determine optimal membrane area requirements, rather than solely using the flux-time method (A_2) and projecting throughputs/volumetric loadings to higher values to estimate areas for process sizing, as is typically done in industry for UF processes. However, this extrapolation method can lead to significant over- or under- estimation of minimum membrane area

requirements for TFF microfiltration involving particulate-heavy feedstock, where the solids are very likely to rapidly foul the membrane (compared to dissolved solutes such as proteins) and thus greatly impact critical fluxes and observed volumetric throughput limits.

6.2.2.3.2 Establishing dynamic permeate flux cascade methodology for high throughput optimisation

The optimised conditions for a 1000 L batch and maximum processing time of 3 hours (from the previous section) was determined to be a constant permeate flux of 127 LMH and a total membrane area of ~2.7 m^2. However, generating data for such optimisation experiments may be hindered by the limited volumes of feedstock available at the early stages of process development, apart from the relatively large membrane area requirements because of the modest operating permeate fluxes used, resulting in a cost-ineffective dewatering process. A greater crossflow rate could be used to enhance the operating fluxes (provided it is lower than or equal to the optimum feed flow rate); however, that would add to the operating costs due to the increased energy requirements of the recirculating pump at higher flow rates.

An alternative approach to maximise throughputs whilst keeping membrane fouling to a minimum would be to incorporate the empirical USD-derived critical flux relationship with cell concentration into the MF process control and operational strategy. The critical flux correlation can be used independently (while maintaining constant membrane loading) optimise a microfiltration process since it was found to provide similar information with regards to maximum achievable concentration and volumetric throughputs to data obtained from volumetric reduction experiments.

The premise of this novel USD-based approach is to actively regulate the permeate flux in a step-down cascade such that the operating flux is always lower than the critical flux at any given concentration and time by using the empirically derived critical flux function to gradually drop permeate fluxes in response to increasing cell concentration. This dynamic permeate flux control requires the use of an automated crossflow system equipped with a programmable PID control. The UNICORN control software was used as the interface to carry out the dynamic permeate flux experiments using the USD membrane device and lab-scale counterpart for concentrating *Chlorella sorokiniana*, since the Sartoflow Advanced lacked the programming capabilities for regulating permeate flux via the external peristaltic

permeate pump. The control strategy is not too dissimilar to the constant C_m/C_{wall} process control for optimising UF processes, where the retentate backpressure is continuously adjusted to maintain a constant permeate flux throughout the operation via an algorithm/control software to calculate the instantaneous protein concentration and mass transfer coefficient as a function of process time (Millipore, 2003). This minimises the membrane area requirements and maximised process yields, but it requires the use of an automated control system like the AKTA Crossflow system.

The dynamic flux control can be carried out in two ways; either as a pseudo-continuous flux decay profile mirroring the critical flux versus cell concentration profile, or as larger, discrete steps ranging from a maximum flux at the start of the concentration to zero at the end. For an initial feed concentration of 0.5 g/L and a desired final concentration of 25 g/L (to ensure operation within the experimental data set, *i.e.*, 0.5-30 g/L), Figure 6.21 illustrates the flux step-down cascade strategy along with the critical flux versus cell concentration data.
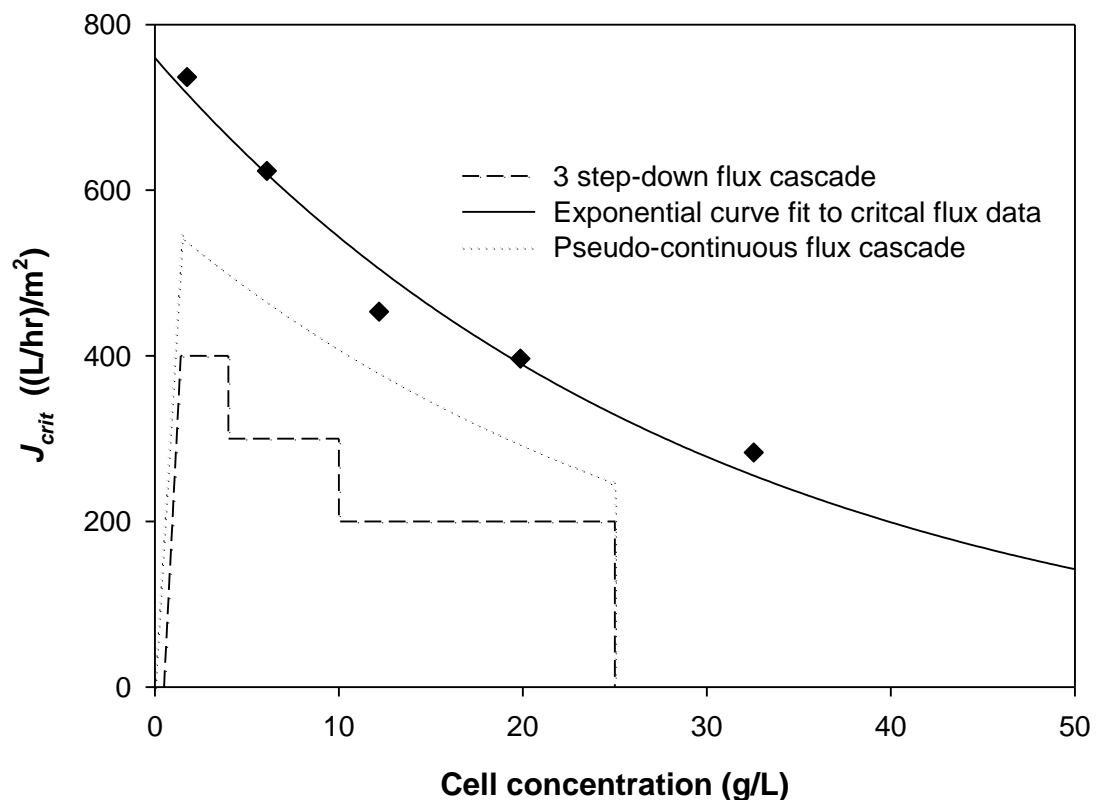
Figure 6.21 Experimental critical flux versus *Chlorella sorokiniana* cell concentration profile (mixotrophic 3N-BBM+V) and dynamic permeate flux control strategies for a

VCF=50; short dashed line represents a 3-step cascade (75% of J_{crit}) and the dotted line a pseudo-continuous step-down strategy.

Both operational strategies control the permeate fluxes to values that are always less than the critical flux curve, at any given concentration. The pseudo-continuous flux decay can be set by using a programmable tangential flow filtration control system using algorithms to calculate and derive operating fluxes as a function of time and cell concentration during the experiment, such that the flux constantly decreases in very small steps. However, this was not possible to achieve using the standard AKTA Crossflow and therefore the second option was chosen, where the permeate flux will be decreased sequentially from an initial maximum to zero over three large steps. In all cases, it was important to slowly ramp up the permeate pump over a time interval to achieve the desired initial flux to prevent a rapid influx of particles towards the membrane which could cause rapid membrane fouling at the start of the process and cause a steep rise in TMP. The primary purpose of the dynamic flux control method is to avoid/minimise membrane fouling during MF operations, which would be indicated by a relatively steady TMP profile during the overall concentration run; a rapidly rising TMP for permeate flux-controlled tangential flow filtration marks the onset of irreversible membrane fouling.

For the dynamic flux control (3-step cascade), a disc rotational speed of 4000 RPM was used for the USD membrane device, corresponding to an average wall shear rate of ~ 30000 s^{-1} for a water-like viscosity (0.0009 Pa.s) of the initial feed concentration of 0.5 g/L (calculated using Equation 3.9). In order to generate the relatively large wall shear rates of 30000 s^{-1} in the lab-scale device, a 125 cm^{2} PVDF Millipore 0.45 µm hollow fibre (now discontinued) was used to carry out the comparative large scale experiment. A screened cassette such as the Pellicon XL or P3 micro was not applicable for concentration of viscous, particulate-heavy feed, primarily due to the large feed flow rate required to generate the large USD-equivalent wall shear rates, which come at the expense of high pressure drops. Thus it was likely to cause severe membrane fouling at the start of the operation and exceed the maximum pressure rating of the module very quickly, especially as the feed gets more concentrated. Hollow fibres, on the other hand, are more suited to processing particulate-rich feed, allowing greater crossflow velocities to be used at a much smaller channel pressure drop (<2 bar) due to the more open structure of the fibres compared to narrow, spacer-filled feed channels. The only downside to using hollow

fibres is the use of much higher feed flow rates required compared to screened cassettes to generate the same average wall shear rates.

CFD modelling was used to model a part of the hollow fibre domain (similar to the concept of unit cells in section 3.1.2.2.2) to determine average wall shear rates as a function of feed flow rate. The EFD hollow fibre module used consists of 6 parallel fibres, 1 mm internal diameter (i.d.) and ~200 cm length. The CFD computational domain and simulation results in the form of a velocity magnitude plot and the average wall shear rate correlation are shown in Figure 6.22 and Figure 6.23 respectively.
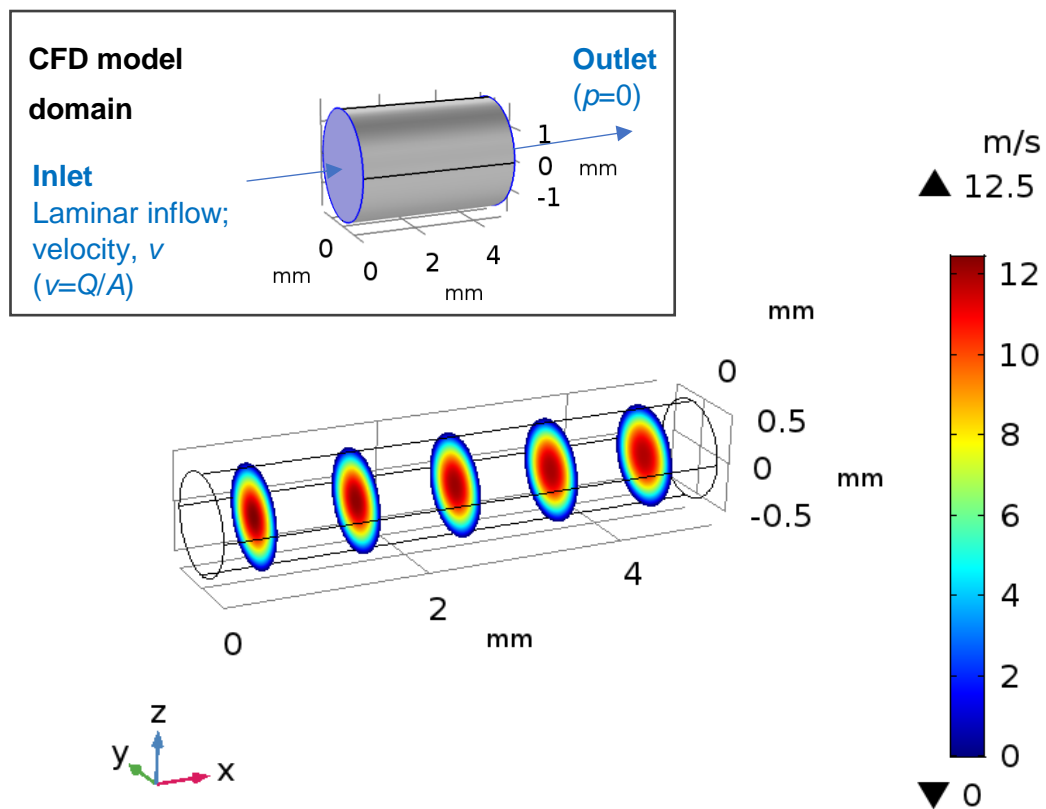
Figure 6.22 The 3D computational domain (test section of length 5 mm and 1 mm fibre diameter) and the simulation results presented as a velocity magnitude slice plot, for a fluid viscosity of 0.001 Pa.s and 36 LMM feed flow rate.
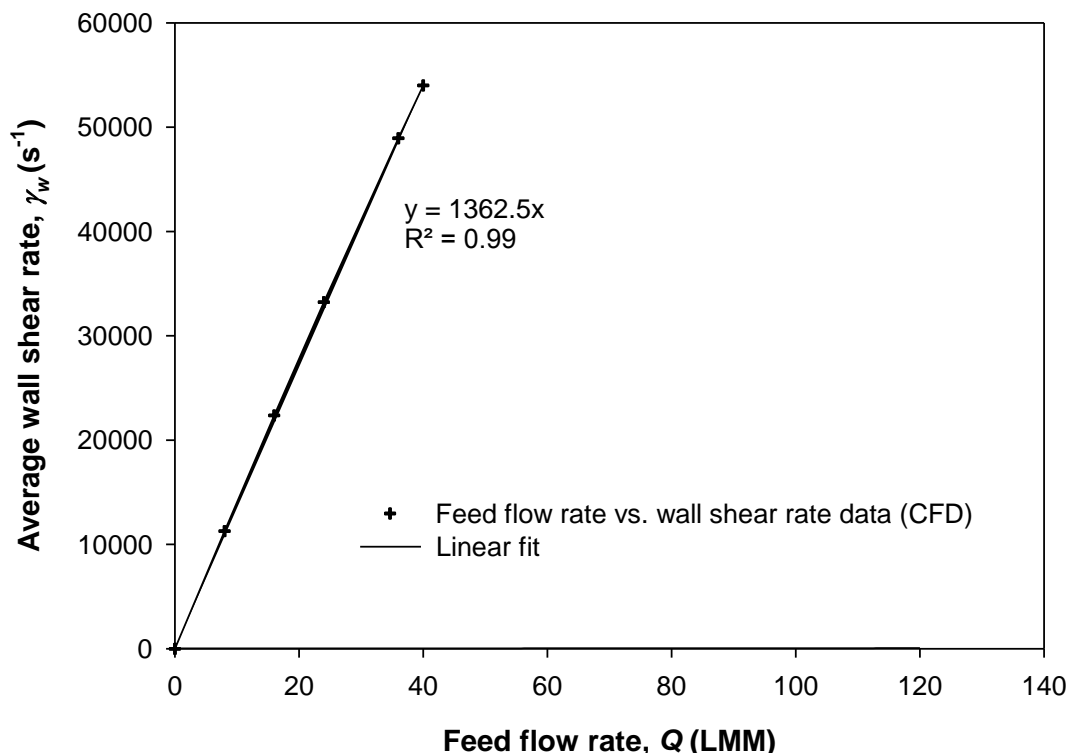
Figure 6.23 CFD simulation results of wall shear rate as a function of feed flow rate for the 125 cm^2 Millipore-HF model, assuming a water-like viscosity (0.0009-0.001 Pa.s).

The average wall shear rate equation from Figure 6.23 was used to determine the operating flow rate for the hollow fibre required to generate the equivalent USD shear rate of 30000 s^{-1}. The feed flow rate required for the hollow fibre module was calculated to be 22.5 LMM, corresponding to a flow rate of 281 mL/min for the 125 cm^2 HF. As discussed earlier, the HF typically requires and operates at a much larger flow rates than TFF cassettes to generate similar average wall shear rates which can challenge the capacity of the feed pump used. However, this was not an issue with the AKTA Crossflow as it is capable of generating feed flowrates up to 600 mL/min. Apart from operating at equivalent average wall shear rates across scales, it was also essential to scale membrane loading in g/L/m^2, *i.e.*, the retentate volume:membrane area ratio for the fed-batch concentration process (where retentate volume in the USD device and in the feed tank for the AKTA Crossflow is constant). Table 6.6 summarises all the scale-up parameters for the dynamic flux control operational methodology using the USD membrane device and the hollow fibre module.

	USD membrane device (13.2 cm^2)	Millipore hollow fibre (125 cm^2)
Membrane area (cm^2)	13.2	125
Final retentate volume (mL)	5.3	50.1
V/A (L/m^2)	204.1	
Average wall shear rate (s^{-1})	30000	
Operating conditions	4000 RPM	22.5 LMM
Target VCF	50 (0.5 g/L → 25 g/L)	
Estimated processing time (min)	51	

Table 6.6 Summary of key operational parameters for the USD membrane device and HF module used to carry out the dynamic flux control experiments.

The method editor in the UNICORN control software was used to control the permeate flux profiles as a function of time and programmed to sequentially lower the permeate flux (in discrete steps) at predefined time intervals (Table 6.7). A feed pressure alarm of 3 bar was also set for the HF module to avoid reaching excessive feed pressures as the feed concentrates.

t (min)	J (LMH)	t (min)	J (LMH)	t (min)	J (LMH)
0	0.0	1	181.3	2	362.6
0.1	18.1	1.1	199.5	2.1	380.8
0.2	36.3	1.2	217.6	2.2	398.9
0.3	54.4	1.3	235.7	2.20	400.0
0.4	72.5	1.4	253.8	5.31	400.0
0.5	90.7	1.5	272.0	5.31	300.0
0.6	108.8	1.6	290.1	14.92	300.0
0.7	126.9	1.7	308.2	14.92	200.0
0.8	145.1	1.8	326.4	50.97	200.0
0.9	163.2	1.9	344.5	50.97	0

Table 6.7 Flux versus time input steps used in the method editor of the UNICORN software to carry out the 3-step flux cascade operational strategy. The initial ramping of the permeate pump to the desired initial flux of 400 LMH over a time interval of 2 minutes is also shown.

The experimental TMP versus processing time for the fed-batch concentration experiments is shown in Figure 6.24.
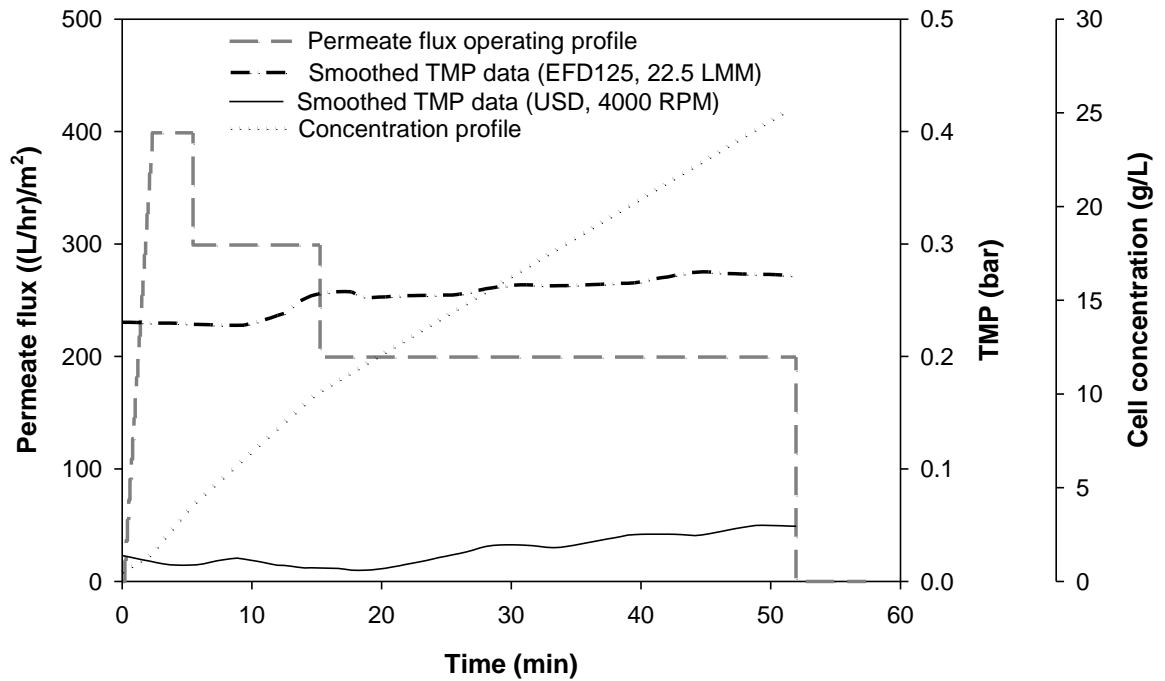
Figure 6.24 Experimental flux and TMP versus processing time data for the 3-step flux cascade control using the USD membrane device and HF module for the concentration of *Chlorella sorokiniana* (mixotrophic 3N-BBM+V cells) at 25±1 °C.

A relatively constant TMP profile was observed for both USD and HF modules, suggesting no significant membrane fouling occurred in both cases, since a rapid increase in TMP (for a flux-controlled process) indicates uncontrollable polarised layer/cake formation at the membrane surface. The TMP profiles thus successfully verified the dynamic flux control methodology to achieve higher throughputs without the expense of membrane fouling. The TMP did not rise significantly with increasing feed viscosity as the retentate concentrates, since the decrease in permeate flux over the 3 steps would even out the increase in feed pressures with increasing feed viscosity. Considering the previous case study to process 1000 L of algal feed in less than 3 hours, the required membrane area for the dynamic flux control operation was compared to the results from flux-capacity optimisation approach, and summarised in Table 6.8.

	Flux-capacity optimised	Dynamic flux control
Total processing volume (L)	1000	
Maximum allowed processing time (hr)	3	
Average permeate flux (LMH)	127	235
Optimum membrane area (m^2)	2.7	1.4

Table 6.8 Comparison of the calculated membrane area requirements for traditional flux-capacity based optimisation approach versus novel USD flux cascade dynamic control method.

The dynamic flux control methodology was seen to generate relatively higher average permeate fluxes during the concentration process, and as a result, the membrane area requirements for the flux cascade operation was significantly lower than the area requirements for a standard flux/capacity-based optimisation approach. The higher average flux allows either a smaller membrane area to be used for a target processing time <3 hrs, or the use of a larger membrane area but with a much smaller processing time. The applicability of the USD membrane device in mimicking tangential flow filtration processes at scale, and subsequently using it to optimise TFF-MF processes, allows the rapid acceleration of process development stages using millilitre quantities of feed. This approach is highly beneficial for dewatering dilute microalgal suspensions using tangential flow filtration, where high processing costs for harvesting as result of low operating fluxes/larger membrane areas, coupled with membrane fouling issues, is a significant bottleneck (Sharma et al., 2013). The dynamic flux control methodology allows the use of a much greater average permeate flux which greatly reduces the membrane area requirements/processing time needed, as well as minimising membrane fouling and thus cleaning requirements, thereby greatly reducing the processing costs associated with tangential flow filtration and making microalgal-derived biofuels more economical to produce compared to the traditional petroleum-derived fuel.

6.2.3 Conclusions

The dewatering efficiency for the harvest of *Chlorella sorokiniana* cultures, like most microalgal suspensions, using TFF microfiltration is generally very low due to the rapid membrane fouling associated with processing large volumes of dilute feed. This chapter demonstrated an USD-based approach to both improve filtration throughputs and minimise membrane fouling by a) investigating the impact of different culture conditions upstream on the effective filterability and fouling characteristics using a 0.45 µm PVDF membrane in the USD device, and b) using USD-derived process information to aid the design and development of an improved high throughput operational strategy for algal biomass concentration using tangential flow filtration.

The experimental critical fluxes and % drop in NWP was seen to vary across the different feedstock; a positive correlation (R^2 value of 0.64) was established between the finer population of particles present in the feed, D_{10}, and the observed critical fluxes, and was seen to increase in the order of autotrophic>heterotrophy>mixotrophy. The degree of irreversible fouling, indicated by the % loss in permeability, was also seen to have a similar positive correlation with the combined fouling factor of the soluble species such as protein, carbohydrates and TEP. At a given crossflow rate, there is a critical particle size below which, smaller particles are not influenced by the shear-induced migration and/or inertial lift effects associated with the crossflow, and thus the smaller particles are more likely to deposit on the membrane and effectively define the overall permeability of the polarisation/cake layer. Similarly, the soluble components were speculated to cause significant internal fouling of the membrane via pore plugging and pore blocking, indicated by the near complete retention of foulants by the membrane using a mass balance derived approach. The fouling mechanism was further validated by the isolated experiments conducted for the TAP minimal feed, where flux excursions for the liquor and resuspended solids compared to the mixed liquor proved the dominant fouling stream to be the liquor, which contained the various soluble foulant species, rather than algal biomass. This opens further avenues for investigation where upstream conditions could be optimised to lower the secretion of potential fouling agents for membrane filtration whilst still maintaining high biomass concentrations and lipid yields.

Similar to the experiments using *Saccharomyces cerevisae* in the previous chapter, volumetric throughput experiments were carried out for the microalgal suspensions,

but at different permeate fluxes. The volumetric capacity and final achievable cell concentration, for a given crossflow rate and initial solids concentration, was observed to decrease with increasing permeate flux, suggesting a trade-off between processing time and achievable volumetric throughput. The next objective of the chapter was to develop a high throughput dewatering strategy for *Chlorella sorokiniana* by deriving a correlation to express critical fluxes as a function of cell concentration using the USD membrane device. The critical flux was found to be inversely proportional to cell concentration at a given crossflow and followed an exponential decay profile. The premise of the novel flux cascade/dynamic flux control methodology was to use the empirical critical flux correlation to design an operating flux strategy, where the permeate flux is always below the critical flux value at any given time (corresponding to a certain cell concentration) during the concentration run. 50-fold volumetric reduction experiments were performed to demonstrate and validate a 3-step flux cascade method, using the USD membrane device (4000 RPM) and hollow fibre module (23.5 LMM) that was operated based on equivalent averaged wall shear rates. A relatively constant TMP profile across both scales was observed, which indicated no significant membrane fouling. For a process scenario where 1000 L algal feed volume is to be processed in under 3 hours, the dynamic flux method reported an average permeate flux of 235 LMH compared to the flux-time/capacity optimised flux of 127 LMH, and a 50% reduction in membrane area requirements. The experimental results highlight the importance of generating small scale process data to have a greater understanding of process-related variables, such as critical flux or TMP profiles as function of cell concentration, which allows a better and more optimised process control to be designed for specific applications. The optimisation approach reported here not only highlights the potential applications of the USD device to optimise microalgal dewatering process that would allow microalgal-derived biofuels to remain competitive with fossil-derived fuel, based on production costs, but also outlines an established strategy that can be applied to any concentration process using TFF microfiltration, provided it is operated within limits and considerations.

7 Conclusions

The use of scale-down models in the biopharmaceutical industry have been on the rise, particularly for downstream purification processes, due to the advent of Quality by Design as part of the FDA's initiative, as well as the increasing pressures of higher upstream titres on the purification processes downstream. Although scale-down tools and techniques are now widely used across many different unit operations, there is still a significant gap when it comes to existing tangential flow filtration scale-down tools and models that can be easily employed to obtain a predictable scale-up performance. Ultra scale-down (USD) technologies allow small scale experiments to be carried out using simple laboratory equipment and relatively small volumes of feedstock, thus enabling high throughput optimisation and accelerated process development. However, most scale-down devices, much like the USD membrane device, have geometries that are dissimilar to the large scale counterparts, which introduces additional complexities and challenges to achieving a predictable and truly scalable performance. The lack of robust scaling methods, both linear and non-linear, have limited the use of USD devices to preliminary experiments such as initial screening and membrane selection, rather than being used for high throughput experimentation, process development and optimisation applications.

Therefore, the central aim of this thesis was to develop a scale-up methodology and USD model that can accurately predict tangential flow filtration performance at scale, irrespective of the system, geometry or mode of operation used, with the aid of a USD membrane device and computational fluid dynamics (CFD) modelling approach. The established form of linear scaling based on equivalent normalised feed flow rates/TMP can often generate significant differences upon scaling, if the system and cassette-specific hydraulic resistances, which are inherently a part of the measured TMP, are not properly accounted for. In this study, the average wall shear rate, proportional to the mass transfer, was used as the scaling parameter, to normalise the flow across different geometries and scales. CFD was used to model the fluid flow in the USD membrane device and Pellicon TFF cassettes to determine the wall shear rate profiles and subsequently establish respective average wall shear rate correlations as a function of the hydrodynamic conditions and fluid viscosity. The average wall shear rate correlations allow the operation conditions to be determined across scales for a particular wall shear rate, providing a direct correlation between disc rotational speed in the USD device and the operating feed flow rate for the Pellicon cassettes. In addition, channel pressure drop models, expressed as

functions of average channel height, feed flow rate and fluid viscosity, were developed as part of the TMP prediction model. The 2D-PIV studies successfully verified the CFD simulations by comparing CFD simulated data with experimental data. The significance of accurately quantifying the wall shear rates across both scales using CFD modelling underpins the overall development and success of the USD methodology and prediction model.

Section 4.2 investigated the various non-TFF related factors, such as the system and cassette hydraulic resistances that cannot be isolated, were adequately characterised and accounted for in the scale-up methodology. Non-zero TMPs with no permeate flow was observed across many cassettes (Figure 4.5), and was attributed to varying permeate channel heights across the flow path leading to uneven pressure normalisation across the feed and permeate channels, illustrated and characterised by CFD simulations (Figure 4.6). Thus, the concept of applied pressure drops (Equation 4.8) was introduced to accurately characterise the cassette-specific resistances as a power-law model, which allows prediction of the flow-initialised TMP as a function of operating feed flow rate, permeate flux and fluid viscosity (Equation 4.9). The impact of variable feed channel heights on resulting channel pressure drops was investigated, following which, an empirical CFD-based model was developed to allow the effective feed channel height for any given Pellicon screened cassette to be accurately determined. Combining the flow-initialised TMP (TMP'), the system resistance (Equation 4.3), pressure drop correlations for feed (Equation 3.19) and permeate channels (Equation 4.5) and the empirical USD model parameters, a mathematical model (Equation 4.10) was developed that allows prediction of performance at scale. The characterisation of the observed non-zero TMP at no net permeate flux and its impact on the cassette hydraulic resistance have not been considered in most scale-up models to date, and therefore including such non-TFF related resistances in the prediction model allows a much more accurate and predictable scale-up performance to be achieved. Apart from that, the scale-up methodology as well as the key rules for scaling such as maintaining constant solids loading on the membrane and cassette feed pressures limits were developed and outlined in sections 4.3.3.1 and 4.3.3.3.

After the scale-up methodology and prediction model was developed, 100-fold non-linear scale-ups from the USD device to Pellicon cassettes were carried out and the model predicted data were compared with the experimental data generated using the Pellicon TFF cassettes. Flux excursions were carried out for different screens and

feedstock ranging from simple, uni-variate feed such as BSA and PVP-40 to more complex, multicomponent feed like *Pichia pastoris* and *Escherichia coli* homogenate. The experimental large scale flux versus TMP profiles were in very good agreement with the model predicted data with an average difference of less than 5% between data across scales, which was well within the current industrially accepted criteria of ±20% difference in average fluxes or TMP for true linear scalability using Pellicon cassettes. Furthermore, transmission results for the recovery of 47 kDa Fab' from *Escherichia coli* homogenate showed a relatively good match between scales, within ±20%; larger discrepancies were observed for the transmission data as operating feed pressures >3 bar, leading to excessive polarisation on the membrane and consequently lower values for the large scale data. Finally, the USD model was modified such that the USD parameters (α, β) were expressed as a function of the disc rotational speed in the USD device, allowing the prediction of any feed flow rate at large scale; *Pichia pastoris* was used to demonstrate an accurate and predictable flux versus TMP performance between scales using this method. Overall, the combination of the USD membrane device, scale-up methodology and prediction model was deemed to provide a successful simulation of the tangential flow filtration processes at scale by more than satisfying the acceptance criteria for scale-up, as well as being robust in terms of no deviations from the model observed across the different screened cassettes and feedstock investigated. Finally, one of the limitations of the prediction model using *Escherichia coli* homogenate at high feed pressures was investigated. The results indicated a potential trade-off between feed pressures and the thickness of the pressure-dependent polarisation layer, and high pressures can cause additional resistances if they exceed an optimum value.

After establishing the robustness and accuracy of the USD methodology and prediction model, some potential applications of the USD membrane device to optimise TFF microfiltration (TFF-MF) processes were studied. MF processes tend to be limited by both flux and capacity constraints and thus have additional complexities and challenges that need to be solved at early stages of process development. A 10-fold concentration of 25 g/L *Saccharomyces cerevisae* was performed using the USD membrane device and Pellicon 2 V screen cassette, using a 0.65 μm PVDF membrane. The developed TMP prediction model was altered to account for the differential viscosity and pressure drop model with increasing cell concentration and subsequently used to predict volumetric capacity limits (at 0.7 bar TMP). The predicted and experimental capacities were in good agreement, with volumetric throughput limits of 49.2 L/m^2 (265 g/L) and 52.0 L/m^2 (321 g/L), respectively. The

relatively small differences can be attributed to the concept of an optimum dP across the TFF cassette, where there exists a trade-off between higher dP (crossflow) and the particle deposition on the membrane as a result, which lowers permeate fluxes and achievable membrane capacity. Even though projecting capacity limits across scales is not entirely reliable nor accurate and usually requires empirical data, the USD model was able to predict the volumetric throughput limits and simulate TMP profiles at large scale TFF. However, due to the relatively simplistic nature of the feed (*Saccharomyces cerevisae* in PBS) used, although it cannot be assumed to independently validate the prediction model with regards to capacity, the extension of the prediction model to incorporate prediction of TMP versus throughput data to determine loading capacities further demonstrated the robustness and applicability of the developed methodology and prediction model.

The final chapter looked at optimising the dewatering of the more complex *Chlorella sorokiniana* microalgal feed using TFF-MF. Firstly, the impact of different media and growth conditions on filterability and membrane fouling was investigated using the USD membrane device and 0.45 μm PVDF membrane. For all the three media, autotrophic cells were observed to have smaller particle sizes on average, followed by heterotrophic and mixotrophic cell cultures, with mixotrophic cell cultures supplemented with glucose generating the greatest biomass at 5 g/L. Furthermore, the amount of soluble TEP in the media was dependent on the species of bacteria co-existing in the media, proved by the lack of soluble TEP measured for the axenic TAP minimal cultures. Other key results included the positive correlation observed between smaller particles sizes (D_{10}) present in the feed and empirical critical fluxes, and the degree of irreversible fouling linked to the concentration of soluble foulants such as EPS, carbohydrates and proteins present in the liquor stream. This was further supported by the isolated flux excursions carried out for the liquor and resuspended cells for TAP minimal media, which proved the liquor to be the more dominant fouling stream rather than the algal biomass. The results of the USD fouling studies suggested a potential optimisation approach that can be used, where upstream optimisation of growth media to lower the concentration of potential foulants secreted into the media could be used to effectively help improve the TFF performance downstream. The fouling studies highlighted the significant interaction and inter-dependability between cell culture conditions and its consequence on tangential flow filtration performance downstream, due to rapid internal membrane fouling caused by the soluble foulants present in the liquor.

The final objective was to develop a novel flux cascade strategy for the concentration of 3N-BBM+V mixotrophic cells by expressing the critical flux decay as a function of cell concentration and using the model to define the permeate flux cascade, where the operating permeate flux is always less than the critical flux at any given time and cell concentration. A 50-fold volumetric concentration was carried out using the USD device and a hollow fibre module (instead of screened cassettes due to pressure limitations) to demonstrate the dynamic flux control methodology using the UNICORN control software. A relatively constant TMP profile was seen during both concentration runs, indicating no irreversible membrane fouling during the concentration process. For a case study of processing 1000 L of feed in less than three hours, average permeate fluxes of 235 LMH were obtained for the dynamic flux control methodology compared to the flux-time/capacity based optimised permeate flux of 127 LMH. Both sets of results proved the effectiveness of the control strategy, as well as the potential of the USD membrane device to generate critical process information to aid design and development of an improved high throughput operational strategy for any given process. This is particularly useful for TFF-MF processes that are inherently susceptible to permeate flux decline and membrane fouling, which translates to larger membrane areas and higher associated processing costs due to lower achievable fluxes. The work in the final section was the first time that the relationships between key process parameters such as flux, TMP, feed flow rate, average wall shear rates and fluid viscosity were all fully characterised, and thus provides a novel method to better understand tangential flow filtration phenomenon via a combined experimental and CFD modelling approach.

8   Considerations for further work

The overall focus of this thesis was to develop a validated USD methodology that is both robust and accurate, and was done sequentially over the many chapters within this thesis. This section presents suggestions for future work that can further aid the development of USD-based applications for tangential flow filtration, as well as discussing potential limitations of the work carried out so far and the recommended research to improve on those.

8.1   Computational fluid dynamics modelling development

- CFD modelling could be used to establish similar models for hollow fibre modules, to be scale up from the USD membrane device or across different membrane formats, using the same approach discussed in this chapter to characterise wall shear rates. Although hollow fibres are relatively easier to model (cylindrical fibres without screens), they tend to be rather cumbersome to scale primarily because the fibre lengths change upon scaling, unlike TFF cassettes which are linearly scalable since the path length is kept constant while surface area is increased by adding channels in parallel upon scaling. CFD modelling can therefore be used to generate feed pressure drop models as functions of effective fibre length, in addition to the flow rate and fluid viscosity, and once the model is developed, validation using similar feedstock can be carried out to confirm scalability and model prediction.

- There have been previous attempts at using CFD to model gel layer, concentration polarisation and other fouling mechanisms, which could also be carried out for TFF cassettes to model the polarisation layer on the membrane that can then be used to predict permeate fluxes/TMP at a given feed flow rate. However, the concept of unit cells is unsuitable for such studies mainly because the quantities such as feed flow rate, concentration, flux and pressures all exhibit spatial variations along the length of the flow channel.

  As a result, finite element analysis (FEM) could be performed for the feed channel, wherein the entire flow length is divided into significantly smaller chunks based on periodicity and identical cross-sectional faces between the intersecting boundaries along the direction of flow. Periodic flow boundary conditions could then be applied to the model and solved for initial conditions, and the solutions for

one section could then be used as initial conditions for the subsequent sections and intersecting boundaries linked via general extrusion operators (solved variables at the outlet for one section used as initial solutions for the inlet of the next section) and solved in series to obtain a solution for the entire length. However, this is still a very computationally intensive task even though the computational domain solved for at any given time is significantly smaller compared to solving for the entire flow domain. The advantage of FEM approach is the simulation of the entire flow channel and quantification of the spatially distributed variables such as wall shear rate/mass transfer, TMP and flux, which can provide invaluable insight into understanding the local phenomenon occurring in TFF cassettes.

- The differences between apparent and actual NWP (Figure 4.1) due to tangential flow pressure drops in TFF cassettes can be bridged using CFD, where a method to determine the true NWP of the membrane within a TFF cassette can be established without invasive methods. In theory, the actual driving force would be the difference between measured dP across the cassette (at a given feed flow rate and permeate flux) and the tangential pressure drop component that is generated due to fluid flow past the feed screen, and not used to derive net flux through the membrane. Thus, Equation 8.1 can be used to estimate the true NWP for a given TFF cassette, once the average feed channel height is determined using crossflow tests at 1 bar dP. The feed channel pressure drop (at zero net flux) for a given flow rate and calculated channel height can then be calculated using Equation 3.19.

$$\text{Apparent NWP (LMH/bar)} = \frac{\text{Permeate flux (LMH)}}{\text{TMP (bar)}}$$

$$\text{Actual NWP (LMH/bar)} = \frac{\text{Permeate flux (LMH)}}{Experimental\ dP_{Q_F}(bar) - CFD\ dP_{\overline{Q_F}(J=0)}\ (bar)}$$

Equation 8.1

$$where\ \overline{Q_F} = Q_F - \frac{Q_P}{2}\ and\ P_P, P_R = 0$$

331

8.2 USD method development

- Prediction models can be developed for other TFF cassettes (from different manufactures/screen types), provided the internal geometries are known and can be modelled using CFD, by applying the same methodology and approach used in this thesis to build up the model

- The validation studies have been carried out over relatively short operation times (<1 hour); however, the potential impact of long-term operation on scale-up performance also needs to be studied and accounted for accordingly. The impact of channel-induced shear within screened TFF cassettes on shear-sensitive molecules can be investigated using CFD and/or experiments, and if significant, accounted for during scale-up. This is particularly an issue for large scale tangential flow filtration, where the feed pumps and valves in the system generate additional shear damage, besides the channel-induced shear. Furthermore, the residence time averaged shear can be characterised for processes with relatively long operational times, where the feed can undergo multiple passes through the pumps and valves over time, imparting time-based shear damage to macromolecules/fragile cells.

   Apart from that, the time-dependent relationship with viscosity for thixotropic feed material could be an issue since the average wall shear rates are influenced by both feed flow rate and the fluid viscosity, and so that is another key parameter that could be investigated and incorporated into the viscosity model.

- Proteins and other macromolecules are known to commonly adsorb onto solid surfaces, and TFF processes offer multiple surfaces for product to adsorb and desorb (Callahan et al., 2014). Consequently, there is a need to investigate two aspects because of this non-specific interaction. Firstly, although stainless steel, polypropylene and to an extent, acrylic, are biocompatible materials and show minimal protein adsorption, control experiments are needed to ensure the composition of the fluid to be filtered is not dissimilar across the USD device and Pellicon cassettes, due to differences in the relative surface areas of the non-membrane components. The control experiment can be done using a static soak of the different materials in known concentrations of BSA solution and measuring change in quantity of BSA on solution, under different conditions such as stirring speed, temperature, contact time and surface area.

332

Secondly, the impact of material of construction and surface roughness, and the different magnitude of shear stresses between the two devices, on product quality and aggregation needs to be studied and compared. Surface roughness has been shown to cause greater rates of monomer reduction and particle aggregation (Bee et al., 2010; Biddlecombe et al., 2007). Analytical techniques such as size exclusion chromatography (SEC)/SEC-HPLC, mass spectrometry and circular dichroism can be used to determine monomer purity and conformation of the proteins investigated.

- Even though replicates were not performed as the polarisation layer is generally the primary barrier to flow during TFF, the impact of using the smaller 47 mm diameter membrane discs need to be investigated. This is due to the larger inherent variability associated with the use of smaller membrane areas that could have a rather different pore size distribution that is not representative to that of a much larger membrane sheet, such as those found within the Pellicon 2 cassettes. Thus, the different discs from different membrane lots using the same feedstock and operating conditions need to be compared against each other, both in terms of flux performance and protein transmission, to ensure the membrane variability does not cause significant variations in performance and so that it can be confidently ruled out as a potential variable in the model.

- Four biological feedstock of varying complexities were used to validate the USD methodology and prediction model. Additional sets of data, in terms of other feedstock, would further strengthen the validation of the model and solidify its robustness. Feedstock such as monoclonal antibodies and shear-sensitive mammalian cells could further challenge the robustness of the model (particular in the case of mammalian cells due to potential shear-induced damage) and help validate it further.

- The prediction model failed at high cell concentrations and feed pressures, as observed in sections 5.2.2.3 and 6.1.2. This could have either been due to an inaccurate viscosity model used (the sisko model) for particulate rich feed with shear-thickening properties rather than shear-thinning, or inadequacies of the rheometer method/geometry used. Different geometries like parallel, cone and plate and cup and bob can be used to compare the viscosities obtained for cell suspensions of different concentrations. The viscosities from the different measurements can then be used to predict pressure drops and compared against

experimental data generated using the fabricated C screen cassette (used in PIV studies). The pressure drop versus flow rate experimental data can be used to validate the pressure drop models (in section 4.3.3.2.3), and establish maximum solids concentration for using the model or incorporate a solids concentration term in the viscosity model to account for concentration-related effects.

- Although UF/DF clarification of the Fab' from *Escherichia coli* homogenate proved to be scalable within associated errors, using a molecule with 100% transmission does not provide a complete validation for the transmission part of the USD model, since observed transmission across scales are not a true test of scalability for UF/DF if the tested molecules are completely transmissible. Thus, feedstock with molecules partially retained by the membrane can be used to further validate the transmission model, since the membrane polarisation layer directly controls the transmission of partially retained particles. Furthermore, the impact of variable NWP of the different membranes and cassettes on product transmission of particulate-free feedstock can be studied.

8.3 Applications of USD methodology and the USD membrane device

- Similar to the previous validation studies, it would be useful to validate both the volumetric capacity and dynamic flux control model further using different feedstock. For example, mammalian cells of varying concentrations can help establish the limits of operation for the model (such as maximum solids concentration, crossflow rate), beyond which the model predicted data starts to deviate significantly.

- The concentration and diafiltration of mAbs could be investigated and the prediction model used to predict final achievable concentrations depending on the flow rate and screen used. The yields and quality of mAbs between the USD membrane device and the Pellicon cassettes can be compared and the applicability of the prediction model at high concentrations and viscosities further investigated.

- From a capacity point of view, it would be interesting to investigate and determine the relationship between volumetric throughput limits and NWP. If a conclusive correlation can be established, a NWP correction factor would need to be

introduced into the prediction model to normalise performances across scales for different measured NWP.

- Another potential weak point in the methodology for capacity determination and using the modified USD model (unlike the established first -order exponential model) is the accuracy of the non-linear curve fit function used. The prediction accuracy for the model depends on the robustness of the curve fitting process, particularly if extrapolating outside the data set for the USD model. Thus, there is merit in carrying out experiments with additional feedstock using the USD membrane device to investigate if a common non-linear function could be derived to capture the TMP versus throughput profiles more accurately.

- Finally, the basis of choosing the concentration to determine the average wall shear rate to be used in order to calculate the feed flow rates equivalent to the disc RPM of the USD membrane device. This is particularly important since the decline of average wall shear rate with increasing cell concentration/viscosity is likely to differ between the USD device and TFF cassette chosen. The average shear rate versus viscosity profile for a given crossflow rate/RPM is dependent on the fluid flow regime within the flow geometries and thus there will be inherent differences, which are reflected in the exponent for the viscosity term in the wall shear rate equations. As a result, there could be significantly different averaged wall shear rates through the filtration run (despite choosing equivalent averaged wall shear rates based on the viscosity value at either initial or final concentration) and thus mass transfer rates between the two scales at any given point, which could skew the predicted results significantly. An example of the average shear rate profiles versus feed concentration (or feed viscosity) for both scales is shown in Figure 8.1.
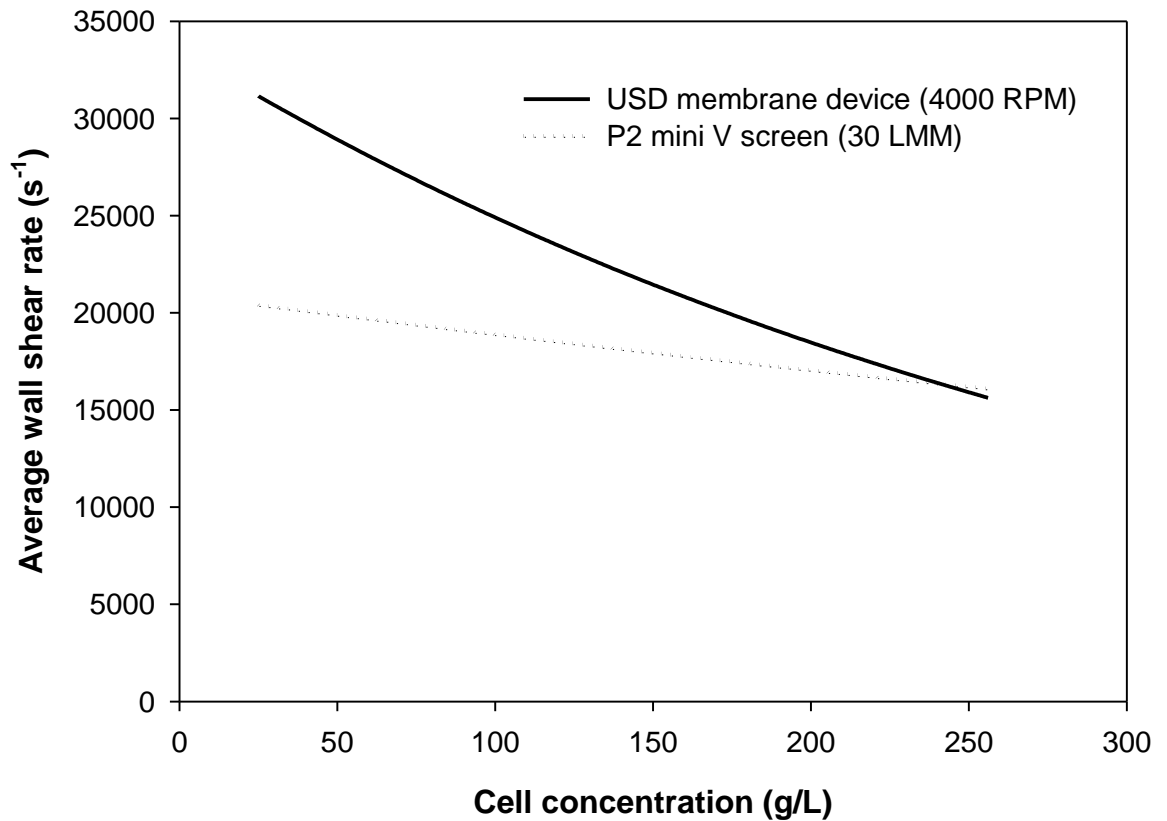
Figure 8.1 Average wall shear rate profile for the USD membrane device and Pellicon 2 mini cassette during the concentration of Saccharomyces cerevisae at 50 LMH, when the final desired concentration of 250 g/L is chosen as the viscosity reference for average wall shear rate determination.

Overall, the average wall shear rates in the USD membrane device at 4000 RPM was much higher than the shear rates in the Pellicon V screen cassette at 30 LMM feed flow rate for all concentrations, before they eventually converged at the final average wall shear rate of ~16000 s^{-1} at 250 g/L. A greater average wall shear rate implies greater mass transfer of particles away from the membrane surface thus minimising fouling and caking as the concentration proceeds. Therefore, the difference in volumetric capacities could be observed depending on whether the initial or final wall shear rate values are used for scaling.

9 References

Aas, E., 1996. Refractive index of phytoplankton derived from its metabolite composition. Journal of Plankton Research 18, 2223–2249.

Akoum, O.A., Jaffrin, M.Y., Ding, L., Paullier, P., Vanhoutte, C., 2002. An hydrodynamic investigation of microfiltration and ultrafiltration in a vibrating membrane module. Journal of Membrane Science 197, 37–52.

Al Hattab, M., Ghaly, A., Hammoud, A., 2015. Microalgae harvesting methods for industrial production of biodiesel: Critical review and comparative analysis. Journal of Fundamentals of Renewable Energy and Applications 5, 1–27.

Amini, E., Mehrnia, M.R., Mousavi, S.M., Mostoufi, N., 2013. Experimental study and computational fluid dynamics simulation of a full-scale membrane bioreactor for municipal wastewater treatment application. Industrial & Engineering Chemistry Research 52, 9930–9939.

Andersen, R.A., 2005. Algal Culturing Techniques. Elsevier.

Anderson, J., 1995. Computational Fluid Dynamics-the basics with applications. McGraw-Hill Education.

Arabi, S., Nakhla, G., 2008. Impact of protein/carbohydrate ratio in the feed wastewater on the membrane fouling in membrane bioreactors. Journal of Membrane Science 324, 142–150.

Arruda Fatibello, S.H.., Henriques Vieira, A.A., Fatibello-Filho, O., 2004. A rapid spectrophotometric method for the determination of transparent exopolymer particles (TEP) in freshwater. Talanta 62, 81–85.

Astudillo-Castro, C.L., 2015. Limiting flux and critical transmembrane pressure determination using an exponential model: The effect of concentration factor, temperature, and cross-flow velocity during casein micelle concentration by microfiltration. Industrial and Engineering Chemistry Research 54, 414–425.

Babel, S., Takizawa, S., 2010. Microfiltration membrane fouling and cake behavior

during algal filtration. Desalination 261, 46–51.

Babel, S., Takizawa, S., 2011. Chemical pretreatment for reduction of membrane fouling caused by algae. Desalination 274, 171–176.

Bacchin, P., Aimar, P., Field, R.W., 2006. Critical and sustainable fluxes:theory, experiments and applications. Journal of Membrane Science 281, 42–69.

Balaev, A.E., Dvoretski, K.N., Doubrovski, V.A., 2002. Refractive index of E*scherichia coli* cells. In: The International Society for Optics and Photonics. pp. 253–260.

Ball, P., 2000. Scale-up and scale-down of membrane-based separation processes. Membrane Technology 2000, 10–13.

Baruah, G.L., Venkiteshwaran, A., Belfort, G., 2005. Global model for optimizing crossflow microfiltration and ultrafiltration processes: a new predictive and design tool. Biotechnology progress 21, 1013–25.

Becht, N.O., Malik, D.J., Tarleton, E.S., 2008. Evaluation and comparison of protein ultrafiltration test results: Dead-end stirred cell compared with a cross-flow system. Separation and Purification Technology 62, 228–239.

Bee, J.S., Davis, M., Freund, E., Carpenter, J.F., Randolph, T.W., 2010. Aggregation of a monoclonal antibody induced by adsorption to stainless steel. Biotechnology and bioengineering 105, 121–9.

Belfort, G., Davis, R.H., Zydney, A.L., 1994. The behavior of suspensions and macromolecular solutions in crossflow microfiltration. Journal of Membrane Science 96, 1–58.

Belfort, G., Pimbley, J.M., Greiner, A., Chung, K.Y., 1993. Diagnosis of membrane fouling using a rotating annular filter. 1. Cell culture media. Journal of Membrane Science 77, 1–22.

Bergman, T.L., Incropera, F.P., 2011. Fundamentals of heat and mass transfer, 7th ed. Wiley.

Berman, T., Passow, U., 2007. Transparent Exopolymer Particles (TEP): an overlooked factor in the process of biofilm formation in aquatic environments. Nature Precedings.

Berrill, A., Ho, S.V., Bracewell, D.G., 2008. Ultra scale-down to define and improve the relationship between flocculation and disc-stack centrifugation. Biotechnology Progress 24, 426–431.

Biddlecombe, J.G., Craig, A.V., Zhang, H., Uddin, S., Mulot, S., Fish, B.C., Bracewell, D.G., 2007. Determining antibody stability: creation of solid-liquid interfacial effects within a high shear environment. Biotechnology Progress 23, 1218–1222.

Bilad, M.R., Arafat, H.A., Vankelecom, I.F.J., 2014. Membrane technology in microalgae cultivation and harvesting: A review. Biotechnology Advances 32, 1283–1300.

Bilad, M.R., Discart, V., Vandamme, D., Foubert, I., Muylaert, K., Vankelecom, I.F.J., 2013. Harvesting microalgal biomass using a magnetically induced membrane vibration (MMV) system: Filtration performance and energy consumption. Bioresource Technology 138, 329–338.

Bilad, M.R., Vandamme, D., Foubert, I., Muylaert, K., Vankelecom, I.F.J., 2012. Harvesting microalgal biomass using submerged microfiltration membranes. Bioresource Technology 111, 343–352.

Bird, R.B., Stewart, W.E., Lightfoot, E.N., 1961. Transport phenomena. AIChE Journal 7, 5J–6J.

Bischoff, H., 1963. Some soil algae from Enchanted Rock and related algal species. University of Texas, Austin Tex.

Blake, E., Johnson, J., Shankar, N., 2011. The Optifilt approach to biopharmaceutical filter testing: scale-up to tangential flow filtration with fouling. Senior Design Reports (CBE) 21, 129.

Bouchard, C.R., Carreau, P.J., Matsuura, T., Sourirajan, S., 1994. Modeling of ultrafiltration: Predictions of concentration polarization effects. Journal of Membrane

Science 97, 215–229.

Bouzerar, R., Ding, L., Jaffrin, M.Y., 2000a. Local permeate flux-shear-pressure relationships in a rotating disk microfiltration module: Implications for global performance. Journal of Membrane Science 170, 127–141.

Bouzerar, R., Jaffrin, M.Y., Ding, L., Paullier, P., 2000b. Influence of geometry and angular velocity on performance of a rotating disk filter. AIChE Journal 46, 257–265.

Brennan, L., Owende, P., 2010. Biofuels from microalgae-A review of technologies for production, processing, and extractions of biofuels and co-products. Renewable and Sustainable Energy Reviews 14, 557–577.

Brown, A.I., Titchener-Hooker, N.J., Lye, G.J., 2011. Scale-down prediction of industrial scale pleated membrane cartridge performance. Biotechnology and Bioengineering 108, 830–838.

Callahan, D.J., Stanley, B., Li, Y., 2014. Control of protein particle formation during ultrafiltration/diafiltration through interfacial protection. Journal of pharmaceutical sciences 103, 862–9.

Campbell, C.N., 2005. Elimination of bacteria from microalgal culture using antibiotics. Culture Collection of Algae and Protozoa 3–4.

Castilho, L.R., Anspach, F.B., 2003. CFD-aided design of a dynamic filter for mammalian cell separation. Biotechnology and bioengineering 83, 514–24.

Castilho, L.R., Moraes, A., Augusto, E., Butler, M., 2008. Animal cell technology: From biopharmaceuticals to gene therapy, 1st ed. Taylor & Francis.

Çengel, Y., Cimbala, J., 2014. Fluid Mechanics: fundamentals and applications, 3rd ed. McGraw-Hill.

Challener, C.A., 2016. Going small to achieve success on the commercial scale. BioPharm International 29, 26–28.

Chan, G., Booth, A.J., Mannweiler, K., Hoare, M., 2006. Ultra scale-down studies of

the effect of flow and impact conditions during E. coli cell processing. Biotechnology and Bioengineering 95, 671–683.

Chandler, M., Zydney, A., 2004. High throughput screening for membrane process development. Journal of Membrane Science 237, 181–188.

Chandler, M., Zydney, A., 2006. Effects of membrane pore geometry on fouling behavior during yeast cell microfiltration. Journal of Membrane Science 285, 334–342.

Chandrasekaran, N., Dimartino, S., Fee, C.J., 2013. Study of the adsorption of proteins on stainless steel surfaces using QCM-D. Chemical Engineering Research and Design 91, 1674–1683.

Chapman, P., Krishnan, M., 2011. Shifting the bioprocess paradigm. BioProcess International 9, 10–13.

Charcosset, C., 2012. Membrane Processes in Biotechnology and Pharmaceutics. In: Membrane Processes in Biotechnologies and Pharmaceutics. pp. 101–141.

Charm, S.E., Wong, B.L., 1981. Shear effects on enzymes. Enzyme and Microbial Technology 3, 111–118.

Chellam, S., Wiesner, M.R., 1997. Particle back-transport and permeate flux behavior in crossflow membrane filters. Environmental Science & Technology 31, 819–824.

Chen, C.-Y., Yeh, K.-L., Aisyah, R., Lee, D.-J., Chang, J.-S., 2011. Cultivation, photobioreactor design and harvesting of microalgae for biodiesel production: A critical review. Bioresource Technology 102, 71–81.

Chen, V., Li, H., Fane, A.G., 2004. Non-invasive observation of synthetic membrane processes - A review of methods. Journal of Membrane Science 241, 23–44.

Chen, W., Zhang, C., Song, L., Sommerfeld, M., Hu, Q., 2009. A high throughput Nile red method for quantitative measurement of neutral lipids in microalgae. Journal of microbiological methods 77, 41–7.

Cheryan, M., 1998. Ultrafiltration and Microfiltration Handbook. CRC Press.

Chilton, T.H., Colburn, A.P., 1934. Mass Transfer (Absorption) Coefficients Prediction from Data on Heat Transfer and Fluid Friction. Industrial & Engineering Chemistry 26, 1183–1187.

Chini Zittelli, G., Rodolfi, L., Biondi, N., Tredici, M.R., 2006. Productivity and photosynthetic efficiency of outdoor cultures of *Tetraselmis suecica* in annular columns. Aquaculture 261, 932–943.

Chisti, Y., 2008. Biodiesel from microalgae beats bioethanol. Trends in Biotechnology 26, 126–131.

Crittenden, J.C., Trussell, R.R., Hand, D.W., Howe, K.J., Tchobanoglous, G., 2012. Principles and Design, Third. ed, MWH's Water Treatment. John Wiley & Sons, Inc., Hoboken, NJ, USA.

Cyganowski, J., 2005. Tangential Flow Filtration: Methods For Successful Scale up. International Workshop on "Vaccine Quality Management" July 10 - 11th 2013 1–15.

Da Costa, A.R., Fane, A.G., Wiley, D.E., 1994. Spacer characterization and pressure drop modelling in spacer-filled channels for ultrafiltration. Journal of Membrane Science 87, 79–98.

Daily, J.W., Nece, R.E., 1960. Chamber Dimension Effects on Induced Flow and Frictional Resistance of Enclosed Rotating Disks. Journal of Basic Engineering 82, 217.

Darvishmanesh, S., Vanneste, J., Degrève, J., Bruggen, B. Van Der, 2010. Computational fluid dynamic simulation of the membrane filtration module. 20 European symposium on Computer Aided Process Engineering 1–6.

Davidson, K.M., Sushil, S., Eggleton, C.D., Marten, M.R., 2003. Using computational fluid dynamics software to estimate circulation time distributions in bioreactors. Biotechnology progress 19, 1480–6.

Deen, W.M., 2011. Analysis of transport phenomena, 2nd ed. Oxford University

Press, USA.

Delahaye, M., Lawrence, K., Ward, S.J., Hoare, M., 2015. An ultra scale-down analysis of the recovery by dead-end centrifugation of human cells for therapy. Biotechnology and bioengineering 112, 997–1011.

DiMasi, J.A., Grabowski, H.G., Hansen, R.W., 2016. Innovation in the pharmaceutical industry: New estimates of R&D costs. Journal of Health Economics 47, 20–33.

Ding, L., Jaffrin, M.Y., Luo, J., 2015. Dynamic filtration with rotating disks, and rotating or vibrating membranes. In: Progress in Filtration and Separation. Academic Press, pp. 27–59.

Discart, V., Bilad, M.R., Vandamme, D., Foubert, I., Muylaert, K., Vankelecom, I.F.J., 2013. Role of transparent exopolymeric particles in membrane fouling: *Chlorella vulgaris* broth filtration. Bioresource Technology 129, 18–25.

Dosmar, M., Meyeroltmanns, F., Gohs, M., 2005. Factors influencing ultrafiltration scale-up. Bioprocess Engineering 3, 40–50.

Drexler, I.L.C., Yeh, D.H., 2014. Membrane applications for microalgae cultivation and harvesting: a review. Reviews in Environmental Science and Biotechnology 13, 487–504.

Dubois, M., Gilles, K.A., Hamilton, J.K., Rebers, P.A., Smith, F., 1956. Colorimetric Method for Determination of Sugars and Related Substances. Analytical Chemistry 28, 350–356.

Duncan, M.R., Lee, J.M., Warchol, M.P., 1995. Influence of surfactants upon protein/peptide adsorption to glass and polypropylene. International Journal of Pharmaceutics 120, 179–188.

Dutta Sinha, S., Chatterjee, S., Maity, P.K., Tarafdar, S., Moulik, S.P., 2015. Studies of protein adsorption on implant materials in relation to biofilm formation. I. Activity of *Pseudomonas aeruginosa* on polypropylene and high density polyethylene in presence of serum albumin, Biological Physics.

Eardley-Patel, R., 2008. Development of engineering methods for the rapid evaluation of membrane filtration within bioprocesses. Thesis (PhD). University College London.

Eustance, E., Gardner, R.D., Moll, K.M., Menicucci, J., Gerlach, R., Peyton, B.M., 2013. Growth, nitrogen utilization and biodiesel potential for two chlorophytes grown on ammonium, nitrate or urea. Journal of Applied Phycology 25, 1663–1677.

Faitli, J., 2001. Pressure loss calculation model for well-graded solid-liquid pipe flows on the basis of systematic pilot plant investigation.

Fan, F., Zhou, H., Husain, H., 2006. Identification of wastewater sludge characteristics to predict critical flux for membrane bioreactor processes. Water Research 40, 205–212.

Fane, A.G., 2012. Microfiltration of algae (*Chlorella sorokiniana*): Critical flux, fouling and transmission. Journal of Membrane Science 387–388, 83–92.

Fernandez-Cerezo, L., Rayat, A.C.M.E., Chatel, A., Pollard, J.M., Lye, G.J., Hoare, M., 2019. An ultra scale-down method to investigate monoclonal antibody processing during tangential flow filtration using ultrafiltration membranes. Biotechnology and Bioengineering 116, 581–590.

Field, R.W., Wu, D., Howell, J. A., Gupta, B.B., 1995. Critical flux concept for microfiltration fouling. Journal of Membrane Science 100, 259–272.

Fimbres-Weihs, G.A., Wiley, D.E., 2007. Numerical study of mass transfer in three-dimensional spacer-filled narrow channels with steady flow. Journal of Membrane Science 306, 228–243.

Foley, G., MacLoughlin, P.F., Malone, D.M., 1995. Membrane fouling during constant flux crossflow microfiltration of dilute suspensions of active dry yeast. Separation Science and Technology 30, 383–398.

Foley, G., Mccarthy, A., Walsh, P., 2005. Evidence for shape-dependent deposition in crossflow microfiltration of microbial cells. Journal of Membrane Science 250, 311–313.

Foster, P.R., Dunnill, P., Lilly, M.D., 1976. The kinetics of protein salting-out: Precipitation of yeast enzymes by ammonium sulfate. Biotechnology and Bioengineering 18, 545–580.

Francis, P., Martinez, D.M., Taghipour, F., Bowen, B.D., Haynes, C.A., 2006. Optimizing the rotor design for controlled-shear affinity filtration using computational fluid dynamics. Biotechnology and bioengineering 95, 1207–17.

Frei, W., 2013. Which Turbulence Model Should I Choose for My CFD Application? [WWW Document]. COMSOL Blog. URL http://www.comsol.com/blogs/which-turbulence-model-should-choose-cfd-application/ (accessed 8.31.15).

Frenander, U., Jönsson, A.S., 1996. Cell harvesting by cross-flow microfiltration using a shear-enhanced module. Biotechnology and bioengineering 52, 397–403.

Fuentes, J.L., Garbayo, I., Cuaresma, M., Montero, Z., González-Del-Valle, M., Vílchez, C., 2016. Impact of microalgae-bacteria interactions on the production of algal biomass and associated compounds. Marine drugs 14, 100.

Fuhr, T., Holcomb, M., Rutten, P., 2009. Why quality-by-design should be on the executive team's agenda. In: Developing New Strategies for New Times. Mckinsey & Company, pp. 195–203.

Gabler, R., Ryan, M., 1985. Processing cell lysate with tangential flow filtration. In: purification of fermentation products. pp. 1–20.

GE Healthcare, 2014. Cross flow filtration method handbook. GE Healthcare.

Ghidossi, R., Veyret, D., Moulin, P., 2006. Computational fluid dynamics applied to membranes: State of the art and opportunities. Chemical Engineering and Processing: Process Intensification 45, 437–454.

Ghosh, R., Cui, Z., 2000. Analysis of protein transport and polarization through membranes using pulsed sample injection technique. Journal of Membrane Science 175, 75–84.

Gispert, M.P., Serro, A.P., Colaço, R., Saramago, B., 2008. Bovine serum albumin

adsorption onto 316L stainless steel and alumina: a comparative study using depletion, protein radiolabeling, quartz crystal microbalance and atomic force microscopy. Surface and Interface Analysis 40, 1529–1537.

González-Fernánde, C., Ballesteros, M., 2013. Microalgae autoflocculation: An alternative to high-energy consuming harvesting methods. Journal of Applied Phycology 25, 991–999.

Gröber, H., Erk, S., Grigull, U., Moszynski, J.R., 1961. Fundamentals of heat transfer.

Guo, S., Kiefer, H., Zhou, D., Guan, Y.H., Wang, S., Wang, H., Lu, Y., Zhuang, Y., 2016. A scale-down cross-flow filtration technology for biopharmaceuticals and the associated theory. Journal of Biotechnology 221, 25–31.

Gurreri, L., Tamburini, A., Cipollina, A., Micale, G., Ciofalo, M., 2014. CFD prediction of concentration polarization phenomena in spacer-filled channels for reverse electrodialysis. Journal of Membrane Science 468, 133–148.

Henderson, R.K., Baker, A., Parsons, S.A., Jefferson, B., 2008. Characterisation of algogenic organic matter extracted from cyanobacteria, green algae and diatoms. Water Research 42, 3435–3445.

Hermia, J., 1982. Constant pressure blocking filtration laws - application to Power-law non-newtonian fluids. Institution of Chemical Engineers 60, 183–187.

Higgins, B.T., VanderGheynst, J.S., 2014. Effects of *Escherichia coli* on mixotrophic growth of *Chlorella minutissima* and production of biofuel precursors. PLoS ONE 9, e96807.

Hongjin, Q., Guangce, W., 2009. Effect of carbon source on growth and lipid accumulation in *Chlorella sorokiniana* GXNN01. Chinese Journal of Oceanology and Limnology 27, 762–768.

Horiuchi, J.-I., Ohba, I., Tada, K., Kobayashi, M., Kanno, T., Kishimoto, M., 2003. Effective cell harvesting of the halotolerant microalgae *Dunaliella tertiolecta* with pH control. Journal of bioscience and bioengineering 95, 412–5.

Huisman, I.H., Vellenga, E., Trägårdh, G., Trägårdh, C., 1999. The influence of the membrane zeta potential on the critical flux for crossflow microfiltration of particle suspensions. Journal of Membrane Science 156, 153–158.

Hwang, K.J., Lin, S.J., 2014. Filtration flux-shear stress-cake mass relationships in microalgae rotating-disk dynamic microfiltration. Chemical Engineering Journal 244, 429–437.

Hwang, K.J., Wu, S.E., 2015. Disk structure on the performance of a rotating-disk dynamic filter: A case study on microalgae microfiltration. Chemical Engineering Research and Design 94, 44–51.

Hyun, B.S., Balachandar, R., Yu, K., Patel, V., 2003. Assessment of PIV to measure mean velocity and turbulence in water flow. Experiments in Fluids 35, 262–267.

Invitrogen Corporation, 2002. Pichia Fermentation Process Guidelines Overview. Progress in Botany 67, 1–11.

Iverson, K., 2003. Troubleshooting Tangential Flow Filtration. CEP Magazine 54–56.

Jaffrin, M.Y., 2008. Dynamic shear-enhanced membrane filtration: A review of rotating disks, rotating membranes and vibrating systems. Journal of Membrane Science 324, 7–25.

Jaffrin, M.Y., 2012. Hydrodynamic techniques to enhance membrane filtration. Annual Review of Fluid Mechanics 44, 77–96.

Janson, J., 2011. Protein purification : principles, high resolution methods and applications. Wiley.

Jepsen, K., Bram, M., Pedersen, S., Yang, Z., 2018. Membrane fouling for produced water treatment: a review study from a process control perspective. Water 10, 847.

Jones, A.K., Rhodes, M.E., Evans, S.C., 1973. The use of antibiotics to obtain axenic cultures of algae. British Phycological Journal 8, 185–196.

Juang, R.S., Chen, H.L., Chen, Y.S., 2008. Resistance-in-series analysis in cross-

flow ultrafiltration of fermentation broths of Bacillus subtilis culture. Journal of Membrane Science 323, 193–200.

Karabelas, A.J., Koutsou, C.P., Sioutopoulos, D.C., 2018. Comprehensive performance assessment of spacers in spiral-wound membrane modules accounting for compressibility effects. Journal of Membrane Science 549, 602–615.

Keskinler, B., Yildiz, E., Erhan, E., Dogru, M., Bayhan, Y.K., Akay, G., 2004. Crossflow microfiltration of low concentration-nonliving yeast suspensions. Journal of Membrane Science 233, 59–69.

Kinzlmaier, D., Goodrich, E., 2016. High viscosity tangential flow filtration (tff) applications. BioProcess International 1.

Koutsou, C.P., Karabelas, A.J., 2012. Shear stresses and mass transfer at the base of a stirred filtration cell and corresponding conditions in narrow channels with spacers. Journal of Membrane Science 399, 60–72.

Koutsou, C.P., Yiantsios, S.G., Karabelas, A.J., 2007. Direct numerical simulation of flow in spacer-filled channels: Effect of spacer geometrical characteristics. Journal of Membrane Science 291, 53–69.

Kumar, K., Dasgupta, C.N., Das, D., 2014. Cell growth kinetics of *Chlorella sorokiniana* and nutritional values of its biomass. Bioresource technology 167, 358–66.

Kuzmin, D., 2006. Introduction to Computational Fluid Dynamics. University of Dortmund.

Kwon, D.Y., Vigneswaran, S., Fane, A.G., Aim, R. Ben, 2007. Experimental determination of critical flux in cross-flow microfiltration 19, 169–181.

Ladeg, S., Zhu, Z., Moulai-Mostefa, N., Ding, L., Jaffrin, M.Y., 2018. CFD simulation of the distribution of pressure and shear rate on the surface of rotating membrane equipped with vanes for the ultrafiltration of dairy effluent. Arabian Journal for Science and Engineering 43, 2237–2245.

Ladner, D.A., Vardon, D.R., Clark, M.M., 2010. Effects of shear on microfiltration and ultrafiltration fouling by marine bloom-forming algae. Journal of Membrane Science 356, 33–43.

Lakaniemi, A.-M., Hulatt, C.J., Thomas, D.N., Tuovinen, O.H., Puhakka, J.A., 2011. Biogenic hydrogen and methane production from *Chlorella vulgaris* and Dunaliella tertiolecta biomass. Biotechnology for biofuels 4, 34.

Lau, E.C., Kong, S., McNulty, S., Entwisle, C., Mcilgorm, A., Dalton, K.A., Hoare, M., 2013. An ultra scale-down characterization of low shear stress primary recovery stages to enhance selectivity of fusion protein recovery from its molecular variants. Biotechnology and Bioengineering 110, 1973–1983.

Le-Clech, P., Chen, V., Fane, T.A.G., 2006. Fouling in membrane bioreactors used in wastewater treatment. Journal of Membrane Science 284, 17–53.

Lee, S.S., Burt, A., Russotti, G., Buckland, B., 1995. Microfiltration of recombinant yeast cells using a rotating disk dynamic filtration system. Biotechnology and bioengineering 48, 386–400.

Lee, Y., Clark, M.M., 1998. Modeling of flux decline during crossflow ultrafiltration of colloidal suspensions. Journal of Membrane Science 149, 181–202.

Leveque, A., 1928. The laws of heat transmission by convection. Dunod, Paris.

Li, F., Meindersma, W., de Haan, A.., Reith, T., 2004. Experimental validation of CFD mass transfer simulations in flat channels with non-woven net spacers. Journal of Membrane Science 232, 19–30.

Li, F., Meindersma, W., de Haan, A.B., Reith, T., 2002. Optimization of commercial net spacers in spiral wound membrane modules. Journal of Membrane Science 208, 289–302.

Li, N.N., Fane, A.G., Ho, W.S.W., Matsuura, T., 2008. Advanced membrane technology and applications. John Wiley & Sons, Hoboken, NJ, USA.

Li, Q., Mannall, G.J., Ali, S., Hoare, M., 2013. An ultra scale-down approach to study

the interaction of fermentation, homogenization, and centrifugation for antibody fragment recovery from rec *E. coli*. Biotechnology and Bioengineering 110, 2150–2160.

Li, T., Zheng, Y., Yu, L., Chen, S., 2013. Bioresource Technology High productivity cultivation of a heat-resistant microalga *Chlorella sorokiniana* for biofuel production. Bioresource Technology 131, 60–67.

Lipnizki, F., Lipnizki, J., Hansen, R., Hvidberg, J., Hjertager, B.H., 2003. Membrane spacers for ultrafiltration: modelling of mass transfer and pressure. In: IMSTEC'03, Paper Number 121. pp. 1–6.

Liu, J., Zhu, Y., Tao, Y., Zhang, Y., Li, A., Li, T., Sang, M., Zhang, C., 2013. Freshwater microalgae harvested via flocculation induced by pH decrease. Biotechnology for biofuels 6, 98.

Lizzul, A.M., Hellier, P., Purton, S., Baganz, F., Ladommatos, N., Campos, L., 2014. Combined remediation and lipid production using *Chlorella sorokiniana* grown on wastewater and exhaust gases. Bioresource Technology 151, 12–18.

Lutz, H., 2015. Ultrafiltration for bioprocessing: development and implementation of robusts processes. Woodhead Publishing, Cambridge.

Lutz, H., Arias, J., Zou, Y., 2016. High concentration biotherapeutic formulation and ultrafiltration: Part 1 pressure limits. Biotechnology Progress 33, 113–124.

Ma, G., 2009. Development of Ultra Scale-down shear filtration system and modelling of large scale diafiltration system. Thesis (PhD). University College London.

Ma, G., Aucamp, J., Gerontas, S., Eardley-Patel, R., Craig, A., Hoare, M., Zhou, Y., 2010. Mimic of a large-scale diafiltration process by using ultra scale-down rotating disc filter. Biotechnology progress 26, 466–76.

MacKay, D., Salusbury, T., 1988. Choosing between centrifugation and crossflow microfiltration. Chemical engineer 447, 45–50.

Malériat, J.P., Jaouen, P., Rossignol, N., Schlumpf, J.P., Quemeneur, F., 2000.

Influence of the adsorption of alginates on the properties of organic membranes for microfiltration and ultrafiltration. Journal of Water Sciences 13, 269–287.

Marcos, B., Moresoli, C., Skorepova, J., Vaughan, B., 2009. CFD modeling of a transient hollow fiber ultrafiltration system for protein concentration. Journal of Membrane Science 337, 136–144.

Masri, M.F., Lawrence, K., Wall, I., Hoare, M., 2017. An ultra scale-down methodology to characterize aspects of the response of human cells to processing by membrane separation operations. Biotechnology and Bioengineering 114, 1241–1251.

McCarthy, A.A., 2002. Experimental techniques for quantifying the cake mass, the cake and membrane resistances and the specific cake resistance during crossflow filtration of microbial suspensions. Journal of Membrane Science 201, 31–45.

McCarthy, A.A., Gilboy, P., Walsh, P.K., Foley, G., 1999. Characterisation of cake compressibility in dead-end microfiltration of microbial suspensions. Chemical Engineering Communications 173, 79–90.

McCarthy, A.A., O'Shea, D.G., Murray, N.T., Walsh, P.K., Foley, G., 1998. Effect of cell morphology on dead-end filtration of the dimorphic yeast *Kluyveromyces marxianus*. Biotechnology progress 14, 279–285.

McCoy, R., Hoare, M., Ward, S., 2009. Ultra scale-down studies of the effect of shear on cell quality; processing of a human cell line for cancer vaccine therapy. Biotechnology Progress 25, 1448–1458.

Meng, S., Liu, Y., 2013. Alginate block fractions and their effects on membrane fouling. Water research 47, 6618–6627.

Merck Life Science KGaA, 2013. PF3654EN00 Pellicon 3 Cassettes with Ultracel Membrane Performance Guide.

Merck Life Science KGaA, 2018. Pellicon 2 Ultrafiltration Cassettes - Pellicon 2 Cassettes FAQ [WWW Document]. URL http://www.merckmillipore.com/DE/en/product/Pellicon-2-Ultrafiltration-Cassettes,MM_NF-C613#documentation (accessed 5.31.18).

Miao, X., Wu, Q., 2006. Biodiesel production from heterotrophic microalgal oil. Bioresource Technology 97, 841–846.

Miller, D.J., Kasemset, S., Paul, D.R., Freeman, B.D., 2014. Comparison of membrane fouling at constant flux and constant transmembrane pressure conditions. Journal of Membrane Science 454, 505–515.

Millipore, 2003. TB032 Protein concentration and diafiltration by tangential flow filtration.

Millipore, 2007. AN1026EN00 Increase product yield in your UF/DF process.

Millipore, 2011. P99101 Ultrafiltration membranes operating manual.

Millipore, 2015. Optimization and process simulation [WWW Document]. Ultrafiltration Learning Center | Biopharmaceutical Manufacturing. URL http://www.merckmillipore.com/GB/en/ps-learning-centers/ultrafiltration-learning-center/optimization-process-simulation/d_eb.qB.ZWQAAAFAUV8ENHoL,nav (accessed 3.13.15).

Millipore, 2016. TB5882EN00 Recovery optimization of process scale ultrafiltration/diafiltration systems.

Millipore, 2018a. PF3654EN00 Pellicon 3 cassettes with Ultracel membrane performance guide.

Millipore, 2018b. AN1045EN00 Clarification and recovery of recombinant proteins using a cascade tangential flow filtration (TFF) system.

Mohs, R.C., Greig, N.H., 2017. Drug discovery and development: Role of basic biological research. Alzheimer's & Dementia: Translational Research & Clinical Interventions 3, 651–657.

Molina Grima, E., Belarbi, E.H., Acién Fernández, F.G., Robles Medina, A., Chisti, Y., 2003. Recovery of microalgal biomass and metabolites: Process options and economics. Biotechnology Advances 20, 491–515.

Morineau-Thomas, O., Jaouen, P., Legentilhomme, P., 2002. The role of exopolysaccharides in fouling phenomenon during ultrafiltration of microalgae (*Chlorella sp.* and *Porphyridium purpureum*): advantage of a swirling decaying flow. Bioprocess and biosystems engineering 25, 35–42.

Moronta, R., Mora, R., Morales, E., 2006. Response of the microalga *Chlorella sorokiniana* to pH, salinity and temperature in axenic and non axenic conditions. Journal of the Faculty of Agronomy 23, 27–41.

Mukherjee, N., 2014. Membrane filtration fouling: Drop in flow rate, why? [WWW Document]. LinkedIn. URL https://www.google.co.uk/search?q=Membrane+filtration+fouling%3A+Drop+in+flow +rate%2C+why%3F&oq=Membrane+filtration+fouling%3A+Drop+in+flow+rate%2C +why%3F&aqs=chrome..69i57j69i60&sourceid=chrome&ie=UTF-8 (accessed 10.3.18).

Murkes, J., Carlsson, C.G., 1988. Crossflow filtration: theory and practice. Wiley, Chichester[England]; New York.

Newton, J., Schofield, D., Vlahopoulou, J., Zhou, Y., 2016. Using rheology as an indicator of cell lysis in *E. coli* fermentations to prevent product loss and determine optimal harvest time. Biotechnology and bioengineering 121, 38–48.

Ngan, C., Zou, Y., Hillier, B., Bartlett, A., 2014. High viscosity TFF device design (US Patent application #20140231339).

Ngangkham, M., Ratha, S.K., Prasanna, R., Saxena, A.K., Dhar, D.W., Sarika, C., Prasad, R.B.N., 2012. Biochemical modulation of growth, lipid quality and productivity in mixotrophic cultures of *Chlorella sorokiniana*. SpringerPlus 1, 33.

Noble, R.D., Stern, S.A., 1995. Membrane separations technology: principles and applications, 1st ed. Elsevier Science.

Novais, J.L., Titchener-Hooker, N.J., Hoare, M., 2001. Economic comparison between conventional and disposables-based technology for the production of biopharmaceuticals. Biotechnology and bioengineering 75, 143–53.

Noyes, A., Basha, J., Frostad, J., Cook, S., Millard, D., Mullin, J., LaCasse, D., Wright, R.S., Huffman, B., Fahrner, R., Godavarti, R., Titchener-Hooker, N., Sunasara, K., Mukhopadhyay, T., 2015. A modular approach for the ultra scale-down of depth filtration. Journal of Membrane Science 496, 199–210.

Ostarcevic, E., Jacangelo, J., Gray, S., Cran, M., Ostarcevic, E.R., Jacangelo, J., Gray, S.R., Cran, M.J., 2018. Current and emerging techniques for high-pressure membrane integrity testing. Membranes 8, 60.

Ousman, M., Bennasar, M., 1995. Determination of various hydraulic resistances during cross-flow filtration of a starch grain suspension through inorganic membranes. Journal of Membrane Science 105, 1–21.

Pak, A., Mohammadi, T., Hosseinalipour, S.M., Allahdini, V., 2008. CFD modeling of porous membranes. Desalination 222, 482–488.

PallSep Biotech Systems, 2009. A gentle, efficient separation technology for complex biotech harvest and clarification applications (GN09.2894).

Panalytical, M., 2015. Using the power law model to quantify shear thinning behavior on a rotational rheometer [WWW Document]. URL https://www.azom.com/article.aspx?ArticleID=11624 (accessed 6.26.19).

Passow, U., 2002. Transparent exopolymer particles (TEP) in aquatic environments. Progress in Oceanography 55, 287–333.

Passow, U., Alldredge, A.L., 1994. Distribution, size and bacterial colonization of transparent exopolymer particles (TEP) in the ocean. Marine Ecology Progress Series 113, 185–198.

Pathak, N., Norman, C., Kundu, S., Nulu, S., Durst, M., Fang, Z., 2008. Modeling flow distribution in large-scale chromatographic columns with computational fluid dynamics. BioProcess International 6, 72–81.

Pattnaik, P., Lau, S.Y., Ito, T., Raghunath, B., 2014. Impact of process loading on optimization and scale-up of TFF microfiltration. BioProcessing Journal 13, 46–55.

Perry, R.H., Green, D.W., 2008. Perry's chemical engineers' handbook, 8th ed. McGraw-Hill Education.

Poelman, E., De Pauw, N., Jeurissen, B., 1997. Potential of electrolytic flocculation for recovery of micro-algae. Resources, Conservation and Recycling 19, 1–10.

Pordal, H.S., Matice, C.J., Fry, T.J., 2002. The role of computational fluid dynamics in the pharmaceutical industry. Pharmaceutical technology 26, 72–80.

Porter, M.C., 1972. Concentration polarization with membrane ultrafiltration. Industrial & Engineering Chemistry Product Research and Development 11, 234–248.

Postlethwaite, J., Lamping, S.R., Leach, G.C., Hurwitz, M.F., Lye, G.J., 2004. Flux and transmission characteristics of a vibrating microfiltration system operated at high biomass loading. Journal of Membrane Science 228, 89–101.

Qu, F., Liang, H., Wang, Z., Wang, H., Yu, H., Li, G., 2012. Ultrafiltration membrane fouling by extracellular organic matters (EOM) of Microcystis aeruginosa in stationary phase: Influences of interfacial characteristics of foulants and fouling mechanisms. Water Research 46, 1490–1500.

Raghunath, B., Bin, W., Pattnaik, P., Janssens, J., 2012. Best practices for optimization and scale-up of microfiltration TFF processes. BioProcessing Journal 11, 29–40.

Rahimi, M., Madaeni, S., Abbasi, K., 2005. CFD modeling of permeate flux in cross-flow microfiltration membrane. Journal of Membrane Science 255, 23–31.

Rainer, M., Höflinger, W., Koch, W., Pongratz, E., Oechsle, D., 2002. 3D-flow simulation and optimization of a crossflow filtration with rotating discs. Separation and Purification Technology 26, 121–131.

Ranade, V. V., Kumar, A., 2006. Fluid dynamics of spacer filled rectangular and curvilinear channels. Journal of Membrane Science 271, 1–15.

Randriamampianina, A., Elena, L., Fontaine, J.P., Schiestel, R., 1997. Numerical prediction of laminar, transitional and turbulent flows in shrouded rotor-stator

systems. Physics of Fluids 9, 1696.

Ratha, S.K., Babu, S., Renuka, N., Prasanna, R., Badari, R., 2013. Exploring nutritional modes of cultivation for enhancing lipid accumulation in microalgae. Journal of Basic Microbiology 53, 440–450.

Ratkovich, N., Chan, C.C. V, Bentzen, T.R., Rasmussen, M.R., 2012. Experimental and CFD simulation studies of wall shear stress for different impeller configurations and MBR activated sludge. Water science and technology 65, 2061–2070.

Rayat, A.C., Chatel, A., Hoare, M., Lye, G.J., 2016. Ultra scale-down approaches to enhance the creation of bioprocesses at scale: impacts of process shear stress and early recovery stages. Current Opinion in Chemical Engineering 14, 150–157.

Rickman, M., Pellegrino, J., Davis, R., 2012. Fouling phenomena during membrane filtration of microalgae. Journal of Membrane Science 423–424, 33–42.

Ripperger, S., Altmann, J., 2002. Crossflow microfiltration-state of the art. Separation and Purification Technology 26, 19–31.

Rodrigues, M.A., da Silva Bon, E.P., 2011. Evaluation of *Chlorella* (Chlorophyta) as source of fermentable sugars via cell wall enzymatic hydrolysis. Enzyme research 2011, 1–5.

Rosenberg, J.N., Kobayashi, N., Barnes, A., Noel, E.A., Betenbaugh, M.J., Oyler, G.A., 2014. Comparative analyses of three chlorella species in response to light and sugar reveal distinctive lipid accumulation patterns in the microalga *C. sorokiniana.* PLoS ONE 9, 1–13.

Santos, J.L.C., Geraldes, V., Velizarov, S., Crespo, J.G., 2007. Investigation of flow patterns and mass transfer in membrane module channels filled with flow-aligned spacers using computational fluid dynamics (CFD). Journal of Membrane Science 305, 103–117.

Santos, O., Nylander, T., Rizzo, G., Müller-Steinhagen, H., Tragardh, C., Paulsson, M., 2003. Study of whey protein adsorption under turbulent flow. In: Heat Exchanger Fouling and Cleaning: Fundamentals and Applications. p. 175.

Saraswat, M., Musante, L., Ravidá, A., Shortt, B., Byrne, B., Holthofer, H., 2013. Preparative purification of recombinant proteins: current status and future trends. BioMed Research International 2013, 1–18.

Schiele, B., 1979. Investigations on the filtration of finely dispersed suspensions and on the flow in the dynamic pressure filter.

Schmidt-Traub, H., Schulte, M., Seidel-Morgenstern, A., 2012. Preparative chromatography, 2nd ed. Wiley-VCH Verlag GmbH & Co. KGaA.

Schwinge, J., Wiley, D.E., Fletcher, D.F., 2002. Simulation of the flow around spacer filaments between channel walls. 2. Mass-transfer enhancement. Industrial and Engineering Chemistry Research 41, 4879–4888.

Sengler, F., Haas, J., Lorenzi, R., 2015. Ultrafiltration/Diafiltration process development of high concentration/viscosity applications [WWW Document]. URL https://es.slideshare.net/FrdricSengler/ultrafiltrationdiafiltration-process-development-of-high-concentrationviscosity-application (accessed 2.3.19).

Serra, C.A., Wiesner, M.R., 2000. A comparison of rotating and stationary membrane disk filters using computational fluid dynamics. Journal of Membrane Science 165, 19–29.

Shakaib, M., Hasani, S.M.F., Mahmood, M., 2007. Study on the effects of spacer geometry in membrane feed channels using three-dimensional computational flow modeling. Journal of Membrane Science 297, 74–89.

Shakaib, M., Hasani, S.M.F., Mahmood, M., 2009. CFD modeling for flow and mass transfer in spacer-obstructed membrane feed channels. Journal of Membrane Science 326, 270–284.

Sharma, K.K., Garg, S., Li, Y., Malekizadeh, A., Schenk, P.M., 2013. Critical analysis of current Microalgae dewatering techniques. Biofuels 4, 397–407.

Sharma, Y.C., Singh, B., Korstad, J., 2011. A critical review on recent methods used for economically viable and eco-friendly development of microalgae as a potential feedstock for synthesis of biodiesel. Green Chemistry 13, 2993–3006.

Shekhawat, L.K., Sarkar, J., Gupta, R., Hadpe, S., Rathore, A.S., 2018. Application of CFD in Bioprocessing: Separation of mammalian cells using disc stack centrifuge during production of biotherapeutics. Journal of Biotechnology 267, 1–11.

Shukla, A.A., Etzel, M.R., Gadam, S., 2007. Process scale bioseparations for the biopharmaceutical industry. CRC/Taylor & Francis.

Slater, C.S., Savelski, M.J., Kostetskyy, P., Johnson, M., 2015. Shear-enhanced microfiltration of microalgae in a vibrating membrane module. Clean Technologies and Environmental Policy 17, 1743–1755.

Smith, K., Colton, C., Merrill, E., Evans, L., 1968. The artificial kidney. American Institute of Chemical Engineering. Chemical Engineering Progress 64, 45.

Song, L., Elimelech, M., 1995. Theory of concentration polarization in crossflow filtration. Journal of the Chemical Society, Faraday Transactions 91, 3389–3398.

Steen, J., 2015. Compact spiral-wound filter elements, modules and systems (US Patent #US 2015/0375173 A1).

Subramani, A., Kim, S., Hoek, E.M., 2006. Pressure, flow, and concentration profiles in open and spacer-filled membrane channels. Journal of Membrane Science 277, 7–17.

Szaub, J.B., 2012. Genetic engineering of green microalgae for the production of biofuel and high value products. Thesis (PhD). University College London.

Taamneh, Y., 2010. Numerical simulation of fluid flow in enclosed rotating filter and disk. Journal of Engineering and Applied Sciences 5, 48–53.

Taha, T., Cui, Z.., 2002. CFD modelling of gas-sparged ultrafiltration in tubular membranes. Journal of Membrane Science 210, 13–27.

Tait, A.S., Aucamp, J.P., Bugeon, A., Hoare, M., 2009. Ultra scale-down prediction using microwell technology of the industrial scale clarification characteristics by centrifugation of mammalian cell broths. Biotechnology and Bioengineering 104, 321–331.

Tarleton, E.S., Wakeman, R.J., 1993. Understanding flux decline in crossflow microfiltration . Part 1 - Effects of particle and pore size. Chemical Engineering Research and Design 71, 399–410.

Thomas, C.R., Dunnill, P., 1979. Action of shear on enzymes: Studies with catalase and urease. Biotechnology and Bioengineering 21, 2279–2302.

Thundil Karuppa Raj, R., Singh, A.D., Tare, S., Varma, S., 2014. Study of fluid flow around impeller blades in rushton turbine in a baffled vessel using computational fluid dynamics. ARPN Journal of Engineering and Applied Sciences 9, 659–666.

Titchener-Hooker, N.J., Dunnill, P., Hoare, M., 2008. Micro biochemical engineering to accelerate the design of industrial-scale downstream processes for biopharmaceutical proteins. Biotechnology and Bioengineering 100, 473–487.

Torras, C., Pallares, J., Garcia-Valls, R., Jaffrin, M.Y., 2006. CFD simulation of a rotating disk flat membrane module. Desalination 200, 453–455.

Torras, C., Pallares, J., Garcia-Valls, R., Jaffrin, M.Y., 2009. Numerical simulation of the flow in a rotating disk filtration module. Desalination 235, 122–138.

Tripathi, N.K., Shrivastava, A., 2018. Scale up of biopharmaceuticals production. In: Grumezescu, A.M. (Ed.), Nanoscale Fabrication, Optimization, Scale-Up and Biological Aspects of Pharmaceutical Nanotechnology. Elsevier, pp. 133–172.

Ujam, S., 2007. A scale-down evaluation of adsorptive process options for the recovery and initial purification of antibody fragments from crude *E. coli* feedstocks. Thesis (PhD). University College London.

Valencia, D., 2010. Flow simulation in a submerged membrane bioreactor at laboratory scale. In: COMSOL Conference 2010, Paris. COMSOL, pp. 1–7.

Van der Berg, G.B., Rácz, I.G., Smolders, C. a., 1989. Mass transfer coefficients in cross-flow ultrafiltration. Journal of Membrane Science 47, 25–51.

van Reis, R., Goodrich, E.M., Yson, C.L., Frautschy, L.N., Dzengeleski, S., Lutz, H., 1997. Linear scale ultrafiltration. Biotechnology and Bioengineering 55, 737–746.

Vigo, F., Uliana, C., Ravina, E., 1990. The vibrating ultrafiltration module. Performance in the low frequency region. Separation Science and Technology 25, 63–82.

Villacorte, L.O., Kennedy, M.D., Amy, G.L., Schippers, J.C., 2009. The fate of Transparent Exopolymer Particles (TEP) in integrated membrane systems: Removal through pre-treatment processes and deposition on reverse osmosis membranes. Water Research 43, 5039–5052.

Vogel, J.H., Kroner, K.H., 1999. Controlled shear filtration: A novel technique for animal cell separation. Biotechnology and bioengineering 63, 663–74.

Vonlanthen, S., Dauvillée, D., Purton, S., 2015. Evaluation of novel starch-deficient mutants of *Chlorella sorokiniana* for hyper-accumulation of lipids. Algal research 12, 109–118.

Wan, M., Wang, R., Xia, J., Rosenberg, J.N., Nie, Z., Kobayashi, N., Oyler, G.A., Betenbaugh, M.J., 2012. Physiological evaluation of a new *Chlorella sorokiniana* isolate for its biomass production and lipid accumulation in photoautotrophic and heterotrophic cultures. Biotechnology and bioengineering 109, 1958–1964.

Wardeh, S., Morvan, H.P., 2008. CFD simulations of flow and concentration polarization in spacer-filled channels for application to water desalination. Chemical Engineering Research and Design 86, 1107–1116.

Watanabe, K., Imase, M., Sasaki, K., Ohmura, N., Saiki, H., Tanaka, H., 2006. Composition of the sheath produced by the green alga *Chlorella sorokiniana*. Letters in Applied Microbiology 42, 538–543.

Watanabe, K., Takihana, N., Aoyagi, H., Hanada, S., Watanabe, Y., Ohmura, N., Saiki, H., Tanaka, H., 2005. Symbiotic association in *Chlorella* culture. FEMS Microbiology Ecology 51, 187–196.

WaterSep, 2009. Cross-flow filtration for discovery, scale-up and process clarification/concentration applications (WS 1001 08 REV 02).

Weyer, K.M., Bush, D.R., Darzins, A., Willson, B.D., 2009. Theoretical maximum algal

oil production. BioEnergy Research 3, 204–213.

Wicaksana, F., Fane, A.G., Pongpairoj, P., Field, R., 2012. Microfiltration of algae (*Chlorella sorokiniana*): Critical flux, fouling and transmission. Journal of Membrane Science 387–388, 83–92.

Wijmans, J.G., Nakao, S., Smolders, C.A., 1984. Flux limitation in ultrafiltration: Osmotic pressure model and gel layer model. Journal of Membrane Science 20, 115–124.

Wiley, D.E., Fletcher, D.F., 2002. Computational fluid dynamics modelling of flow and permeation for pressure-driven membrane processes. Desalination 145, 183–186.

Williams, K.A., Saini, S., Wick, T.M., 2002. Computational fluid dynamics modeling of steady-state momentum and mass transport in a bioreactor for cartilage tissue engineering. Biotechnology progress 18, 951–63.

Xiao, R., Zheng, Y., 2016. Overview of microalgal extracellular polymeric substances (EPS) and their applications. Biotechnology Advances 34, 1225–1244.

Yeh, D., Drexler, I.L.C., 2014. Membrane applications for microalgae cultivation and harvesting: a review. Reviews in Environmental Science and Bio/Technology 13, 487–504.

Yeh, H.M., Tsai, J.W., 1998. Membrane ultrafiltration in multipass hollow-fiber modules. Journal of Membrane Science 142, 61–73.

Yoon, S., 2011. Constant flux vs constant TMP [WWW Document]. URL http://onlinembr.info/Principles/Cons Flux vs Cons Pres.htm (accessed 3.4.15).

Yuanfa, L.I.U., Gaohong, H.E., Luhui, D., Hong, D.O.U., Jia, J.U., Baojun, L.I., 2012. Experimental and CFD studies on the performance of microfiltration enhanced by a turbulence promoter. Chinese Journal of Chemical Engineering 20, 617–624.

Zahka, J., Leahy, T.J., 1985. Practical aspects of tangential flow filtration in cell separations. In: Comstock, M.J. (Ed.), Purification of Fermentation Products. American Chemical Society, Washington, DC, pp. 51–69.

Zare, M., Zokaee Ashtiani, F., Fouladitajar, A., 2013. CFD modeling and simulation of concentration polarization in microfiltration of oil–water emulsions; Application of an Eulerian multiphase model. Desalination 324, 37–47.

Zhang, X., Fan, L., Roddick, F.A., 2012. Characterisation of the influence of algal organic matter on the fouling of a ceramic MF membrane. In: Advances in Civil, Environmental, and Materials Research (ACEM' 12). Seoul, Korea, pp. 1647–1656.

Zhang, X., Fan, L., Roddick, F.A., 2013. Influence of the characteristics of soluble algal organic matter released from *Microcystis aeruginosa* on the fouling of a ceramic microfiltration membrane. Journal of Membrane Science 425–426, 23–29.

Zhang, X., Hu, Q., Sommerfeld, M., Puruhito, E., Chen, Y., 2010. Harvesting algal biomass for biofuels using ultrafiltration membranes. Bioresource Technology 101, 5297–5304.

Zhu, L.D., Takala, J., Hiltunen, E., Wang, Z.M., 2013. Recycling harvest water to cultivate *Chlorella zofingiensis* under nutrient limitation for biodiesel production. Bioresource Technology 144, 14–20.

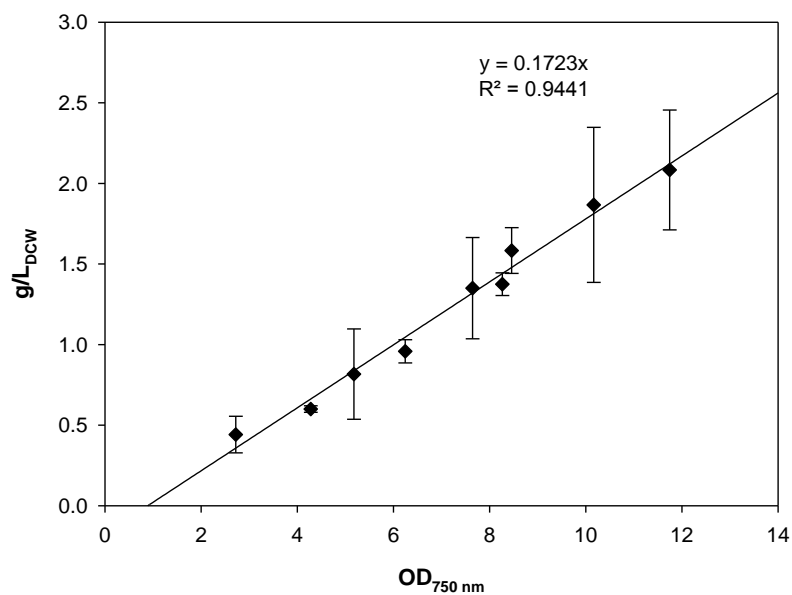# 10 Appendix

10.1 Calibration curves

Figure 10.1 OD$_{750\ nm}$ versus *Chlorella sorokiniana* g/L$_{DCW}$ calibration curve.
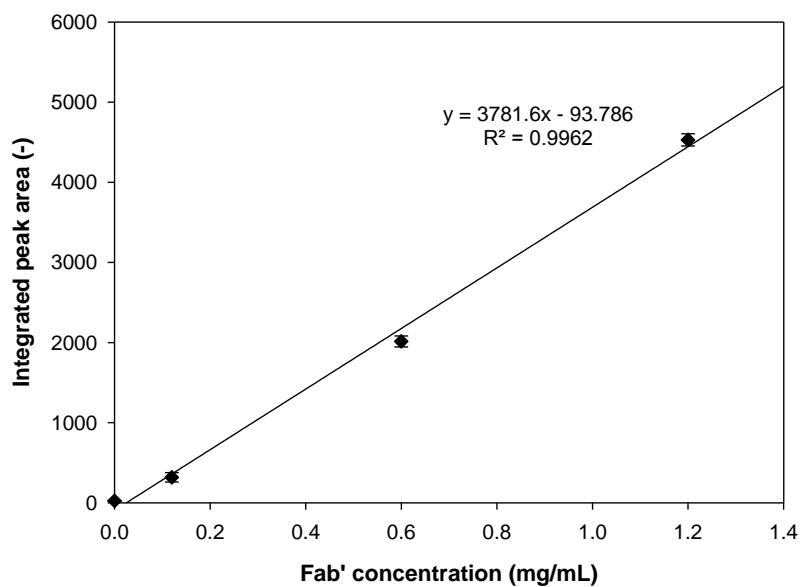

Figure 10.2 Standard curve for integrated peak areas (HPLC protein G) versus known standard concentrations of purified Fab'.
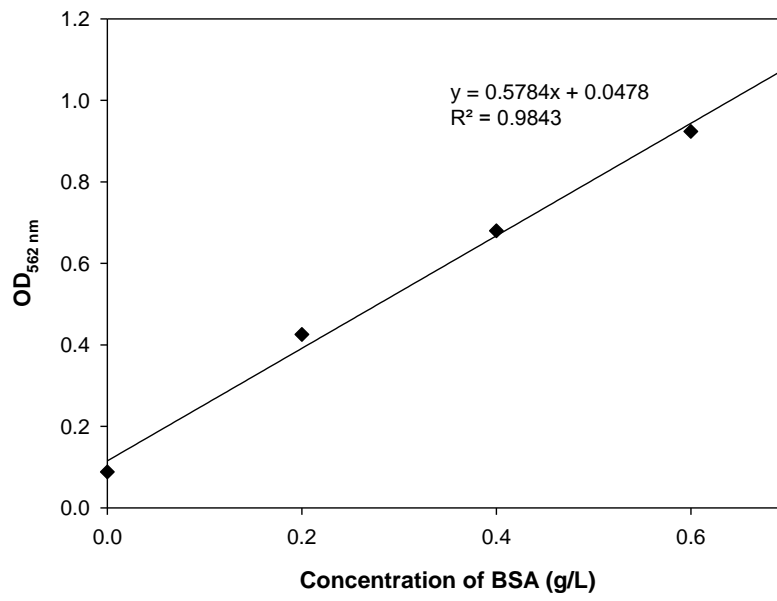
Figure 10.3 $OD_{562 nm}$ versus BSA solutions (0-1 g/L) standard curve for BCA protein assay.

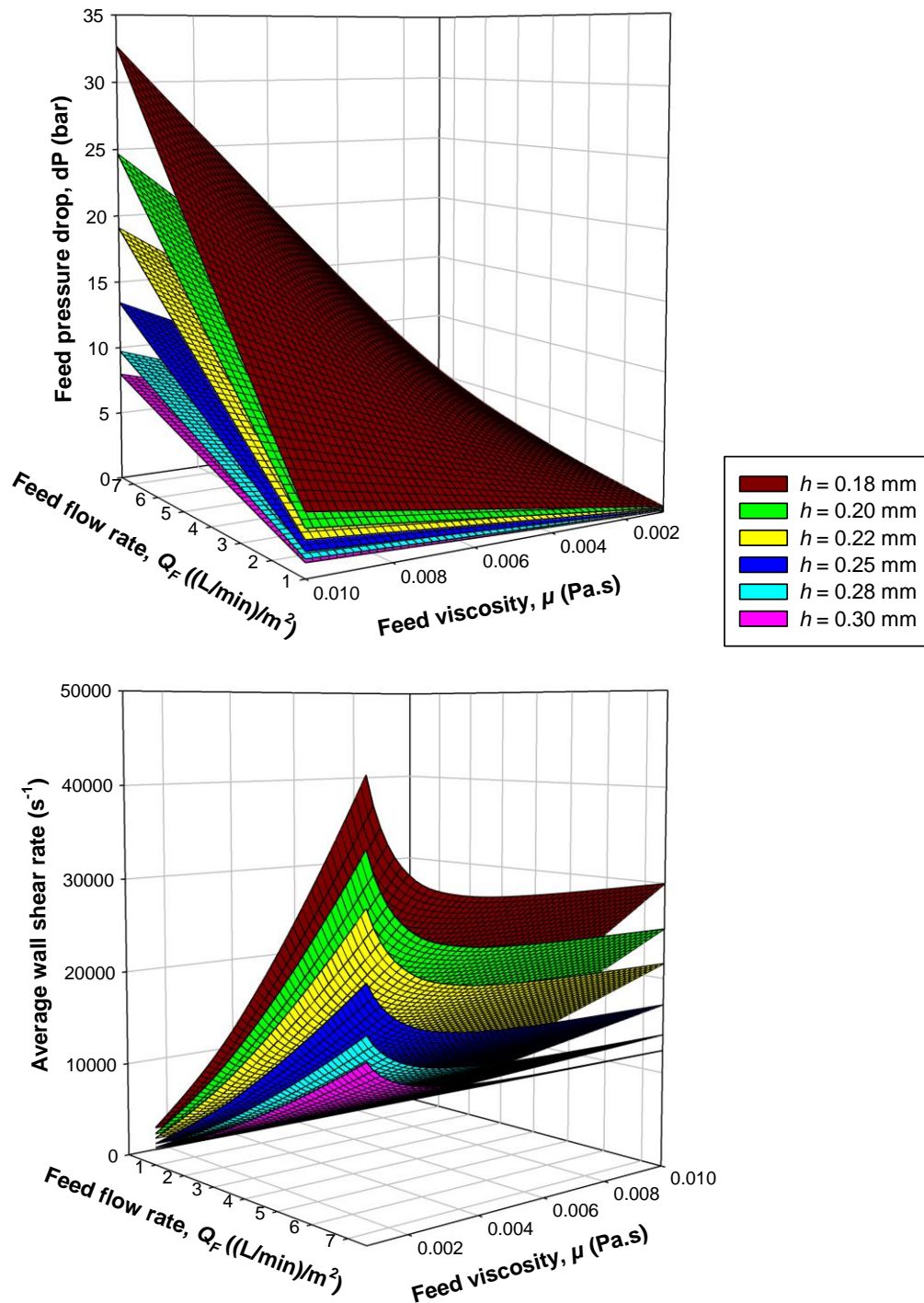## 10.2 CFD correlations for pressure drop and average wall shear rate for the Pellicon cassettes
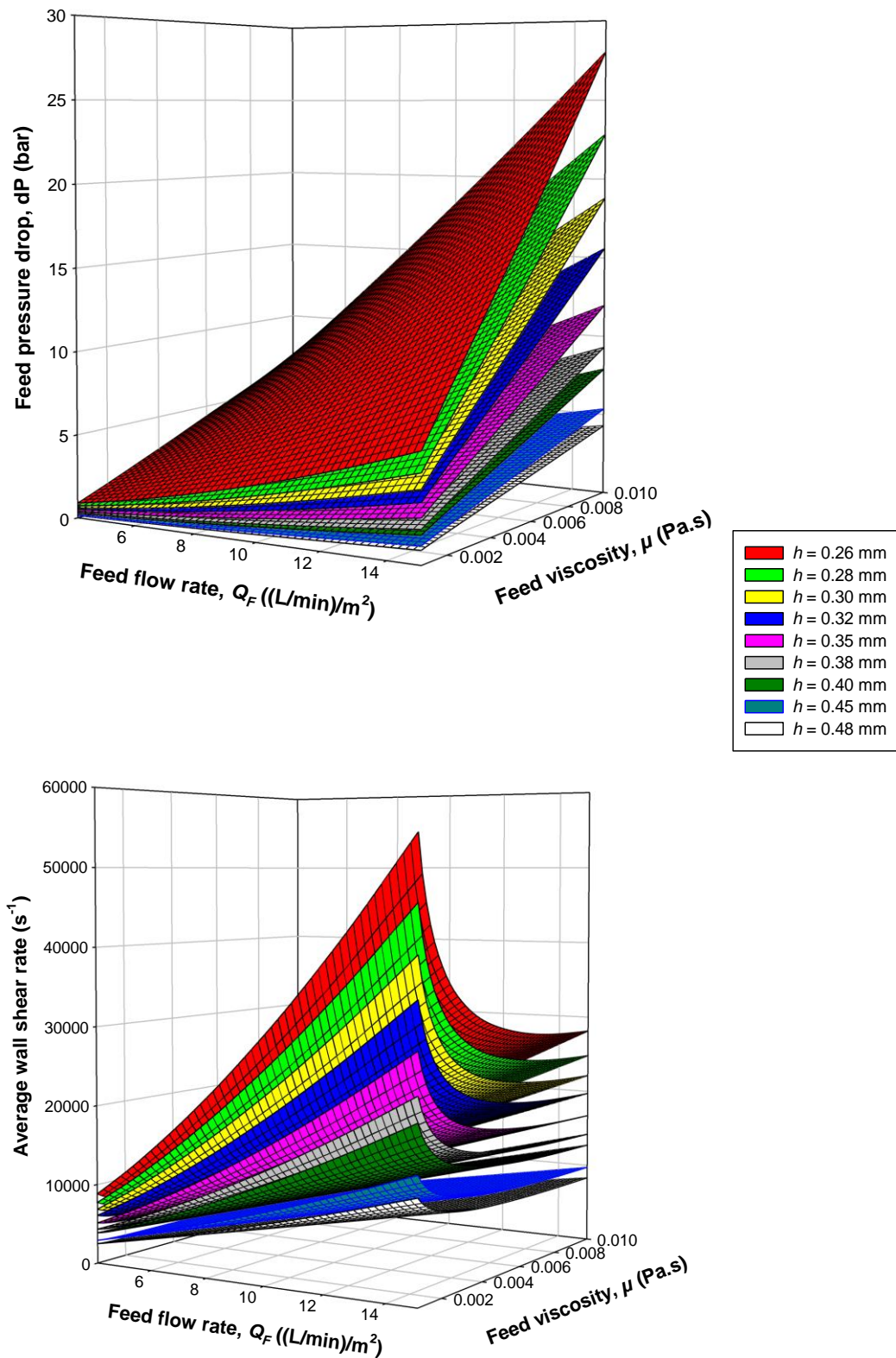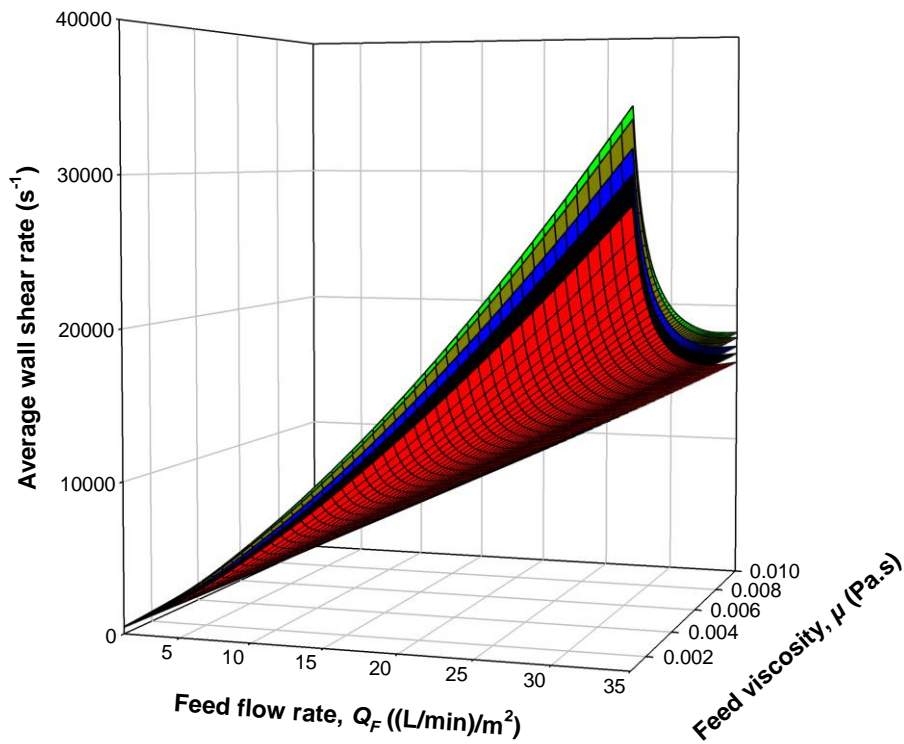
A screen:

Figure 10.4 Pressure drop (top) and average wall shear rate (bottom) versus flow rate and viscosity data for A screen cassette for different feed channel heights, *h*.

C screen:

Figure 10.5 Pressure drop (top) and average wall shear rate (bottom) versus flow rate and viscosity data for C screen cassette for different feed channel heights, h.
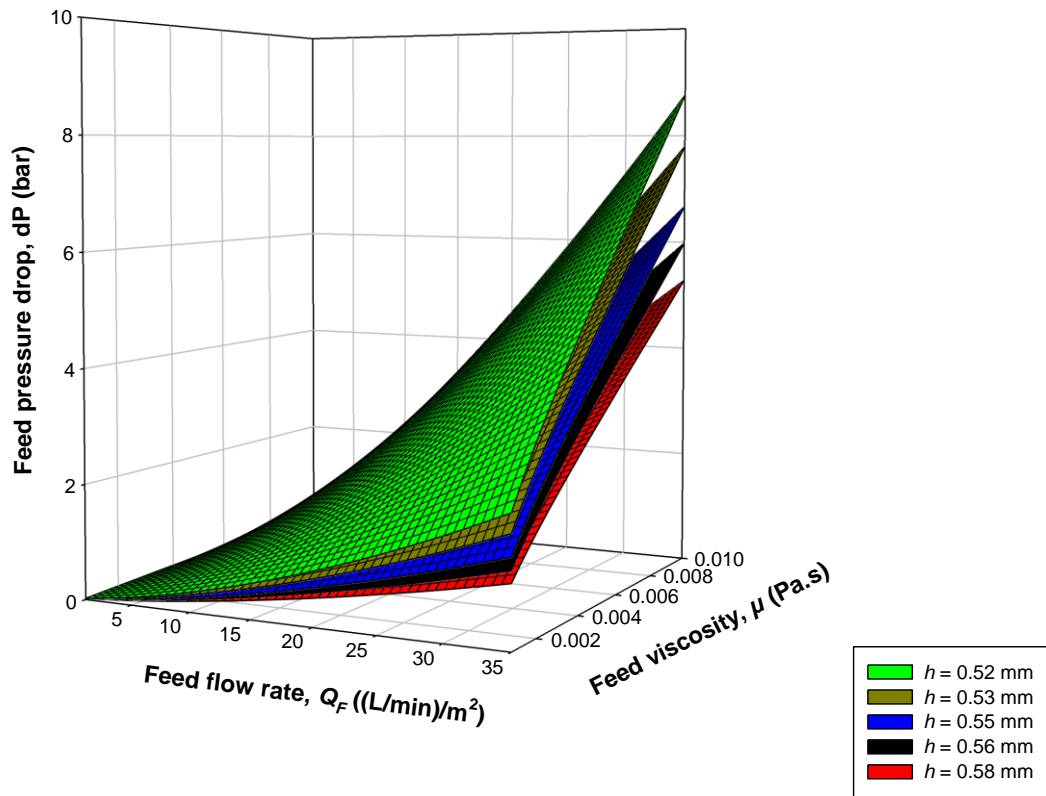
V screen:

Figure 10.6 Pressure drop (top) and average wall shear rate (bottom) versus flow rate and viscosity data for V screen cassette for different feed channel heights, h.